Technical University of Munich
Department of Physics
E19a - Nonequilibrium Chemical Physics

Carbon dioxide reduction on metal nanostructures on silicon

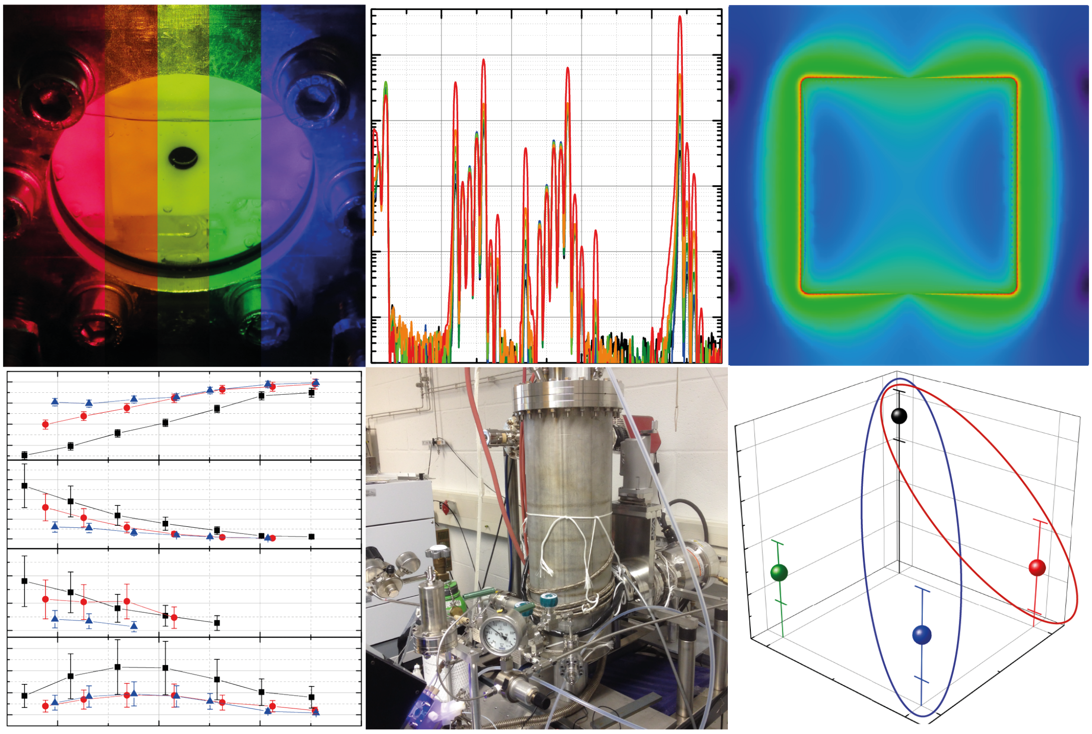

Dissertation

Simon Filser

Technical University of Munich
Department of Physics
E19a - Nonequilibrium Chemical Physics

Carbon dioxide reduction on metal nanostructures on silicon

Simon Filser

Vollständiger Abdruck der von der Fakultät für Physik der Technischen Universität München zur Erlangung des akademischen Grades eines

Doktors der Naturwissenschaften (Dr. rer. nat.)

genehmigten Dissertation.

Vorsitzender: Prof. Dr. David Egger

Prüfende der Dissertation:

1. Prof. Dr. Katharina Krischer
2. Prof. Dr. Aliaksandr Bandarenka

Die Dissertation wurde am 20.08.2019 bei der Technischen Universität München eingereicht und durch die Fakultät für Physik am 22.10.2019 angenommen.

.

Picture credits (title page): Upper left: Josef Zimmermann, lower left: Thomas Maier, upper right: Robin Nagel

Danksagung

An dieser Stelle will ich allen danken, die zu dieser Arbeit beigetragen haben. Als allererstes ist dies **Prof. Dr. Katharina Krischer**, die mir während der letzten Jahre eine wahre Doktormutter war. Sie gab mir nicht nur die Möglichkeit, in einem ungemein spannenden Thema zu promovieren, sondern hatte stets Verständnis für die Probleme, die unterwegs aufgetreten sind. Die Freiheit, meine Arbeit selbst einzuteilen und dabei viel zu lernen, weiß ich sehr zu schätzen. Ein besonderer Dank gilt **Dr. Werner Schindler**, der mir so viele große und kleine Dinge über experimentelles Arbeiten und Wissenschaft beigebracht hat. Einen großen Beitrag zu den Experimenten in dieser Arbeit haben die Bachelor-, Master- und Werkstudenten **Josef Zimmermann, Thomas L. Maier, Kilian Vettori** und **Lautaro Díaz Piola** geleistet. Meinem langjährigen Kooperationspartner **Robin Nagel** danke ich für die exzellente Zusammenarbeit und unzählige Proben in verschiedensten Ausführungen. Auch **Dr. Tianyue Zhang, Aurora Manzi, Matthias Golibrzuch, Simon Mendisch** und **Dr. Harald Oberhofer** danke ich für die erfolgreiche Zusammenarbeit.
Großer Dank gebührt der gesamten Arbeitsgruppe E19a, in der ich mich immer sehr wohlgefühlt habe, besonders **Dr. Qi Li**, der mich über meine ganze Zeit begleitet hat und mir ein toller Konferenzpartner war, **Dr. Konrad Schönleber**, der mich in mein Thema eingearbeitet und mir viele wertvolle Dinge nicht nur über Physik mitgegeben hat, **Markus Hass, Matthias Maier** und **Michael Stanglmeier** für die geduldige Bearbeitung meiner vielen Werkstattaufträge, **Dr. Katrin Bickel, Maximilian Patzauer, Anton Tosolini, Siegfried Schreier, Dr. Daniel Heger, Dr. Pierre-Yves Olu, Munir Salman, Dr. Felix Kemeth, Francesco Casablanca, Dr. Lennart Schmidt, Andreas Heine** und **Sindre Haugland** sowie allen anderen Kolleginnen und Kollegen für die tolle Zeit im Team. Für die Unterstützung bei verschiedenen experimentellen Aufgaben danke ich **Karl Eberle, Sonja Matich, Hubert Riedl, Egon Lenker, Prof. Dr. Michael Schuster, Stephan Fromm, Kai Saller, Max Kraut, Prof. Dr. Alexander Holleitner, Marcus Altzschner, Daniel Melzer** und ganz besonders **Prof. Dr. Andreas Ulrich**, der mir sehr bei meinem optischen Aufbau geholfen hat.
Nicht zuletzt gebührt meiner Familie großer Dank: Meinen Eltern **Angela** und **Hubert Filser** danke ich für die jahrelange Unterstützung und Wertschätzung, die mich durch mein Studium begleitet hat. Meiner Frau **Karin** und meinen Töchtern **Miriam, Theresa** und **Josefa** danke ich für die Aufmunterung und die Geduld, wenn es mal wieder etwas länger gedauert hat.

Abstract

In this thesis, the photoelectrochemical reduction of carbon dioxide on arrays of mesoscopic gold and copper structures on silicon is investigated. Such electrodes constitute a good model system for the investigation of fundamental processes in integrated solar fuel production. The main focus of this work lies on the impact of structuring on the behavior of metal/semiconductor samples: One major topic is the influence of structure size variation in the mesoscopic range on the electrochemical performance and product spectrum stemming from carbon dioxide reduction and hydrogen evolution. The second focal point is set on localized surface plasmon resonances occurring at gold nanostructures under resonant illumination. This includes simulation, tuning and measuring of these resonances and the examination of plasmonic effects on electrochemical reactions. Therefore, the current response under modulated illumination is probed and the impact of other heating mechanisms on the reactions is modeled. Further emphasis is put on the realization of a novel cold trap for the analysis of carbon dioxide reduction products by mass spectrometry. Its working principle is the desublimation of water and carbon dioxide, which usually make up the major part of the typical gas mixtures from carbon dioxide reduction experiments, on a cold surface.

Contents

1 Introduction 1

2 Background 5
- 2.1 Selected topics of semiconductor physics . . . 5
  - 2.1.1 Absorption and photoelectric effect in silicon . . . 5
  - 2.1.2 Metal/semiconductor interfaces . . . 7
  - 2.1.3 Electrolyte/semiconductor interfaces . . . 10
  - 2.1.4 Electrolyte/metal/insulator/semiconductor interfaces . . . 11
- 2.2 Important electrochemical reactions . . . 13
  - 2.2.1 Buffer solutions . . . 13
  - 2.2.2 Hydrogen and oxygen evolution reactions . . . 13
  - 2.2.3 Electrochemical CO_2 reduction . . . 14
- 2.3 Localized surface plasmon resonances . . . 16
  - 2.3.1 Plasmonic resonance wavelength . . . 16
  - 2.3.2 Plasmonic heating . . . 17
  - 2.3.3 Further plasmonic effects . . . 18

3 Experimental and theoretical methods 19
- 3.1 Sample preparation . . . 19
  - 3.1.1 Silicon samples and back contacts . . . 19
  - 3.1.2 Nanoimprint lithography . . . 20
  - 3.1.3 Nanotransfer printing . . . 22
  - 3.1.4 Cleaning . . . 22
  - 3.1.5 Copper deposition . . . 23
- 3.2 Sample geometry . . . 24
- 3.3 Photoelectrochemical setup . . . 26
  - 3.3.1 Electrodes and potentiostat . . . 26
  - 3.3.2 Electrochemical cells . . . 27
  - 3.3.3 Electrolytes and light sources . . . 28
- 3.4 Optical characterization . . . 30
- 3.5 X-ray photoelectron spectroscopy (XPS) . . . 30
- 3.6 Product analysis using gas chromatography (GC) . . . 31
- 3.7 Simulations . . . 33
- 3.8 Data analysis using Fourier Transformation and Welch's method . . . 34

4 Design of a cold trap for DEMS 36
- 4.1 Mass spectrometer and cold trap setup . . . 38
  - 4.1.1 Mass spectrometer and vacuum chamber . . . 38
  - 4.1.2 Sample inlet valve . . . 40
  - 4.1.3 Cold trap . . . 41
  - 4.1.4 Temperature control and nitrogen refilling . . . 43
- 4.2 Characterization and calibration . . . 44
  - 4.2.1 Vacuum quality . . . 44
  - 4.2.2 Temperature control and feedback mechanisms . . . 44
  - 4.2.3 Mass spectra of pure gases . . . 46
  - 4.2.4 Calibration with pure gases . . . 46
  - 4.2.5 Correction method for gas mixtures . . . 51
  - 4.2.6 Ideal operation temperature . . . 54

4.2.7 Correction for ethene 58
4.2.8 Comparison to gas chromatography measurements 59
4.2.9 Estimation of errors 61
4.3 Summary and outlook 62

5 Reactivity of arrays of mesoscopic (Cu/)Au/Ti/SiO_2/Si structures 64
5.1 Influence of fabrication method on MIS interface 65
5.2 Metal-semiconductor interface 66
5.3 Illumination limitation on p-Si 68
5.4 Sample stability 71
5.5 Influence of electrode structuring on electrochemical performance 72
5.5.1 Difference between continuous and structured Au films on Si 73
5.5.2 Influence of structure size of gold nanostructures on the electrochemical activity 75
5.6 Copper deposition on gold 78
5.6.1 Electrochemical deposition 79
5.6.2 Chemical deposition 82
5.6.3 Influence of the Cu deposition method on the product distribution 85
5.6.4 Stability of Cu layers 86
5.7 Influence of size of Cu/Au nanostructures on electrochemical activity 88
5.8 Discussion of size-dependent overpotential and product distribution 90
5.9 Summary and outlook 95

6 Plasmonic effects in electrochemistry 97
6.1 Simulations of the electric field 98
6.2 Optical characterization 99
6.2.1 Estimation of errors 105
6.3 Plasmonic resonances in electrochemical experiments 106
6.4 Plasmonic excitation of molecular vibrations and plasmonic heating 107
6.4.1 Influence of heating and temperature 108
6.4.2 Influence of heat transport on involved timescales 111
6.4.3 Plasmonic effects on the electrochemical performance 112
6.4.4 Influence of applied potential 116
6.4.5 Discussion of errors 117
6.5 Discussion 119
6.5.1 Optical characterization 119
6.5.2 Influence of the photoelectric effect 120
6.5.3 Influence of heat transfer and temperature 120
6.5.4 Origin of plasmonic effects 135
6.6 Summary and outlook 136

7 Conclusion 139

List of publications 142

Bibliography 143

Chapter 1

Introduction

For the past two centuries and in particular after the second world war, mankind has continuously increased its consumption of fossil energy carriers, in particular oil, coal and gas. This is critical in two aspects: First, the resources that are the basis of our energy supply and of most organic compounds used in industry are finite and their exploitation becomes more and more expensive; second, numerous scientific publications strongly suggest that the increasing carbon dioxide (CO_2) content in the atmosphere is responsible for global warming. This threatens biodiversity, agriculture, coastal cities and general safety all over the world. Recent studies predict that positive feedback processes of global warming, as e.g. the release of methane from thawing permafrost soil or damages in forests, could lead to a greenhouse effect, which is much stronger than anticipated so far [Ste18]. Therefore, it would be very attractive to develop a method for the conversion of CO_2 into fuels and base chemicals using renewables, in particular solar energy. Such a technology could then not only replace fossil fuels as the basis of our economy, it would also open a route for a "negative emission technology"[1].

Many scientists all over the world are following various routes to this so-called artificial photosynthesis, which aims for the production of base chemicals such as synthesis gas (a mixture of carbon dioxide (CO) and hydrogen (H_2)), ethene (C_2H_4) or methanol (CH_3OH) or energy carriers, in particular methane (CH_4). The latter compound could store energy for mobile applications and electricity generation over long periods of time and it shall serve as an example for different routes of artificial photosynthesis.

At least five principal methods for its production from CO_2 are discussed and researched: First, it is possible to produce so-called biogas by fermentation of plant parts in special reactors. This is already realized in large scale, but with a solar-to-methane efficiency of only 0.3%-0.5% [FNR17].

The second method feeds electricity from a solar cell into a water-splitting electrolyzer, which produces H_2 [Nak15, Age15]. The latter can be used for the so-called power-to-gas process, where it is mixed with CO_2 and reacts to CH_4 and water (H_2O) in the so-called Sabatier process. Thus, an overall efficiency of 9-12% could be achieved [Ste11]. This is also already possible on industrial scale, but not yet economically competitive to natural gas.

Third, one could merge a solar cell and an electrolyzer into a photoelectrochemical cell [Wal10, Age15, Kir16]. An inherent advantage of the resulting integrated design would lie in its thermal behavior: In conventional solar cells, the efficiency is reduced if they heat up under illumination. An attached electrocatalyst can compensate this drawback because at the same time it gains efficiency due to the improved kinetics at elevated temperature [Urb16]. In

---

[1] This means the possibility to actively decrease the CO_2 content in the atmosphere by converting it into compounds, which can be stored over centuries [May19].

addition, losses from the additional energy conversion step into electricity could be avoided. It has already been experimentally proven that such a system based on multi-junction cells can work with solar-to-hydrogen efficiencies up to 16.2 % using III-V semiconductors [You17] or 6.8 % with pure Si multi-junction cells[Zie14, Urb15, Tro18]. In connection to a Sabatier reactor, about 11.4 % or 4.8 %, respectively, of solar-to-methane efficiency would be currently possible.

In an analogous way, one can replace the combination of water electrolysis and Sabatier process by direct electrochemical CO_2 reduction (CO_2RR) - method number four. In this way, also valuable base chemicals such as synthesis gas and C_2H_4 could be produced [Kum12, Qia14, Sch15c, Sin15]. In addition, it would be possible to use CO_2 mixed with nitrogen (N_2) as it typically results from combustion processes. In contrast to the Sabatier process, where the reactant gas has to be heated and where an increase of the gas volume would increase the energy consumption for heating, a reduced partial pressure of CO_2 does only slightly affect the reaction energetics of an electrochemical reaction via the Nernst equation. Since the CO_2 extraction from exhaust gas and its purification is very energy consuming [Has09, BH14], this is a valuable advantage.

Fifth, it is also possible to merge a solar cell and a CO_2 reduction cell into a device for photoelectrochemical CO_2 reduction. Many electrode materials for this task are subject to intensive studies and first prototypes with solar-to-chemical efficiencies up to 4.3 % were reported [Hab13, Urb17, Nah17]. Although this approach is very complex and challenging, the goal of an efficient "all-in-one CO_2 reduction device", which could work independently from a power grid, is very appealing and constitutes the framework of this thesis. Many considerations are important for the design of such a device, the scientifically most interesting ones are certainly the choice of materials for the photoabsorber and for the catalysts as well as the electrode geometry.

The photoabsorber has to meet two major conditions: a voltage sufficient for driving the respective electrochemical reaction and a good exploitation of the solar spectrum. Due to overvoltages stemming from reaction kinetics, mass transport and ohmic losses, a maximum power point (MPP) voltage of about 2.4 V is ideal for CO_2 reduction on copper (Cu). Using a single-junction solar cell, this would correspond to a bandgap of about 3 eV, which is typical for the high-bandgap semiconductor titanium dioxide (TiO_2). Unfortunately, such materials cannot absorb the major part of the solar spectrum, which results in a poor efficiency. Another possibility lies in the use of multi-junction cells, e.g., a-Si/µc-Si (amorphous and microcrystalline silicon) triple or quadruple cells, which can be cheaply manufactured [Urb14]. Such cells can simultaneously provide an applicable voltage and a good efficiency, so that they constitute the preferred absorber system. Since the last layer of such a cell, which typically consists of µc-Si, will finally be the one closest to the electrochemical part of the cell, this work uses conventional c-Si as a simplified version of this substrate.

For the development of an efficient device, such an absorber has to be combined with a suitable CO_2RR catalyst. Two materials for the electrochemical CO_2 reduction, which are well investigated and suitable for this task, are gold (Au) or Cu. Au can produce synthesis gas with a high CO content at moderate overpotentials, while Cu is the material, which yields the highest selectivity for CH_4 and C_2H_4 [Hor85][2]. Furthermore, the combination of the two metals allows the strong oxidiation of Cu in air to be avoided by preparing Au samples, which are electrochemically plated with Cu inside an electrolysis cell purged with an inert gas. It appears therefore sensible to use Au and Cu on Si substrates.

Although it would be possible to work with continuous catalyst layers on semiconductor substrates, there are various reasons for a structuring of the catalyst on the absorber surface. The most obvious reason is a reduction of the consumption of precious catalyst materials [Kem15]. If the absorber shall be illuminated through electrolyte and catalyst, the latter has to be transparent, which also requires a structuring of the catalyst, at least if it is an intransparent material [Che15b]. Other authors reported an enhanced electrochemical and photoelectrochemical performance [Hin98, Esp13, Ji14, Che15b]. This structuring goes along with an even more interesting feature of photoelectrochemistry with noble metal structures, which is not available in a separated photovoltaic and electrolysis design, namely the utilization of localized surface plasmon resonances (LSPRs) [Mai07]. These excitations of the electron gas in confined metal particles with sub-wavelength dimensions require a tailored nanostructuring of the metal in order to tune their resonances to the desired resonance wavelength.

Nanostructuring can also increase the number of sites where substrate and catalyst are in contact to each other and the electrolyte simultaneously. Such sites could be subject to bifunctional mechanisms, which also influence the catalytic activity [Sub11, Dan12, Sub12]. For small nanoparticles, it is known that nanostructuring of catalyst materials leads to a change in surface morphology and therefore in the occurrence of active sites on the catalyst surface [Wie03, Wel06]. In addition, the band bending on nanostructured metal-semiconductor interfaces is reported to differ from expanded contacts [Nak92, Hin98]. Many of these aspects of structuring of metal-semiconductor electrodes, in particular the role of structure size in the mesoscopic range (between several 10 nm and few µm) for the catalytic properties and product distribution as well as the occurrence of LSPRs are the central topics of this thesis.

The samples that are necessary for these studies are fabricated using the technique of Nanoimprint Lift-Off Lithography (LO-NIL) [Nag17], which allows for a reliable feature size and geometry on the macroscopic areas necessary for the subsequent electrochemical analysis, especially for the production of measurable amounts of product gases. Since especially the fast and sensitive investigation of reaction products is important for this task, a special emphasis lies on the development of a novel device, a differential electrochemical mass spectrometer (DEMS) equipped with a cold trap.

This thesis starts by introducing selected theoretical concepts that are important for the understanding of the later experiments in chapter 2. Then, the LO-NIL sample preparation procedure, the photoelectrochemical setup, spectroscopic and product analysis techniques as well as the simulations and data analysis methods used in this work are introduced in chapter 3. A novel cold trap for DEMS analysis was developed in the framework of this thesis and its development and characterization is separately discussed in chapter 4. Next, chapter 5 discusses the behavior of Au nanostructures on Si with regard to interfacial properties, charge

---

[2] Until 2018, Cu used to be the only material, which was known to produce significant amounts of these species. Recently, also silver nanofoams were reported to yield CH_4 and C_2H_4 with competitive selectivities [Dut18].

transfer between semiconductor, metal and electrolyte, Cu deposition and, in particular, the effect of structure size on the electrochemical behavior of the samples. Chapter 6 compiles the second part of the results concerning LSPRs - both their resonances in experiments and simulations and their impact on electrochemical reactions - before a short summary concludes the thesis with chapter 7.

Chapter 2

Background

This chapter discusses theoretical models and literature data from different fields of physics and chemistry, which are necessary for understanding the photoelectrochemical measurements presented later. First, light absorption in semiconductors as well as the characteristics of semiconductor interfaces are discussed in section 2.1. A discussion of the experiments of this thesis also requires to introduce the fundamentals of the electrochemical hydrogen evolution reaction (HER) and the CO_2RR in section 2.2. Furthermore, the examination of localized surface plasmon resonances (LSPRs) and their impact requires some background about plasmonic resonances and plasmonic effects (cf. section 2.3).

2.1 Selected topics of semiconductor physics

For the following discussion about the properties of metal nanostructures on silicon (Si) substrates, it is important to introduce some selected concepts of semiconductor physics. Most important for this work are the absorption of light in Si (cf. section 2.1.1) and the behavior of metal/semiconductor (cf. section 2.1.2) as well as electrolyte/semiconductor contacts (cf. section 2.1.3) and the complete electrolyte/metal/insulator/semiconductor interface (cf. section 2.1.4). This section follows the textbooks [Sze07], [Sch10] and [Kri15], which also contain more detailed descriptions about semiconductor physics.

2.1.1 Absorption and photoelectric effect in silicon

In general, semiconductors are known to absorb photons with energies higher than the bandgap energy. These photons are capable to transfer electrons from the valence band (VB) into the conduction band (CB), which results in the creation of electron-hole pairs. The spectral behavior of this absorptivity is dependent on the detailed band structure of the semiconductor. Si is an indirect semiconductor, i.e. the minimum of the conduction band is not at the same position in phase space as the maximum of the valence band[1]. This results in an indirect bandgap (the minimum distance between VB and CB) of 1.12 eV and a direct bandgap (the difference between the bands at the Γ point, which represents a crystal momentum of 0 eV) of 3.4 eV [Phi62]. The nature of the bandgap is important for the absorption properties of the semiconductor: Since the momentum of an absorbed photon is negligible compared to the electron crystal momentum, a direct transition, which is almost vertical in a band diagram, is a two-particle process with a high cross-section. For an indirect transition, an additional momentum, typically supplied by phonon absorption or creation, is necessary. This leads to a three-particle process, the cross-section of which is drastically reduced compared to direct absorption. This results in a relatively low absorption coefficient for energies slightly

---

[1] The position of the conduction band minimum is located along the <100> axis in phase space corresponding to about 85% of the way to the X point.

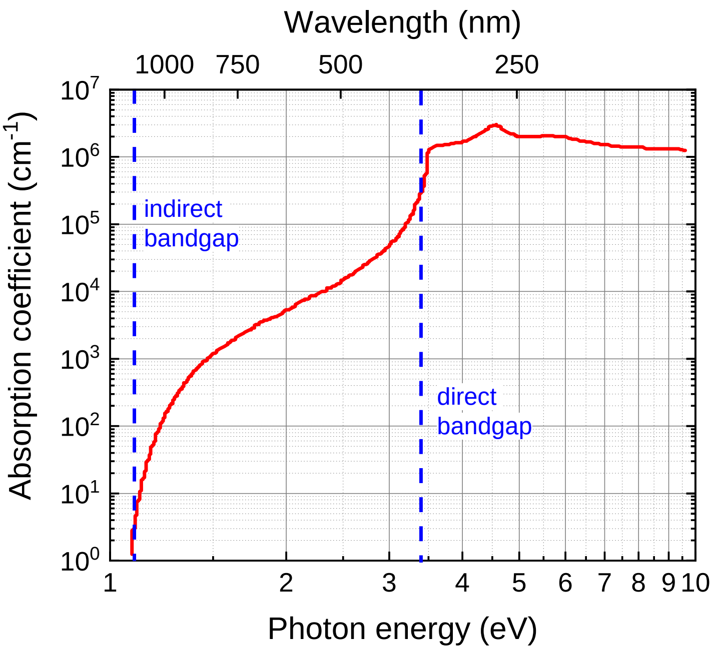

Figure 2.1: Absorption coefficient of Si as a function of on the photon energy, reproduced from [Sze07].

above the indirect bandgap. With increasing photon energy, the absorption also increases and the spectrum shows a second absorption edge at the direct bandgap energy (cf. figure 2.1).

Before describing the resulting energy distribution of the charge carriers under illumination, the case without illumination is discussed in the following. The occupation of states with energy E by electrons in the bands of an unilluminated semiconductor is generally described via a Fermi-Dirac distribution, which is determined by the electrochemical potential $\widetilde{\mu}$ of the electrons[2] [Gro18]:

$$f(E,T) = \frac{1}{e^{(E-\widetilde{\mu})/k_{\mathrm{B}}T}+1} \tag{2.1}$$

with the Boltzmann constant k_{B} and the absolute temperature T. Note that this equation gives the occupation for electrons; for holes, one has to consider that they are made up by the states, which are not occupied by electrons [Gro18]:

$$h(E,T) = 1 - f(E,T) = \frac{1}{e^{(\widetilde{\mu}-E)/k_{\mathrm{B}}T}+1} \tag{2.2}$$

For moderately n-doped semiconductors around room temperature (assuming that all donor atoms are ionized), $\widetilde{\mu}$ can be described as [Gro18]

$$\widetilde{\mu} = E_{\mathrm{CB}} + k_{\mathrm{B}}T \ln \frac{N_{\mathrm{D}}}{N_{\mathrm{CB}}} \tag{2.3}$$

with the conduction band edge energy E_{CB}, the density of donor atoms N_{D} and the effective density of states in the conduction band $N_{\mathrm{CB}} = 2\left(\frac{2\pi m_e^* k_{\mathrm{B}}T}{h^2}\right)^{3/2}$. m_e^* is the effective mass of the conduction band electrons and h is the Planck constant. For moderately p-doped semi-

---

[2] Often, it is somewhat sloppy referred to as "Fermi level".

conductors, the respective equation for $\widetilde{\mu}$ is [Gro18]

$$\widetilde{\mu} = E_{\mathrm{VB}} + k_{\mathrm{B}}T \ln \frac{N_{\mathrm{VB}}}{N_{\mathrm{A}}} \tag{2.4}$$

with the valence band edge energy E_{VB}, the density of acceptor atoms N_{A}, the effective density of states in the valence band $N_{\mathrm{VB}} = 2\left(\frac{2\pi m_h^* k_{\mathrm{B}}T}{h^2}\right)^{3/2}$ and the effective mass of holes in the valence band m_h^*.

Typically, the absorption of photons with energies above the bandgap energy lifts electrons from the valence band into the conduction band and thus creates one electron-hole pair per photon. Consequently, the free charge carrier densities in both bands are drastically increased; the gain of the minority charge carrier density in a doped semiconductor is most pronounced. Depending on the absorbed photon energies, the generated charge carriers have certain energy distances to the band edges. They thermalize quickly (on a ps timescale) within the respective band, which means that they form an energy distribution similar to a thermal excitation [Kri15].

Under illumination, the additional charge carriers lead to a higher population of states in both bands compared to the unilluminated case. They can no longer be described by a single Fermi-Dirac distribution, so that $\widetilde{\mu}$ is replaced by two independent quasi-electrochemical potentials $\widetilde{\mu}_{\mathrm{CB}}$ and $\widetilde{\mu}_{\mathrm{VB}}$, which can be used to describe the energy distribution of electrons in the conduction band, respectively holes in the valence band, according to equations 2.1 and 2.2. They can be calculated via [Kri15]:

$$\begin{aligned}\widetilde{\mu}_{\mathrm{CB}} &= E_{\mathrm{CB}} + k_{\mathrm{B}}T \ln\left(\frac{n_{\mathrm{e}}}{N_{\mathrm{CB}}}\right)\\ \widetilde{\mu}_{\mathrm{VB}} &= E_{\mathrm{VB}} - k_{\mathrm{B}}T \ln\left(\frac{n_{\mathrm{h}}}{N_{\mathrm{VB}}}\right)\end{aligned} \tag{2.5}$$

where n_{e} denotes the actual density of electrons in the conduction band and n_{h} the one of the holes in the valence band. The difference between $\widetilde{\mu}_{\mathrm{CB}}$ and $\widetilde{\mu}_{\mathrm{VB}}$ now gives the maximum energy per charge carrier, which could be extracted theoretically.

2.1.2 Metal/semiconductor interfaces

In order to use the energy of the photo-induced carriers in a semiconductor, it is necessary to extract them. This involves charge carrier transfers, typically over a metal/semiconductor interface, which is discussed in this section (the case of charge carrier transfer via an electrolyte/semiconductor interface is the topic of section 2.1.3). The properties of such metal/semiconductor interfaces are very important for this work because it deals with currents flowing between metal nanostructures and a semiconductor substrate over a (Cu)/Au/Ti/SiO_2/Si interface (cf. also the sample design in figure 3.2)[3].

Depending on the doping of the Si substrate, different interfaces can occur. For normal doping levels, several properties influence the contact behavior. In principle, when two conducting or semiconducting materials are brought into contact, the electrochemical potential of the electrons in the two phases aligns. At the same time, the electron affinity (energy dis-

---

[3] The extended situation with electrochemical reactions taking place on the metal surface is the topic of section 2.1.4.

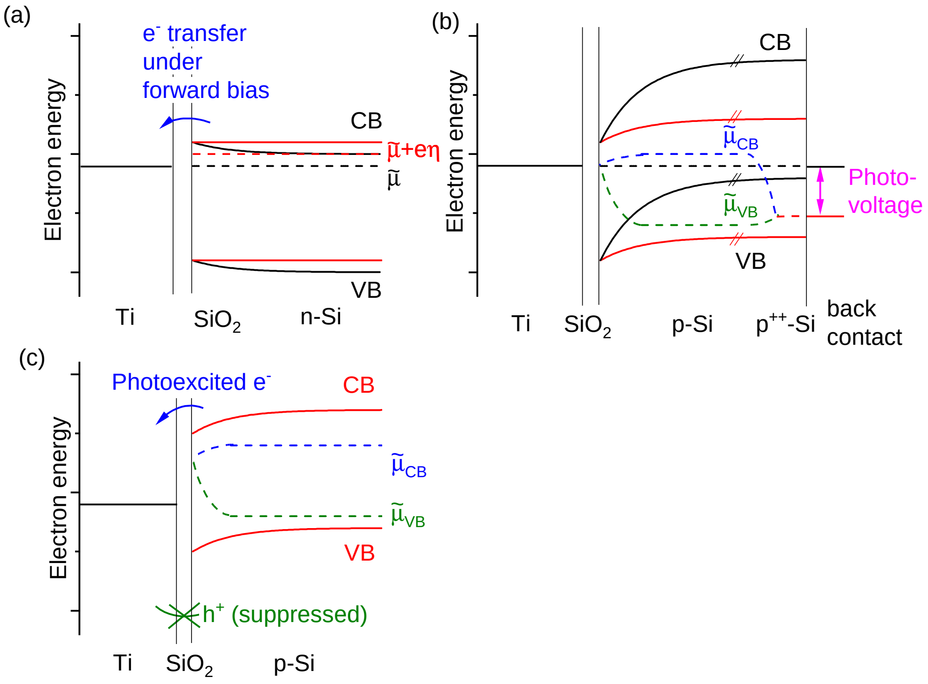

Figure 2.2: Band diagrams of different Ti/SiO$_2$/Si interfaces: (a) n-type doping without Fermi level pinning: For cathodic bias (red), electron transfer is possible over the Schottky contact. (b) p-type doping without Fermi level pinning: Without illumination (black) there is a large barrier, which prevents hole transfer from the metal to the semiconductor. Under illumination, quasi-electrochemical potentials $\tilde{\mu}_{\mathrm{CB}}$ (blue) and $\tilde{\mu}_{\mathrm{VB}}$ (green) describe the energy distribution of electrons in the conductions band, respectively holes in the valence band. The band bending reduces (red) and a photovoltage (pink) can be measured between front and back contact. Note that the preparation of the back contact results in a degenerately doped region close to the back contact. (c) If the circuit is closed, a large part of the photovoltage drops over the Schottky contact and can induce a cathodic current carried by photoexcited electrons.

tance between vacuum energy and conduction band edge) of the semiconductor as well as the work function (energy distance between vacuum energy and electrochemical potential of the electrons) of the metal remain constant and are pinned at the interface. The space charge region in the semiconductor, which is induced by a compensation of the resulting potential difference, causes band bending [Sze07]. According to this principle, called Schottky-Mott rule, the band bending of ideal Ti/SiO$_2$/Si interfaces would lead to Schottky contacts for both doping types (as shown in figure 2.2 for an electron affinity of Si of 4.05 eV [Sze07]).

In general, a Schottky contact leads to a rectifying behavior, which can be described by two different barriers for charge carrier transport, depending on the direction of current flow: When majority charge carriers move from the metal into the semiconductor, they have to overcome a pinned energy barrier as defined by the work functions of the metal and the electron affinity of the semiconductor. In contrast, the barrier for majority charge carriers moving from the semiconductor to the metal is depending on the band bending and consequently on the applied bias (cf. the case of Au/Ti/SiO$_2$/n-Si in figure 2.2(a)). Since the minority charge carrier density is negligible in doped semiconductors, all currents carried by them are neglected.

For the Au/Ti/SiO_2/p-Si interface shown in figure 2.2(b)[4], the Schottky contact is under reverse bias for an applied cathodic voltage. In this case, the majority charge carriers (holes) would have to overcome a large, fixed energy barrier in order to move from the metal into the semiconductor, which suppresses cathodic currents. Under illumination, additional holes and electrons are created in valence and conduction band, respectively, so that a significant minority charge carrier distribution evolves. The energy distribution of the charge carriers can be described by quasi-electrochemical potentials $\widetilde{\mu}_{\mathrm{CB}}$ (blue) and $\widetilde{\mu}_{\mathrm{VB}}$ (green). The resulting transfer of electrons into the metal leads to a compensation of the negative charge density, which arose from hole depletion after forming the Schottky contact. Therefore, the band bending is reduced.

The use of two different contact materials, e.g. Au/Ti and the front and Al at the back contact, allows for the extraction of electrons at a higher potential than at the ohmic back contact, resulting in a photovoltage (pink) between the contacts (cf. also [Kri15])[5] If the electric circuit is closed, the major part of the photovoltage drops over the Schottky contact and allows photoexcited electrons to flow from the conduction band into the adjacent metal (figure 2.2(c)).

In some cases, the band alignment can deviate from the Schottky-Mott behavior due to so-called Fermi level pinning [Mea64]: Interband energy states at the interface may lead to a band bending, which can significantly differ from the Schottky-Mott rule described above. The presence of Fermi level pinning at Au/Ti/SiO_2/Si interfaces can lead to an ohmic contact for n-Si (cf. [Yu70]), while the Schottky contact between p-Si and Ti only changes quantitatively. In the experiments described below (cf. section 5.2), an ohmic contact can indeed be observed for Au/Ti/SiO_2/n-Si.

In our system, there are two further factors, which complicate the theoretical description of the Au/Ti/SiO_2/Si interface: First, the presence of an oxide layer within the complex interface and second, the exact value of the metal work function at a Au/Ti/SiO_2/Si interface with a very thin Ti layer. For a Ti layer thicker than several 10 nm, a closed metal film is present and the work function at the interface is the one of Ti (Φ =4.33 eV [Hö79]). If the Ti thickness is reduced to only a few nm, there can be holes in the Ti layer and the resulting contact between parts of the Au layer and the Si/SiO_2 surface can shift the effective work function of the combined Au/Ti layer to a value between the one of Ti and the one of Au (work function Φ =5.1−5.5 eV [Hö79]). As this behavior is not exactly known, the value for Ti can be understood as a lower limit of the work function.

The case of a degenerately doped semiconductor, which has a so-called impurity band inside the main bandgap, is more difficult in its theoretical description. However, the resulting charge transfer behavior is simpler than for ordinary metal-semiconductor contacts: Since the electrochemical potential of the electrons lies inside this impurity band, the material can be treated similar to a metal. If it gets into contact to a normal metal, a contact with ohmic behavior will occur.

---

[4] Here, no Fermi level pinning is considered.

[5] For the p-Si samples used in this work, a degenerately doped p^{++} region evolves close to the Al back contact during an intensive annealing (cf. sample preparation in section 3.1.1), so that an ohmic contact is formed. This is only shown in figure 2.2(b).

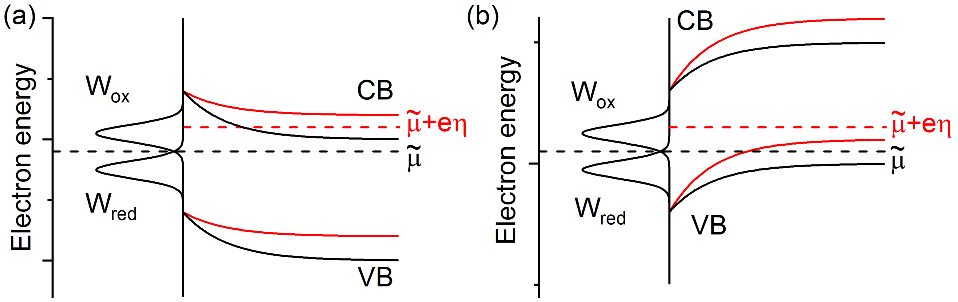

Figure 2.3: Gerischer diagrams for (a) an n-type and (b) a p-type semiconductor without illumination in contact to an electrolyte with equal surface concentrations of reduced and oxidized species described by distribution functions W_{red} and W_{ox}. The intersection of these distributions aligns with $\tilde{\mu} + e\eta$ in the semiconductor. The black lines show the equilibrium situation, while the red lines represent the situation under cathodic bias conditions.

2.1.3 Electrolyte/semiconductor interfaces

The situation is very similar if the metal is replaced by an electrolyte containing one or more redox couples. The presence of such redox couples now provides states for electrons on the electrolyte side, which can be occupied and emptied via charge transfer reactions. In the typical case of one dominating redox couple, these states define the electrochemical potential of the electrons within the electrolyte. They can be described using distributions functions W_{red} and W_{ox} for the reduced and oxidized species, respectively, which give the probability to find a reduced or oxidized state of energy ϵ in the electrolyte. They are defined as [Sch10]

$$\begin{aligned} W_{\mathrm{red}}(\epsilon, (\tilde{\mu} + e\eta)) &= c_{\mathrm{red}}\sqrt{\pi/(4\lambda k_{\mathrm{B}}T)}\,\exp\left(-\frac{(\epsilon - \tilde{\mu} - e\eta + \lambda)^2}{4\lambda k_{\mathrm{B}}T}\right) \\ W_{\mathrm{ox}}(\epsilon, (\tilde{\mu} + e\eta)) &= c_{\mathrm{ox}}\sqrt{\pi/(4\lambda k_{\mathrm{B}}T)}\,\exp\left(-\frac{(\epsilon - \tilde{\mu} - e\eta - \lambda)^2}{4\lambda k_{\mathrm{B}}T}\right) \end{aligned} \tag{2.6}$$

with the surface concentrations c_{red} and c_{ox}, the Boltzmann constant k_{B}, temperature T, the overpotential η and the energy of reorganization λ[6] [Ger61]. The maxima of these distributions are shifted away from $\tilde{\mu} + e\eta$ by the value $+\lambda$ for the oxidized species and $-\lambda$ for the reduced species. In figure 2.3, the resulting interface is shown for an n-type and a p-type semiconductor with and without cathodic bias.

These distributions can be used to derive expressions for the current densities stemming from both bands. The electron transfer rates for oxidation and reduction reactions, $k_{\mathrm{ox}}(\epsilon)$ and $k_{\mathrm{red}}(\epsilon)$, at a certain energy ϵ are depending on the energetic overlap of states on both sides of the interface. They are given by the relations [Sch10]

$$\begin{aligned} k_{\mathrm{ox}}(\epsilon) &\propto \rho(\epsilon)(1 - f(\epsilon, T))W_{\mathrm{red}}(\epsilon, (\tilde{\mu} + e\eta)) \\ k_{\mathrm{red}}(\epsilon) &\propto \rho(\epsilon)f(\epsilon, T)W_{\mathrm{ox}}(\epsilon, (\tilde{\mu} + e\eta)) \end{aligned} \tag{2.7}$$

---

[6] The solvation shell made up by H_2O molecules around the species of interest differs between an oxidized and a reduced molecule. Together with possible energy differences induced by rearranging ligands and further covalently bound atoms, this leads to an energy difference due to the rearrangement of the solvation shell during the redox reaction.

using the density of states in the semiconductor $\rho(\epsilon)$ and the Fermi-Dirac distribution $f(\epsilon, T)$. Note that these transfer rates do not denote the total charge carrier transfer, but only an infinitesimal contribution to the current density at the energy ϵ. Energy regions with both free charge carriers in one of the bands in the semiconductor and empty states in the redox couple lead to high transfer rates. The actual current density can then be calculated via integration over the energy ϵ. The derivation of the current density contributions of the valence band and the conduction band is only done for reduction reactions, i.e. cathodic current densities $j_{\mathrm{c}}^{\mathrm{VB}}$ and $j_{\mathrm{c}}^{\mathrm{CB}}$ [7], in the following [Sch10][8]:

$$\begin{aligned} j_{\mathrm{c}}^{\mathrm{VB}}(\eta) &\propto \int_{-\infty}^{E_{\mathrm{VB}}+e\eta} d\epsilon\, \rho(\epsilon) f(\epsilon, T) W_{\mathrm{ox}}(\epsilon, (\widetilde{\mu} + e\eta)) \\ j_{\mathrm{c}}^{\mathrm{CB}}(\eta) &\propto \int_{E_{\mathrm{CB}}+e\eta}^{\infty} d\epsilon\, \rho(\epsilon) f(\epsilon, T) W_{\mathrm{ox}}(\epsilon, (\widetilde{\mu} + e\eta)) \end{aligned} \tag{2.8}$$

Using the approximations $f(\epsilon, T) \approx 1$ in the valence band and $f(\epsilon, T) \approx \exp\left(\frac{\epsilon}{k_{\mathrm{B}}T}\right)$ in the conduction band, a weak dependence of $\rho(\epsilon)$ on the energy ϵ, as well as a substitution $\xi = \epsilon - e\eta$, one ends up with [Sch10]:

$$\begin{aligned} j_{\mathrm{c}}^{\mathrm{VB}}(\eta) &\propto \int_{-\infty}^{E_{\mathrm{VB}}} d\xi\, W_{\mathrm{ox}}(\xi, \widetilde{\mu}) \\ j_{\mathrm{c}}^{\mathrm{VB}}(\eta) &= j_{\mathrm{c}}^{\mathrm{VB}}(\eta = 0) \\ j_{\mathrm{c}}^{\mathrm{CB}}(\eta) &\propto \int_{E_{\mathrm{CB}}}^{\infty} d\xi\, \exp\left(-\frac{\xi + e\eta}{k_{\mathrm{B}}T}\right) W_{\mathrm{ox}}(\xi, \widetilde{\mu}) \\ j_{\mathrm{c}}^{\mathrm{CB}}(\eta) &= j_{\mathrm{c}}^{\mathrm{CB}}(\eta = 0) \cdot \exp\left(-\frac{e\eta}{k_{\mathrm{B}}T}\right) \end{aligned} \tag{2.9}$$

For anodic currents, the situation is analogue [Sch10]:

$$\begin{aligned} j_{\mathrm{a}}^{\mathrm{VB}}(\eta) &= j_{\mathrm{a}}^{\mathrm{VB}}(\eta = 0) \cdot \exp\left(\frac{e\eta}{k_{\mathrm{B}}T}\right) \\ j_{\mathrm{a}}^{\mathrm{CB}}(\eta) &= j_{\mathrm{a}}^{\mathrm{CB}}(\eta = 0) \end{aligned} \tag{2.10}$$

Considering the case of a doped semiconductor, only one band (the conduction band for n-type and the valence band for p-type semiconductors) significantly contributes to the current flowing. The combination of a constant current density for one direction and an exponentially increasing current density for the other direction results in rectifying properties of the interface, which differ between the bands and are determined by the type of doping.

2.1.4 Electrolyte/metal/insulator/semiconductor interfaces

This work deals with the examination of structured Au/Ti/SiO_2/Si electrodes, which in principle show two kinds of electrochemical interfaces: The sites covered with Au structures involve current flowing over an electrolyte/Au/Ti/SiO_2/Si interface, while the uncovered areas feature an electrolyte/SiO_2/Si interface. Because of the much higher electrocatalytic activity of the metal surfaces, the dominating current contribution in the experiments flows over the electrolyte/Au/Ti/SiO_2/Si interface, not over the electrolyte/SiO_2/Si one. On most

---

[7] The case for anodic currents is treated analogously and can be found, e.g., in [Sch10].

[8] In contrast to [Sch10], $\widetilde{\mu}$ is not used as the reference potential here.

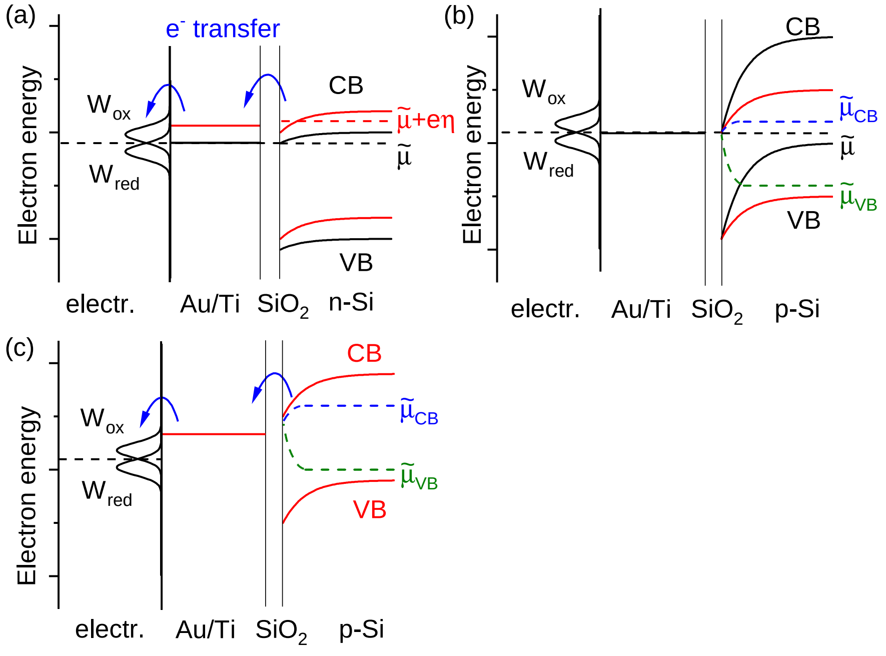

Figure 2.4: Band diagrams for electrolyte/Au/Ti/SiO$_2$/Si interfaces: (a) In n-Si with Fermi level pinning and without illumination, electron transfer is possible from n-Si into the Ti by trap-assisted tunneling through the SiO$_2$ under cathodic bias (red). In the electrolyte, a redox pair consisting of reduced and oxidized species described by distribution functions W_{red} and W_{ox} with equal surface concentrations is present. (b) In p-Si without illumination, a cathodic current carried by hole transfer from the Ti to the p-Si is suppressed by the energy barrier. Under illumination, the excitation of electron-hole pairs leads to increased charge carrier densities. Now, quasi-electrochemical potentials $\tilde{\mu}_{\mathrm{CB}}$ (blue) and $\tilde{\mu}_{\mathrm{VB}}$ (green) describe the energy distribution of electrons in the conduction band, respectively holes in the valence band. (c) Under illumination, photoexcited electrons can carry a cathodic current over the Ti/SiO$_2$/p-Si interface. For a suitable energetic position of the redox couple in the electrolyte, a cathodic current can be driven by the photovoltage. This leads to potential drops over the electrolyte/Au interface and the Ti/p-Si interface because of their resistance.

samples, the exposed silicon surface is even completely passivated by a thick layer of thermal SiO$_2$ so that any semiconductor-electrolyte contribution can be completely neglected there.

As a consequence, it is important to discuss how the transport of charge carriers over an electrolyte/Au/Ti/SiO$_2$/Si interface can be modeled. Figure 2.4(a) shows the case of n-type doping without illumination and with Fermi level pinning. In order to drive a reduction reaction on the electrolyte/Au interface under cathodic bias, an electron has to move from the conduction band of the n-Si into the Ti through the SiO$_2$ layer in between. Although the oxide is 1-2 nm thick, a certain defect density inside the oxide can lead to a significant current transport via trap-assisted tunneling [Cho97, Cha01]. The contact as it appears in the experiments even has a virtually ohmic j-U characteristic. From the metal, the electron can be transferred over the electrolyte/metal interface via reduction of an oxidized species in the electrolyte close to the metal surface.

In the case of an electrolyte/Au/Ti/SiO$_2$/p-Si interface (cf. figure 2.4(b)), one has to consider that the transfer of holes from the Ti into the p-Si is suppressed by the energy barrier at the interface (cf. section 2.1.2). A cathodic current can only flow if photoelectrons in the conduction band are excited by illumination. Both the electron transfer over the electrolyte/metal interface and over the Schottky contact are subject to significant resistances, therefore a potential drop appears at both interfaces, if the electric circuit is closed. The corresponding situation with quasi-electrochemical potentials (cf. equation 2.5) under illumination is shown in figure 2.4(c).

2.2 Important electrochemical reactions

So far, the electrochemical redox reactions occurring on the electrode surface were only abstractly mentioned, but the reaction pathways of the electrochemical CO_2RR in aqueous electrolyte are of paramount importance for this work and are therefore introduced in this section. Since the CO_2RR occurs at potentials, which can also drive the hydrogen evolution reaction (HER), both reactions typically occur simultaneously. In this section, they are still treated separately so that they can be more easily understood. After a short introduction to buffer solutions (cf. section 2.2.1), the HER and the oxygen evolution reaction (OER) (cf. section 2.2.2) as well as the most important CO_2RR pathways are explained (cf. section 2.2.3).

2.2.1 Buffer solutions

To achieve conditions suitable for CO_2RR, neutral electrolytes (pH≈7) are typically used. The reason for this is that under acidic conditions, the Faraday efficiency for carbon-based products decreases, in particular for C_2H_4 [Sch14], while alkaline bulk pH values are not possible in the presence of CO_2, which neutralizes bases. Due to the low absolute concentrations of H_3O^+ and OH^- ions in the neutral range, electrochemical reactions involving proton transfers can quickly change the pH at the electrode. Under cathodic current flow, it cannot be avoided that the surface pH becomes more alkaline at the electrode surface [Gup06] because OH^- ions are produced (cf. in particular the HER in equation 2.13 and the CO_2RR reaction in equation 2.16).

In principle, this pH shift can be suppressed in the presence of a sufficient buffer concentration. Around the pK_a value of the respective acid/base couple, the buffer capacity is maximal. In electrolytes containing CO_2, the system [Gup06]

$$\mathrm{H_2CO_3 + 2OH^- \rightleftharpoons HCO_3^- + OH^- + H_2O \rightleftharpoons CO_3^{2-} + 2H_2O,\ pK_a = 6.4\,and\,10.3} \tag{2.11}$$

already constitutes a buffer, which can be supported by additional buffers as e.g. a phosphate buffer [Smi16]:

$$\mathrm{H_2PO_4^- + OH^- \rightleftharpoons HPO_4^{2-} + H_2O,\ pK_a = 7.2} \tag{2.12}$$

However, the typical current densities used for the CO_2RR quickly deplete the buffer capacities, which were used in this work, so that an alkaline surface pH is present under current flow. Therefore, many reaction equations in the following are given in the form involving OH^- ions, which represents the case of alkaline pH.

2.2.2 Hydrogen and oxygen evolution reactions

In water electrolysis, the reaction from H_2O to H_2 and O_2 is split into two half reactions, the HER and the OER [Kri15]. Although the final products are the same for alkaline and acidic environment, the reaction mechanism depends on the pH value at the electrode. In acidic media, the current through the electrolyte is carried by H_3O^+, in alkaline solutions by OH^- ions, so that the HER can be written as[9] [Kri15]:

$$\begin{aligned}&\text{HER in acidic solution}: \quad 4H_3O^+ + 4e^- \rightarrow 2H_2 + 4H_2O,\ E_0 = 0\ \text{V vs SHE (pH} = 0),\\&\text{HER in alkaline solution}: \quad 4H_2O + 4e^- \rightarrow 2H_2 + 4OH^-,\ E_0 = -0.83\ \text{V vs SHE (pH} = 14)\end{aligned} \tag{2.13}$$

Since the HER is one of the best-researched electrochemical reactions, its three basic steps have distinct names, namely Volmer, Heyrovsky and Tafel steps. In alkaline media, they are [Mah18]:

$$\begin{aligned}&\text{Volmer step}: H_2O + e^- \rightarrow H_{\text{ads}} + OH^-,\\&\text{Heyrovsky step}: H_2O + e^- + H_{\text{ads}} \rightarrow H_2 + OH^-,\\&\text{Tafel step}: 2H_{\text{ads}} \rightarrow H_2\end{aligned} \tag{2.14}$$

The OER is less important for this work; if the working electrode has to supply a cathodic current, it only occurs on the counter electrode. It is still given here for completeness [Kri15]:

$$\begin{aligned}&\text{OER in acidic solution}: \quad 6H_2O \rightarrow O_2 + 4H_3O^+ + 4e^-,\ E_0 = +1.23\ \text{V vs SHE (pH} = 0),\\&\text{OER in alkaline solution}: \quad 4OH^- \rightarrow O_2 + 2H_2O + 4e^-,\ E_0 = +0.40\ \text{V vs SHE (pH} = 14)\end{aligned} \tag{2.15}$$

2.2.3 Electrochemical CO_2 reduction

While the theoretical understanding of hydrogen evolution is already quite advanced, it is much more complicated to describe the reduction of CO_2, which can lead to at least 16 different reaction products [Kuh12]. The detailed composition of the product spectrum depends on various parameters, such as electrode material [Hor85, Hor94, Kuh14], electrolyte composition [Hor89, Kan06, Var16a], surface pH [Kas15, Var16b], surface orientation [Hor02, Sch13] and morphology (in particular the presence of nanocrystals) [Tan12, Che15a, Eil16] or applied potential (virtually all publications about products from CO_2RR report a potential dependence of the product distribution).

Among all catalyst materials, Cu takes a prominent role, since it gives by far the highest yields for CH_4 and C_2H_4 reported so far. Other metal surfaces such as Au lead to a significantly reduced product spectrum. The most important half reactions, all of which occur on Cu, are the ones to the products CO, formic acid (HCOOH), methanol (CH_3OH), CH_4, ethanol (C_2H_5OH) and C_2H_4 [Kor15]:

---

[9] It is common to use the reversible hydrogen electrode scale for HER and OER, since it allows for a convenient comparison between reaction mechanisms depending on the pH value without having to deal with different activities of reactants and products. However, this scale can be misleading when a significant pH shift takes place, in particular for neutral electrolytes. In this case, the surface pH is not constant in time so that only a pH-independent reference electrode scale permits a correct interpretation.

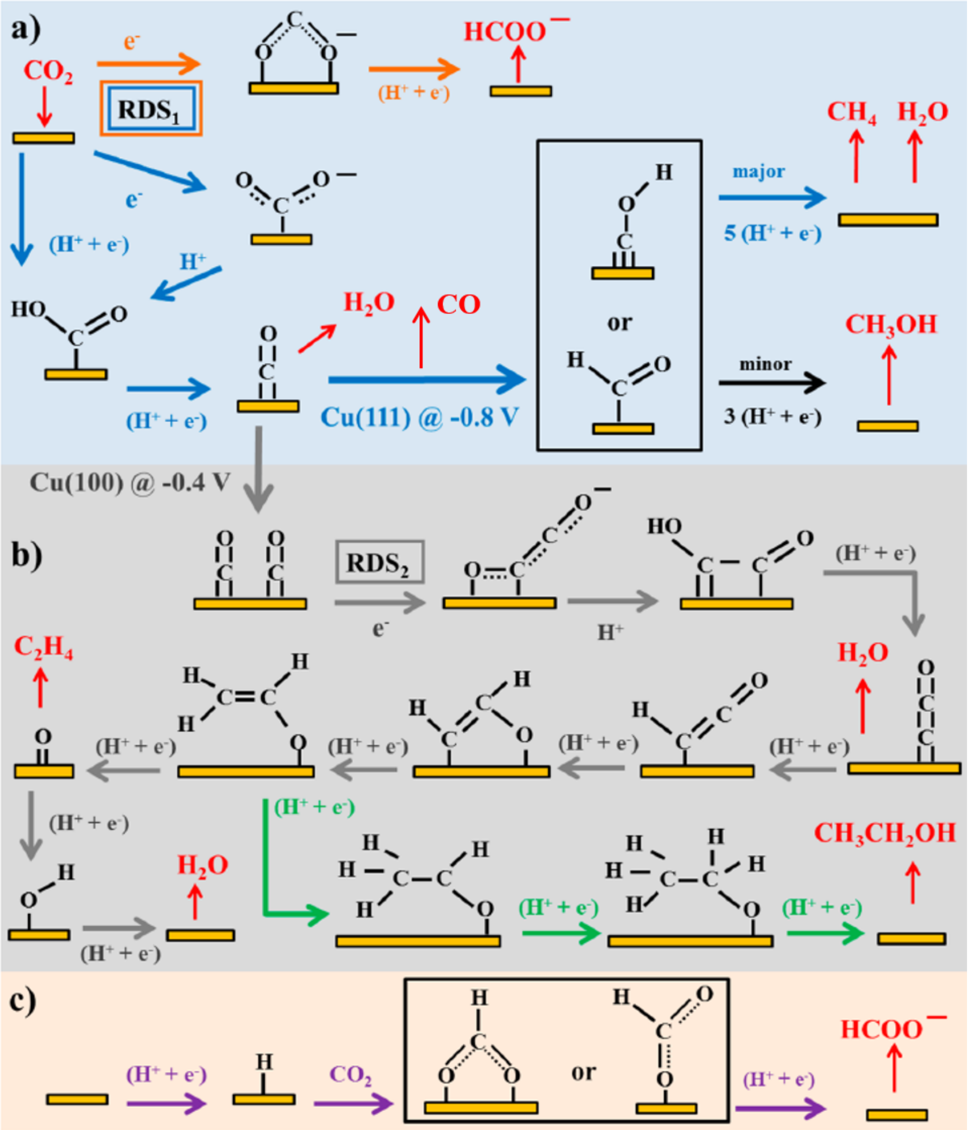

Figure 2.5: Pathways of CO_2RR according to Kortlever et al.: Red species are reactants and products in solution while black species are adsorbed to the surface. The steps indicated with "RDS" are the rate-determining steps of the respective pathways and the potentials are given with respect to reversible hydrogen electrode (RHE). In alkaline environment, each e^-/H^+ transfer stands for a $H_2O \rightarrow OH^-$ step with electron transfer. Image adapted from [Kor15].

$$\begin{aligned}
CO_2 + H_2O + 2e^- &\rightarrow CO + 2OH^-,\ E_0 = -0.51 \text{ V vs SHE (pH} = 7)\\
CO_2 + 2H_2O + 2e^- &\rightarrow HCOOH + 2OH^-,\ E_0 = -0.44 \text{ V vs SHE (pH} = 7)\\
CO_2 + 5H_2O + 6e^- &\rightarrow CH_3OH + 6OH^-,\ E_0 = -0.39 \text{ V vs SHE (pH} = 7)\\
CO_2 + 6H_2O + 8e^- &\rightarrow CH_4 + 8OH^-,\ E_0 = -0.24 \text{ V vs SHE (pH} = 7)\\
2CO_2 + 8H_2O + 12e^- &\rightarrow C_2H_4 + 12OH^-,\ E_0 = -0.32 \text{ V vs SHE (pH} = 7)\\
2CO_2 + 9H_2O + 12e^- &\rightarrow C_2H_5OH + 12OH^-,\ E_0 = -0.33 \text{ V vs SHE (pH} = 7)
\end{aligned} \tag{2.16}$$

Many very complex reaction networks have been proposed in the literature. One, which covers the current state of the art concerning these six reaction products, was developed by Kortlever et al. [Kor15]. As shown in figure 2.5, the first reaction step can either be the adsorption and reduction of CO_2 (2.5(a)) or the adsorption of a H^+ together with an e^- transfer[10] (2.5(c)). While the latter pathway only leads to the formation of $HCOO^-$, the first one can proceed to an OOC^-_{ads} (O atoms are adsorbed; this also results in $HCOO^-$) or an $COO^-_{ads}/COOH_{ads}$ (C atom is adsorbed), which leads to CO as an important intermediate product. CO can either directly desorb or be further reduced in two different pathways, depending on the catalyst surface. One pathway involving 4 or 6 e^-/H^+ transfers finishes in CH_3OH or CH_4, respectively. The rate-determining step (RDS_1) for these species containing one C atom is proposed to be already the first electron transfer. The second route (2.5(b)) leading to species with two C atoms, C_2H_5OH and C_2H_4, requires the dimerization of 2 CO absorbates as the rate-determining step of this process (RDS_2), followed by 8 further e^-/H^+ transfers for both products.

In addition, it shall be noted that dissolved CO_2 is the actual reactant of CO_2RR, but it is in equilibrium with bicarbonate (HCO_3^-) (cf. equation 2.11). The latter was found to be an important source of CO_2 and it is simultaneously consumed during CO_2RR [Dun17].

2.3 Localized surface plasmon resonances

For the understanding and interpretation of the experiments with plasmonic resonances in chapter 6 it is important to introduce several concepts related to the occurrence of LSPRs in illuminated noble metal nanostructures. After starting with the dependence of plasmonic resonance wavelengths on the nanostructure geometry and surrounding, some plasmonic effects, in particular plasmonic heating, are introduced.

2.3.1 Plasmonic resonance wavelength

The LSPRs of real noble metal particles depend on numerous parameters and many of these dependencies can be deduced from classical electrodynamics. Therefore, this section starts with the most simple case of a small spherical noble metal particle with radius r. Using Legendre polynoms, one can derive the polarizability α_s of such a particle depending on its volume $V = \frac{4\pi}{3}r^3$, its complex dielectric function ϵ and the one of the surrounding ϵ_m [Mai07]:

$$\alpha_\mathrm{s} = 3V\frac{\epsilon - \epsilon_\mathrm{m}}{\epsilon + 2\epsilon_\mathrm{m}} \tag{2.17}$$

Under electromagnetic radiation, this polarizability leads to the evolution of a dipole moment, which amplifies the electric field in its vicinity, this is also called "plasmonic field enhancement". α_s becomes maximal for minimum values of $|\epsilon + 2\epsilon_\mathrm{m}|$ and a plasmonic resonance can be observed. For Drude metals with a plasma frequency ω_p and negligible damping one can use a simplified representation of the dielectric function $\epsilon(\omega)$ [Mai07]:

$$\epsilon(\omega) \approx 1 - \frac{\omega_\mathrm{p}^2}{\omega^2} \tag{2.18}$$

---

[10] To be more correct, each "e^-/H^+ transfer" in the figure should rather be replaced by a "e^- transfer, H_2O addition and OH^- subtraction" due to the typically alkaline surface pH. Since this formulation is much longer than the one used in the original, a more correct version would significantly lose clarity, so it is not changed.

resulting in a plasmonic resonance, if $Re(\epsilon(\omega)) = -2\epsilon_{\mathrm{m}}$ [Mai07]:

$$\omega = \frac{1}{\sqrt{1+2\epsilon_{\mathrm{m}}}}\omega_{\mathrm{p}} \tag{2.19}$$

This can already explain that an increase of ϵ_{m}, e.g. due to a dielectric substrate or immersion of the nanostructure in water, leads to a redshift of the resonance.

So far, it was assumed that the metal particles were much smaller than the illumination wavelength. For a particle radius r becoming comparable to the vacuum wavelength λ_0, the quasi-static approximation has to be amended by a size parameter $\xi = \frac{\pi r}{\lambda_0}$, which accounts for retardation and resulting phase shifts at different positions within the particle. Then, equation 2.17 becomes significantly more complicated [Mei83, Kuw03, Mai07]:

$$\alpha_{\mathrm{s}} = \frac{1 - \frac{1}{10}(\epsilon+\epsilon_{\mathrm{m}})\xi^2 + \mathcal{O}(\xi^4)}{\left(\frac{1}{3} + \frac{\epsilon_{\mathrm{m}}}{\epsilon-\epsilon_{\mathrm{m}}}\right) - \frac{1}{30}(\epsilon+10\epsilon_{\mathrm{m}})\xi^2 - i\frac{4\pi^2\epsilon_{\mathrm{m}}^{3/2}V}{3\lambda_0^3}\mathcal{O}(\xi^4)}V \tag{2.20}$$

This means that an increase of particle size leads to a redshift and a broadening of the resonance.

In addition, the Au structures used in the experiments are not spherical. If the assumption of a sphere is generalized towards ellipsoids, one gets different modes for the principal axes r_1, r_2 and r_3 of this ellipsoid with polarizabilities [Boh04]

$$\alpha_{\mathrm{i}} = 4\pi r_1 r_2 r_3 \frac{\epsilon(\omega) - \epsilon_{\mathrm{m}}}{3\epsilon_{\mathrm{m}} + 3L_i(\epsilon(\omega) - \epsilon_{\mathrm{m}})} \tag{2.21}$$

along the principal axes i depending on the geometrical factors [Boh04]

$$L_i = 0.5 r_1 r_2 r_3 \int_0^\infty \frac{dq}{(r_i^2+q)\sqrt{(q+r_1^2)(q+r_2^2)(q+r_3^2)}} \tag{2.22}$$

They result in a mode with individual resonance wavelength for each principal axis.

Cylindrical nanostructures comparable to the ones used in this work can no longer be treated analytically. Therefore, several authors have shown experimentally [Moc02, Lan06, Zor11] that the main resonance of such nanodisks is redshifted with increasing diameter and consequently increasing aspect ratio (here defined as diameter/height; the height was kept constant in the cited experiments). For the geometry in our experiments, where cylindrical or quadratic structures are vertically illuminated, only the (degenerate) modes within the circle or square plane are excited.

2.3.2 Plasmonic heating

One of the most important plasmonic effects is the so-called plasmonic heating, which is the result of non-radiative plasmon decay. According to Link et al. [Lin99], one can describe it in good approximation by a heating of the electron gas followed by electron-electron and electron-phonon relaxations. The separation between electrons and lattice is justified by their very different heat capacity leading to different thermal response timescales [Ani74]. Within femtoseconds (fs) after the absorption of the first photon, the electron gas is excited into a non-equilibrium state, which quickly (100 fs timescale) thermalizes into a Fermi-Dirac distribution by electron-electron relaxation (energy is transferred between electrons). Therefore, it can also be described by an increased electron temperature. Simultaneously, but on a slightly longer timescale of few picoseconds (ps), the electrons pass energy to the lattice via electron-phonon relaxation. These processes can then be followed by phonon-phonon relaxation and finally the conduction of heat into the surrounding medium [Lin99]. The latter finally leads to a complete thermalization of the particle after times, which are much longer than the ones mentioned before, but sensitively depend on the geometry of the particle and its surrounding. In the discussion of plasmonic effects in chapter 6, plasmonic heating is approximated by an infinitely fast heating of the noble metal nanostructure volume while the heat transfer from the particle into its surrounding is considered separately.

In addition to this "pure" plasmonic heating, there can be another heating contribution due to absorption of light with enhanced intensity close to the plasmonic structures. This contribution is hard to distinguish from the "pure" plasmonic heating inside the metal with subsequent heat transfer and also leads to a similar temperature increase. Therefore, it is considered as a contribution to plasmonic heating in the following.

The increased temperature induced by plasmonic heating [Gov07] can in turn influence its surrounding, in particular it has been reported for various systems that it can accelerate chemical reactions [Che08, Adl09, Yen09, Wan13, Bor16].

2.3.3 Further plasmonic effects

Due to their ability to excite electrons, LSPRs show various other effects besides plasmonic heating. One of them, which promises interesting applications, is the enhancement of electron transfer via the increased temperature of the electron gas as explained above. The higher energy allows these hot electrons to overcome energy barriers more easily and it has been shown for heterogenous catalysis [Chr11, Chr12, Ava14, Kal14a, Lin15, Son18] and electrochemistry [Wan17] that this can significantly increase reaction rates.

Another theory, which is less supported by experimental evidence, is an influence of plasmonically enhanced electric fields on adsorbed molecules. It was postulated that these fields could lead to an induced dipole moment, which would then influence the adsorption of reactants [Sun09] or the product desorption [Hoh88].

In addition, an interaction between LSPRs and molecular vibrations can be conceived, although it has not been reported in the literature, yet. The idea of a reaction enhancement via plasmonically excited molecular vibrations is subject of chapter 6.

Chapter 3

Experimental and theoretical methods

In the course of this thesis, different experimental and also theoretical techniques were applied and it is essential to describe all of these methods in order to allow for a reproduction of the experiments. Since most equipment used is commercially available, it is only briefly described. In contrast, the devices, which were designed and built up during this thesis, in particular the miniaturized electrochemical cell (cf. section 3.3.2) and the mass spectrometry system (cf. chapter 4) get more space.
This chapter covers the sample fabrication including nanoimprint techniques and Cu deposition (cf. section 3.1) together with an overview of the resulting sample geometries (cf. section 3.2), all components of our photoelectrochemical setup (cf. section 3.3), optical and X-ray photoelectron spectroscopy (cf. sections 3.4 and 3.5) as well as product analysis via gas chromatography in section 3.6. This is complemented by an explanation of optical and thermal simulations (cf. section 3.7) and a description of the data analysis using Fourier transformation (cf. section3.8).

3.1 Sample preparation

Over the course of the work described in this thesis, most steps of the sample preparation have been optimized and the fabrication procedure used for the samples used in the following measurements is presented in this section. The most important steps of the sample fabrication, in particular nanoimprint lithography (NIL), nanotransfer printing (nTP) and evaporation of metal layers, were performed by Robin Nagel (Institute for Nanoelectronics, TUM), Thomas L. Maier (Nonequilibrium chemical physics group, TUM), Matthias Golibrzuch and James Lindsly (both Institute for Nanoelectronics) within a very close cooperation.

3.1.1 Silicon samples and back contacts

The first aspect of the samples is made up by the substrates used. If not further specified, they consist of crystalline Si of about 400 µm thickness (p-type doping: CZ(111)$\pm$ 0.5, 5–25 Ωcm, [B]=5 $\cdot 10^{15}$ - $4 \cdot 10^{16}$cm^{-3}; n-type doping: CZ(111)± 0.5, 1–10 Ωcm, [P]=5 $\cdot 10^{14}$ – $5 \cdot 10^{15}$cm^{-3}, Si-Mat, Germany, single side polished; degenerate p-type (p^{++}): CZ(111), [B] $> 1 \cdot 10^{19}$ cm^{-3}, <0.01 Ωcm, single side polished, Si-Mat, Germany) equipped with an Al back contact on the unpolished side. Some of these wafers were thermally oxidized for a better passivation. This was achieved by placing them in an O_2 atmosphere at 1000 °C for 8 minutes, leading to a thermal oxide layer thickness of about 30 nm. To achieve a more suitable thickness of (15$\pm$1) nm, the oxide was thinned down in buffered oxide etch (BOE), a 98:2 mixture of 40% ammonium fluoride (NH_4F) and 50% hydrofluoric acid (HF) solution within 30-40 s. This thermal oxide layer (which was later removed below the Au nanostructures) was shown to form a stable passivation layer, which prevents unwanted current flow over the Si-SiO_2 interface (cf. [Mai17]). The samples, which were used for experiments investigating plasmonic resonances, were produced without thermal oxide. Those samples were additionally cleaned by further oxidizing the front side in an oxygen plasma for 5 min and removing the complete oxide layer again by another BOE step. Finally, the samples were oxidized again in oxygen plasma. Next, the wafers were protected from dust by a layer of photoresist and cleaved into 11.3×11.3 mm^2 pieces, which were cleaned with acetone, isopropanol, and deionized water. The back contact of all samples in this thesis was made with aluminum (Al), which usually leads to an ohmic contact for n-Si and a Schottky contact for p-Si. However, an annealing of the Al/p-Si interface can lead to diffusion of Al atoms into the Si material and the formation of a strong local increase in acceptor density, which leads to degenerate doping close to the interface inducing an ohmic contact [Sch15b].

For the preparation of the back contact, first the oxide on the back side was removed by BOE with 6:1 mixing ratio. A 200 nm thick layer of Al was evaporated onto this surface by physical vapor deposition and annealed under vacuum ($< 3 \cdot 10^{-4}$ mbar) to achieve ohmic contacts (cf. also 2.1.2). For n-Si this was done at 250 °C for 15 min, for p-Si and p^{++}-Si at 400 °C for 30 min. The more intensive annealing of p-Si was necessary to allow for Al diffusion into the adjacent p-Si, forming a degenerately doped layer, which then led to an ohmic contact.

For experiments with illumination through the Si, transparent contacts made from an Al mesh on double side polished n-Si (CZ(100), thickness 525±25 µm, doping: 1–5 Ωcm, [P]=1 $\cdot 10^{15}$ – $5 \cdot 10^{15}$cm^{-3}, Microchemicals GmbH, Germany) were used. The mesh consists of 5.5 µm wide, 200 nm thick stripes with distances of 50 µm (vertical) and 300 µm (horizontal) and was also annealed in vacuum at 250 °C for 15 min.

The samples carrying a Au stripe used for the measurement of electrolyte heating were fabricated on n-Si with a thermal oxide layer and a structured Al back contact. On four Au patches at the edges of the stripe, 0.1 mm thick Cu wires were attached using conductive epoxy (Electrodag 5810, Henkel, Germany).

3.1.2 Nanoimprint lithography

NIL is the central sample structuring method for this work, since it allows for the economical structuring of macroscopic areas with feature sizes of only a few 10 nm. It is used in two separate steps in the sample fabrication process: First, it was necessary to replicate the master stamp, which was written into a Si wafer by e-beam lithography (which was done by IMS CHIPS, Germany). The replication was performed using a UV-curable polymer (OrmoStamp, Microresist technology GmbH, Berlin) in order to get a less brittle stamp, which adapts to tiny inhomogeneities on the substrate without breaking. Especially for the method of nTP, it was a strong improvement that copies and not the master stamp were used. In previous versions of the process, the original stamp had been covered with Au for every nanotransfer printing step and a critical cleaning between each nTP process had been required. In the improved process, the polymer stamp, which was a negative of the original template, was replicated again by a UV-NIL step using OrmoStamp, thus leading to single-use stamps which were then used for nTP as well as for LO-NIL. More details about the stamp replication process can be found in [Nag16].

The second step using NIL was the structuring of a polymer layer to form a mask for the decoration of the surface with metal nanostructures via a lift-off process [Nag17]. A reliable

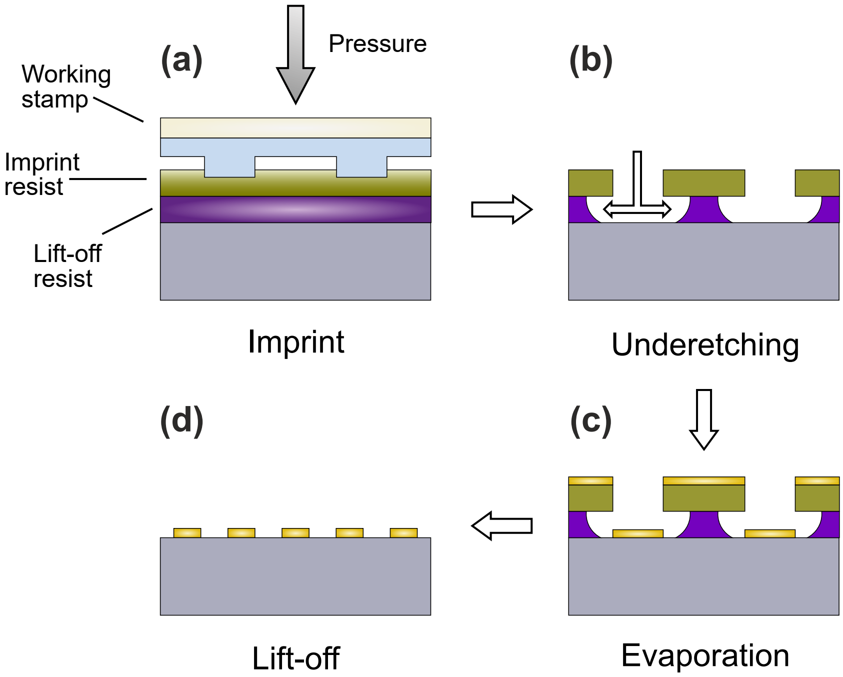

Figure 3.1: Schematic of the LO-NIL process: (a) First the imprint resist is patterned using conventional NIL. (b) The residual imprint polymer layer is removed by anisotropic reactive ion etching. Next, an isotropic etching of the lift-off resist leads to an artificial undercut. (c) A thin metal layer is deposited and (d) finally partially removed by lift-off [Nag17].

lift-off requires an undercut to avoid the formation of a completely closed layer during evaporation of metal atoms.

As it is inherently impossible with NIL to reproduce a stamp with undercut, a trick was used: a bi-layer lithography technique. Therefore, first a layer of PMGI SF6 (Michrochem, USA) diluted in a ratio of 1:4 with G-thinner (also Michrochem, USA) was spin-coated at 4000 rpm for 45 s onto the substrate as a liftoff resist (in the following abbreviated as LOR). It was baked at 255 °C for 3 min resulting in a thickness of 30 nm. For some samples with thicker metal layers, the LOR thickness was also increased to keep the lift-off process possible. On top of the LOR, a thermal imprint polymer (in the following named imprint resist) consisting of mr-I 8020R thinned with ma-T1050 (both Microresist, Germany) in a ratio of 1:1.35, was deposited. It was spin-coated at a speed of 3000 rpm for 30 s and subsequently soft-baked at 100 °C for 1 min, resulting in a layer thickness of 77 nm.

Then, the imprint resist was patterned in a thermal imprint process in an Obducat nanoimprinter 2.5 (Obducat, Sweden) at 165 °C and a gas pressure of 30 bars applied for over 3 min (cf. figure 3.1). After cooling down to 90 °C, stamp and sample were demolded using a sharp razor blade. Since NIL is not able to completely perforate the imprint resist, a residual layer stayed on the substrate. This layer was removed with an anisotropic reactive ion etching (RIE) step (PlasmaLab 80 Plus, Oxford instruments, UK) using a mixture of 27 sccm O_2 and 25 sccm C_4F_8 at a plasma rf power of 200 W to achieve a highly anisotropic etching. Some samples, which had an increased feature diameter, were etched more isotropically using 25 sccm O_2 at a plasma rf power of 35 W. This step already etched into the LOR, but to achieve the undercut, an isotropic wet-chemical etching step was performed using a buffered potassium hydroxide (KOH) based developer (AZ400 K, Microchemicals, Germany) in a 1:5 dilution followed by rinsing with deionized water. For the samples with thermal oxide, the oxide below the future Au nanostructures was removed by a second anisotropic RIE step and the Si surface was plasma-oxidized again.

Then, a stack of typically 3 nm Ti and 18 nm Au was evaporated in a high-vacuum physical vapor deposition (HV-PVD) system (Leybold L560, Germany). The Ti was evaporated at a rate of 1 Å/s at an evaporation pressure of $5 \cdot 10^{-8}$ mbar and the Au at a rate of 3 Å/s at $8 \cdot 10^{-8}$ mbar. In order to achieve less plasmon damping, also samples without or with thinner Ti layers (0.5-2 nm) were made, although the adhesion between Au and SiO_2 was reduced compared to thicker Ti adhesion layers. Also the Au thickness was changed to verify its influence on the plasmonic resonance frequency.

Finally, all resist layers and the metal on their surface were lifted off using N-methyl-2-pyrrolidon (NMP) (Merck KGaA, Germany) at a temperature of 50 °C in an ultrasonic bath.

3.1.3 Nanotransfer printing

In addition to the LO-NIL process, a second method based on the NIL principle, namely nTP, was used. It allows for the addition of metal structures to plain surfaces with high spatial resolution and less effort than LO-NIL. Both methods have in common that they start with a replicated stamp, but in nTP, the stamp itself is completely evaporated with the desired metal. Then, it is pressed onto the target substrate and due to a stronger adhesion to this surface than to the stamp, the metal structures from the elevated surfaces are transferred. More information about nTP can be found in the work of Robin Nagel [Nag16, Nag17].

In practice, the following procedure was performed: First, the replicated stamp was treated with an anti-sticking layer and coated with a Ti/Au metal stack[1] in a high-vacuum physical vapor deposition system (Leybold L560, Germany) at an evaporation pressure of $6 \cdot 10^{8}$ mbar. The Au layer of typically 18 nm thickness was evaporated at a rate of 3 Å/s while the 3 nm Ti layer was evaporated at 1 Å/s (if a different Ti layer thickness was used, this is separately indicated). In parallel, the substrate was cleaned in acetone and isopropanol and oxidized in an oxygen plasma (100 sccm, 100 Pa, 600 W, 2 min), while the stamp was activated in a less aggressive oxygen plasma (90 sccm, 100 Pa, 100 W, 1 min) to improve the adhesion properties. Then, the coated stamp was positioned on the substrate and pressed onto it for 3 min at a pressure of 3 MPa applied via compressed nitrogen and 200 °C in an imprint machine (Obducat imprinter 2.5, Sweden). The stamp was separated from the substrate while it was still hot.

The most special feature of nTP is the complete avoidance of chemicals in contact to the sample. Compared to LO-NIL, it is also significantly simpler, but the electrochemical properties of the resulting structures are of lower quality (cf also section 5.1).

3.1.4 Cleaning

Between the fabrication in a cleanroom and the electrochemical experiments, the samples were exposed to normal air, which contaminated their surface. Since the Al back contacts are not stable in caroic acid, the samples were cleaned in three ultrasonic bath steps of 5 min each, using acetone (AnalaR Normapur, VWR, USA), ethanol (96%, AnalaR Normapur, VWR, USA) and deionized H_2O (18.2 MΩ from ELGA Purelab, Veolia Environnement S.A., France)

---

[1] The order of the layers has to be reversed to achieve the correct order after the transfer.

with subsequent rinsing in H_2O.

3.1.5 Copper deposition

For the measurements using Cu-plated Au surfaces, one further preparation step, the Cu deposition, was introduced. Therefore, two different methods were used: The electrochemical reduction of Cu^{2+} and the chemical deposition using a commercial plating solution (EXPT Seedplate, Atotech, Germany).

The electrolyte employed for the electrochemical deposition method was CO_2-saturated 50 µM $CuSO_4$ and 100 mM K_2SO_4 stirred with a magnet at a rotation speed of 200 rounds per minute (rpm). These parameters differ from typical conditions in the literature where higher $CuSO_4$ concentrations in Ar-saturated sulfuric acid (H_2SO_4) were used. The reason is that K_2SO_4 showed a higher deposition rate compared to H_2SO_4, while at the same time avoiding outgassing of CO_2 in contact with the acidic solution during electrolyte change (cf. also section 5.6.1). CO_2RR in the Cu-containing electrolyte does not take place under the moderate overpotentials during Cu depositions and the saturation of the electrolyte with CO_2 avoids the need for a gas change during the experiments, which could cause irreproducibilites. The described potentiostatic deposition method was developed by Thomas L. Maier during his master's thesis [Mai17].

The deposition potential was chosen significantly more negative than the equilibrium potential of the reaction $Cu^{2+} + 2e^- \rightleftharpoons Cu$ (+0.22 V vs SHE at the given concentration), at -0.16 V vs SHE, to avoid Cu stripping during the electrolyte exchange when the Cu concentration was decreased. Still, this potential does not yet deposit Cu on SiO_2 surfaces so that only the Au surfaces were plated with Cu. After several minutes of potentiostatic deposition, layers of typically several tens of monolayer equivalents (MLeq; assuming that the mainly diffusion-controlled process does not lead to homogeneous layers) were formed.

In order to achieve a quick reduction of Cu concentration, the electrolyte was completely extracted and replaced by buffered electrolyte (75 mM K_2CO_3 + 100 mM H_3PO_4) using a syringe. This procedure was repeated four times under continuous CO_2 purging and potential control at -0.16 V vs SHE.

After all electrolysis measurements with such a layer were finished, the Cu layer was stripped off via a potentiostatic scan from -0.16 V vs SHE to +0.84 V vs SHE where the potential was held constant for 10 minutes. From the electric charge flowing during the stripping process, it was possible to calculate the amount of stripped Cu, which is assumed to be equivalent to the amount of Cu present on the electrode during the previous electrolyses. After electrolyte change and electrolysis measurements with such layers, the corresponding stripping curves typically showed a wide shoulder after a pronounced main stripping peak (cf. also figure 5.16). This was the reason, why the potential was held for 10 min as mentioned above.

The chemical deposition process was established by Kilian Vettori during a working student project. Therefore, a bulk Au sample was polished using polishing pastes (Winter Diaplast D 0.25 SS in Winter Diaplastol, both from Saint-Gobain S.A., France) with grain sizes down to 0.25 µm and cleaned in a bath of cold caroic acid. Afterwards, the sample was immersed in seedplate solution (41:1 mixture of Expt Seedplate Make Up 55 and Expt Seedplate FFT R1, both from Atotech), which was tempered in a H_2O bath on a hotplate between 25 °C and 35 °C. Using a tailored sample holder, which ensures contact of virtually the complete sample

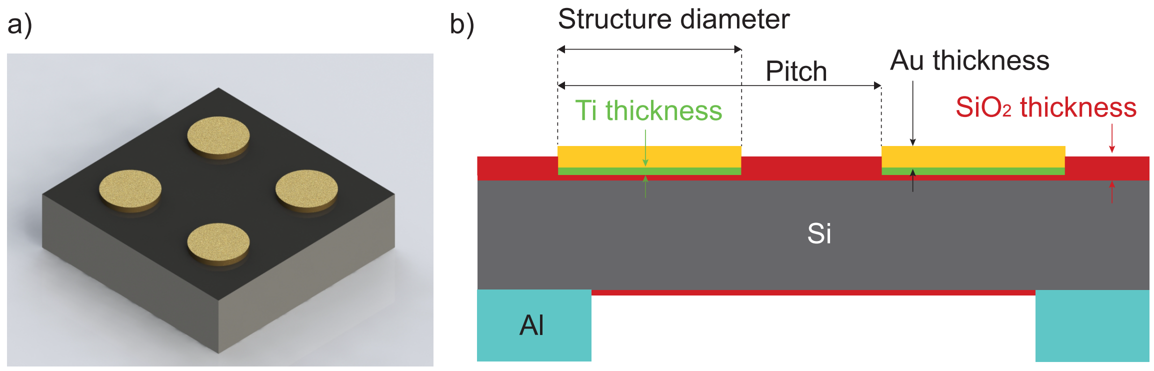

Figure 3.2: Sketch of a typical Si sample with nanodisks, (a) CAD image, (b) vertical cut through a sample with thermal oxide and structured back contact, indicating variable parameters such as the structure diameter, distance between two neighboring structures/pitch, Au thickness, Ti layer thickness and Si oxide layer thickness between the Au structures. Both images are not to scale.

surface with the surrounding liquid, the sample was cleaned by organic solvents. Therefore, it was ultrasonicated in acetone for 20 s, rinsed with ethanol for 10 s, ultrasonicated in ethanol for 20 s, rinsed with water for 10 s and finally ultrasonicated in water for 20s. This relatively quick procedure was used to minimize Cu dissolution into the cleaning agents.

3.2 Sample geometry

The described sample fabrication results in very regular arrays of Au nanostructures, the geometry of which plays an outstanding role in this work. Therefore, two sketches of a Si sample carrying cylindrical nanostructures (nanodisks) are depicted in figure 3.2. A simplified CAD image (figure 3.2(a)) gives a first impression of the layout, while the cross section in 3.2(b) shows a sample with thermal oxide and structured back contact. In the course of this work, also two variations, namely samples with a homogeneous plasma oxide layer (this means that the oxide thickness below structures and on free areas is equal) of 1.5-2 nm thickness and samples with a continuous Al layer as back contact, are discussed.

In general, the structure dimensions and shapes as well as the occurrence of voids in the structure patterns are evaluated using scanning electron microscopy (SEM) after sample fabrication. When changes in the fabrication process were performed and evaluated, SEM images between the important fabrication steps were added, although they are not shown here (more details in [Nag19]). In figure 3.3 a series of differently magnified details of a 75 nm sample fabricated by LO-NIL is presented. They show that there are virtually no missing nanodisks (except at the corners) and that the structures are indeed cylindric.

In this work, Au nanostructures with sizes of 1400 nm, 350 nm, 200 nm, 75 nm and 45 nm were prepared and characterized. The Au coverage, which remained almost constant over the range of structure size variation, assured a diffusional mass transport, which does not significantly vary between the structure sizes and a comparable optical transmission (at least in the spectral regions without LSPRs). Due to the available master stamps for the NIL process, different nanostructure geometries had to be used: the ones with 75 nm and 45 nm are cylinders/nanodisks with a pitch of twice the structure diameter, resulting in a coverage of

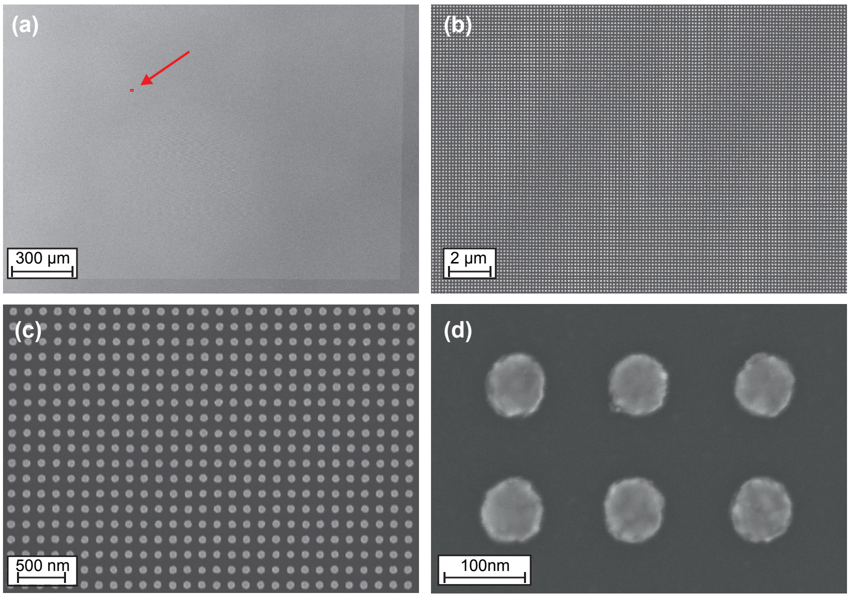

Figure 3.3: SEM images of a sample with 75 nm structure size fabricated using the LO-NIL method. (a) Overview of a larger part of the sample; the location of the other details is shown in red, (b-d) details of the sample with increasing magnification. SEM images by Robin Nagel [Nag17].

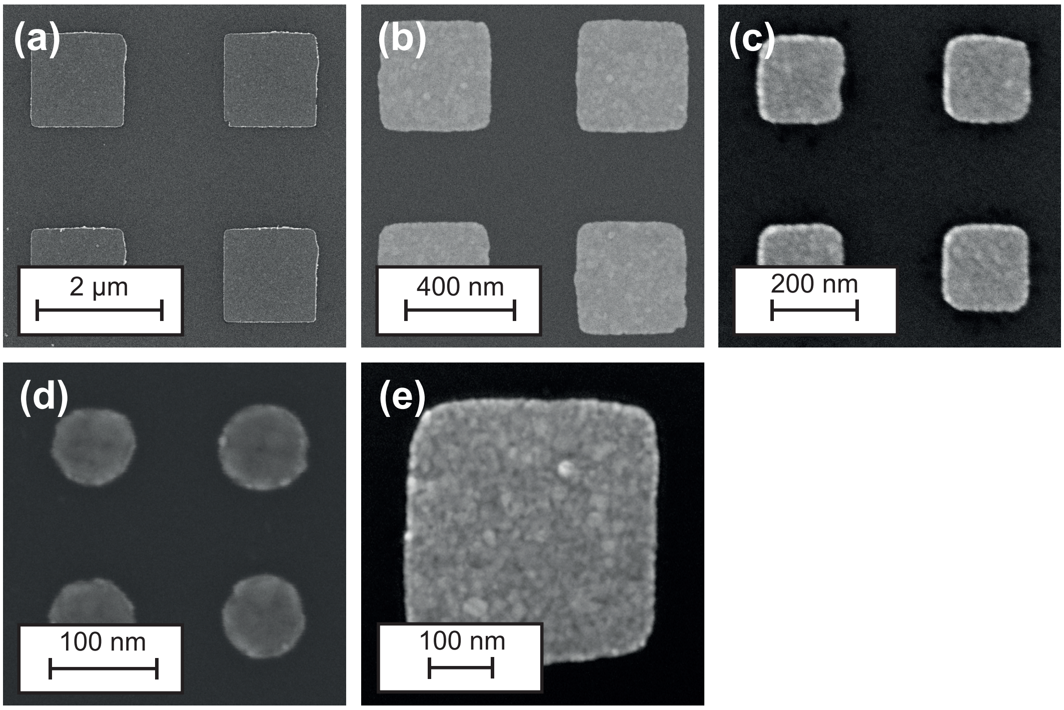

Figure 3.4: SEM images of differently sized nanostructures: nanosquares with side lengths of (a) 1400 nm, (b) 350 nm, (c) 200 nm and nanodisks with (d) 75 nm diameter. (e) 350 nm nanosquares with increased resolution. SEM images by Robin Nagel [Fil18].

Structure size a/nm	ratio pitch/ structure diameter	Surface share covered by Au/%	Ratio Au area/ substrate area/%	edge length per area/10^{10}nm cm^{-2}
1400 (square)	2.15	22	22	6.2
350 (square)	2	25	26	28
200 (square)	2.15	22	24	43
75 (disk)	2	20	25	105
45 (disk)	2	20	28	174

Table 3.1: Geometrical parameters of the nanostructures used in this work. The ratio between Au area and substrate area is given for samples with 15 nm thermal oxide thickness. Table reproduced from [Fil18].

19.6% (cf. table 3.2). The sizes 1400 nm and 200 nm are nanosquares with rounded edges[2] and a comparable coverage of 21.6%, this corresponds to a pitch, which is 2.15 times larger than the structure diameter. The pitch size of the 350 nm nanosquare master stamp was again twice the structure diameter, resulting in a coverage of 25%. As it can be seen in figure 3.4, the nanosquares have rounded edges with a corner radius of about 30 nm.

Using Si substrates, the surface passivation is of great importance: Since H-terminated Si surfaces are not stable in air and electrolytes, the Si surface had to be stabilized, which was achieved with a layer of SiO_2 on the whole Si surface. Depending on the experiments performed with the respective sample, homogeneous plasma oxide layers of 1.5-2 nm thickness or thermal oxide layers of 10-15 nm thickness were used. In the latter case, the oxide beneath the Au is also a plasma oxide layer of only 1.5-2 nm thickness (cf. section 3.1 for fabrication details). Consequently, the resulting sample design can be regarded as a metal/insulator/semiconductor (MIS) structure: The oxide layer between Si and metal structures is so thin that electrons can easily move through it via trap-assisted tunneling, but its preparation and the contact size equivalent to the adjacent structure size significantly influence the interfacial band alignment and therefore the overall sample performance.

The last aspect of sample appearance, which is discussed here, is the morphology of the Au layer. In the magnified view of a 350 nm structure (Figure 3.4(e)) one can very well see that the surface of the polycrystalline structures features a high density of grain boundaries, which are structural defects between different crystal facets.

3.3 Photoelectrochemical setup

3.3.1 Electrodes and potentiostat

Most experiments in this work used electrochemical and photoelectrochemical methods, which were performed in a three-electrode setup consisting of a working electrode (WE), a reference electrode (RE) and a counter electrode (CE). This allows for the simultaneous measurement of potential and current of a single electrode, the WE, which is the sample of interest. The difference between WE potential and the well-known and stable RE potential is measured by a potentiostat. Therefore it is necessary to assure a high impedance of the RE

---

[2] The structure shapes were determined by the fabrication process of the master stamps using electron beam lithography

to minimize current flow through it, which would disturb the measurement of the potential difference between RE and WE. Simultaneously, the potentiostat applies a current between WE and CE, which is also recorded. The value of this current is adjusted such that the WE potential reaches the predefined value.

For the measurements, two different versions of saturated mercury/mercurous sulfate electrodes (sat. MSE) were used as REs (REF601, Hach, USA and RE-2CP, ALS Co., Ltd, Japan). They only differed in their dimensions and shaft material (REF601: glass, RE-2CP: polymethylpentene). In order to achieve a potential representation versus standard hydrogen electrode (SHE), the potentials measured with this electrode are shifted by +640 mV. Depending on the respective cells, counter electrodes made of Au and glassy carbon (Sigradur, HTW Hochtemperatur-Werkstoffe GmbH, Germany) were used.

The electrical, electrochemical and photoelectrochemical measurements were performed on a Zahner Zennium potentiostat, connected to a PP211 slave potentiostat, which controlled a TLS-03 tunable light source (all from Zahner-Elektrik GmbH & Co KG, Germany). This potentiostat was also used for resistivity measurements using 4-point wiring, which allowed us to get rid of any impact of cable resistance. One single experiment, the one shown in figure 5.14(a), was recorded using a WaveDriver potentiostat (Pine research instrumentation inc., USA).

3.3.2 Electrochemical cells

Besides the working electrode and the potentiostat, the electrochemical cell is a key element of every electrochemical setup. In the course of this thesis, several cells were developed. For simplicity, only the latest version of a three-compartment electrolysis cell is presented in this section. This three-electrode cell was optimized for product analysis under illumination from front or rear side and enabled a controlled electrolyte exchange. Some of the measurements described below were done with older versions of it, but using a similar principle design.

The miniaturized cell made of polychlorotrifluoroethylene (PCTFE), which is shown in figure 3.5, consists of a main cell body with about 5 ml inner volume (filled with about 3 ml of electrolyte and 2 ml of gas overhead). The working electrode, which was sealed by a fluoroelastomer (FPM) O-ring of 9 mm inner diameter (leading to 0.64 mm^2 exposed area) and 1 mm cord size, was mounted such that its surface was in contact to this electrolyte volume. The WE compartment also featured a gas inlet and outlet connected to a CO_2/Ar bottle respectively the product analysis setup, as well as an electrolyte inlet and outlet allowing for an electrolyte exchange. The electrolyte outlet was positioned at the height of the liquid level and it was designed in such a way that it sealed the main compartment with a very low dead volume in closed state and with the possibility to directly pipe electrolyte into an outlet tube when opened. Above the upper electrolyte surface, a bar prevented liquid droplets dispersed by purge gas bubbles from flying into the gas outlet. Additionally, a tiny, polytetrafluoroethylene (PTFE)-coated magnet (8x1.5 mm, VWR collection, Avantor, USA) was introduced into the cell. On the one hand, it allowed us to stir the electrolyte using a rotating permanent magnet outside the cell, on the other hand, it made it possible to remove bubbles from the electrode surface, that blocked parts of it. In addition, the gaseous products trapped in the bubbles on the WE surface were thus released into the gas overhead, which was analyzed subsequently.

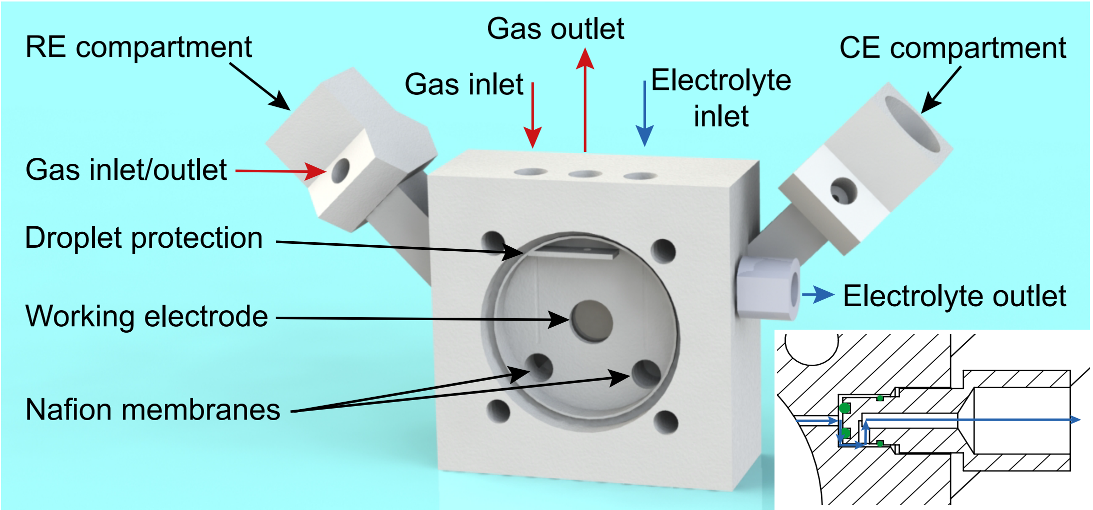

Figure 3.5: CAD image of the three-compartment cell made from PCTFE. Black arrows denominate components, red ones show gas flow and blue arrows indicate electrolyte flow. The inset shows a cut through the plug, which allows for a controlled electrolyte outlet with the option to connect it to a tube and o-rings colored in green.

Another trick for an easier removal of gas bubbles was a tilt of the hole cell by 45° so that the electrode surface pointed diagonally upwards and bubbles could more easily detach from it. The compartments for RE and CE were also tilted upwards by 45° and separated from the WE compartment by Nafion membranes (Nafion 117, DuPont, USA, thickness 0.18 mm, activated in cold caroic acid). Since such a membrane has a high permeability for gas diffusion [Sch15a], the compartments had additional gas inlets and outlets that made it possible to purge them individually. This was only used for the measurement with DEMS product analysis where traces of N_2 are spurious, for all other measurements, it was not used.

The rear side of the working electrode was electrically contacted by a Cu cylinder or by a ring of Cu foil permitting illumination from the back.

Between the experiments, all cell parts were regularly cleaned in caroic acid (1:1 mixture of 95% sulfuric acid (AnalaR Normapur, VWR, USA) and 30% hydrogen peroxide (AnalaR Normapur, VWR, USA)).

At this point, it has to be noted that the geometry of the cell led to an ohmic resistance, which was higher than for conventional cells. For a 75 mM K_2CO_3 + 100 mM H_3PO_4 electrolyte purged with CO_2, about 46 Ω stemmed from the electrolyte and about 13 Ω from the membrane[3]. These values were determined using impedance spectroscopy with bulk Au and they were used for an IR (current $\times$ resistance) correction.

3.3.3 Electrolytes and light sources

The last two elements of photoelectrochemical experiments described here are the electrolytes and the light sources. While an electrolyte both conducts current and supplies reactants, the purpose of a light source obviously lies in the provision of photons. Since the two major groups of experiments in this work each used specific versions of these items, it is more coherent to separate this section according to the respective experiments.

---

[3] This was assumed to be temporally constant.

Electrolytes and light source for experiments investigating the impact of electrode structuring

The setup for the experiments investigating the impact of electrode structuring (in section 5) was chosen with the aim of a reduced surface pH drift, which resulted in the use of a phosphate buffer, and of flexible illumination options, which suggested the use of a tunable light source.

The most common electrolytes in CO_2 reduction are aqueous solutions of potassium bicarbonate ($KHCO_3$). Since the latter compound was only commercially available in mediocre quality, we used potassium carbonate ($K_2CO_3 \cdot 1.5H_2O$, suprapur, Merck KGaA, Germany), which reacts to $KHCO_3$ under CO_2 purging. For the measurements, which shall evaluate the influence of electrode structuring and feature size (cf. chapter 5), the $KHCO_3$ solution was complemented by an additional phosophate buffer. This buffer was prepared by introducing phosphoric acid (H_3PO_4, suprapur, Merck KGaA, Germany) into a K_2CO_3 solution. Only for the measurements in sections 5.1 and 6.3, a solution of $KHCO_3$, K_2HPO_4 (both AnalaR Normapur, VWR, USA) and KH_2PO_4 (suprapur, Merck KGaA, Germany) was used.

For the electrodeposition of Cu, solutions of Cu(II) sulfate ($CuSO_4$) (for analysis, Merck KGaA, 99.0%) and potassium sulfate (K_2SO_4, Merck KGaA, for analysis, 99.0%) were used.

All electrolytes were purged for at least 30 min with CO_2 (Westfalen AG, purity 4.5 and Air liquide S.A., purity 5.5 for MS measurements) or Ar (Westfalen AG, purity 5.0).

In order to assure cleanliness of the cells and electrolytes, several measures were taken in the course of this work. Next to the regular intensive cleaning of all cell parts and the use of the purest available chemicals, the gas lines were equipped with particle filters to retain metal particles, Nafion membranes were introduced between the cell compartments and the exposure time of the clean parts to air was minimized. Still, some pathways of contaminant intake could not be completely prohibited. This includes the diffusion of impurities out of the cell materials, contact of the sample and cell parts to air during cell assembly, metal particles evolving in the gas line downstream of the particle filter or dust particles entering the chemical or electrolyte bottles, while they were opened. Therefore, the cleanliness level of the experiments was regarded as high, but remaining metal ions in the electrolytes could not be completely excluded.

For the measurements using p-Si, a TLS-03 tunable light source (Zahner, Germany) was used. This device was directly controlled by the potentiostat and consisted of a set of 24 light-emitting diodes (LEDs) with wavelengths between 365 nm and 1015 nm. They could be accessed individually and in the range of 420-710 nm, an additional monochromator could be used for a better spectral resolution.

Electrolytes and light source for experiments investigating plasmonic excitations

In the experiments investigating plasmonic excitation of molecular vibrations of CO_2 in section 6, both the electrolyte and the light source were chosen with the aim of an illumination at a wavelength of 2.8 μm.

Due to the strong absorption of H_2O around this wavelength, heavy water (D_2O)-based electrolytes were used. They were prepared from $K_2CO_3 \cdot 1.5H_2O$ (suprapur, Merck KGaA, Germany) and sulfuric acid (H_2SO_4, suprapur, Merck KGaA, Germany) in D_2O (99,9 %, Sigma-Aldrich, Merck KGaA, Germany). The supporting electrolyte for the RE and CE compartments in the experiments about molecular vibrations of CO_2 was potassium sulfate (K_2SO_4, Merck KGaA, for analysis, 99.0%) in D_2O.

Again, the electrolytes were purged for at least 30 min with CO_2 (Westfalen AG, purity 4.5) or Ar (Westfalen AG, purity 5.0).

The light source for these experiments was a 400 W halogen lamp (HLX 64665, Osram, Germany) with bandpass filters, which could deliver a reasonable intensity in the near and short-wavelength infrared range. A BP2770-240 filter (Spectrogon AB, Sweden) allowed for an illumination with 2.77 µm central wavelength and a full width at half maximum (FWHM) of 0.24 µm at a nominal lamp voltage of 30 V and a current of 11 A (330 W) and a SWBP-2017-001623 filter (Northumbria Optical Coatings Ltd, UK) for illumination with a central wavelength of 2.02 µm and a FWHM of 0.37 µm, then using a nominal lamp voltage of 10 V and a current of 6.1 A (61 W). The matching of both filters to the absorption spectra of H_2O and D_2O is shown below in figure 6.12. For both filters, the light was focused by a 2" CaF_2 lens (Edmund optics, UK) and a Au-plated concave mirror (Thorlabs, USA) to a rectangular spot of about 7x7 mm and an intensity of 80 mW/cm^2. Chopping of the light was achieved by a slitted cylinder between lens and filter, which was rotated by a stepper motor. This allowed for chopping frequencies between 0.3 Hz and about 50 Hz. While the minimum frequency was determined by the frequency generator of the stepper motor, which drove the chopping wheel, the maximum frequency was limited by the torque of the motor. For the actual measurements, the detection limit of the experiment was a more relevant factor for the upper limit of the frequency, as the modulation amplitudes decreased with increasing chopping frequency.

This setup was designed in close collaboration with Prof. Dr. Andreas Ulrich (Chair for Experimental Astro-Particle Physics, TUM) and Josef Zimmermann during his master's thesis [Zim17].

3.4 Optical characterization

The currently most established method for a direct evaluation of sample design and geometry is scanning electron microscopy (SEM), which yields images of high resolution. The SEM pictures shown in this thesis were recorded on a Zeiss NVision 40 SEM (Zeiss, Germany) by Robin Nagel.

In addition, optical and NIR spectra of the samples are important for a characterization of LSPRs. The optical reflectivity spectra and a part of the transmittivity spectra were recorded on a Perkin Elmer UV-Vis-NIR Spectrometer 301 Lambda 900 (PerkinElmer, USA) in reflection cf. transmission mode.

A Varian Cary 5000 UV-Vis-NIR (Varian, USA) spectrometer was used for transmission spectra of Au structures on glass. These measurements were performed in collaboration with Aurora Manzi (Chair for Photonics and Optoelectronics, LMU München).

3.5 X-ray photoelectron spectroscopy (XPS)

XPS, the analysis of photoelectrons extracted by X-ray irradiation, is a powerful tool for the analysis of solid surfaces and it was used in this work to assess the quality and selectivity

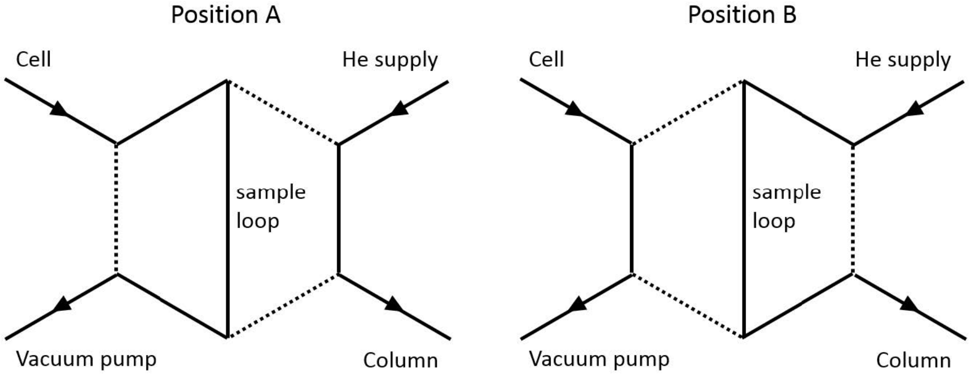

Figure 3.6: Working principle of the 6-port valve. Image from [Mai17].

of the Cu deposition methods. The XP spectra shown in this work were either recorded with a commercial device using the Mg source of an XR 50 x-ray tube (1486.6 eV) and a Phoibos 150 analyzer (both from Specs GmbH, Germany) or on a home-built setup using the Mg source of a XR-50 x-ray tube, a Specs PCU 300 MCD-5 spectrometer and a Phoibos 100-MCD detector (all from Specs GmbH, Germany).

3.6 Product analysis using gas chromatography (GC)

Since the product distribution arising from CO_2 reduction is probably the most complex and most interesting measurement parameter of this thesis, the analysis of these products is of paramount importance. These measurements were either performed using the gas chromatograph (GC) described in this section or using the mass spectrometry setup, which is treated extensively in chapter 4.

GC measurements were done with a GC2010 Plus (Shimadzu, Japan) equipped with a barrier discharge ionization detector (BID 2010 Plus, Shimadzu, Japan) operated at a temperature of 300 °C and a micropacked ShinCarbon ST 80/100 (inner diameter 0.53 mm, length 2 m; Restek GmbH, Germany) column. It was continuously purged by helium (He, purity 6.0, Westfalen AG), which was further refined by two heated gas purifiers.

An important part of the GC setup was the semiautomatic sample collection with several valves controlled by the GC: A 6-port valve connected the He supply line over a sample loop of 100 µl volume with the GC column in standby position (Position B , cf. figure 3.6). Over the other two ports, a vacuum pump was connected to the electrochemical cell; both lines were equipped with an additional magnetic 2-way valve. To draw a gas sample, the 6-port valve switched into position A so that the He line was directly connected to the column, while the sample loop was connected between vacuum pump and cell.

By subsequently opening the valve in front of the pump, the sample loop could be evacuated. When this valve was closed and the one in front of the cell was opened, the vacuum inside the sample loop was filled by gas from the cell. Now, the analyte gas was transported into the column by switching the 6-port valve into position B. Before starting the next electrolysis, cell, tubes and pump were purged with CO_2 under a small overpressure of 200 mbar, which was controlled by an additional pressure controller in the CO_2 supply line directly in front of the cell.

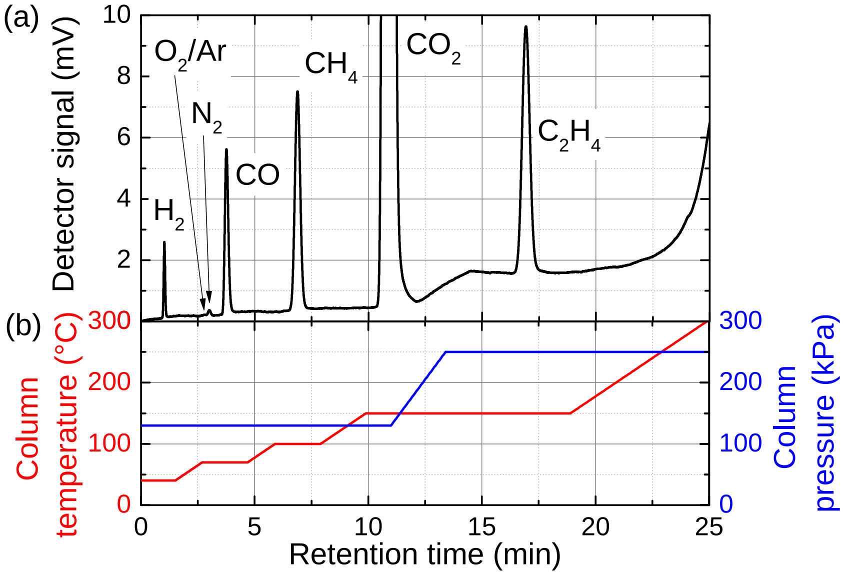

Figure 3.7: (a) Exemplary product gas chromatogram of the test gas containing 1.08% H_2, 1.02% CH_4, 1.27% C_2H_4, 1.01% CO and 95.6% CO_2. (b) Column temperature and pressure transients of the method used.

In order to achieve a separation of all relevant gas peaks, the measurements started at 40 °C, going up to 150 °C where measurement time and peak broadening of less mobile species were reduced. After all relevant peaks appeared, the column was baked out at 250°C to remove remaining H_2O from the column. Next to the temperature transient, the column pressure was ramped up after 11 minutes to further decrease the time between CO_2 and the C_2H_4 peak, which had a long retention time (cf. figure 3.7).

The measurement routine was calibrated using a gas mixture containing 1.08% H_2, 1.02% CH_4, 1.27% C_2H_4, 1.01% CO and 95.6% CO_2 (custom mixed by Linde AG; Relative measurement error: 2%) and using the calibration method of the LabSolutions software (GC software from Shimadzu, Japan). Since the BID detector had a very linear behavior and a reproducible dilution of gases could not be guaranteed, only the original gas mixture was measured three times without dilution and the average values for each species were used.

The main source of error in the GC measurements was the finite noise level in the background of the gas chromatograms. It led to a statistical error, which was estimated according to the ratio between this noise level and the respective peak heights. It was also regarded as the detection limit for each gaseous species. The resulting error values were regarded as independent from the measured concentrations (which is indicated by the index "conc"):

$$\begin{aligned}
\Delta_{\mathrm{bg}} c_{\mathrm{H_2}} &= \pm 0.095\%_{\mathrm{conc}} \\
\Delta_{\mathrm{bg}} c_{\mathrm{CH_4}} &= \pm 0.009\%_{\mathrm{conc}} \\
\Delta_{\mathrm{bg}} c_{\mathrm{C_2H_4}} &= \pm 0.007\%_{\mathrm{conc}} \\
\Delta_{\mathrm{bg}} c_{\mathrm{CO}} &= \pm 0.019\%_{\mathrm{conc}}
\end{aligned}$$

The individual values differ due to the different sensitivity of the detector for the tested species.

In addition, a systematic error of 2 % due to the calibration with the test gas and errors due to the dissolution of the gases in the electrolyte were considered. Since their solubility in H_2O is different, the ratio between gas dissolved in the electrolyte and gas in the gas overhead changes. For our cell geometry, about 2.5 % of the H_2, 5 % of the CH_4, 16 % of the C_2H_4 and 3 % of the CO content would be in solution in the electrolyte under equilibrium conditions (solubility data from [Hay10, ET19]). With the extraction method used, which applied an underpressure to the electrolyte, it was estimated that only 10-20 % of the dissolved gases remained in the electrolyte so that additional proportional errors of $\Delta_{\mathrm{sol}}\eta_{\mathrm{g,H_2}} = \pm 0.5\%_{\mathrm{rel}}$, $\Delta_{\mathrm{sol}}\eta_{\mathrm{g,CH_4}} = \pm 1\%_{\mathrm{rel}}$, $\Delta_{\mathrm{sol}}\eta_{\mathrm{g,C_2H4}} = \pm 3.2\%_{\mathrm{rel}}$ and $\Delta_{\mathrm{sol}}\eta_{\mathrm{g,CO}} = \pm 0.6\%_{\mathrm{rel}}$ were considered. In contrast, demixing of the gas by different diffusion constants or thin orifices is hard to quantify and was therefore not considered.

The calculation of weighted product gas concentrations $\eta_{\mathrm{g},i}$ using the sum over all four gaseous species according to

$$\eta_{\mathrm{g},i} = \frac{z_i c_i}{\sum_j z_j c_j} \tag{3.1}$$

with $i, j \in \{\mathrm{H_2}, \mathrm{CH_4}, \mathrm{C_2H_4}, \mathrm{CO}\}$ and the electron numbers $z_{\mathrm{H_2}} = 2$, $z_{\mathrm{CO}} = 2$, $z_{\mathrm{CH_4}} = 8$ and $z_{\mathrm{C_2H_4}} = 12$ (cf. also section 2.2.3) led to some error propagation. Therefore, the corresponding error for each species depends on the others following

$$\Delta\eta_{\mathrm{g,i}} = \frac{\eta_{\mathrm{g,i}} \sum_{j \neq i}(z_j \Delta c_j) + z_i \Delta c_i \sum_{j \neq i}(\eta_{\mathrm{g,j}})}{\sum_j z_j c_j} \tag{3.2}$$

3.7 Simulations

In parallel to the optical UV-Vis spectra, numerical simulations of transmission and reflection spectra were performed by Robin Nagel and Tianyue Zhang (Chair for Photonics and Optoelectronics, LMU München). These simulations, which ran on the commercial programs finite difference time-domain (FDTD) Solutions (Lumerical Solutions, Inc., Canada) and Comsol Multiphysics (Comsol Inc., Sweden), were based on geometrical dimensions of the nanostructures, that were determined by SEM and atomic force microscopy (AFM) in advance. The half-space $z \leq 0$ nm was filled by the Si substrate covered with a 1 nm oxide layer and a Ti adhesion layer of 3 nm thickness underneath the Au structures (cf. sketch in figure 3.8). The dielectric functions and corresponding optical properties of all materials were taken from Johnson and Christy [Joh72], Palik [Pal03] and Green [Gre08] respectively. Due to the symmetric structure, periodic boundary conditions were used around the edges within the xy plane to reduce computation cost. The top and bottom boundaries should avoid unwanted reflections and were therefore defined as scattering boundaries. While a maximum grid size of 15 nm was applied at the edges of the simulation area, a fine mesh grid of 1 nm resolution was used on the Au nanostructures. For the simulations of transmittivity and reflectivity spectra, the corresponding power monitors were recorded under illumination with a linearly polarized plane wave with normal incidence on the nanostructured surface.

Furthermore, one-dimensional simulations of the heat equation were performed using a custom written script in Mathematica 9 (Wolfram Research, USA) in order to model the temperature distribution on a large illuminated electrode. All relevant formulas are given in section 6.5.3.

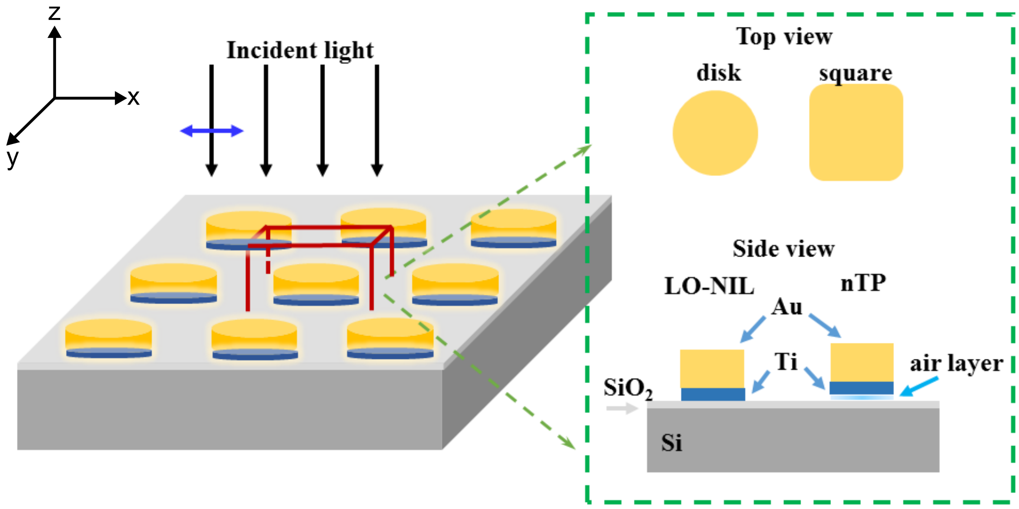

Figure 3.8: Sketch of the model used for the simulations. The red box indicates the simulation volume (adapted from [Nag17]).

3.8 Data analysis using Fourier Transformation and Welch's method

In the electrolysis measurements probing the influence of plasmonic excitation of molecular vibrations, tiny, periodic current modulations on a drifting background with a certain level of noise were recorded. A reasonable method for the extraction of such signals is the Fast Fourier Transformation (FFT) algorithm, which results in so-called periodograms of the current transient. The method was chosen instead of lock-in amplification of the current signal because it allowed to choose arbitrarily long time windows and is less sensitive to slow drifts in the background.

One way to further optimize the quantitative analysis of periodograms is Welch's method, which means a splitting of the time transient into overlapping pieces, which are then averaged [Wel67]. For this work, Hamming windows [Kai77] with a width of 40 s and an overlap of 20 s were Fourier transformed using the FFT routine in OriginPro 2015. Single periodograms with artifacts, e.g. a broad noisy background caused by bubble-induced jumps of the current, were manually rejected before averaging. The remaining noise background of amplitude $I_{\text{background}}$ is not correlated to the actual signal and both contributions are complex values with arbitrary phases (cf. figure 3.9(a)). One way to determine the absolute value of the actual amplitude I_{net} is to take an average value of various individual measurements with random phases. Then, the background, which was manually read out in the region around the peak, was quadratically subtracted from the amplitude I_{meas} of the resulting averaged periodogram via $I_{\text{net}} = \sqrt{I^2_{\text{meas}} - I^2_{\text{background}}}$. The averaging method is exemplarily depicted in figure 3.9(b), which shows a detail of a series of 6 periodograms of electrolysis measurements at a central illumination wavelength of 2.8 µm and a chopping frequency of 0.67 Hz on a sample with 1400 nm structures. According to Welch's method, their average (bold black line) is used for interpretation.

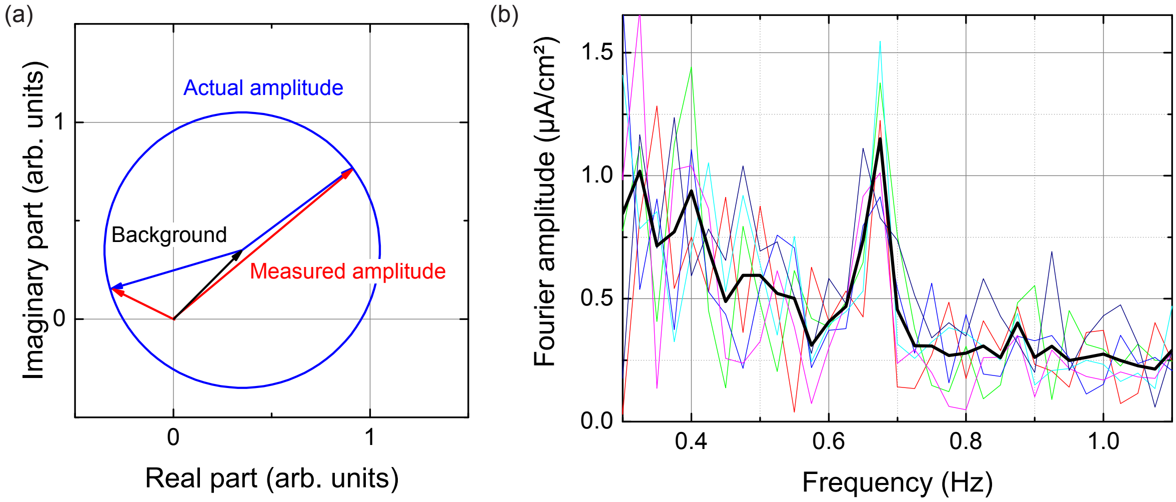

Figure 3.9: (a) Visualization of the consequences of a finite background level (black) with arbitrary phase in the complex plane. Depending on the phase of the actual signal (blue), which is added to the background, the measured amplitude (red) yields very different values. (b) Periodograms of 6 electrolysis measurements at a central illumination wavelength of 2.8 µm and a chopping frequency of 0.67 Hz on a sample with 1400 nm structures in CO_2-saturated 50 mM K_2CO_3 in D_2O. An average background current density of 11.7 mA/cm^2 (represented by a corresponding peak at 0 Hz, not shown in this spectrum detail) with respect to the Au area is achieved in an electrolysis of 4 min length at a potential of -1.46 V vs SHE. The bold black line is the average of the individual periodograms. Note that the amplitude shown here is half of the peak-to-peak amplitude.

Chapter 4

Design of a cold trap for DEMS

A main challenge in the research on the CO_2RR is the analysis of the emerging product spectrum. One of the most powerful methods for the analysis of gaseous reaction products stemming from electrocatalytic reactions is electrochemical mass spectrometry, respectively differential electrochemical mass spectrometry (DEMS) [Bru71], the analysis of electrochemical reaction products using a mass spectrometer. Its typical design combines a vacuum setup consisting of two differentially pumped chambers and a sample gas inlet into the high pressure chamber with a mass spectrometer in the low pressure chamber. Its main advantage - in particular compared to the more widespread methods of gas chromatography (GC) and gas chromatography–mass spectrometry (GC-MS) - is the possibility of very fast measurements. Although DEMS is meanwhile quite established[1], it is hardly used for quantitative analyses of CO_2RR products due to two drawbacks.

The first problem is that the mass spectrum of a mixture of gases can contain contributions of several species in a single mass channel so that a quantification becomes more complicated. In this work, we present an analysis method, which allows us to disentangle the spectra from mixtures of H_2, CH_4, C_2H_4, CO, N_2 and CO_2 (which are typical for the CO_2RR on Cu surfaces) and quantify the actual concentrations of these species.

The second challenge in typical DEMS measurements of CO_2RR products is that they are diluted in a matrix of CO_2 and H_2O. These molecules do not only introduce a high base pressure in the vacuum chamber without gaining additional measurement accuracy from it, they also create background peaks in the mass spectra, which introduce a certain error in the measurement of the analyte species. One way to get rid of the major part of CO_2 and H_2O is the installation of a cold trap in the vacuum system. Its functional part is a large surface with a constant, low temperature. If the partial pressure of a species inside the vacuum chamber (which is in contact to this surface) exceeds its vapor pressure at the cold trap temperature, a part of it is frozen out[2].

For advantageous combinations of gases, in particular for mixtures of H_2O, CO_2 and other permanent gases with a higher vapor pressure, such a cold trap allows for the selective reduction of the partial pressure of CO_2 and H_2O and thereby to drastically increase the measurement accuracy for the other species. The phase diagrams of hydrogen (H_2), nitrogen (N_2), carbon monoxide (CO), oxygen (O_2), methane (CH_4), ethene (C_2H_4), CO_2 and H_2O in

---

[1] At this point it has to be noted that almost all DEMS systems currently used in various groups are installed in a configuration where the sample gas is directly introduced into the vacuum system over a porous membrane. In these configurations, the term "differential" becomes a second meaning, as the product formation rates can be directly measured [Wol84, Har90] in contrast to "integrating" approaches, which first accumulate product gas and then introduce it into the vacuum system. Since the membrane technique allows for a detection in almost real time, it is also sometimes called "online electrochemical mass spectrometry" (OLEMS) [Won06].

[2] The term "freeze out" is used for selective deposition (or desublimation) of certain species out of a mixture of gases in the following

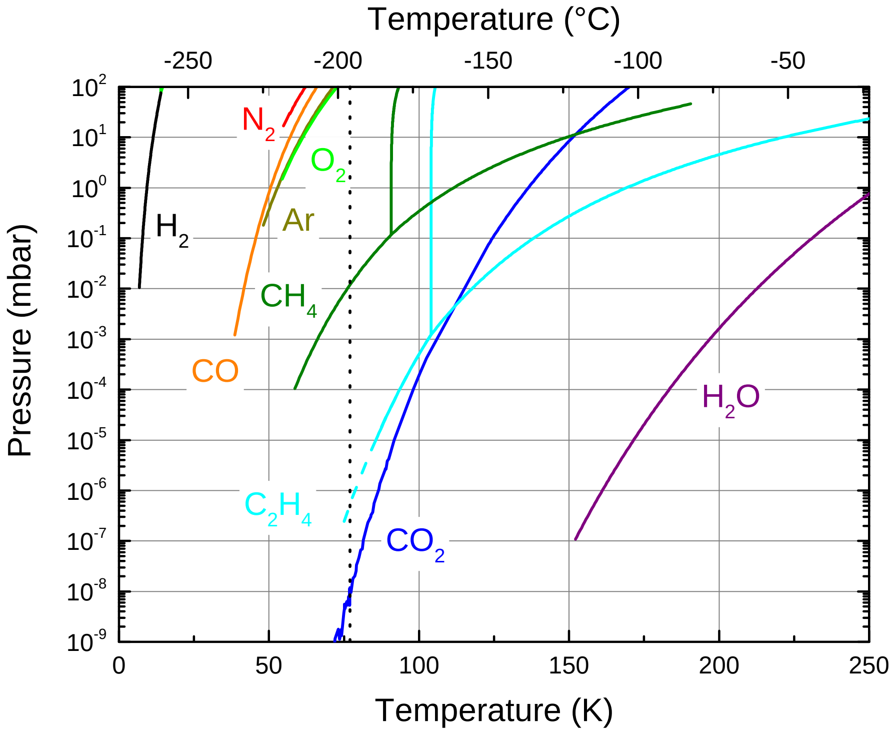

Figure 4.1: Phase diagrams of selected compounds, which typically occur under CO_2RR conditions (CO_2 data reproduced from [DDBSSTG17], all other curves from [ALSA17]). For parameters left of or above the curves, the species occur in solid form, right of or below the curves in gaseous form. In the shown parameter region, CH_4 and C_2H_4 also occur in the liquid phase. This phase is present in the upper right region bounded by two dark green and light blue curves, respectively. The dashed light blue line is an extrapolation using a second order polynomial, the vertical dotted black line at 77 K indicates the temperature of liquid N_2 at ambient pressure.

figure 4.1 show that it is possible to selectively reduce the partial pressures of CO_2 and H_2O without affecting the typical gaseous products of CO_2RR, namely H_2, CO, CH_4 and C_2H_4: At temperatures between 77 K - the temperature of liquid N_2 at ambient pressure - and 110 K, the vapor pressures of theses product species lie above the ones of CO_2 and H_2O. Therefore, it is possible to concentrate these products from a dilute mixture in CO_2 and H_2O by reducing the temperature to this range and thus freezing out a large part of the CO_2 and H_2O present.

Another instructive way to describe such a cold trap is the picture of a selective pump: Usually, two differentially pumped vacuum stages at different pressures are used to reduce the response time of the mass spectrometer setup and to keep the pressure at the mass spectrometer low enough. In principle, there is a simple connection between pumping speed, pressure and gas inlet flow in a vacuum system: The product of the inlet flow rate multiplied with its pressure is equal to the vacuum pressure multiplied with the turbo pumping speed (neglecting other gas sources or sinks). Since a mass spectrometer has to be operated in high vacuum, one must assure a very low inlet flow rate or inlet pressure. In the first case, one would drastically increase measuring time, so it is common to decrease the pressure of the gas inlet by an upstream vacuum chamber, the pressure of which lies between the high vacuum at the mass spectrometer (MS) and atmospheric pressure. Thus, one throws away a large part of the sample gas, but on the other hand one gains a much faster detection rate. The appealing property of a cold trap at this position is the possibility to selectively pump away CO_2 and H_2O as a first pumping stage: This simultaneously decreases the pressure and avoids the disposal of precious product gases in a conventional pump. This means, that a cold trap can indeed significantly mitigate the problem of a high background level.

A drawback of this design is however that one also loses the possibility of measuring volatile liquid products such as C_2H_5OH, which are also frozen out. But for many CO_2RR experiments, which analyze the influence of experimental parameters on the electrochemical reactions, it is not necessary to measure the complete product spectrum, one can focus on the gaseous products H_2, CO, CH_4 and C_2H_4.

In this chapter, the design of the cold trap is first introduced and explained in detail in section 4.1, then several characterization and calibration measurements are presented and discussed in section 4.2, followed by a short summary in section 4.3.

4.1 Mass spectrometer and cold trap setup

4.1.1 Mass spectrometer and vacuum chamber

The vacuum system built in the course of this work consists of a differentially pumped vacuum system with two high vacuum chambers, a sample inlet chamber and a quadrupole mass spectrometer (Prisma Plus QMG 220, Pfeiffer Vacuum, Germany), as depicted in figure 4.2.

The latter contains an ion source operated with an acceleration voltage of ≈65 V[3], a quadrupole analyzer and a secondary electron multiplier detector. Depending on the parameters of the electric quadrupole field, only ions with a distinct mass-to-charge-number ratio m/z are transferred from the analyzer into the detector, while the trajectories of all other ions are destabilized so that the ions do not reach the detector [Daw76]. This leads to a very good separation and sensitivity.

Both vacuum chambers are evacuated via a combination of a backing pump and a turbo pump. The backing pump of the cold trap chamber is an Adixen ACP15 multistage Roots dry pump, the one of the spectrometer chamber a DUO 008 B rotary vane pump (both Pfeiffer Vacuum, Germany); both turbo pumps are STP 301/451 (Edwards, Japan). The two chambers are connected over an all-metal gas dosing valve (UDV 046, Pfeiffer Vacuum, Germany). In addition, there is a plate valve (Gate valve series 10.8, DN100, VAT, Switzerland) between the cold trap chamber and its turbo pump, which can be used to deactivate the high pumping power of the turbo pump during cold trap operation to avoid the loss of a large part of the gas molecules. If it is closed, only the selective pumping power of the cold surface acts on the gas mixture, but it can be opened to pump out the chamber between two experiments.

In addition to the actual vacuum chamber, a sample inlet chamber with a total volume of 18.4 ml is introduced between electrochemical cell and cold trap chamber (cf. figure 4.2). It is equipped with several valves in order to allow for the dosing of sample gas, the mixing of gases[4] and changing the effective sample volume. Between this volume and the outlet of

---

[3] The value is decreased from the standard value 70 V to reduce fragmentation of CO_2. Thus, the background from CO fragments in channel 28 is lowered

[4] This is necessary to find out the concentration-dependent influence of the CO_2 matrix on the freeze-out of C_2H_4 in section 4.2.7.

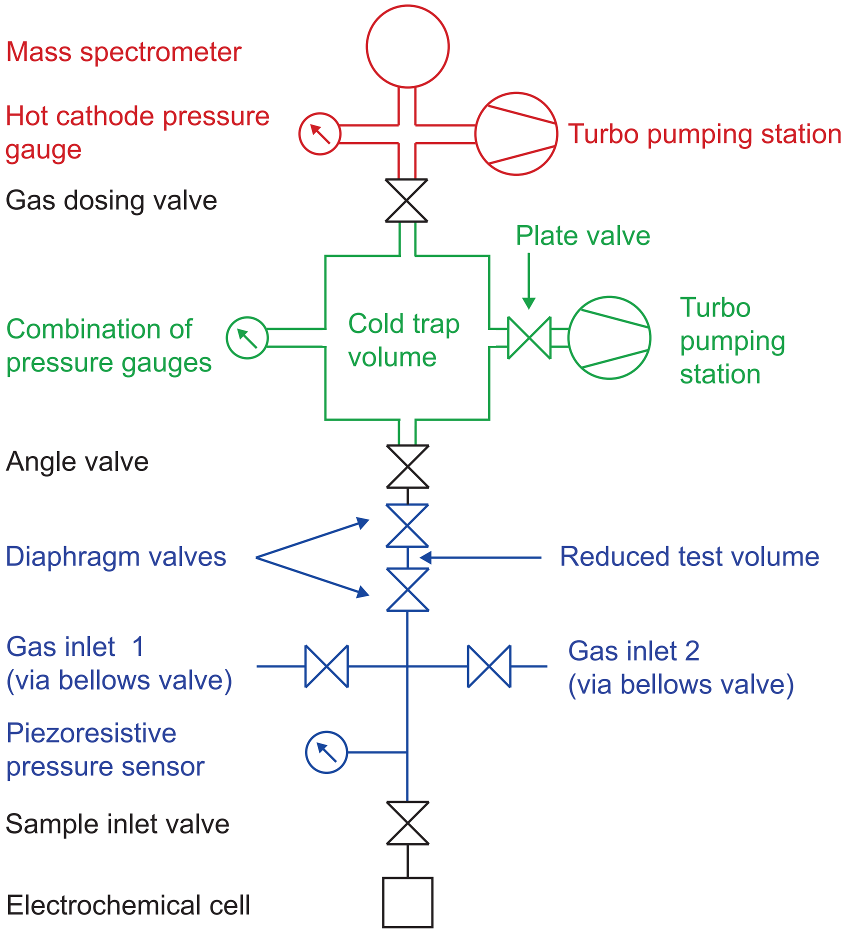

Figure 4.2: Sketch of the DEMS system with mass spectrometer chamber (red), cold trap chamber (green) and sample inlet chamber (blue).

the electrochemical cell, a custom-made bellows valve (cf. section 4.1.2) with a minimized volume on the high pressure side is installed. In addition, two gas inlets are attached via commercial bellows valves (SWSS-ML6-2, Fitok group, Germany). The part of the sample inlet chamber, which is closest to the cold trap chamber, a small volume of 1.50 ml between two diaphragm valves (DQSS-ML6-RA, Fitok group, Germany), can be used to introduce only a part of the sample gas volume into the vacuum (cf. figure 4.2). An additional angle valve (F57-60219-129, VAT, Switzerland) in front of the cold trap volume is installed to allow for changes at the sample inlet chamber without venting the cold trap chamber.

In the spectrometer chamber the pressure is measured over a hot cathode gauge (Granville Phillips 307 Vacuum Gauge, MKS instruments, USA), in the cold trap chamber over a compact full range gauge (PKR 251, Pfeiffer Vacuum, Germany) and a capacitance diaphragm gauge (CDG025D-X3, Inficon, Switzerland) and in the sample inlet chamber over a piezoresistive pressure transmitter (PAA-35X, Keller AG, Switzerland). Since the PKR 251 uses a cold cathode at lower pressures, it operates with an ionizing electron beam. This ionization triggers chemical reactions as for example water splitting or oxidation of organic molecules within the sample gas and changes its chemical composition. Therefore, only the capacitance diaphragm gauge is used to monitor the pressure during MS measurements and the full range gauge is switched off. In our setup, the gas molecules have a much higher dwell time inside the cold trap chamber than in the mass spectrometer chamber, therefore the effect of the

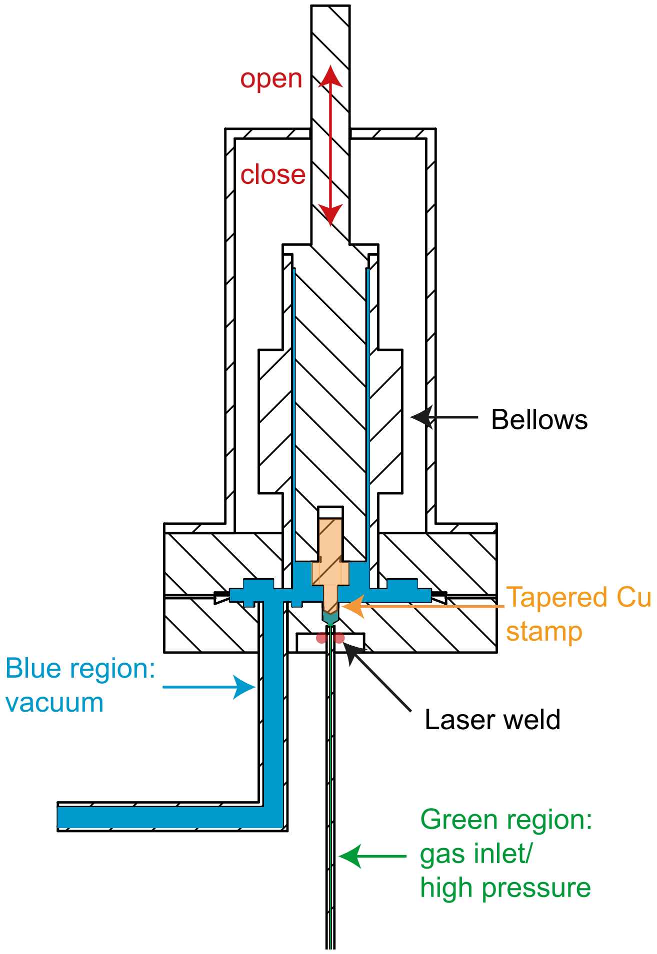

Figure 4.3: Mechanical drawing of the sample inlet valve. The blue areas show, which volume belongs to the vacuum volume, the green areas are filled with gas at a higher pressure. The shaded regions indicate the presence of solid steel in the cutting plane (the Cu stamp is indicated by shaded orange), the laser weldseam is indicated by red dots.

electron beam on it is also much more severe.

The described mass spectrometer system was installed during this thesis in close collaboration with PD Dr. Werner Schindler, Josef Zimmermann during his Master's Thesis [Zim17] and Lautaro Díaz Piola during a working student project. It is based on a previous version of the vacuum system without cold trap, which was built up by Qi Li during his diploma thesis ([Li12]).

4.1.2 Sample inlet valve

One part of this upgrade was the development of a custom-made all-metal sample inlet valve (cf. figure 4.3). Its special feature is the miniaturized valve seat, which consists of a tapered hole, the bottom of which is welded to a capillary with 1.59 mm outer and 0.13 mm inner diameter and a length of 100 mm (Techlab GmbH, Germany). This reduces the volume on the high pressure side to less than 2.5 µl in closed state. By pressing or releasing a tapered Cu stamp into the valve seat, it can be closed or opened. The resulting high flow resistance is used to reproducibly insert sample gas into the vacuum chamber. The challenge of attaching the capillary to the valve without welding inside the valve seat was solved using laser welding at the outside of the valve body. Therefore, it was necessary to minimize the gap between capillary and valve seat and to purge the surface with Ar gas during the welding process. Then the workpiece was turned while a pulsed YAG laser (power line E, Rofin, USA) melted the steel at the weldseam. This welding step was performed in collaboration with Lasermex Dipl. Ing. R.Czapka & J. Glück GbR. Due to the sensitivity of the weldseam, the capillary is fixed by an additional metal clamp outside of the valve body. Originally, the valve was designed in such a way that the Cu conus directly sealed the hole in the steel body. However, in the experiments it turned out that sealing via an FKM O-ring leads to a more reliable sealing, although it prevents a bake-out of the valve.

Using diaphragm bellows, it is possible to vertically move the Cu stamp from outside without disturbing the vacuum. The valve is designed to reproducibly switch between an open and a closed position. In the current version, it can regulate the gas flow only very roughly in a small range, but it would be possible to introduce the ability of gas flow adjustment by changing the shape of the Cu stamp.

4.1.3 Cold trap

The unique feature and the heart of the described DEMS system is its cold trap, which selectively removes CO_2 and H_2O from a product gas containing species with higher vapor pressures. The development and construction of this device is a major part of this chapter and is therefore described in more detail.

The task of the cold trap, namely the separation of different chemical species by their thermodynamic properties in vacuum, requires a sufficiently large surface with a temperature as constant as possible (mainly temporally, but ideally also spatially) while at the same time keeping up high vacuum conditions. The ideal temperature for the separation of CO_2 from ethene (C_2H_4), the least volatile gaseous product of CO_2 reduction, lies several degrees above liquid nitrogen (LN_2) temperature (77 K), while the exact value depends on the partial pressures of all involved species. This requires a good thermal insulation to the environment, a cold source with a controlled temperature, a thermal insulation with a defined, intermediate thermal conductivity between LN_2 and cold trap surface as well as an active temperature control. Since high vacuum is known as an excellent insulator, a cylindrical design with the measurement vacuum being the outer thermal insulation is chosen.

The custom-made vacuum vessel, which constitutes the main part of the cold trap, consists of three intertwining steel cylinders (cf. figure 4.4). The height of the outer cylinder is 600 mm with an outer diameter of 210 mm (resulting in a vacuum volume of 9.6 l), the middle one has outer dimensions of 500 mm respectively 160 mm and the inner cylinder is 470 mm high and 130 mm wide [5]. The outer cylinder, which is evacuated to high vacuum conditions, has connections to the turbo pump (this one can be closed by the gate valve), the sample gas inlet valve, the gas dosing valve connecting it to the MS chamber and the two pressure sensors connected over a DN40CF T-fitting, as well as an additional port for the direct connection of an electrochemical cell, which is not used in this work. The top surface of this volume is closed by a DN200CF blind flange with various feedthroughs for electric connections (two

---

[5] In the following, the three volumes between and inside these steel cylinders are referred to as "cylinders" for simplicity reasons, although the outer two of them would rather be right circular hollow cylinders with cylindrical disks on top and bottom.

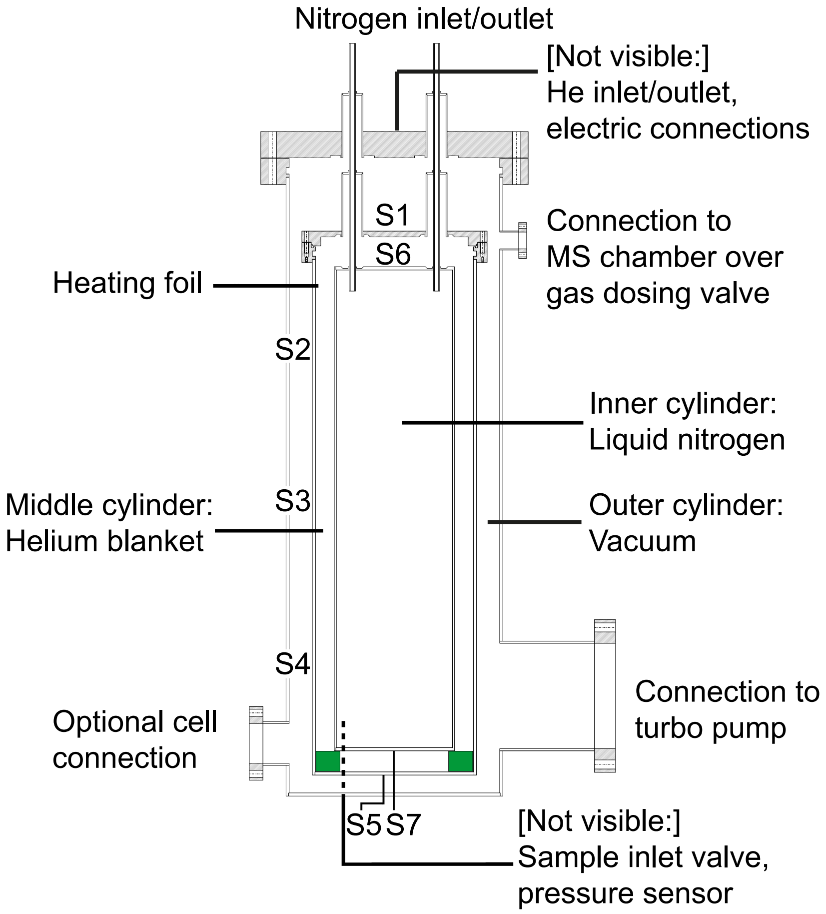

Figure 4.4: Mechanical drawing of the cold trap vessel. The positions of the 7 Pt100 temperature sensors are indicated by "S1-S7", the green areas depict an additional polymer foam, which thermally separates the bottom and the barrel volumes. The drawing was generated by PD Dr. Werner Schindler, cf. also [Zim17].

with 6 pins, ID6-16S from VAb, Germany and A3514-1-CF and one with 10 pins, A3532-1-CF, the latter two from MPF, USA), He gas (inlet and outlet over 6x1 mm steel tubes, connected to middle cylinder) and LN_2 (inlet and outlet over 6x1 mm steel tubes, connected to inner cylinder). The corresponding tubes are welded into this flange as well as the top flange of the middle cylinder and (for the LN_2 tubes) the top surface of the inner one so that they are permanently connected. In addition, they are not welded directly into the lids, but through elevated connections to reduce heat input. The main surfaces of both the inner and the outer surface of the outer cylinder were mechanically polished to reduce thermal radiation. The inner surface, which constitutes the actual cold trap, is the part whose temperature is most important. Therefore, 5 resistive temperature sensors (PT100 KN 1515, Omega Engineering, USA) are distributed over its length (S1-S5) using a special glue suitable to ultra high vacuum (Omega bond 200 Epoxy; Omega Engineering, USA).

Inside of these sensors, at the outer barrel and floor of the middle cylinder, two heating cycles based on adhesive polyimide foils are attached. The barrel heating consists of four heating foils with a total specified power of 100 W under a voltage of 48 V, the circular bottom heating delivers 15 W at a voltage of 12 V (both from Thermo Flächenheizungs GmbH, Germany). The volume of this cylinder is filled with He since it has a rather high thermal conductivity of

0.16 W/m · K (at room temperature) reducing the thermal response time of the system. Another reasonable choice would be N_2, which reduces the heating power consumption, but increases the minimal reachable temperature and the response time due to its lower thermal conductivity. In principle, Ar would also be a possible medium, but its vapor pressure of 260 mbar at 77 K limits its maximal heat transport and prevents to reach temperatures low enough for reasonable cold trap application.

At the inner wall of the middle cylinder, or rather at top and bottom of the inner steel vessel, two additional temperature sensors named S6 and S7 are attached. The temperature of S6 is also used as a trigger for the LN_2 filling level. Due to space reasons, the lid of this cylinder is sealed by an indium (In) gasket made of a 2 mm In wire.

Finally, the inner cylinder is filled with LN_2 and therefore kept at a constant temperature of 77 K in the complete liquid phase of the N_2. It is completely welded shut with the exception of an inlet and outlet tube at the top.

4.1.4 Temperature control and nitrogen refilling

In principle, a cold trap could also be operated directly at LN_2 temperature, but in order to not freeze out C_2H_4, it has to be somewhat warmer. Fluctuations in the temperature of equipment and environment, LN_2 filling level and vacuum pressure have a direct impact on the temperature of the cold trap surface. This makes it necessary to install an active temperature control.

The heating cycles in the middle cylinder are each powered by a LNG 50-4 power supply (Heinzinger electronic GmbH, Germany), which is controlled via a Eurotherm 3216 controller (Schneider-electric SE, France). This controller regulates a feedback loop consisting of a Pt100 sensor and the respective heating. The barrel heating is controlled via the temperature of sensor S3, while the floor heating is regulated with respect to the temperature of sensor S5.

In the presented design, there is always a temperature gradient from bottom to top because the top lid has solid metal connections to the outer vessel, which conduct heat into the system and the cooling power of the LN_2 is maximal where its liquid phase touches the steel vessel. This temperature gradient is not constant over time since the top lid of the middle cylinder has a high heat capacity and therefore cools down with an hour timescale. In addition, the LN_2 filling level influences the temperature profile along the cylinder barrel and consequently the available cooling power. Therefore, it is beneficial to keep the filling level as constant as possible by an automatic LN_2 refilling system. In the setup used here, a 100 l Dewar is closed by a back-pressure valve (SS-6C-MM-10, Swagelok, USA) that opens at 0.7 bar and builds up this pressure in the dewar. The pressured air above the LN_2 pushes LN_2 from the Dewar into the cold trap, when a magnetic cryo valve (E263K210S1TD0F8, ASCO Numatics, USA) inside the tube is in its open position. A digital indicator (M2 1CD, Montwill GmbH, Germany) closes the magnetic valve at a temperature of -189 °C (at sensor S6 according to figure 4.4) and opens it at -155 °C. This turned out to be a useful pair of values as it leads to refill intervals of 20-30 minutes. For switching temperatures, which are closer together, there would be a more constant temperature distribution, but the LN_2 tube, which introduces a surface with a temperature close to 77 K inside the vacuum chamber, leads to strong variations of the CO_2 background during refill so that the intervals have to be long enough apart.

4.2 Characterization and calibration

As the cold trap is based on a completely novel design, it is very important to characterize its components and the complete system as well as their specifications. In particular, this section deals with a quantitative calibration of the setup for the analysis of discrete volumes of sample gas.

4.2.1 Vacuum quality

A good vacuum quality is decisive for a functioning mass spectrometer operation for two reasons: On the one hand, quadrupole mass spectrometry requires ions to fly through a volume without scattering at other particles, on the other hand the vacuum quality decides over the background level in the mass spectrum, in particular in the typical mass channels of common molecules such as H_2O, N_2, O_2 or CO_2. While the background level of N_2 is unwanted due to its signal in channel 28 (which is also the main channel of CO gas), H_2O in contact to hot surfaces (as e.g. an ion source in a MS) creates a certain background level of H_2, which is not well pumped by the turbo pump. N_2 and O_2 can be suppressed by a good pumping system and a tight vacuum vessel, the background of H_2O and CO_2 is drastically reduced by baking out the chamber. In our case, the mass spectrometer limits the bakeout temperature to nominally 200 °C so that the MS chamber was baked out at 150 °C for 7 days. The resulting pressure level of less than $1 \cdot 10^{-11}$ mbar brings all remaining peaks to an almost negligible level. This is confirmed by the mass spectrum in figure 4.5, which only shows significant peaks in the channels 2, 18, 28 and 1, which stem from H_2, H_2O, N_2 and H. Minor fragment peaks at 44 (CO_2), 17 (OH) and 16 (O) can be found close to the detection limit at a slow scan rate of 5 s/amu. If the cold trap chamber is connected to the MS chamber, a significant increase in channel 2 can be found, which comes from H_2, which is only moderately pumped away by the turbo pump, and seems to be the major remaining component in the rest gas of the cold trap chamber. At least in cold state with the turbo running, no contribution from typical adsorbants such as H_2O or CO_2 is detected and no detectable leakage (indicated by N_2 in channel 28) is found.

4.2.2 Temperature control and feedback mechanisms

Since the thermodynamic properties of the involved gases sensitively depend on the cold trap temperature (cf. also figure 4.1), its precise control is very important for reproducible separation properties with respect to the product gas. The temperature regulation via two feedback loops with Pt100 sensors and temperature controllers permits a very accurate control with less than 0.1 K fluctuation under steady state operation after a settling time of about 10 min. However, there are two nonlinear feedback mechanisms, which can affect the regulation and which have to be considered: One is a coupling of the two heating mechanisms via convection, the other one is based on the thermal conductivity, which increases with increasing pressure and can lead to a further increasing partial pressure of CO_2.

The original purpose of the He blanket between LN_2 container and vacuum volume was to assure a defined, low thermal conductivity. Thus, it should be assured that surface tempera-

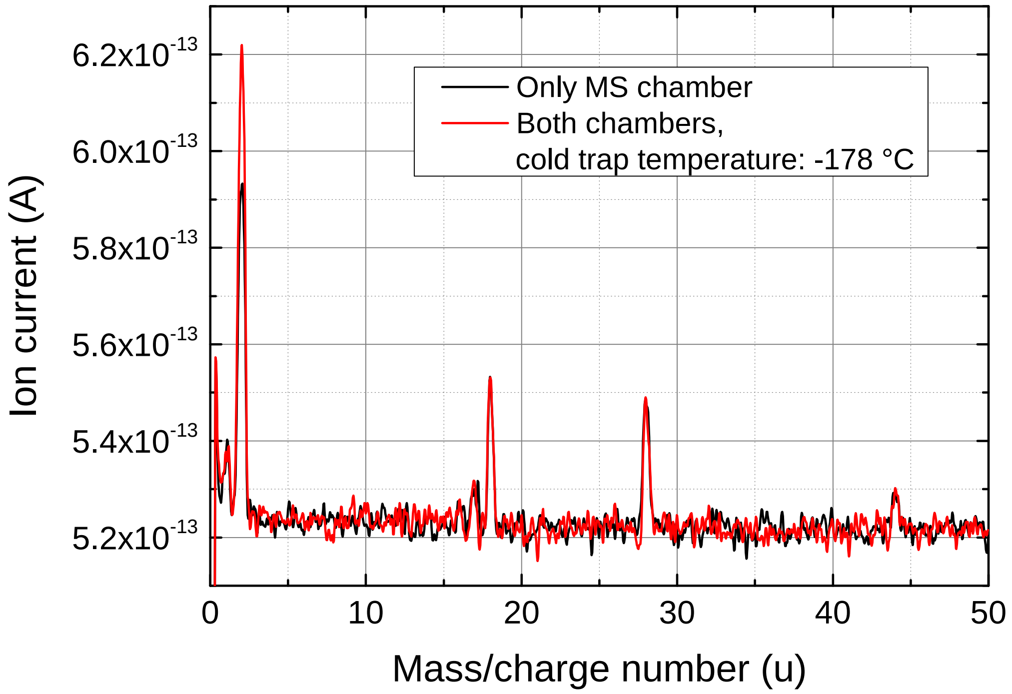

Figure 4.5: Background mass spectrum of the empty MS chamber (black) and the combination of both chambers via the opened gas dosing valve with the cold trap at -178 °C and both turbo pumps opened (red). Recorded at 5 s/u.

tures several degrees above 77 K could be achieved at moderate heating power and LN_2 consumption. Convection inside this volume increased the effective thermal conductivity of the gas and could cause two detrimental effects: First, our geometry allowed cold gas flowing downwards at the cold inner wall to hit the floor of the middle cylinder and cool it down. The He gas warmed up this way could then transport heat from the floor heating to the side walls while streaming upwards again. This resulted in a coupling of the two feedback loops and to instabilities in the temperature control. Therefore, we introduced a ring of polyethene foam between the floor and the side volume (green areas in figure 4.4) to decouple them from each other. The second problem was that by convection, cold gas streaming upwards at the warmer outer surface heated up so that it cooled the lower parts stronger than the upper parts. In the experiment, we observed that the temperature at the lower part of the barrel wall (S4) could be several degrees colder than at its center (S3). Especially when air from the environment entered the He volume and increased the pressure, the impact of convection was increased relative to the one of conduction and the temperature difference increased. Although it was not done in the course of this work, it seems realistic that this can be tackled by replacing He by N_2, which behaves more similar to air, so that air leakages do less affect the temperature distribution. Alternatively, the observation of the He pressure with a mechanical pressure sensor and a regular evacuation of the volume to lower pressures would assure stability of the temperatures over longer timescales.

Another feedback mechanism was observed when CO_2-rich gas was introduced into the cold trap chamber: CO_2 was frozen out until its vapor pressure is reached. For temperatures above about 110 K (-163 °C) or gas mixtures with a significant content of gases with a higher vapor pressure, sample gas injection led to a pressure increase up to the 10^{-2} mbar range. This increased the thermal conductivity of the vacuum, which resulted in a further temperature rise connected to an increase in pressure. The Eurotherm controllers reacted very quickly on such changes of the parameters, so that the temperature increase could be limited to less than 0.5 K at about $1 \cdot 10^{-3}$ mbar maximum pressure in the cold trap volume (depending on gas composition and analysis time). Still, the feedback mechanism can induce oscillations in pressure and temperature as the temperature controllers assume a constant thermal resistance. Therefore, it is necessary to limit the amount of product gas, which is fed into the vacuum chamber, because a drift in temperature caused by the increased thermal conductivity affects the partial pressures of the gases in contact to the cold surface. Another limitation is that the temperature controllers cannot use their complete functionality at very low temperatures where a decrease of the heating power to 0 is not sufficient to compensate for the enlarged heat input through the vacuum.

4.2.3 Mass spectra of pure gases

Before coming to the quantitative calibration of the setup, it is instructive to have a look on complete mass spectra of several pure gases and gas mixtures. To obtain reasonable spectra, it was necessary to maintain stable conditions in the vacuum setup, which could only be achieved under continuous flow conditions. This means that a constant, small gas flow was adjusted via one of the gas inlet valves and both turbo pumps were active. This configuration was possible for CH_4, C_2H_4, Ar and CO_2 as well as the test gas described in section 3.6 with 1.08% H_2, 1.02% CH_4, 1.27% C_2H_4, 1.01% CO and 95.6% CO_2, as these gases were safely available at the mass spectrometer workplace. Figure 4.6 shows mass spectra of these gases recorded between 0 and 50 u and a speed of 5 s/u under continuous flow conditions. They show signals resulting from intact and fragmented, singly and doubly ionized species as well as isotopes from these species and contaminations with air or He (e.g. in channel 4 for the C_2H_4 spectrum). An overview of the most important ions that are found in these spectra is given in table 4.1.

As every real measurement device, also the quadrupole mass spectrometer used here measured with a certain background current, which is temperature dependent. Typically, it lay between $4.5 \cdot 10^{-13}$ A and $7 \cdot 10^{-13}$ A, while a temperature change of 1 K led to a shift of about $7 \cdot 10^{-14}$ A in the background. Since the device temperature could not be kept completely constant, the background was determined from "empty" mass channels for each measurement and subtracted. In figure 4.6 as well as all following figures, this background was already subtracted.

4.2.4 Calibration with pure gases

In this section, a quantitative calibration of the DEMS setup with discrete volumes of single gases is conducted. In principle, it would be interesting to calibrate all stages of the setup individually, but for the use as a product analysis tool, only the sensitivity of the complete setup towards the individual gas species is of interest.

Nevertheless, processes, which have a different impact on the individual gas species, are discussed in the following to get a better understanding of the system: Already in the sample inlet chamber, the mixing of gas proportions with different product concentrations can lead to an inhomogeneous distribution of gases, especially when different gases (injected at differ-

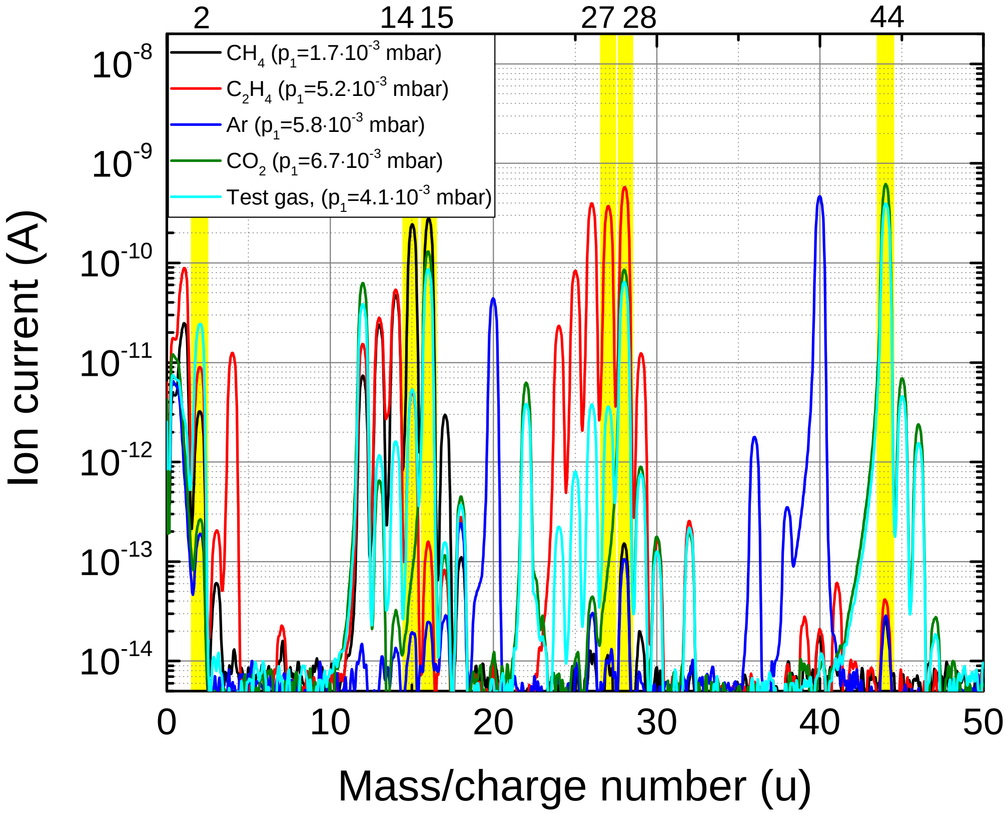

Figure 4.6: Mass spectra of CH_4, C_2H_4, Ar, CO_2 and test gas with with 1.08% H_2, 1.02% CH_4, 1.27% C_2H_4, 1.01% CO and 95.6% CO_2 at room temperature. The constant background of 5.3-5.4 $\cdot 10^{-13}$ A is already subtracted. The channels, which are used for the determination of the product gas distribution, are marked in yellow and the gas pressure p_1 in the cold trap chamber is given for comparison. Recorded at 5 s/u.

ent sides of the chamber) shall be mixed inside the sample volume for calibration purposes. As soon as the gas mixture is introduced into the cold trap chamber, it should however distribute evenly and homogeneously so that this phenomenon can be neglected there. The next process, the deposition of gases on the cold surface very differently affects the species in contact to it. This property is even the basis of the cold trap working principle. However, one should additionally consider concentration-dependent effects as e.g. a dissolution of C_2H_4 in solid CO_2 (cf. section 4.2.6). The remaining gas then streams through the gas dosing valve into the spectrometer chamber. As the channel through the valve is much narrower than the mean free path of the gas molecules (about 100 mm at 10^{-3} mbar), the mass-dependent thermal velocity of the various gas species could also lead to a slight separation effect. This can be observed in the transients of the signals of different species after injection into the cold trap chamber (cf. also figure 4.8 shown below), which leads to a slope for H_2, which is about four times as high as for the other species. This increased flow rate of light molecules through the gas dosing valve results in a higher partial pressure in the mass spectrometer chamber and consequently in a higher sensitivity of the system towards such molecules, in particular H_2. Another consequence, which also comes from the molecular movement, is a reduced pumping speed of the turbo pump for molecules with a low mass. In particular H_2 can remain in the spectrometer chamber for a longer time and accumulate there compared to the other species. Last, but not least, the mass spectrometer itself has a variable sensitivity for

Mass channel	Typical fragment (original molecule(s) in brackets)
1	H^+ (H_2, CH_4, C_2H_4)
2	H_2^+ (also from CH_4, C_2H_4)
4	He^+
7	CH_2^{2+} (CH_4, C_2H_4), N^{2+} (N_2)
12	C^+ (CH_4, C_2H_4, CO, CO_2)
13	CH^+ (CH_4, C_2H_4), $^{13}C^+$ (CH_4, C_2H_4, CO, CO_2)
14	CH_2^+ (CH_4, C_2H_4), N^+ (N_2)
15	CH_3^+ (CH_4), $^{13}CH_2^+$ (CH_4, C_2H_4)
16	CH_4^+, O^+ (H_2O, CO, O_2, CO_2), $^{13}CH_3^+$ (CH_4)
17	OH^+ (H_2O), $^{13}CH_4^+$
18	H_2O^+
20	Ar^{2+}
22	CO_2^{2+}
24	C_2^+ (C_2H_4)
25	C_2H^+ (C_2H_4)
26	$C_2H_2^+$ (C_2H_4)
27	$C_2H_3^+$ (C_2H_4)
28	CO^+ (also from CO_2), $C_2H_4^+$, N_2^+
29	$^{13}CO^+$ (also from CO_2), $^{13}C_2H_4^+$, $^{15}N_2^+$
30	NO^+ (from N_2 and O_2)
32	O_2^+
36	$^{36}Ar^+$
38	$^{38}Ar^+$
39	C_3H_3 (from organic contaminations in C_2H_4)
40	Ar^+, C_3H_4 (from organic contaminations in C_2H_4)
41	C_3H_5 (from organic contaminations in C_2H_4)
44	CO_2^+
45-47	various heavier isotopes of CO_2^+

Table 4.1: Most important mass channels occurring in our experiments and their corresponding typical fragments (original molecule(s) in brackets).

different species. The molecules in the range of the electron beam of the ion source are ionized and partly fragmented with a certain cross section. The resulting spectrum of fragments distributes over several mass channels and the detection efficiency for a species in a particular mass channel depends on the fraction of original molecules ending up with a fragment of the respective mass. In addition, the continuous secondary electron multiplier has a certain dependence of the first electron emission on the incoming ion mass so that the mass spectrometer also contributes to the molecule-dependent sensitivity of the setup. As mentioned above, only the combination of all these processes shall be quantified here.

Since typical product gas measurements are based on discrete gas volumes, which are introduced into the cold trap chamber with closed turbo pump, the quantitative calibration was performed by introducing similar defined volumes of pure gases. This allowed us to also measure H_2, CO and N_2, which were transferred to the MS setup from other lab workplaces in closed volumes (in addition to CH_4, C_2H_4, Ar, CO_2 and test gas). Especially in the cases of H_2 and CO this was much safer, but no spectra under constant flow conditions could be recorded with these volumes.

For the calibration measurements of this section, the sample inlet chamber with a volume of

18.4 ml[6] was filled with pure or mixed gases, which were then abruptly introduced into the cold trap chamber. For pure gases, only the reduced test volume of 1.50 ml was used in order to not exaggerate the pressure. For mixtures, it was preferred to introduce the complete sample inlet chamber volume so that all inhomogeneous mixing effects could be neglected. As these mixtures were only measured in cold state and contained large amounts of CO_2, the freeze-out prevented strong pressure increases.

In order to compare the measurements based on different pressures and volumes, the quantity "amount of gas", which is defined as the product of pressure and volume, is used in the following[7]. Under the assumption of ideal gases and without consideration of freeze-out, this quantity does not change upon expansion of the gas from the sample inlet chamber into the cold trap chamber.

Typically, the injection of a gas sample gives an abrupt rise in all involved channels followed by an exponential decrease with time constants between 1 min (H_2) and 4 min (CO_2) (see below in figure 4.8). This decrease comes from a flow of gas from the cold trap chamber into the MS chamber with a rate proportional to their partial pressure inside the cold trap chamber. Due to the sequential measurement principle, the maximum in each channel is recorded at a different point in time and an evaluation of the maximum value of each curve would be affected by a large error because it could also be recorded up to 3.3 s (which is the sampling interval of each channel in the measurement method used) after the physical maximum of the respective partial pressure. Therefore, the characteristic signal jump in the active channels was used to determine the injection time with an accuracy of 0.5 s. Then, all curves were interpolated and evaluated exactly 5 s after this point in time. Figure 4.7 shows the respective current response of the channels 2, 14, 15, 27, 28, 32 and 44 for H_2 (Westfalen AG, purity 5.0), CH_4 (Linde AG, purity 3.5), C_2H_4 (Linde AG, purity 3.0), CO (Linde AG, purity 4.7), CO_2 (Air liquide, purity 5.5) and N_2 (Linde AG, purity 5.0). The series resulting from a pressure variation were fitted by a power function between 1 $\text{mbar} \cdot \text{ml}$ and 200 $\text{mbar} \cdot \text{ml}$, which indicated a very linear relation between amount of gas and ion current (cf. figure 4.7). As all measurements suffered from small leakages in the sample preparation chamber connected to air input, a corresponding correction was performed for the signals of C_2H_4, CO and CO_2 in channel 28. For this purpose, the O_2 content derived from channel 32 was used to determine the N_2 contribution to channel 28, which was subtracted. Although the relative error of this correction method may be high, these corrections were small compared to the total signals and thus led to an improvement in the reproduction of the real values.

The resulting ratios between the amounts of gas (in terms of pressure $\cdot$ volume) and the respective ion currents led to the calibration parameters given in table 4.2. It may strike that some signals of figure 4.7) are not considered in table 4.2, e.g. the signals of CH_4 and C_2H_4 in channel 2. Even for a 1:1 mixture between H_2 and these species, they would only make up 0.1% of the signal and even much less in typical product gas mixtures. Therefore they are neglected. In addition, the contributions of, e.g., CO to channel 2 or of CH_4 to channel 27 are

---

[6] The volume was determined by measuring the pressure inside the sample inlet chamber while introducing air through a glass pipette. From the level of H_2O flowing into the pipette and the two pressure levels inside and outside the chamber, the volume could be determined with less than 1% error. The error is not considered in the measurements with product gas as it is does not affect relative concentrations.

[7] The product of pressure and volume is sometimes also referred to as "standard volume", especially in the gas industry.

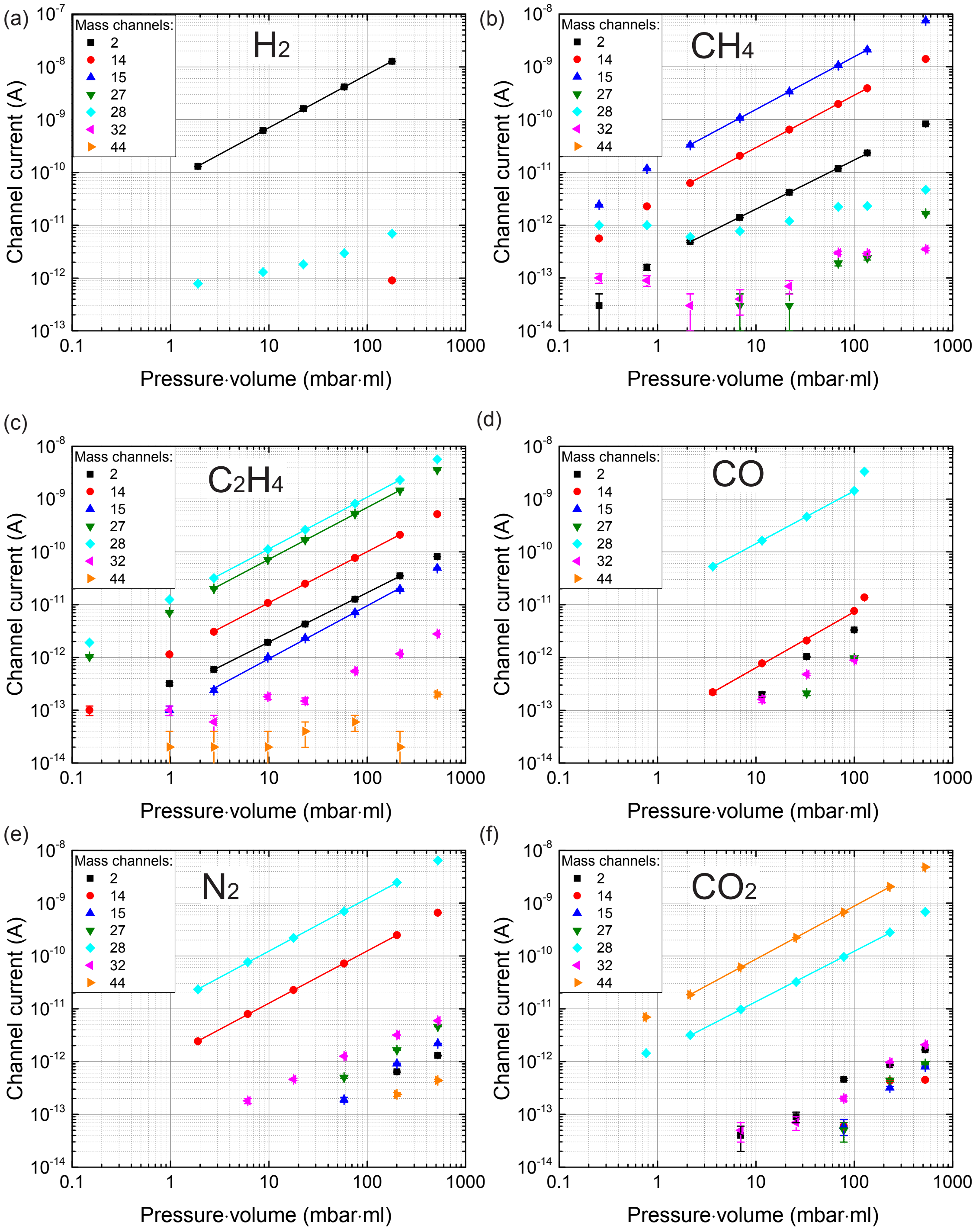

Figure 4.7: Ion currents in the most important mass channels 5 s after injection for the gases (a) H_2, (b) CH_4, (c) C_2H_4, (d) CO, (e) N_2 and (f) CO_2. The curves were determined by measuring different discrete amounts of pure gases coming from a test volume of 1.50 ml at varying pressure. The error bars consider background correction, noise and injection time (cf. section 4.2.9). Further parameters: cold trap at room temperature; cold trap turbo pump closed; measuring time: 0.1 s per point (channel 32), 0.5 s per point (all other channels).

	Mass channel					
$\psi(i,j)$	**2**	**14**	**15**	**27**	**28**	**44**
$\psi(\mathrm{H_2},j)$	$7.13 \cdot 10^{-11}$	-	-	-	-	-
$\psi(\mathrm{CH_4},j)$	neglected	$2.93 \cdot 10^{-12}$	$1.55 \cdot 10^{-11}$	-	-	-
$\psi(\mathrm{C_2H_4},j)$	neglected	$1.01 \cdot 10^{-12}$	$9.55 \cdot 10^{-14}$	$6.93 \cdot 10^{-12}$	$1.09 \cdot 10^{-11}$	-
$\psi(\mathrm{CO},j)$	-	$6.23 \cdot 10^{-14}$	-	-	$1.43 \cdot 10^{-11}$	-
$\psi(\mathrm{N_2},j)$	-	$1.25 \cdot 10^{-12}$	-	-	$1.23 \cdot 10^{-11}$	-
$\psi(\mathrm{CO_2},j)$	-	-	-	-	$1.23 \cdot 10^{-12}$	$8.91 \cdot 10^{-12}$

Table 4.2: Ion current sensitivities $\psi(i,j)$ of the considered gaseous species i in the main mass spectrometer channels j in A/(mbar · ml) with respect to the amount of gas determined from the calibration curves in figure 4.7. The parameters were measured with the cold trap being at room temperature.

assigned to contaminations, as they cannot be explained by fragmentation or isotopes. All in all, the spectra correspond quite well to literature values from the National Institute for Standards and Technology (NIST, [NIS18]), but in comparison, the exact peak ratios are somewhat shifted to heavier fragments in our setup, probably due to the reduced acceleration voltage.

4.2.5 Correction method for gas mixtures

Every compound, which is analyzed by mass spectrometry, yields a spectrum of peaks in different mass channels. Especially for organic molecules, rich spectra are obtained. Usually, one peak belongs to the singly ionized form of the basic molecule and the others are made up by fragments of this molecule, occurrence of other isotopes and multiply ionized forms of these species. If pure species are introduced into the vacuum system, the spectra can be used as fingerprints for the compounds (as described, e.g., in [Was45, O'N51]), as the fragmentation differs and gives different spectra even between isomers. For a mixture of gases, the task becomes more complicated since the resulting spectrum is a weighted sum of spectra of the individual mixture components. In particular mass channels, which occur for multiple compounds, complicate the interpretation. If the components of this mixture are known and only their relative shares shall be determined, one can set up a system of equations, which still permits a quantification - however flawed with a certain error propagation. In the following, a data analysis method based on this approach is presented.

In our case with mixtures of H_2, CH_4, H_2O, CO, C_2H_4, N_2, O_2 and CO_2, the channels 14 (CH_2, from CH_4 and C_2H_4 as well as N from N_2), 15 (CH_3 from CH_4 and C_2H_4) and in particular 28 (CO, C_2H_4, N_2 and CO from CO_2) are multiply occupied. The first implication is certainly to minimize the background levels of N_2 and CO_2 - which was one of the main reasons for the design of the cold trap. Still, these gases can never be completely avoided: N_2 as the main component of air is present in trace amounts in all pure gases and it comes into the sample gas via the finite leakage rates of all sealings in gas supply and electrochemical cell, CO_2 naturally makes up the major part of the gas mixture before its partial pressure is reduced to the vapor pressure of CO_2 at the cold trap temperature. Therefore, it is necessary to find a correction method for the remaining concentrations of these gases and for the signals in other channels caused by CH_4 and C_2H_4.

For our typical gas mixtures, it is useful to start the conversion with H_2, C_2H_4 and CO_2, which each have an "exclusive" mass channel, namely the channel 2, 27 and 44, respectively[8]:

$$\begin{aligned} pV(\mathrm{H_2}) &= s(\mathrm{Ch2})/\psi(\mathrm{H_2},\mathrm{Ch2}) \\ pV(\mathrm{C_2H_4}) &= s(\mathrm{Ch27})/\psi(\mathrm{C_2H_4},\mathrm{Ch27}) \\ pV(\mathrm{CO_2}) &= s(\mathrm{Ch44})/\psi(\mathrm{CO_2},\mathrm{Ch44}) \end{aligned} \tag{4.1}$$

with $pV(i)$ being the partial pressure · volume of species i, $s(\mathrm{Ch}j)$ the signal in channel j with subtracted background level 5 s after gas injection, and ion current sensitivities $\psi(i,\mathrm{Ch}j)$ for the signal of species i in channel j from table 4.2. From this, the partial pressures multiplied by the volumes of CH_4, N_2 and CO can be calculated via:

$$\begin{aligned} pV(\mathrm{CH_4}) &= \left(s(\mathrm{Ch15}) - \psi(\mathrm{C_2H_4},\mathrm{Ch15})\cdot pV(\mathrm{C_2H_4})\right)/\psi(\mathrm{CH_4},\mathrm{Ch15}) \\ pV(\mathrm{CO}) &= [(s(\mathrm{Ch28}) - \psi(\mathrm{CO_2},\mathrm{Ch28})\cdot pV(\mathrm{CO_2}) - \psi(\mathrm{C_2H_4},\mathrm{Ch28})\cdot pV(\mathrm{C_2H_4}))\cdot\psi(\mathrm{N_2},\mathrm{Ch14}) - \\ &\quad (s(\mathrm{Ch14}) - \psi(\mathrm{CH_4},\mathrm{Ch14})\cdot pV(\mathrm{CH_4}) - \psi(\mathrm{C_2H_4},\mathrm{Ch14})\cdot pV(\mathrm{C_2H_4}))\cdot\psi(\mathrm{N_2},\mathrm{Ch28})] \div \\ &\quad [\psi(\mathrm{N_2},\mathrm{Ch14})\cdot\psi(\mathrm{CO},\mathrm{Ch28}) - \psi(\mathrm{CO},\mathrm{Ch14})\cdot\psi(\mathrm{N_2},\mathrm{Ch28})] \\ pV(\mathrm{N_2}) &= [(s(\mathrm{Ch14}) - \psi(\mathrm{CH_4},\mathrm{Ch14})\cdot pV(\mathrm{CH_4}) - \psi(\mathrm{C_2H_4},\mathrm{Ch14})\cdot pV(\mathrm{C_2H_4}))\cdot\psi(\mathrm{CO},\mathrm{Ch28}) - \\ &\quad (s(\mathrm{Ch28}) - \psi(\mathrm{CO_2},\mathrm{Ch28})\cdot pV(\mathrm{CO_2}) - \psi(\mathrm{C_2H_4},\mathrm{Ch28})\cdot pV(\mathrm{C_2H_4}))\cdot\psi(\mathrm{CO},\mathrm{Ch14})] \div \\ &\quad [\psi(\mathrm{N_2},\mathrm{Ch14})\cdot\psi(\mathrm{CO},\mathrm{Ch28}) - \psi(\mathrm{CO},\mathrm{Ch14})\cdot\psi(\mathrm{N_2},\mathrm{Ch28})] \end{aligned} \tag{4.2}$$

Figure 4.8 shows the result of this method using the example of time transients of the mass channels 2, 14, 15, 27, 28, 32 and 44 after injection of 1.49 mbar · ml of test gas into the cold trap chamber at a temperature of -169 °C. At a relative time of 68 s, the gas was injected and at 140 s, the plate valve in front of the turbo pump was opened up again so that the major part of the products was quickly pumped away. One can see how the raw data (Figure 4.8(a)) were converted into signals, which were proportional to the partial pressures of H_2, CH_4, C_2H_4, CO, N_2 and CO_2 in the cold trap chamber, using equations 4.1 and 4.2 (Figure 4.8(b)). In order to simplify the interpretation below, the absolute values of these curves are given in such a way that their values 5 s after gas injection correspond to the pV values of the respective species.

Before doing the conversion according to equations 4.1 and 4.2, an interpolation of all curves with a resolution of 0.2 s was performed. This significantly increased the accuracy of the conversion since the mass spectrometer serially measured the individual channels with a time resolution of about 3.3 s in each channel. As the product concentrations in the cold trap chamber decreased when gas was transferred into the MS chamber, the signals in all channels were not constant over time. Without interpolation, this would mean that signals from different points in time would be used for the calculation of a single concentration. In the H_2 signal, which was only calculated from a single channel, there was a typical difference of 4.5 % between two adjacent points so that interpolation made the analysis much more accu-

---

[8] There are contributions of CH_4 and C_2H_4 to channel 2, but they are many orders of magnitudes smaller than the contribution of H_2, especially as these organic gases are much less concentrated than H_2 in typical product gases. Channel 27 is slightly affected by a tail of the peak in channel 28, which was considered in measurements with low C_2H_4 content. In addition, H_2O can also induce a signal in channel 2, but this is caused by a reaction on hot components of the mass spectrometer combined with a weak pumping power for the resulting H_2 by turbo pumps. As its temporal behavior is virtually independent from the injection of sample gas, it is more useful to correct for the resulting background than to use a simultaneous correction as for the other components.

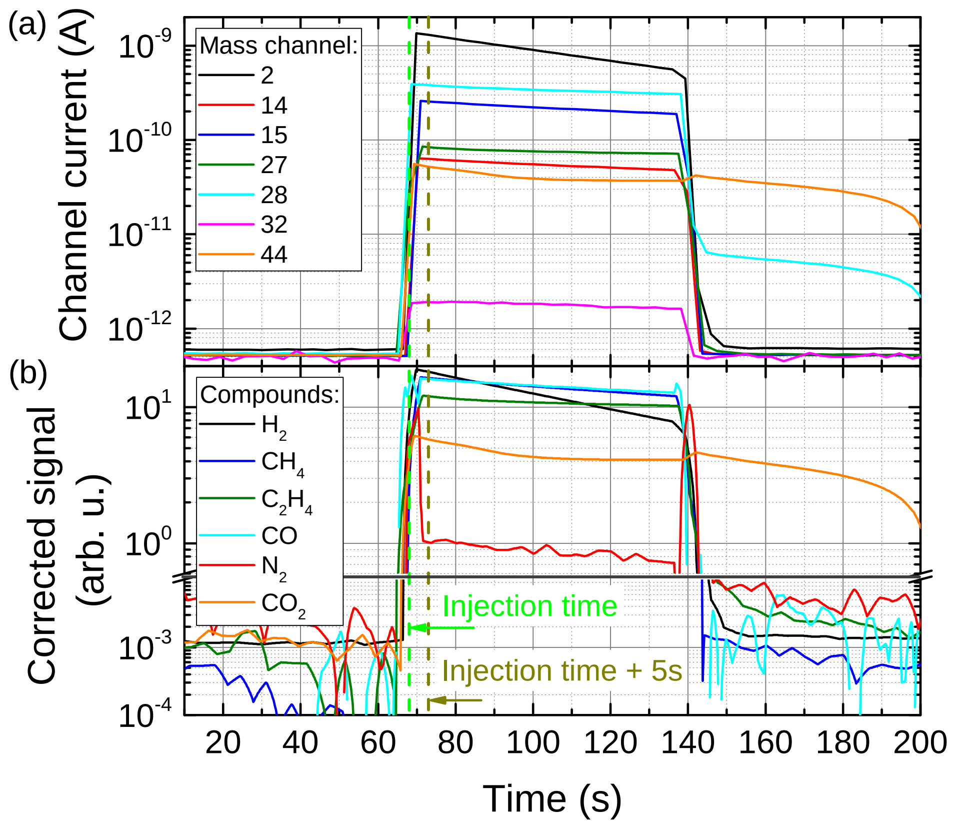

Figure 4.8: (a) Transients of the ion currents in the mass channels 2, 14, 15, 27, 28, 32 and 44 after injection of 1.49 mbar · ml of test gas (1.08% H_2, 1.02% CH_4, 1.27% C_2H_4, 1.01% CO and 95.6% CO_2) at a cold trap temperature of -169 °C. (b) Corrected signals of H_2, CH_4, C_2H_2, CO, N_2 and CO_2 after interpolation and correction according to equation 4.2. The light green line indicates the time of gas injection, the olive-colored line shows the point in time 5 s later. The quantitative values of the corrected signal 5 s after injection correspond to the amount of the respective species in the sample inlet chamber before injection. Measuring time: 0.1 s per point (channel 32), 0.5 s per point (all other channels).

rate. In addition, effects of the serial measurement were most drastically visible when large jumps occured in the spectrometer channels. E.g. in the N_2 level in figure 4.8 there were huge artifacts[9] around 70 s and 140 s, which disappeared in regions with smooth curves[10].

Several features can be used to check the plausibility of the correction method: It is well visible that the signals in channels 44 and 28 only slowly decreased after opening the plate valve. This was attributed to subliming CO_2, which had been deposited before. Around 190 s, the level started decreasing as the last portion of solid CO_2 evaporated. After the correction, this characteristic shape was only visible in the CO_2 signal and not in the ones of CO or N_2. Also the signal in channel 2 was about a factor of 5 above the one in channel 15 in the raw data. After correction, the values for H_2 and CH_4 were quite similar as it was expected for the test gas used. Finally, the background levels of all species were 3-4 orders of magnitude smaller than the signals with product gases present. Their background levels drifted with the back-

---

[9] The reason for these spike-like artifacts lies in the sequential recording of the individual channels: If the contribution of, e.g., C_2H_4 to channel 28 was subtracted at a point in time when the signal jump due to gas injection was only recorded in channel 28 and not yet in channel 27, an erroneously high N_2 level was calculated.

[10] The value of 5 s after injection for the interpretation was chosen to avoid these regions with jumps and to achieve a state close to the equilibrium between gaseous and solid CO_2, while at the same time keeping up a high sensitivity.

ground current of the spectrometer, which was not constant in time, but they gave reasonable values. Especially for small product concentrations it is advisable to subtract these individual background levels from the signals. In addition, it is remarkable that the slopes of the different curves between 70 s and 140 s differed. By trend, smaller molecules, in particular H_2, showed a steeper slope after injection. Together with the observation that they also gave a higher signal, this suggests that they diffused faster through the angle valve between the vacuum chambers, probably due to a higher particle velocity.
Besides the described method of considering the fragmentation ratio of the molecules, there seems to be an unexpected effect of interference between the channels. In the measurement of gas mixtures with H_2/CO ratios above 50, the time transients of the CO level were less steep than, e.g., in figure 4.8 or even positive. In the presence of a large H_2 partial pressure (or a high total pressure, which was hard to discern as H_2 typically was the main component), the signal in channel 28 was reduced; at a pressure of $1 \cdot 10^{-7}$ mbar in the mass spectrometer chamber, it was reduced by about 10%. The observed mechanism has to influence different channels differently, otherwise the reduction in channel 28 would have been accompanied by a proportional reduction in the other channels and the shape of the CO transient would have been unaffected. However, the reason for this observation remains unclear. Both a mass-dependent scattering of ions in the quadrupole field (at a total pressure in the mass spectrometer chamber about 2 orders of magnitude below the maximum operation pressure of the MS system) and a change in the fragmentation of the molecules is not plausible, especially since the fragmentation ratios of all species seem to be pressure-independent according to figure 4.7. Nevertheless, a phenomenological, negative ion current sensitivity of $\psi(\mathrm{H_2}, \mathrm{Ch28}) = -9 \cdot 10^{-14}$ could compensate for the observable part of this artifact.

4.2.6 Ideal operation temperature

The central parameter of the cold trap is its surface temperature, which determines its main separation properties. Generally, the temperature should be as spatially and temporally constant as possible, which motivated the relatively large design of the vessel. However, it is very important to find an optimum between a stronger reduction of CO_2 vapor pressure at low temperatures and a lower suppression of product gases, in particular C_2H_4 at higher temperatures (cf. phase diagrams in figure 4.1).
In addition, there are also secondary effects of temperature, which can be important: Without heating, a minimum temperature of less than -180 °C can be achieved at the bottom of the middle cylinder. However, this temperature cannot be used for stable operation because an increase in pressure in connection with a reduced insulation of the vacuum would lead to warming of the surface (cf. also section 4.2.2). As the heating is already at zero power under these conditions, the temperature control cannot compensate for this temperature increase. Therefore, a reasonable operation can only by achieved for temperatures above -175 °C.
On the other hand, the large background pressure of CO_2 at high temperatures (above about -160 °C) leads to a similar problem: There, the heat conduction through the residual gas in the vacuum volume plays a significant role and changes in the pressure can also destabilize the temperature control by a feedback between thermal insulation and temperature (cf. section 4.2.2). Also, the increased LN_2 consumption is a drawback of a warmer cold trap surface. In the remaining temperature range between -175 °C and -160 °C, one can optimize the ther-

modynamic separation properties according to the vapor pressures of the involved gases. At this point, it has to be noted that entropic effects, namely the dissolution of other gases in solid CO_2, can play a role under the described conditions. Therefore, the actual partial pressure, in particular the one of C_2H_4 in the presence of CO_2, is reduced. The proposed mechanism is analogue to the dissolution of permanent gases in H_2O at room temperature and has to be considered in the calibration (which is done in section 4.2.7). In contrast to an ordinary phase transition at the vapor pressure, which can be observed for a pure gas, this mechanism depends on various parameters such as the amounts of frozen CO_2 and the partial pressure of C_2H_4. As this effect significantly decreases with increasing temperature, this implies an operation at slightly elevated temperature.

The first experiment, which was performed to find out the influence of temperature, was a series of complete spectra of the test gas (1.08% H_2, 1.02% CH_4, 1.27% C_2H_4, 1.01% CO and 95.6% CO_2) in the range 0-50 u at different cold trap temperatures (cf. figure 4.9). Due to the necessity to keep the pressure constant over the measurement, the spectra were recorded under continuous gas flow, which was adjusted by a bellows valve. The limited reproducibility of this method (the valves are not optimized for precise gas flow adjustment) led to different pressure values and fluctuations in the product gas signals between the individual measurements, therefore, the pressure in the sample inlet chamber is also indicated[11]. Besides these fluctuations, the signals in the channels related to CO_2 (44, 16, 28, 12, 45, 22, 46, 29 and 32) as well as H_2O (18, 17) decrease with decreasing temperature. Remarkably, the exclusive channels of C_2H_4 (26, 27) do not show a systematic temperature dependence. Probably, the dissolution of C_2H_4 in CO_2 saturates under continuous flow conditions and the reduction of the C_2H_4 partial pressure is negligible compared to the case of the injection of a discrete amount of gas.

The apparent pV values of the gas species contained in discrete amounts of test gas (1.08% H_2, 1.02% CH_4, 1.27% C_2H_4, 1.01% CO and 95.6% CO_2) at various temperatures are shown in figure 4.10. The values for CH_4 (figure 4.10(b)) perfectly match the expectations and CO (figure 4.10(d)) only suffers from fluctuations at low partial pressures (which come from the complex correction involving 4 mass channels, but are much smaller than the error bars), but also lies well on the expected curve. In contrast, the H_2 levels, especially for lower pressures, seem to be overestimated (figure 4.10(a)). If the reason for this was a wrong concentration in the gas bottle or a wrong calibration factor, all points should be shifted by a constant factor. Since they show a dependence on the partial pressure, it is most reasonable that the discrepancy stems from the injection of the gas mixture from the gas bottle into the sample inlet volume. For lower partial pressures, lower flow rates of the bellows valve were adjusted and probably H_2 can pass narrow slits more easily than larger molecules. This effect was more pronounced, the narrower the slit in the valve was. For C_2H_4 (figure 4.10(c)), one can see that the apparent signal decreases with decreasing temperature and that there is a dependence on the total amount of gas: At -181 °C, the signal is reduced by a factor of 6 for 150 mbar · ml of test gas, and even by a factor of 26 for 1.5 mbar · ml of test gas. This dependence is reduced with increasing temperature, which would also motivate higher cold trap temperatures. Nev-

---

[11] The pressure in the cold trap chamber is not proportional to the gas flow due to freeze-out of CO_2, therefore only the pressure in the sample inlet chamber is used.

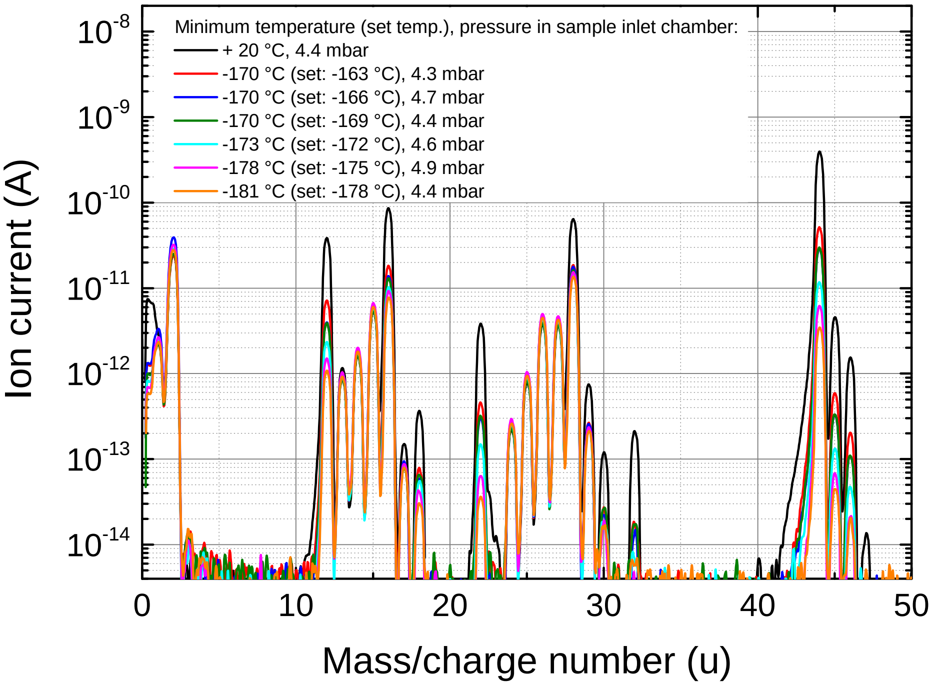

Figure 4.9: Mass spectra of test gas with with 1.08% H_2, 1.02% CH_4, 1.27% C_2H_4, 1.01% CO and 95.6% CO_2 at various cold trap temperatures, the set temperatures are given in brackets. The pressure in the sample inlet chamber is also given since it was not identical in each measurement. The constant background of $4.7\text{-}5.4 \cdot 10^{-13}$ A is already subtracted. Further parameters: continuous flow; cold trap turbo pump open; recorded at 5 s/u.

ertheless, the apparent C_2H_4 curve is steeper than the expected curve (which has a slope of 1 on a double-logarithmic scale) for all temperatures, which disproves that C_2H_4 undergoes a classical phase transition from gaseous to solid state. This dependence of the freeze-out on the C_2H_4 partial pressure could also explain, why there were no signs of C_2H_4 freeze-out visible in the continuous flow spectra shown above in figure 4.9. Finally, there is also a strong temperature dependence in the values of CO_2 (figure 4.10(e)), which proves the main function of the cold trap. Here, the apparent CO_2 levels also increase with increasing test gas pressure, but much less steeply than the curve without freeze-out ("expected CO_2" in figure 4.10(e)). For a cold trap in perfect equilibrium, one would even expect horizontal curves at the vapor pressure of the respective temperature (shown as solid lines, values interpolated from [DDBSSTG17]). In the real experiments, there is indeed a pressure dependence and all measured values lie below the vapor pressure curves. This could mean errors in the literature data or in the temperature measurements. However, due to the gradient in the cold trap temperature, it is probable, that the T sensor at the lower part of the cylinder barrel ("S4" in figure 4.4) does not show the actual minimum temperature. As the coldest region only has a finite surface area, also slightly warmer regions of the surface contribute if more gas is injected. This results in a higher signal for larger amounts of test gas. A quantity, which is relevant for interpreting the performance of the cold trap, is the reduction factor in the CO_2 signal by freeze-out, which is strongly dependent on temperature and amount of test gas. For realistic operation conditions of -170 °C and an injected test gas amount of 150 mbar · ml, the CO_2 signal is reduced by a factor of 80, for -181 °C, even by a factor of 1300. This factor increases with increasing amount of injected gas so that it can take values within a very wide range.

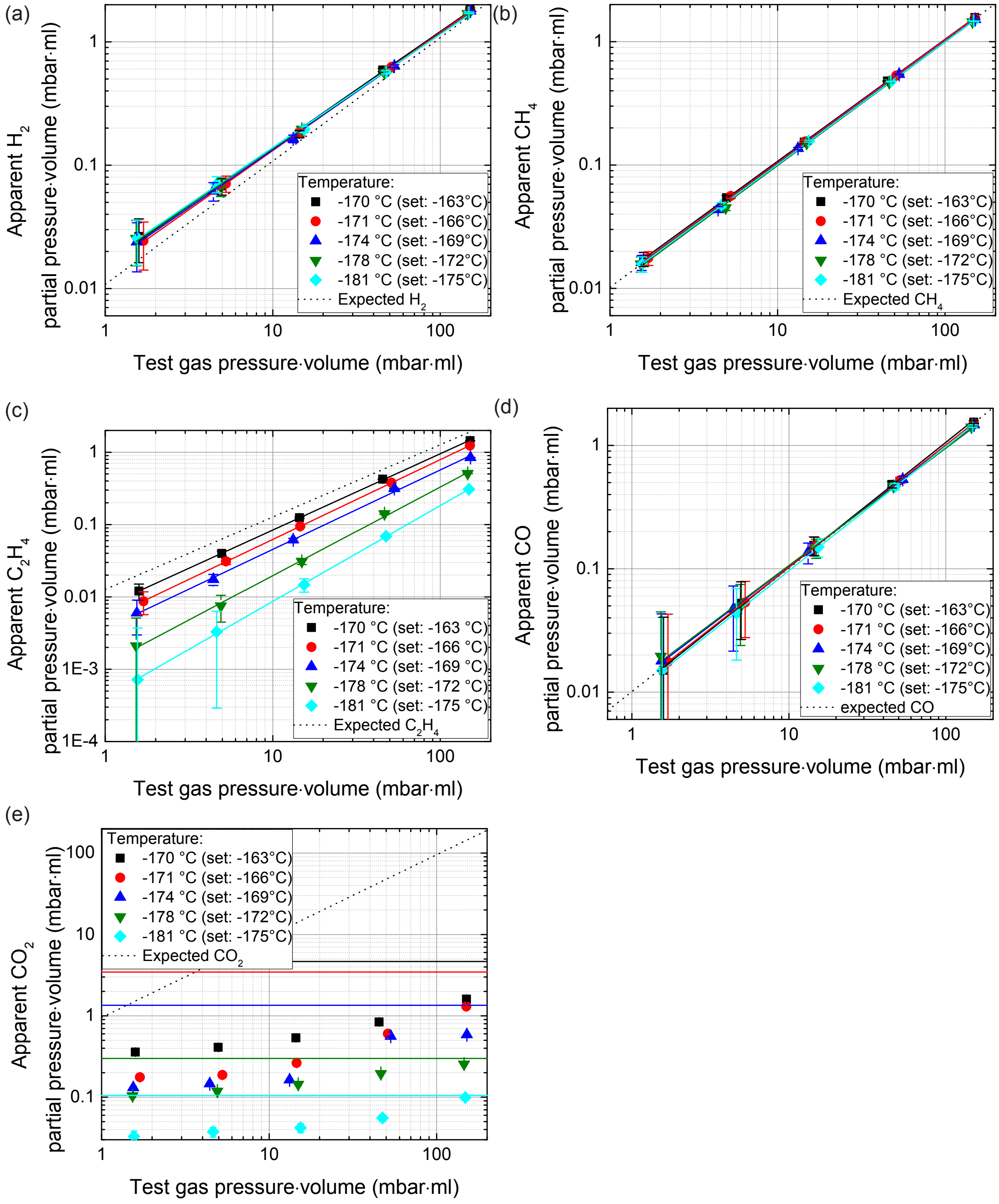

Figure 4.10: Apparent pV values of (a) H_2, (b) CH_4, (c) C_2H_4, (d) CO and (e) CO_2 from MS measurements of test gas (1.08% H_2, 1.02% CH_4, 1.27% C_2H_4, 1.01% CO and 95.6% CO_2) at various cold trap temperatures (set temperatures differing from the minimum temperature given in brackets) and varying amount of test gas. The dashed lines show the expected values according to the nominal gas concentrations inside the test gas, the solid lines in (e) depict the vapor pressures of CO_2 at the respective temperatures (values interpolated from [DDBSSTG17]). The error bars consider background correction, noise, cross correlations between channels and injection time (cf. section 4.2.9). Further parameters: test volume: 1.50 ml; cold trap turbo pump closed; Measuring time: 0.5 s per point.

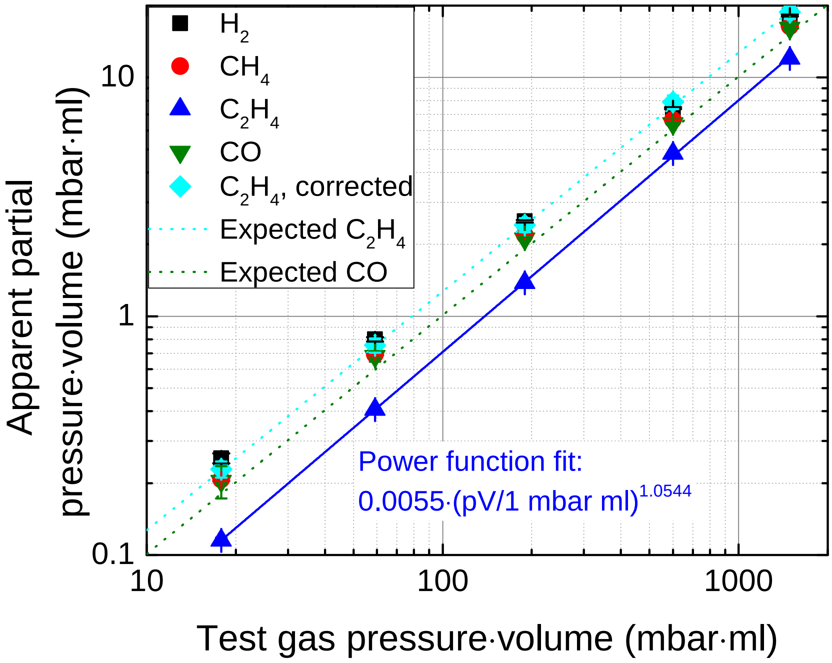

Figure 4.11: Apparent pV values of H_2, CH_4, C_2H_4 and CO from MS measurements of test gas (1.08% H_2, 1.02% CH_4, 1.27% C_2H_4, 1.01% CO and 95.6% CO_2) diluted in CO_2 in varying ratios at a cold trap temperature of -169°C and varying amount of test gas. The dashed lines show the expected values of C_2H_4 and CO according to the nominal gas concentrations inside the test gas, the solid line is a power function fit of the C_2H_4 data. The error bars consider background correction, noise, cross correlations between channels and injection time (cf. section 4.2.9), the error bars of the corrected C_2H_4 curve also consider the temperature correction. Further parameters: test volume: 18.4 ml; cold trap turbo pump closed; measuring time: 0.5 s per point.

The choice of the final operation temperature is mainly a weighting between the better freeze-out of spurious CO_2 at lower temperatures and the simultaneous loss of C_2H_4 signal. The other requirements such as pressure stability and thermal conductivity of the remaining gas tolerate a wider range of conditions. For this work, a set temperature of -169°C was chosen as a good compromise. For the following measurements, also the He pressure in the middle cylinder was reduced so that a more homogeneous temperature distribution could be achieved and the set temperature was equal to the minimum temperature.

4.2.7 Correction for ethene

As mentioned before, the quantification of the C_2H_4 content is the most critical task in the application of the described cold trap. There seems to be a relation between the amount of CO_2 on the cold trap surface and the freeze-out of C_2H_4. Therefore, the curves from figure 4.10(c), which were recorded with varying partial pressure of CO_2, may deviate from electrolysis measurements where only small amounts of products are added to a large background of CO_2, the concentration of which stays almost constant. A more reliable experiment is a series of various test gas (1.08% H_2, 1.02% CH_4, 1.27% C_2H_4, 1.01% CO and 95.6% CO_2) concentrations diluted in CO_2 with comparable total amount of gas and at a constant temperature of -169 °C. Figure 4.11 shows the apparent pV values of H_2, CH_4, C_2H_4 and CO from this series. While the values of H_2 and even of CH_4 and CO are slightly above the expected values, the C_2H_4 values are reduced similarly to figure 4.10(c). A simple power law fit of the apparent amount of C_2H_4 ($pV_{\mathrm{C_2H_4,app}}$) depending on the amount of test gas (pV_{testgas}) or the expected amount of C_2H_4 ($pV_{\mathrm{C_2H_4,exp}}$) yields

$$pV_{\mathrm{C_2H_4,app}} = 0.0055 \cdot (pV_{\mathrm{testgas}})^{1.0544} (\mathrm{mbar} \cdot \mathrm{ml})^{-0.0544} = 0.433 \cdot (pV_{\mathrm{C_2H_4,exp}})^{1.0544} (\mathrm{mbar} \cdot \mathrm{ml})^{-0.0544} \tag{4.3}$$

For the further measurements the representation depending on $pV_{\mathrm{C_2H_4,app}}$ is used:

$$pV_{\mathrm{C_2H_4,exp}} = 1.78 \cdot (pV_{\mathrm{C_2H_4,app}})^{0.948} (\mathrm{mbar} \cdot \mathrm{ml})^{0.052} \tag{4.4}$$

4.2.8 Comparison to gas chromatography measurements

As a further test of the performance of the DEMS setup, its measurement data and sensitivity are compared to the ones of the established GC setup (which is described in section 3.6). The most straight-forward way to do this is the production of a typical product gas by electrolysis followed by the injection of parts of this gas into both product analysis setups. Here, an additional lockable volume was attached to the sample inlet chamber (via gas inlet valve 1), filled with product gas, closed, detached and manually transported to the GC setup[12]. Although this method excluded errors, which were caused by changes in the actual product spectrum, it did not allow us to fill the test volume in the GC setup with CO_2 until atmospheric pressure was reached. Therefore, the gas in the test volume was expanded into the evacuated sample loop and the resulting underpressure reduced the sensitivity of the GC compared to the case when additional CO_2 was refilled from the other side. In the experiment shown here, the product gas was pushed into the test volumes for both GC and DEMS by filling up the complete sample inlet chamber to a pressure of 1000 mbar. Then, after waiting 2 min in order to achieve a more homogeneous gas distribution between the test volumes by diffusion, both samples were analyzed.

In the following, all product spectra are given in terms of "weighted product gas concentrations". This means that the measured concentrations/amounts of product gases are weighted with the number of electrons necessary for the production of one molecule by the reduction of CO_2 (according to equation 2.16), so that weighted product gas concentrations $\eta_{g,i}$ are calculated according to equation 3.1. In the literature, it is common to give Faraday efficiencies, which describe the actual share of the total current going into each product. In this thesis, only gaseous products were measured so that in particular formic acid and ethanol are neglected and a complete analysis of the Faraday efficiencies is not possible. In addition, the GC is not able to reliably measure absolute amounts of product gases, only concentrations. The weighted product gas concentrations are therefore systematically overestimated compared to real Faraday efficiencies.

Figure 4.12 shows the weighted product gas concentrations for H_2, CH_4, C_2H_4 and CO from 30 min electrolysis with a Cu layer (nominal thickness: 40 MLeq, but inhomogeneous distribution) on bulk Au at -1.35 V vs SHE in 75 mM K_2CO_3 + 100 mM H_3PO_4 purged with CO_2

---

[12] Due to a change in the column setup within the GC, the original method, which was used for all other GC measurements in this thesis (cf. figure 3.7), had to be refined. The resulting method, which was only used for this measurement, had a smoother transient in parameters, it already started from 60 °C with a ramp of 3 $\frac{°\mathrm{C}}{\mathrm{min}}$ until 80 °C, where the ramp rate was increased to 10 $\frac{°\mathrm{C}}{\mathrm{min}}$ up to a temperature of 150 °C. There, it stayed for 4 min and finally ramped up to 200 °C with 40 $\frac{°\mathrm{C}}{\mathrm{min}}$. In parallel, a pressure ramp started from 0 min at 130 kPa with 12 $\frac{\mathrm{kPa}}{\mathrm{min}}$ up to 250 kPa where it stayed for the rest of the measurement.

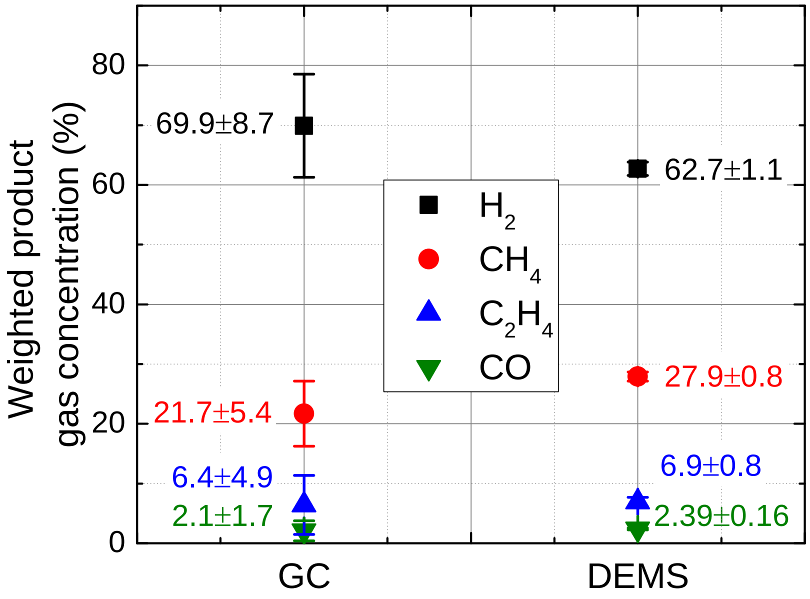

Figure 4.12: Weighted product gas concentrations for H_2, CH_4, C_2H_4 and CO from 30 min electrolysis on a Cu layer on bulk Au at -1.35 V vs SHE in 75 mM K_2CO_3 + 100 mM H_3PO_4 purged with CO_2. The symbols on the left show the concentrations determined by GC, on the right by DEMS. The error bars consider all contributions mentioned in sections 4.2.9 respectively 5.4. Further DEMS parameters: cold trap temperature -169°C, test volume: 1.50 ml; cold trap turbo pump closed; Measuring time: 0.5 s per point.

determined by GC and DEMS (cold trap temperature: -169°C). The resulting weighted product gas concentrations agreed quite well, but the value of H_2 measured by DEMS was reduced by about 10 $\%_{\mathrm{rel}}$ compared to one from the GC measurement. As the values had to add up to 100 %, the other weighted product gas concentrations were increased respectively.

Although the mismatch in the H_2 signal was covered by the statistical error, it was reproduced in repetitions of the measurement (which are not shown here) and it was therefore assumed to be of systematic origin. Furthermore, the deviation was larger than the systematic error in the calibrations of both devices. One explanation for the mismatch could be found in the geometry of the sample inlet chamber, which was disadvantageous for the described experiment: Usually, the sample gas introduced into the GC was pushed into the sample loop by additional CO_2 gas streaming through the cell. Here, a part of the sample inlet chamber was closed and transported to the GC setup, where it was transferred into the sample loop by underpressure. Therefore, it was beneficial to increase the pressure in the sample inlet chamber to 1000 mbar by introducing additional CO_2. Interdiffusion of the product gas species (which had different diffusion constants) into the additional CO_2 could now lead to a change in the relative shares of the product gases. In addition, the setup was not symmetric with respect to the sample volumes used for both product analyses so that different errors could evolve (leading to the mismatch described above). Note that this error was suppressed in measurements with only one product analysis tool: In the normal GC setup, only a negligible effect of interdiffusion in the long tubes remained; in the DEMS, where the complete sample inlet chamber was injected into the vacuum system, it completely disappears.

For a comparison between the two techniques under normal operation conditions, the de-

	GC	**DEMS**
Det. limit H_2	950 ppm	0.1 ppm
Det. limit CH_4	90 ppm	0.6 ppm
Det. limit C_2H_4	70 ppm	1.5 ppm
Det. limit CO	190 ppm	10 ppm
Error H_2	950 ppm + 2.5% $\cdot\, c(H_2)$	10 ppm + 1.4% $\cdot\, c(H_2)$
Error CH_4	90 ppm + 3% $\cdot\, c(CH_4)$	2.2 ppm + 1.3% $\cdot\, c(CH_4)$ $+\, 1 \cdot 10^{-4} \cdot c(C_2H_4)$
Error C_2H_4	70 ppm + 5.2% $\cdot\, c(C_2H_4)$	3.0 ppm + 9.5% $\cdot\, c(CH_4)$
Error CO	190 ppm + 2.6% $\cdot\, c(CO)$	25 ppm + 1.1% $\cdot\, c(CO) + 5 \cdot 10^{-3} \cdot c(C_2H_4)$ $+\, 6 \cdot 10^{-3} \cdot c(N_2) + 6 \cdot 10^{-4} \cdot c(CO_2)$ $+\, 1 \cdot 10^{-3} \cdot c(H_2)$

Table 4.3: Detection limits and error contributions for H_2, CH_4, C_2H_4 and CO measured with GC and DEMS at a cold trap temperature of -169 °C. The values for the DEMS technique were calculated using a total amount of gas of 1000 mbar · ml.

tection limits are compared using a typical test gas amount of 1000 mbar · ml for the DEMS[13]. As table 4.3 shows, the DEMS is between one and four orders of magnitude more sensitive than the GC, depending on the respective gas species[14]. On the other hand, the DEMS technique has a quite high relative error in the C_2H_4 signal and error propagation from N_2, CO_2 and C_2H_4 concentrations into the CO signal. The derivation of the errors can be found in section 5.4 for the GC and in section 4.2.9 for the DEMS technique.

4.2.9 Estimation of errors

In the following, all sources of errors, which occured during MS measurements with cold trap, shall be estimated and compared. In the end, an absolute and a relative error for each species are given. Due to the data correction method with multiple channels, some errors also depended on the concentrations of other species.

The first contribution, a statistical one, which was independent from the gas concentrations, was the background noise in the MS channels. The noise level in the original current data was identical for each channel (about $8 \cdot 10^{-15}$ A), but the corrections according to equation 4.2 led to different noise levels in the corrected measurement curves. While the method was quite sensitive for H_2 where the error by noise was only $1 \cdot 10^{-4}$ mbar · ml, the latter contribution increased to about $6 \cdot 10^{-4}$ mbar · ml for CH_4 and $1.5 \cdot 10^{-3}$ mbar · ml for C_2H_4, for which the system was less sensitive. For CO, which was determined using signals from four different channels, the noise-induced error was even $8 \cdot 10^{-3}$ mbar · ml[15].

In addition, there was a systematic error due to the background correction, which could be performed with an accuracy of about $1 \cdot 10^{-14}$ A. This led to errors of $1 \cdot 10^{-4}$ mbar · ml for H_2, $6 \cdot 10^{-4}$ mbar · ml for both CH_4 and C_2H_4 as well as $5 \cdot 10^{-3}$ mbar · ml for CO. As the accuracy

---

[13] The detection limit is only depending on the total amount of a certain species, the detection limit in terms of concentration is indirectly proportional to the amount of gas. Consequently, for a maximum amount of 10000 mbar · ml, one could detect down to one order of magnitude less.

[14] A further refinement of the GC setup and method by Thomas L. Maier after the measurements for this thesis meanwhile permits a detection limit more than one order of magnitude smaller than the one used here.

[15] The main part of this error contribution stemmed from noise in the signal of N_2, which was determined over the insensitive channel 14. As derived from the values in table 4.2, N_2 already suffered from an error of $6 \cdot 10^{-3}$ mbar · ml, which also corresponded to its contribution to the CO error. The C_2H_4 correction contributed further $1 \cdot 10^{-3}$ mbar · ml, the rest stemmed from the CO signal itself and the CO_2 correction.

of the background determination depended on the noise level, the resulting values were very similar.

Next, the relative, systematic error from the calibration was estimated to be about $0.9\%_{\mathrm{rel}}$ for H_2 and $0.3\%_{\mathrm{rel}}$ for the other species. The major contribution to this error was caused by deviations of about 0.5 s in the determination of the inlet time. According to the slope of the curves (cf. also the time transients in figure 4.8), a time shift of 0.5 s led to the given errors.

The temperature compensation of the C_2H_4 signal caused an uncertainty, which came from varying C_2H_4 freeze-out by temperature fluctuations. According to the data in figure 4.10, 0.5 °C temperature uncertainty caused a relative error of about 6 $\%_{\mathrm{rel}}$ in the C_2H_4 signal.

Furthermore, the correction method calculating one concentration from more than one channel led to error propagation between the channels. While the relative error of the C_2H_4 signal in channel 14, which influenced the measured CH_4 concentration, was only $\Delta pV_{\mathrm{CH_4,corr}} = 1 \cdot 10^{-4} \cdot pV_{\mathrm{C_2H_4}}$ (estimated by the systematic errors of both calibration factors, which determined the channel correction), it was $\Delta pV_{\mathrm{CO,corr}} = 5 \cdot 10^{-3} \cdot pV_{\mathrm{C_2H_4}} + 6 \cdot 10^{-3} \cdot pV_{\mathrm{N_2}} + 6 \cdot 10^{-4} \cdot pV_{\mathrm{CO_2}}$ for CO.

Additionally, there was an artifact caused by the mass spectrometer, when the pressure during a typical transient reduces and the measurement sensitivity of the device switched from one range to the next. Then, a jump in the background level occurred. As it was quite reproducible, this contribution could be considered and compensated. The remaining error was estimated be about $1 \cdot 10^{-2}$ mbar · ml for H_2 and CO as well as $1 \cdot 10^{-3}$ mbar · ml for CH_4 and C_2H_4.

Finally, there were deviations, which stemmed from a different solubility of the different gas species in the electrolyte similar to the ones described in section 3.6. Again, values of $\Delta_{\mathrm{sol}}\eta_{\mathrm{g,H_2}} = \pm 0.5\%_{\mathrm{rel}}$, $\Delta_{\mathrm{sol}}\eta_{\mathrm{g,CH_4}} = \pm\ 1\%_{\mathrm{rel}}$, $\Delta_{\mathrm{sol}}\eta_{\mathrm{g,C_2H4}} = \pm 3.2\%_{\mathrm{rel}}$ and $\Delta_{\mathrm{sol}}\eta_{\mathrm{g,CO}} = \pm 0.6\%_{\mathrm{rel}}$ were estimated.

When weighted product gas concentrations are given, their error propagation was calculated according to equation 3.2.

4.3 Summary and outlook

The presented novel cold trap/DEMS system was designed in order to quickly and sensitively measure mixtures of gaseous CO_2RR products, in particular H_2, CH_4, C_2H_4 and CO diluted in CO_2 and H_2O. A detailed characterization of the setup confirmed that it indeed fulfills this task: For CO, a detection limit of 10 ppm could be reached so that the method was about 20 times more sensitive than the GC setup, which was also used in this work, for H_2 the difference in sensitivity was even 4 orders of magnitude, achieving a detection limit of 0.1 ppm. At the same time, the minimum measurement interval for series of electrolyses could be reduced from 35 to 10 minutes, which was mainly dominated by the gas purging between two electrolyses.

The reasons for this high performance lay in a good vacuum quality, which reduced the background peaks to levels of at least a factor of 5 lower than the level of background current, a stable temperature control, which regulated the cold trap surface to a temperature with less than 0.5 °C fluctuation, a calibration using pure gases and a sophisticated correction scheme, which accounted for the occurrence of various molecule fragments in certain single channels. This correction uses the contributions of H_2, CH_4, C_2H_4, CO, N_2 and CO_2 to 6 mass channels to calculate the respective partial pressures, which were present in the sample gas before injecting it into the vacuum system. One particular challenge was the dissolution and freeze-out of C_2H_4 in solid CO_2. It was solved using a phenomenological correction formula, which was derived by a dilution series of this test gas in CO_2. The resulting product analysis performance was compared to the one of the GC setup used by splitting the product gas of a single electrolysis and introducing it both into the GC and the DEMS.

So far, the cold trap was only used in an "integrating" configuration (in contrast to an OLEMS configuration with membrane extraction), which means the accumulation of product gases with subsequent transfer into the cold trap volume. Its advantage is that the accumulation of product gas further increases the absolute amounts of the product species resulting in an increased sensitivity. In addition, the "integrating" DEMS technique is more suitable for a reliable calibration (which can also be used for later experiments in OLEMS configuration) and can be more easily compared to GC measurements than OLEMS. In addition, it is not yet clear, how well the cold trap technique can be combined with on-line sample extraction because of a high input of H_2O and CO_2. An increasing coverage of the cold trap surface with these compounds could lead to a temporal drift of its separation properties.

However, the cold trap could provide a strong advantage in combination with on-line sample extraction: Usually, H_2O vapor makes up a large part of the gas extracted from the electrolyte through a porous membrane and leads to a high background pressure in the mass spectrometer system. Since the cold trap is capable of freezing out H_2O, it effectively tackles this disadvantage and should dramatically improve the sensitivity compared to a conventional OLEMS system. In comparison to the current setup, this would permit to continuously purge the cell with CO_2 gas at a position separated from the extraction membrane to reduce the N_2 background and to measure with a high time resolution.

The main requirement for this upgrade would be a specialized cell. This could either be a flow cell or a stagnant one with a membrane close to the electrode surface. Special challenges in such a cell design are the prevention of gas bubbles and the implementation of sample illumination.

Chapter 5

Reactivity of arrays of mesoscopic (Cu/)Au/Ti/SiO_2/Si structures

The superordinate topic of this thesis is the examination of the impact of decorating Si electrodes with mesoscopic Au and Cu/Au nanostructures for photoelectrochemical CO_2 reduction. The most promising strategy to do this is varying the size of Au and Cu nanostructures on Si substrates and probing the electrical and photoelectrochemical behavior of the resulting samples.

Many studies in the literature already reported various effects of structure size, but the mesoscopic range between several 10 nm and a few µm, which is the one relevant for this thesis, is hardly understood so far. For very small nanoparticles with sizes below 10 nm, it is broadly accepted that they are often much more catalytically active than their bulk counterparts due to quantum confinement of the electronic states and an increased density of undercoordinated, more reactive, sites on the surface [Wie03, Wel06]. Also an increase in photovoltage and a more favorable band bending induced by metal/semiconductor contacts in the nm range were proposed [Hin98].

There are a few more recent studies of well-defined structured metal/semiconductor systems, respectively metal/insulator/semiconductor systems similar to the one in this work with arrays of mesoscopic metal structures from 50 nm [Ji14] to several hundred µm size [Esp13]. Over the whole range, the activity for hydrogen evolution from protons was reported to increase with decreasing structure size. Typical explanations for these systems are based on mechanisms inside the semiconductor substrate and its interfaces. In addition to Hinogami's explanation mentioned above, Esposito et al. and Ji et al. assigned the observation of an activity enhancement to an inversion channel for enhanced electron transfer and to hydrogen spillover [Esp13, Ji14].

Not all of the mentioned effects can also be expected in our system, but this overview shows that a variety of dependencies of the photoelectrochemical activity on the involved structure size caused by different mechanisms was proposed in the literature. Since possible size-dependent effects in measurements with our samples could still be explained by several of the mentioned mechanisms, it is important to disentangle the respective contributions, in particular the influence of the semiconductor together with its contacts and the electrochemical reactions.

This chapter starts with probing important aspects of the metal/insulator/semiconductor (MIS) interface by comparing samples, which were fabricated by two different methods, namely nanotransfer printing (nTP) and liftoff-nanoimprint lithography (LO-NIL) (cf. section 5.1), and motivates the choice of the LO-NIL method. In order to understand the influence of structured MIS interfaces, they are further characterized by electrical measurements

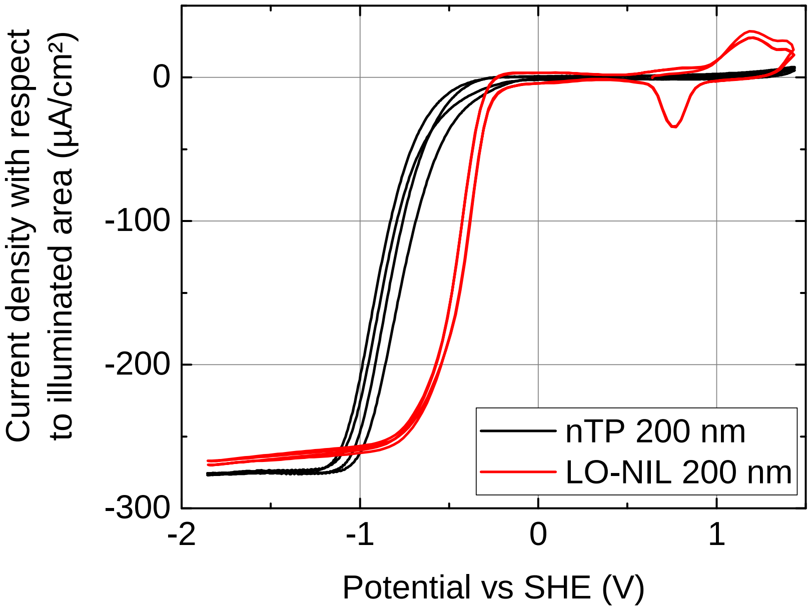

Figure 5.1: Cyclic voltammograms of 200 nm Au nanosquares on p-Si with 1-2 nm plasma oxide under illumination at a wavelength of 848 nm and an intensity of 0.5 mW/cm^2. Compared to the nTP sample (black), the sample fabricated by LO-NIL (red) needs 400 mV less overpotential for HER and CO_2RR, the typical features of Au oxidation and AuO_x reduction are clearly visible and the stability is increased. As a measure for the stability, we take the shift of the cathodic onset potentials between the first two scans, which is significant for the nTP sample and hardly measurable for the LO-NIL sample. The curves were smoothed using a 5-point adjacent averaging filter and corrected for a slight tilt. Further parameters: Electrolyte: 0.1 M $KHCO_3$ + 50 mM K_2HPO_4 + 50 mM KH_2PO_4 saturated with CO_2; scan rate: 50 mV/s [Nag17].

of samples with varying structure sizes and doping (cf. section 5.2). Next, the photocurrent over Au/Ti/SiO_2/p-Si contacts is discussed since it is important for understanding the photoelectrochemical measurements below. Under cathodic current flow on such electrodes, the finite density of photoelectrons leads to an illumination limitation. The resulting behavior is the topic of section 5.3, which is followed by a short discussion about sample stability (cf. section 5.4). With this foundation, several electrochemical measurement series of Au structures with structure sizes from 1400 nm to 75 nm are discussed in section 5.5. Subsequently, different methods for Cu deposition on Au structures and their influence on the electrochemical activity of the resulting bimetallic structures are evaluated in section 5.6, before dealing with electrochemical measurements of Au structures plated with Cu (cf. section 5.7). Finally, the results of the electrochemical measurements and error sources are discussed in section 5.8 before finishing with a summary (cf. section 5.9).

5.1 Influence of fabrication method on MIS interface

At the beginning of this project, an important task was to find a sample fabrication method, which allowed us to reliably produce arrays of Au nanostructures with a sufficient quality and stability. Therefore, two methods, namely nTP and LO-NIL (for details of sample fabrication see section 3.1), were considered. Samples fabricated by both techniques were compared with respect to their electrochemical behavior. The cyclic voltammograms shown in figure 5.1 were both recorded with 200 nm nanosquares on p-Si substrates - one sample fabricated by nTP, the other one by LO-NIL - under identical conditions (illuminated at a wavelength of 848 nm and an intensity of 0.5 mW/cm^2 with 50 mV/s in 0.1 M $KHCO_3$ + 50 mM K_2HPO_4 + 50 mM KH_2PO_4 solution saturated with CO_2). It is striking that both samples differ drastically not only in resistance, but also in stability and optical properties (in particular the plasmonic resonances shown below in figure 6.5). The first two differences can already be seen in cyclic voltammograms (CVs) of two samples fabricated by nTP and LO-NIL with otherwise identical properties under equal conditions. Although both samples have the same nominal geometry, the overpotential necessary for an identical cathodic current density resulting from CO_2RR and HER is shifted by 400 mV and the typical redox features of Au and AuO_x can only be seen on the LO-NIL sample. Both observations indicate that the resistance of the Au/Ti/SiO_2/Si interface is drastically increased by the nTP process. This can be explained by a large number of voids evolving when two rough surfaces are brought into contact instead of the compact evaporated interface resulting from the LO-NIL process. An additional difference can stem from oxidation of the Ti adhesion layer, which necessarily comes into contact with air during the nTP process. Although an oxidation cannot be completely excluded during the evaporation of Ti in ultra high vacuum, the degree of oxidation is certainly higher in the nTP process, affecting the interfacial properties.

The resulting voids and other defects at the interface also serve as an explanation for the reduced stability of the nTP sample. As it can be observed in figure 5.1, there is a significant shift in overpotential between the first two CV scans with the nTP sample, while the scans obtained with the LO-NIL structures lie well on top of each other. The porous Au/Ti/SiO_2 interface below the nTP structures could be wetted by electrolyte, which would permit redox reactions to take place inside the interface. These reactions could increase the resistance by a further oxidation of Ti or create H_2 bubbles, which lead to mechanical stress. The sealed interfaces of the LO-NIL samples can only be attacked at their edges, which makes them more stable.

Because of these advantages, all further electrochemical measurements of this thesis were recorded using LO-NIL samples. On the other hand, nTP still has some advantages compared to LO-NIL: in particular it is a much easier process and it allows slightly smaller structure sizes to be fabricated. More details about the nTP method, surface morphology and optical properties resulting from both fabrication methods can be found in the articles of Robin Nagel et al. [Nag16, Nag17].

5.2 Metal-semiconductor interface

A central feature of the structured MIS electrodes is the interface between semiconductor and metal, which is of high importance for their electrical properties. Especially the dependence of its characteristics on the structure size is decisive for understanding the origin of the size effect on the photoelectrochemical performance, which is discussed in more detail in section 5.5.

Depending on the alignment of the bands, the Au/Ti/SiO_2/Si interface can create ohmic or Schottky contacts as well as intermediates between these two forms, mainly depending on the doping and interface states (cf. section 2.1.2). In our system, we observe that p^{++}-doping leads to ohmic contacts, normal p-doping to Schottky contacts and n-doping to interme-

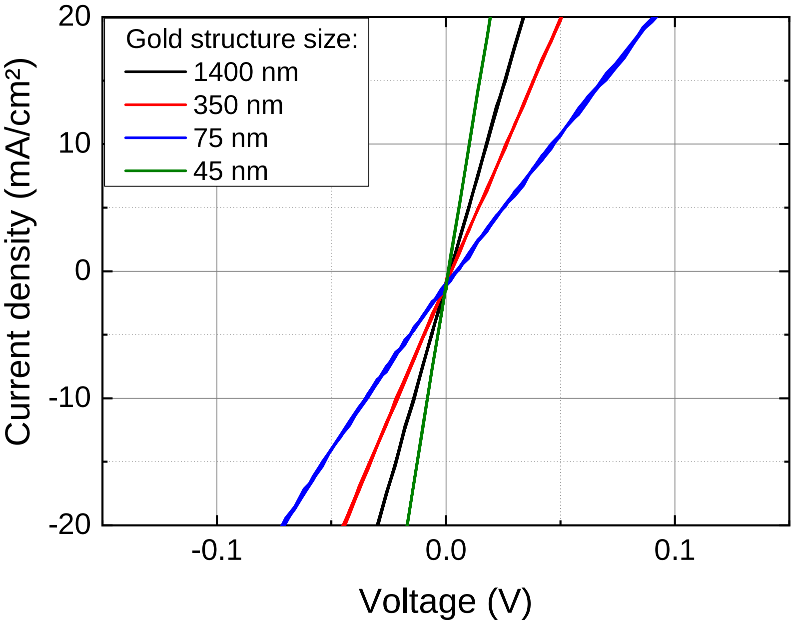

Figure 5.2: "Dry" current density-voltage characteristics of nanostructured Au/Ti/SiO_2/n-Si interfaces with varying structure size. The current density is normalized with respect to the interface area between Ti and SiO_2. Scan rate: 200 mV/s.

diate forms, which behave ohmically for moderate current densities. These differences also allowed us to compare measurements between samples with and without a real semiconductor substrate[1], which is important for the evaluation of effects occurring in the semiconductor substrate.

Figure 5.2 shows a series of j-U characteristics for Au/Ti/SiO_2/n-Si contacts with structure sizes between 1400 nm and 45 nm. They were measured by directly connecting the Au structures over an additionally evaporated Au layer, which was electrically insulated from the underlying Si substrate by SiO_2 and imprint polymer between the actual structures, and the Al back contact to the potentiostat. It shows an intermediate behavior, which manifests in an almost linear (ohmic) curve in the relevant current density range and an additional exponential contribution in forward direction (here negative, but outside of the relevant range). Both the linear and the exponential contribution are not well reproducible or clearly dependent on the structure size. These deviations could stem from fluctuations in Fermi level pinning ([Sze07]), on which the band alignment and consequently the j-U curve is very sensitive, or from the structure of the Ti layer, which could influence the effective metal work function (cf. also section 2.1.2) at the interface and they do not show a clear dependence on structure size. Fortunately, the resistivity in the ohmic region is moderate (between 1 and 12 Ωcm^2, resulting in a similar resistance as the typical electrolytes used in this work), so that the resistivity of the metal/semiconductor contact just has a small impact on the behavior of the samples, which in addition only occurs for high current densities.

The Schottky behavior of Au/Ti/SiO_2/p-Si interfaces is more reproducible. "Dry" j-U curves for sizes between 1400 nm and 75 nm are depicted in figure 5.3. The potential shift of 12 mV at a current density of +1 mA/cm^2 between the largest and smallest structures can be more

---

[1] The electrical behavior of p^{++}-Si is more comparable to a metal than to a semiconductor in many aspects, especially concerning the resulting contacts.

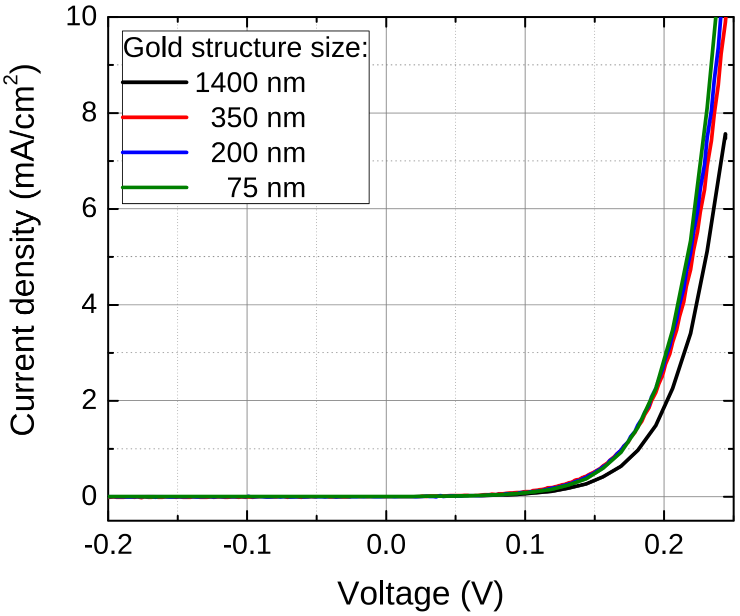

Figure 5.3: "Dry" current density-voltage characteristics of nanostructured Au/Ti/SiO$_2$/p-Si interfaces with varying structure size. The current density is normalized with respect to the interface area between Au/Ti and SiO$_2$. Scan rate: 200 mV/s [Fil18].

precisely described as a shift between 1400 nm and 350 nm structures, while there is no significant difference between the smaller nanostructures. Therefore, an influence of structure size on the metal-semiconductor interface is regarded as negligible. For the sake of completeness, it should be added, that there is indeed a pronounced size effect of Schottky contacts reported in the literature: It is known that small contacts suffer from a large leakage current and an unfortunate reverse-breakdown characteristic induced by a concentration of the electric field beneath the contact [Sze07]. This results in a dependence of the breakdown voltage on the geometrical diameter of the metal-semiconductor contact. Since the necessary high reverse bias is not applicable for our conditions, one can omit this mechanism in our system.

5.3 Illumination limitation on p-Si

Another very important aspect of the semiconducting substrate and its MIS contact is the photoelectric effect, which occurs under illumination. In the following, it is particularly relevant for the electrochemical characterization of metal structures on p-Si in sections 5.5 and 5.7. In order to better understand the results shown there, a detailed view on typical photoelectrochemical measurements with such samples is given in this section.

Although photoexcitation of charge carriers (cf. section 2.1.1) can occur in Si of any doping, we only observe a significant photovoltage for p-Si and not for n-Si and p^{++}-Si. For metal-like p^{++}-Si, the adjacent metal aligns with an additional impurity band forming ohmic contacts and preventing a measurable photoelectric effect. For the moderately doped samples, the difference in behavior can be explained by taking the role of selective contacts into account [Wü05]: As n-Si forms ohmic contacts to the conduction band both with the Al back contact and the Au front contact, both contacts are electron-selective and the photoexcited energy of the holes cannot be utilized. In contrast, p-Si has a hole-selective ohmic contact between the

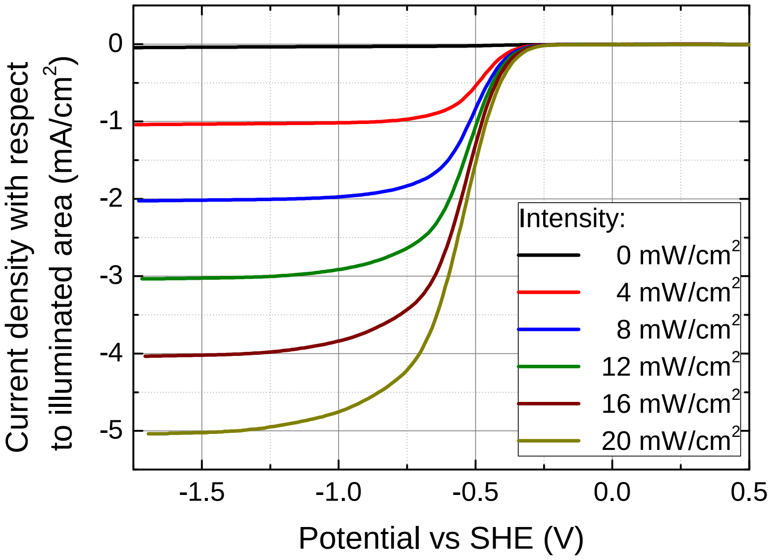

Figure 5.4: Linear sweep voltammograms of 200 nm nanosquares on p-Si with thermal oxide illuminated at a wavelength of 444 nm with varying intensity. The current densities are normalized to the illuminated area. Further parameters: Electrolyte: 75 mM K_2CO_3 + 100 mM H_3PO_4 saturated with CO_2; Scan rate: 50 mV/s in negative direction [Fil18].

highly Al-doped region (p^{++}-Si) at the rear side and an electron selective Schottky contact to the Ti/Au layer (cf. section 2.1.2). This permits the extraction of a part of the photoexcited energy, although the system is not optimized for a high photovoltage.

Since Au/Ti/SiO_2/p-Si interfaces form Schottky contacts, which are under reverse bias for cathodic overpotential (cf. section 5.2), they do not drive cathodic reactions without illumination. The resulting current density under highly negative bias is virtually proportional to the illumination intensity as figure 5.4 shows. This is examined by a series of linear sweep voltammograms (LSVs) of 200 nm Au nanosquares on p-Si in CO_2-saturated 75 mM K_2CO_3 + 100 mM H_3PO_4 solution and a scan rate of 50 mV/s in negative direction. The illumination intensity at 444 nm was varied between 0 and 20 mW/cm^2. In the dark (black line), the reduction current density stays close to zero and under illumination, a negative current density can be observed for potentials lower than about -300 mV vs SHE. This current corresponds to faradaic reactions, in particular HER and CO_2RR. For more negative potentials, it saturates at a level which is proportional to the illumination intensity, as it would be predicted for illuminated Schottky diodes under reverse bias. This also means that for moderate overpotentials, the behavior is kinetically limited, while the number of photoelectrons limits the current density for more negative overpotentials.

In order to examine wavelength-dependent effects, a series of LSVs with a 75 nm nanodisk sample on p-Si in 125 mM K_2CO_3 + 100 mM H_3PO_4 solution saturated with CO_2 was recorded with a scan rate of 200 mV/s in negative direction. While varying the photon wavelength between 365 nm and 1015 nm, the photon flux was kept constant at $8.0 \cdot 10^{15} \frac{\mathrm{Photons}}{\mathrm{cm^2 s}}$ (cf. figure 5.5(a)). Thus, the external quantum efficiency (EQE, defined as the ratio between electrochemically transferred charge carriers and incoming photons) showed a strong wavelength dependence and a maximum at about 530 nm (cf. figure 5.5(b)).

One remarkable detail is the remaining slope of the current in the illumination limited region and its wavelength dependence (here determined by linearly fitting the LSVs between -0.46 V

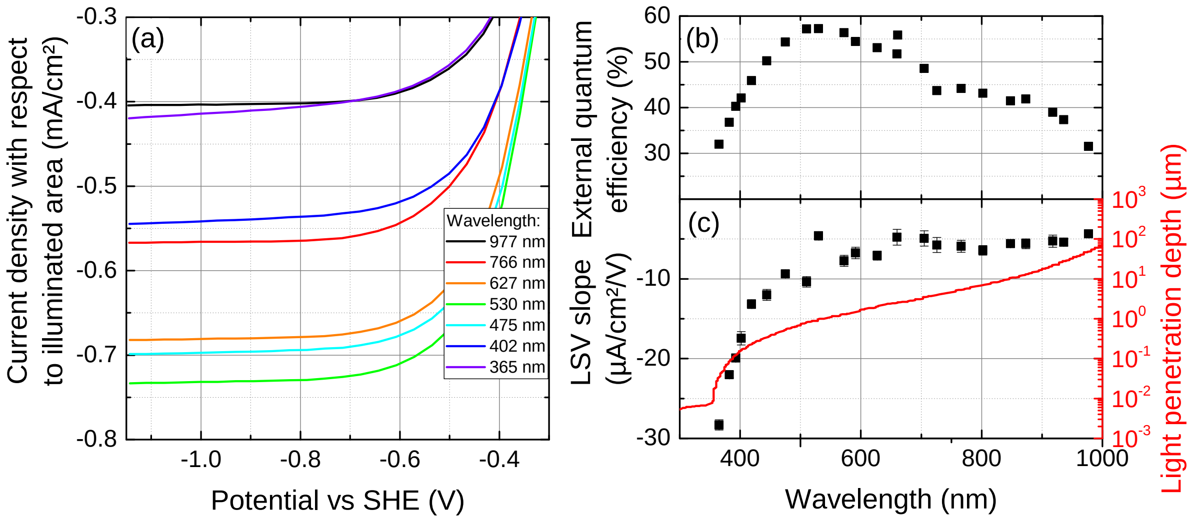

Figure 5.5: (a) Linear sweep voltammograms of 75 nm nanodisks on p-Si with 1-2 nm plasma oxide illuminated at varying wavelength with a constant photon flux of $8.0 \cdot 10^{15} \frac{\mathrm{Photons}}{\mathrm{cm^2 s}}$. The current densities are normalized to the illuminated area. (b) External quantum efficiency as a function of wavelength (c) Slopes of the LSVs in the illumination limited region (black squares, determined from linear fits between -0.46 V and -0.17 V vs SHE) and penetration depth of light as a function of the wavelength (red line, [Sze07]). Further parameters: Electrolyte: 125 mM K_2CO_3 + 100 mM H_3PO_4 saturated with CO_2; Scan rate: 200 mV/s in negative direction.

and -0.17 V vs SHE (cf. figure 5.5(c)). Since it gets much steeper for wavelengths below about 500 nm, it is instructive to look at the quantity with the strongest wavelength dependence - the light penetration depth (the inverse of the absorptivity), which strongly decreases with decreasing wavelength (cf. also section 2.1.1). Therefore it is plausible that photons with shorter wavelength are absorbed closer to the surface. There, electronic states within the bandgap act as recombination sites so that the lifetime of photoexcited electrons is reduced. In the presence of an electric field, electrons can migrate into the metal structures before they recombine and the recombination rate is reduced with increasing applied overpotential. This mechanism is stronger for photoelectrons, which are generated closer to the surface (due to the shorter wavelength) and thus suffer more from surface recombination. In addition, the slopes of LSVs in the illumination limited regime strongly vary between different samples, which is attributed to variations in the MIS interface.

Another interesting aspect of illumination limitation is what happens on the catalytic surface, if the overpotential is further increased in the illumination limited regime. This is examined experimentally by a series of GC product analyses from electrolyses with 200 nm Au structures on p-Si with thermal oxide under constant illumination with 10 mW/cm^2 at a wavelength of 572 nm in 75 mM K_2CO_3 + 100 mM H_3PO_4 solution saturated with CO_2. When the electrode potential was reduced, one was first able to observe an increase of CO efficiency. However, as soon as illumination limitation was reached, the product distribution remained constant (cf. figure 5.6). This suggests that in this regime all additional potential dropped over the semiconductor, the resistivity of which increased due to charge carrier depletion analogously to the concentration overpotential in mass transport limited electrochemical experiments. Apart from that, the notion of a changing electrode potential with simultaneously

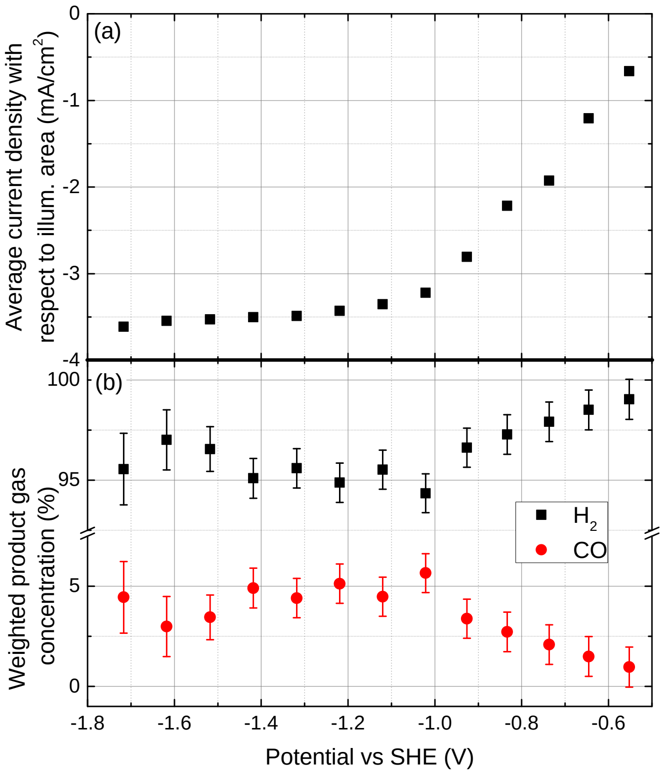

Figure 5.6: (a) Average current densities normalized to the illuminated area and (b) weighted product gas concentrations measured by GC (cf. equation 3.1 for definition) of electrolysis measurements of 200 nm Au structures on p-Si with thermal oxide as a function of the potential under constant illumination with 10 mW/cm^2 at a wavelength of 572 nm. Electrolyte: 75 mM K_2CO_3 + 100 mM H_3PO_4 saturated with CO_2 [Fil18].

constant current density is not plausible, since both parameters are closely coupled.

5.4 Sample stability

Another requirement for a reliable comparison between different measurements is to assure and evaluate the stability of the structures used. Suitable methods for this task are a comparison of both the electrochemical performance and the outer appearance of the samples via SEM before and after electrochemical measurements. Various mechanisms of sample degradation also make up one important group of sources of systematic errors.

Possible sample degradation mechanisms are changes in surface roughness, contaminations deposited on the sample surface, detachment of complete nanostructures or parts of them as well as a change (oxidation, desorption or surface alloying) of Cu layers on Au (the stability of Cu layers is discussed in section 5.6.4). These processes are very much dependent on the electrochemical parameters (as oxidation/reduction cycles can roughen the surface or evolving gas bubbles lead to mechanical stress), concentration of metal contaminations (which can be decreased, but not be completely avoided, their concentration influences the number of deposited atoms) and irreproducibilities in sample preparation (which can lead to damaged or even detached structures).

Since the most direct impact of sample instability can be found in the difference between the first two cycles of a CV, it is common to compare these cycles. Figure 5.7 shows two CVs

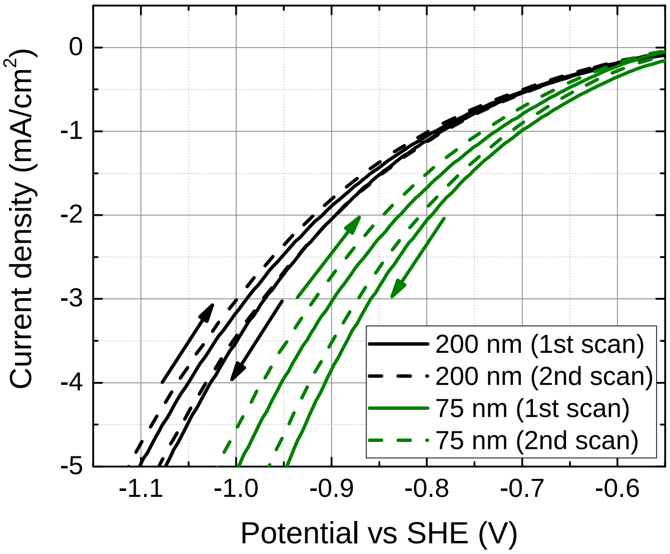

Figure 5.7: First two CV scans of Au nanostructures with sizes of 200 nm and 75 nm on p^{++}-Si with thermal oxide in 75 mM K_2CO_3 + 100 mM H_3PO_4 saturated with CO_2 at a scan rate of 100 mV/s without illumination. The slightly increasing stability with increasing structure size could also be a consequence of the decreased current density which would result in less degeneration. The current densities are given with respect to the geometrical Au surface area [Fil18].

recorded with 200 nm and 75 nm structures on p^{++}-Si. The potential difference between the first and second scan at a current density of 5 mA/cm² is about 10 mV for the 200 nm sample and about 20 mV for the 75 nm one, which could be a hint for a decreased stability of smaller structures. On the first glance, this would be plausible due to the increased edge length, which could be more sensitive towards degradation. However, the CVs shown here were recorded using the same minimum potential, which resulted in a lower cathodic current density on the larger structures (cf. section 5.5.2). Since the current density not only influences the stress on the samples, but also the pH shift on the surface (which makes the electrode seem less active in the second scan), it is therefore probable that the shift observed here mainly stems from a surface pH shift.

Usually, there were only slight changes visible in SEM images of the Au structures before and after series of electrolyses. However, some samples showed a drastically reduced electrochemical stability - probably due to errors in the sample fabrication and in particular for Ti layer thicknesses below 3 nm. In several cases, a detachment of parts of structures could be found, e.g. in the SEM image in figure 5.8. Such samples showed a decreased electrochemical performance and a blueshift of the plasmonic resonance (cf. also figure 6.8). The described sample degradation mechanisms differ strongly from sample to sample, therefore it was not possible to quantitatively consider them.

5.5 Influence of electrode structuring on electrochemical performance

One of the major questions covered in this work is, if and how the size of Au nanostructures determines their electrochemical behavior. Therefore, a series of Au structures on Si

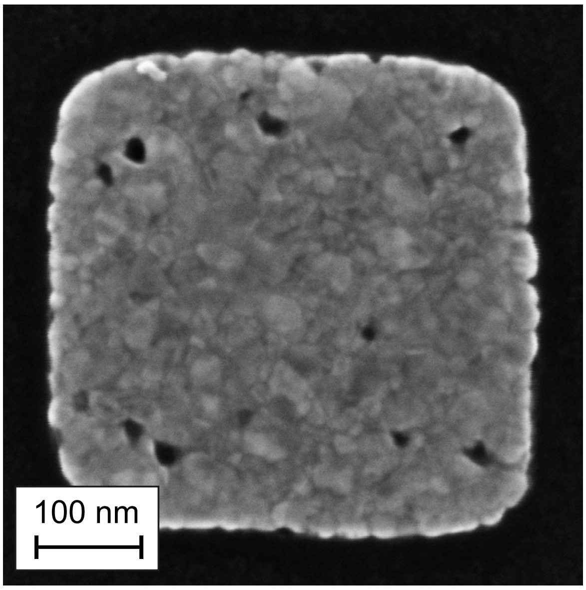

Figure 5.8: SEM images of 350 nm nanosquares after series of electrolyses. The hole formation shown here leads to a distinct reduction of electrochemical performance and a shift in plasmonic resonance. SEM image by Robin Nagel.

substrates with several doping types was fabricated, examined and compared to continuous Au layers (cf. section 5.5.1). Also systematic measurements of the shifts in overpotential and product distribution as a function of the structure size was performed using pure and Cu-plated Au structures (cf. sections 5.5.2 and 5.7).

5.5.1 Difference between continuous and structured Au films on Si

Before systematically varying the structure size, we start with a comparison between continuous and structured Au films, both on p-Si and n-Si. First, the LSV of a bulk Au electrode and of a continuous Au layer on p-Si in CO_2-saturated 75 mM K_2CO_3 + 100 mM H_3PO_4 solution under illumination with an intensity of 20 mW/cm² and 444 nm wavelength (for Au/p-Si)[2] and a scan rate of 100 mV/s are compared (black and red curves in figure 5.9). Most strikingly, a shift of the LSV curve of the Au/p-Si sample to about 110 mV more positive potential at a current density of -1 mA/cm^2 compared to the curve of bulk Au can be observed. In the curve shape of the Au/p-Si sample one can again see that the need for photoelectrons is accompanied by illumination limitation (cf. section 5.3).

The next step towards an interpretation of the influence of structure size is the comparison between this continuous layer and Au nanostructures, in this case 200 nm nanosquares on p-Si. Due to the different transmittivities of continuous and structured Au films for the incoming light, an equal illumination intensity would lead to very different photovoltages and photocurrents. Since the photocurrent can be determined much more accurately than the photovoltage and the assumption of a direct correlation between these two quantities is justified (because both have a well-defined dependence on photoinduced charge carrier density), it is the best approximation for equal photovoltages (of about 0.2 V here) to adjust equal

---

[2] When using p-Si as a substrate, it has to be illuminated to enable cathodic currents and the photovoltage it shows under illumination has to be considered and distinguished from potential shifts, which are caused by a change in electrochemical activity.

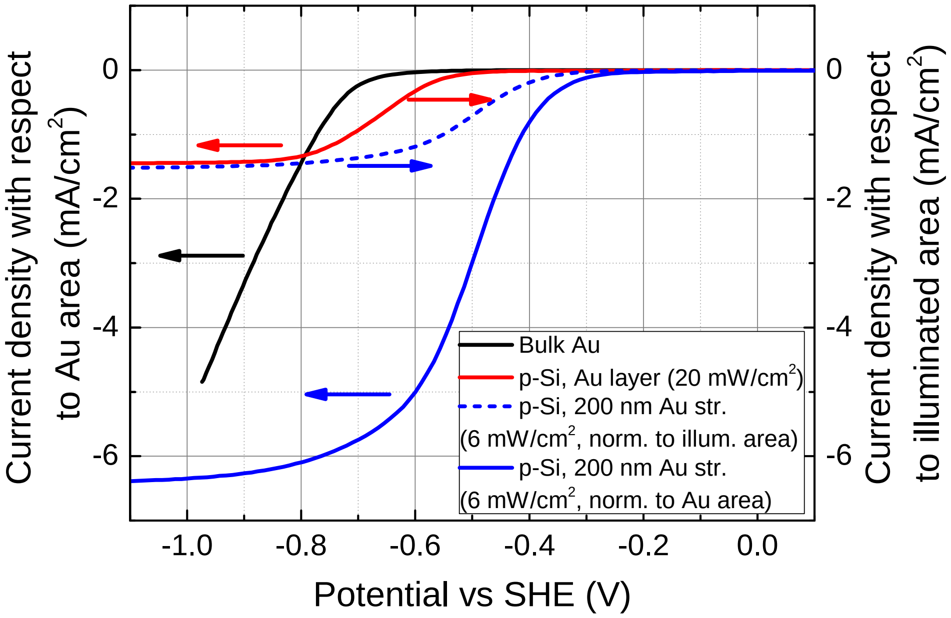

Figure 5.9: Linear sweep voltammograms of bulk Au, p-Si plated with a continuous Au layer and 200 nm Au nanosquares on p-Si with thermal oxide. The illumination intensities were chosen such that the different transmittivities of continuous and nanostructured Au films were compensated. For all three samples, the current densities are given with respect to the geometrical Au surface area (solid lines). While the normalization to the illuminated area did not change the curve of the continuous film, it reduced the current density of the structured sample (dashed line). Further parameters: Electrolyte: 75 mM K_2CO_3 + 100 mM H_3PO_4 saturated with CO_2; illumination wavelength: 444 nm; scan rate: 100 mV/s in negative direction [Fil18].

current densities under illumination limitation, which results in an intensity of 6 mW/cm² for the 200 nm structures. The real Au areas are very different between these two samples. Therefore, we used a screen with an open area of 20.25 mm^2, which is slightly smaller than the structured area (in order to prevent illumination of unstructured areas), to define the illuminated area for both samples and normalized the currents with respect to this quantity. The dashed blue curve in figure 5.9 shows that already with this normalization, a potential shift of +150 mV between the 200 nm and the continuous Au/p-Si sample can be observed (at a current density of -1 mA/cm^2).

If the current density normalization is done with respect to the geometrical Au area within the illuminated region (solid blue curve in figure 5.9), the current density obtained for the structured sample increases drastically. As a consequence, also the potential shift with respect to the Au/p-Si sample (at a current density of -1 mA/cm^2) increases to more than 250 mV. This is already a first important hint towards an increased electrochemical activity induced by nanostructuring. If one would even normalize the curve of the Au/p-Si sample with respect to the complete wetted area (because the complete Au surface, also the areas without illumination, is electrically shortcut), this would even increase the potential difference to the structured sample. Therefore, the potential shift value of 150 mV is taken as a lower boundary value.

The deduction of an electrochemical reason for the observed activity enhancement can be substantiated by similar measurements using n-Si-based samples in the dark. Au/Ti/SiO$_2$/n-

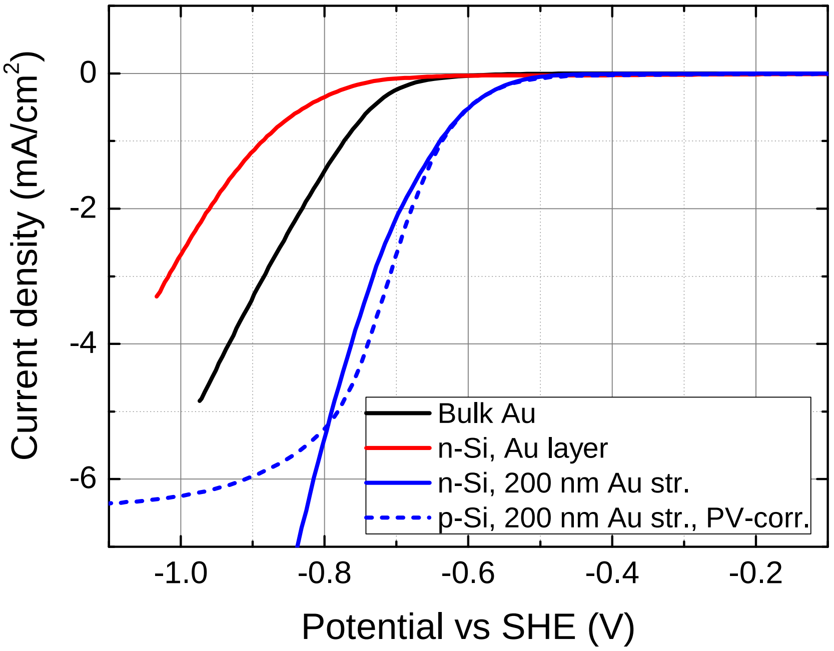

Figure 5.10: Linear sweep voltammograms of bulk Au, n-Si plated with a continuous Au layer and 200 nm nanosquares on n-Si with thermal oxide. The dashed blue line shows a LSV of 200 nm structures on p-Si with thermal oxide (from figure 5.9) corrected by the photovoltage. The current densities are calculated with respect to the geometrical Au surface area. Further parameters: Electrolyte: 75 mM K_2CO_3 + 100 mM H_3PO_4 saturated with CO_2;, illumination (only p-Si + 200 nm structures): 444 nm, 6 mW/cm²; Scan rate: 50 mV/s in negative direction (except blue dashed curve with 100 mV/s) [Fil18].

Si junctions are suitable for measurements without illumination since their j-U behavior is largely ohmic (cf. figure 5.2). The LSVs of bulk Au, continuous Au on n-Si and 200 nm nanosquares on n-Si shown in figure 5.10 confirm the observation from above that structured Au films need less overpotential for the same current density than continuous ones (as shown in figure 5.9). However, the LSV curve of the continuous Au layer on n-Si is 120 mV more negative than the one of bulk Au at a current density of -1 mA/cm^2). This change in direction of the shift is in contrast to the layer on p-Si, where an influence of photovoltage had shifted the LSV curves to less negative potentials. Nevertheless, the 200 nm structures on n-Si show a higher activity than bulk Au, compared to continuous Au on n-Si, it is shifted by $\approx$250 mV (again at a current density of -1 mA/cm^2). The LSV of illuminated 200 nm structures on p-Si (dashed blue curve in figure 5.10), which was corrected with respect to the photovoltage using the "dry" j-U characteristic is very similar to the corresponding curve on n-Si down to -2 mA/cm^2. Together with the "dry" measurements from section 5.2, this supports the interpretation of an electrochemical rather than a semiconductor effect.

5.5.2 Influence of structure size of gold nanostructures on the electrochemical activity

The next step towards understanding the role of structure size is the investigation of a series of structured electrodes with varying feature diameter, but similar surface coverage (cf. table 3.2). In the following this is done using p-Si with Au structures between 1400 nm and 75 nm size. Figure 5.11(a) shows LSVs of these samples in CO_2-saturated 75 mM K_2CO_3 +

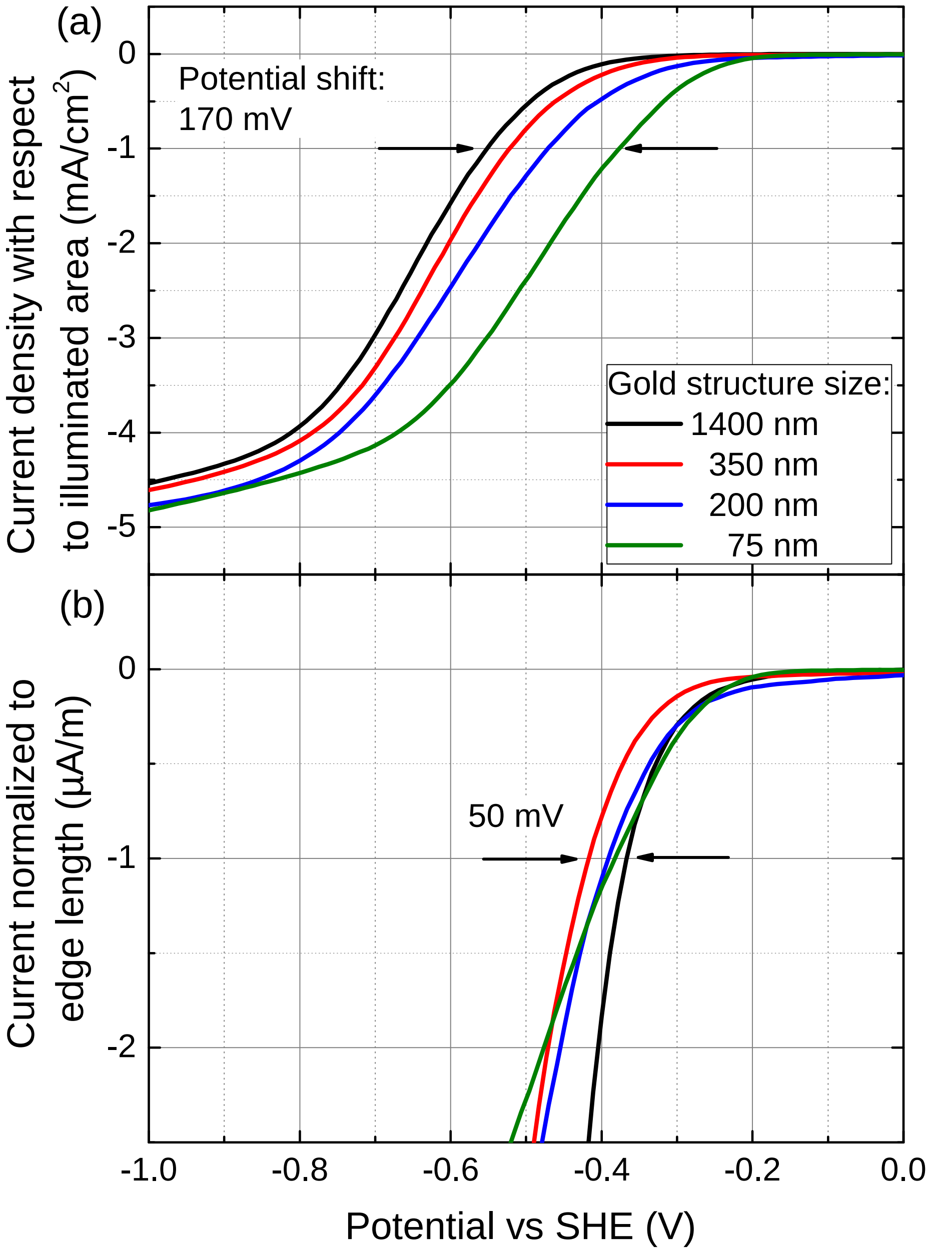

Figure 5.11: (a) Linear sweep voltammograms of Au nanostructures on p-Si with thermal oxide and structure sizes of 1400 nm, 350 nm, 200 nm and 75 nm. The current densities are normalized with respect to the illuminated surface area. The Au coverage of the 350 nm sample is slightly larger than of the rest, but it very well follows the trend of the other samples. b) The same data normalized with respect to the edge length of the nanostructures. Further parameters: Electrolyte: 75 mM K_2CO_3 + 100 mM H_3PO_4 saturated with CO_2; illumination: 444 nm, 20 mW/cm^2, scan rate: 100 mV/s in negative direction [Fil18].

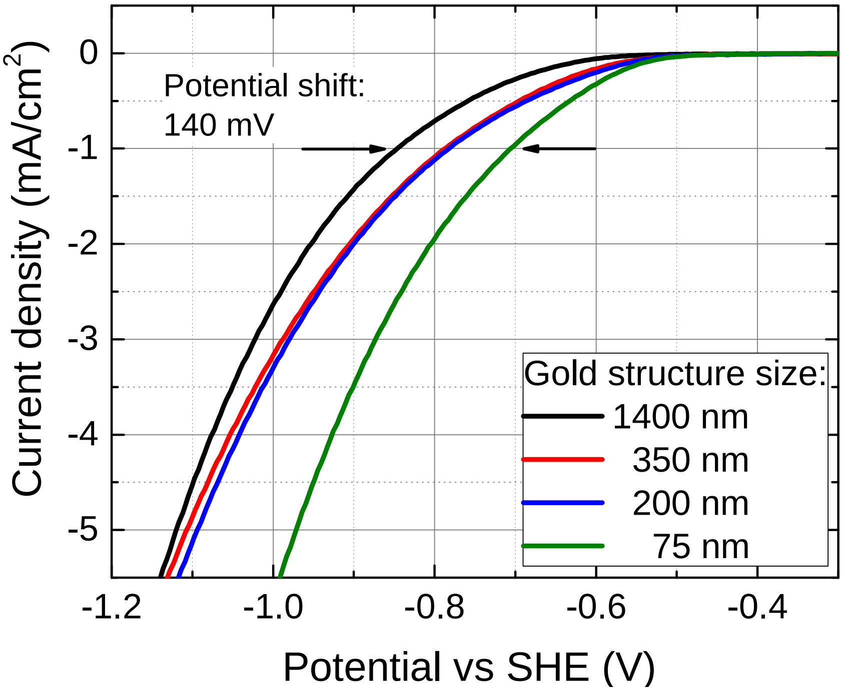

Figure 5.12: Linear sweep voltammograms of Au nanostructures on p^{++}-Si with thermal oxide and structure sizes of 1400 nm, 350 nm, 200 nm and 75 nm. The current densities are given with respect to the geometrical Au surface area. Further parameters: Electrolyte: 75 mM K_2CO_3 + 100 mM H_3PO_4 saturated with CO_2; no illumination; scan rate: 50 mV/s in negative direction [Fil18].

100 mM H_3PO_4 solution under illumination at 444 nm wavelength and 20 mW/cm^2 intensity at a scan rate of 100 mV/s with current densities normalized to the illuminated area. The most striking trend is a continuous increase of the activity with decreasing structure size. The overpotential necessary to support a current density of -1 mA/cm^2 is 170 mV lower for 75 nm structures compared to 1400 nm ones or even 340 mV lower than for the continuous film. One obvious consequence of different structure sizes is a different ratio between structure circumference and surface area (cf. also table 3.2). Indeed, the difference between the potentials necessary for a certain current-to-length ratio of the different structures is drastically reduced when the current is normalized with respect to the edge length. Even without considering accuracy limitations of the measurement such as slightly varying Au coverage and the observation that there is no monotonic trend with structure size, a normalization of the current with respect to the edge length reduces the variation in the potential necessary for a value of -1 µA/m to 50 mV (cf. figure 5.11(b)). Therefore it is plausible that the origin of the observed size effect is connected to the edges of the Au structures.

This hypothesis is substantiated by another size series with Au nanostructures on p^{++}-Si (cf. figure 5.12): The Au/Ti/SiO_2/p^{++}-Si interface is a purely ohmic contact and still the potential, which is necessary to achieve -1 mA/cm^2, is shifted 140 mV in positive direction for the electrode with the 75 nm structures compared to the one with 1400 nm structures, although there is little difference between the 200 nm and 350 nm curves. Together with the previous LSVs and the "dry" j-U curves on p-Si (5.3), this further strengthens the interpretation that processes at the electrocatalytical surface rather than effects at the metal/semiconductor interface are responsible for the observed influence of structure size.

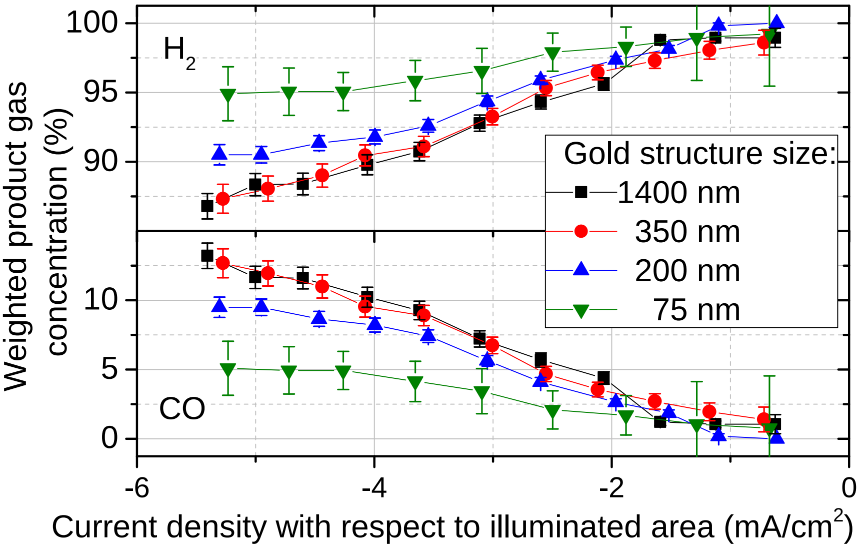

Figure 5.13: Weighted product gas concentrations of electrolysis measurements of Au structures on p-Si with thermal oxide and structure sizes between 1400 nm and 75 nm as a function of the current density in the illumination limited regime at -1.76 V vs SHE. Electrolyte: 75 mM K_2CO_3 + 100 mM H_3PO_4 saturated with CO_2 [Fil18].

For an interpretation of the observed size effect, it is also very instructive to investigate, if the increased activity with decreasing structure size influences the product distribution. It is known from the literature [Hor85] that CO_2 reduction on Au almost exclusively yields the product CO, only accompanied by H_2 from the HER. In our experiments, we could not detect any other gaseous products by GC either[3]. Figure 5.13 shows the weighted product gas concentrations (as defined in equation 3.1) as a function of the current density for Au structures between 1400 nm and 75 nm on p-Si under illumination limitation at a constant potential of -1.76 V vs SHE. An adjustment of the illumination intensity (similar to figure 5.4) leads to quasi-galvanostatic conditions, under which the weighted product gas concentrations for CO increase with increasingly negative current density. In addition, one can observe that the weighted product gas concentrations for CO decrease with decreasing structure size. This suggests that the increased activity in figures 5.11 and 5.12 is more due to an accelerated HER than due to an increased CO_2RR rate.

5.6 Copper deposition on gold

As already mentioned, Cu surfaces are the ones with the highest CO_2RR selectivity towards CH_4 and C_2H_4. They are therefore most interesting for electrochemical studies. Unfortunately, Cu is very sensitive towards oxidation in air and therefore it is quite challenging to achieve reproducible sample surfaces. On the other hand, it is possible to prepare Au samples, which are very stable in air, and plate them with Cu. In the following, an electrochemical as well as a chemical Cu deposition method are presented and the resulting Cu layers are characterized. One motivation for using two different methods was to test if surface roughness induced by diffusion-limited electrochemical deposition might lead to electrochemical properties that differ from smoother surfaces deposited from a chemical plating solution. In

---

[3] Formic acid, which would be expected at trace levels, was not examined in this work

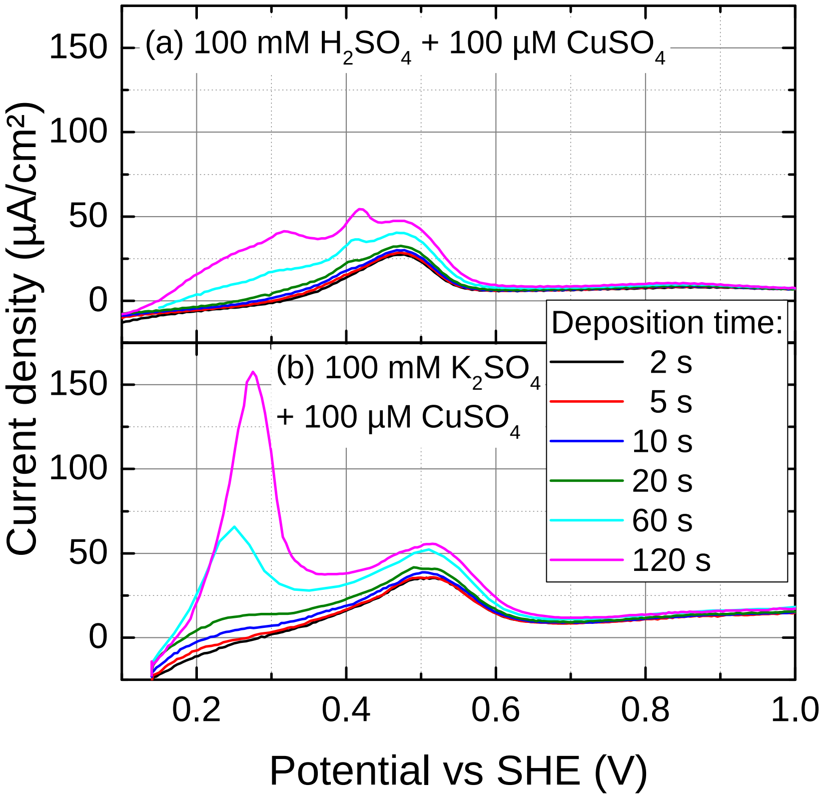

Figure 5.14: Current density transients of the stripping of Cu, which was potentiostatically deposited at a potential of +0.14 V vs SHE on bulk Au from (a) Ar-saturated 100 mM H_2SO_4 + 100 µM $CuSO_4$ solution and (b) Ar-saturated 100 mM K_2SO_4 + 100 µM $CuSO_4$ solution. The stripping curves were recorded directly after deposition at a scan rate of 20 mV/s.

particular a comparison of the product distributions stemming from two different samples with Cu-plated Au structures, which only differ in the plating method, is important for the evaluation of the impact of the surface morphology on the electrochemical properties.
The measurements in this section were to a large extent performed by Thomas L. Maier (electrochemical deposition), Kilian Vettori and Josef Zimmermann (both chemical deposition).

5.6.1 Electrochemical deposition

When Cu is electrochemically deposited on Au surfaces, it is important to characterize both the deposition process and the stability of the layers upon exchange of the Cu plating solution with the CO_2RR electrolyte and subsequent electrolyses. Here, only potentiostatic depositions are discussed[4], starting with the choice of the supporting electrolyte, electrolysis time and potential.

In the literature, H_2SO_4 is commonly used as a supporting electrolyte for Cu deposition [Hac91, Bat92], but for experiments with subsequent CO_2 reduction, it would be convenient to use a neutral supporting electrolyte, e.g. K_2SO_4 because this would reduce the formation of CO_2 bubbles during electrolyte exchange. In order to compare the Cu layers resulting from both acidic and neutral electrolytes, two series of Cu depositions on Au were performed, one in Ar-saturated 100 mM H_2SO_4 + 100 µM $CuSO_4$ solution, the second one in Ar-saturated 100 mM K_2SO_4 + 100 µM $CuSO_4$ solution. After holding the potential at +0.14 V vs SHE for

---

[4] Thomas L. Maier showed in the framework of his master's thesis that a potentiostatic Cu deposition is more reliable and that it yields more carbon-based products and less H_2 than a comparable galvanostatic one [Mai17].

times between 2 s and 120 s, a potential ramp with +20 mV/s was performed and the resulting stripping peaks are shown in figure 5.14. While the stripping curves in H_2SO_4 in figure 5.14(a) showed more features (up to four discriminable peaks for the longest deposition times), not more than two peaks could be distinguished when using K_2SO_4 (cf. figure 5.14(b)). The peak (pair) around 0.25 V - 0.3 V vs SHE is attributed to bulk Cu stripping, while the one at 0.45 V - 0.5 V vs SHE is interpreted as the stripping of the under potential deposition (UPD, [Mag90, Hac91, Bat92]) layer. Consequently, the bulk stripping significantly increases with increasing deposition time, while the UPD stripping peak only slightly grows - probably the UPD layer is not completely developed for short deposition times. The splitting of the stripping peaks, especially the UPD peak, in the curves recorded in H_2SO_4, could stem from different stability of Cu layers on Au(100) and Au(111) facets (cf. [Her01]), which cannot be resolved in K_2SO_4. Remarkably, the bulk stripping peaks in K_2SO_4 are larger, which is attributed to a faster deposition rate, although the reason for this difference remains unclear. While the distinguishable peaks for the different crystal facets are beneficial for fundamental studies of UPD layers, this is not important for the use as CO_2RR electrodes and the faster deposition rate in K_2SO_4 is regarded as an advantage.

After choosing 100 mM K_2SO_4 as the preferred supporting electrolyte for Cu deposition, the dependence of Cu deposition on the potential was investigated by performing a series of 60 s long depositions on bulk Au in Ar-saturated 100 mM K_2SO_4 + 100 µM $CuSO_4$ solution with subsequent upscans at a scan rate of +20 mV/s (cf. figure 5.15). For deposition potentials of +0.34 V and +0.24 V vs SHE, only the UPD stripping peak was observed, while bulk stripping was clearly visible for more negative deposition potentials. Remarkably, the bulk stripping peak growed much less between +0.04 V and -0.06V vs SHE compared to the growth between +0.14 V and +0.04 V vs SHE, which is probably caused by diffusion limitation during deposition leading to a virtually potential-independent deposition current density in the diffusion-limited potential range.

The deposition method, which was chosen for the electrolyses below, was a potentiostatic deposition at -0.16 V vs SHE[5] of 1200 s length in stirred CO_2-saturated solution of 50 µM $CuSO_4$ and 100 mM K_2SO_4 (cf. section 3.1.5 for more details). The low Cu concentration was chosen to minimize further Cu deposition from trace concentrations in the electrolyte after its exchange and is the main reason for the diffusion limitation during the electroplating. By integrating the deposition current over the deposition time, the amount of deposited Cu can be determined.

Since the electrolyte was exchanged after Cu deposition and series of electrolyses were subsequently performed, it was important to verify that the deposited layers were stable against dissolution during the experiments. This was tested using a series of three Cu depositions on a continuous Au layer of 16 nm thickness on n-Si with Cu stripping at different steps in the series of experiments - once directly after deposition, once after electrolyte exchange (to 75 mM K_2CO_3 + 100 mM H_3PO_4 saturated with CO_2) and once after an additional series of electrolyses (3 electrolysis measurements of 10 min at -1.4 V, -1.6 V and -1.8 V vs SHE). The deposition charges between 6.3 mC/cm^2 and 8.6 mC/cm^2 (normalized to the geometrical surface area)

---

[5] A cross-check with a pure Si sample showed no Cu deposition at this potential, therefore a Cu deposition under these conditions is concluded to be very selective towards Au surfaces. Therefore, it was possible to choose a potential slightly more negative than the electrolyses in figure 5.15.

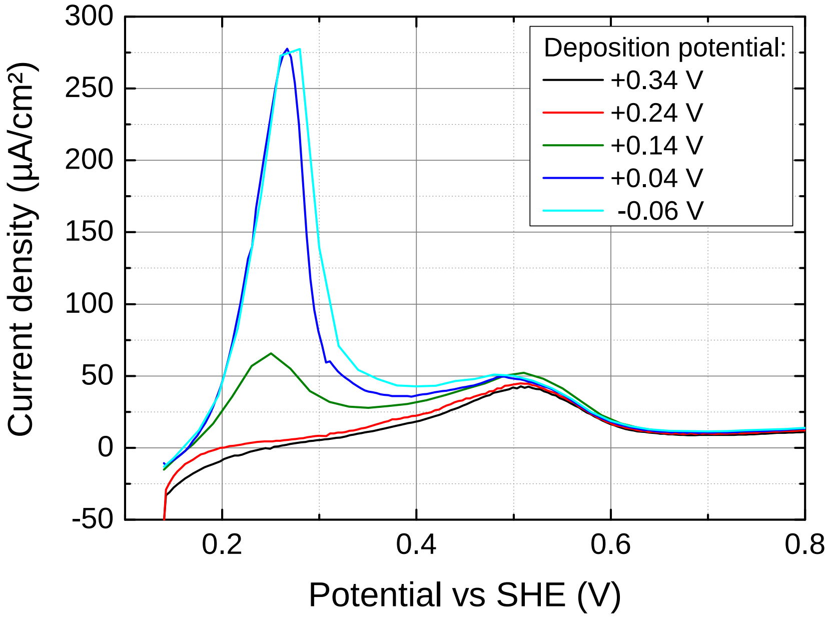

Figure 5.15: Current density transients of the stripping of Cu, which was potentiostatically deposited for 60 s at different potentials on bulk Au from Ar-saturated 100 mM K_2SO_4 + 100 µM $CuSO_4$ solution. The stripping curves were recorded directly after deposition at a scan rate of 20 mV/s.

led to nominal coverages of 14 - 19 monolayer equivalents (MLeq) using a conversion factor of 0.46 mC/cm^2 per monolayer equivalent [Hac91].

The stripping itself was done by a potentiostatic scan from -0.16 V to +0.84 V vs SHE with 50 mV/s and a subsequent constant potential step at +0.84 V vs SHE for 600 s. It is remarkable that the stripping directly after deposition shows a prominent peak at +0.4 V vs SHE (12 s) with a small shoulder at +0.53 V vs SHE (15 s in figure 5.16). As explained above, it is assumed that the shoulder belongs to UPD, while the larger peak corresponds to bulk Cu stripping. After this shoulder, the current density approaches the zero level again. For the stripping experiment after electrolyte exchange and even more for the one after a series of electrolyses, the maximum of the curve became less prominent and the UPD layer stripping disappeared. On the other hand, a significant, but decreasing, current density remained present over the complete time when the potential was held at +0.84 V vs SHE for the latter two measurements. The most reasonable explanation for this behavior is that diffusional alloying takes place at the Cu/Au interface and that Cu atoms, which were already alloyed into the Au, needed some time to diffuse to this surface again. Due to the diffusive nature of this mechanism, it only asymptotically approached zero current and after 10 min there were still Cu atoms remaining. A longer duration of the stripping step would be favorable to remove further Cu atoms, but with longer times, errors due to current offsets would increase. Since this delayed Cu stripping was much less prominent after waiting without electrolyte exchange, it is probable that it was partly caused by the presence of other ions in the electrolyte.

The overall stripping charge of 6.7 mC/cm^2 to 7.2 mC/cm^2 did not differ much between the measurements, yet the third measurement (after electrolysis), which started with the highest deposition charge, actually showed the lowest stripping charge. This could either mean that Cu got lost during electrolysis or that the longer time together with the application of electric

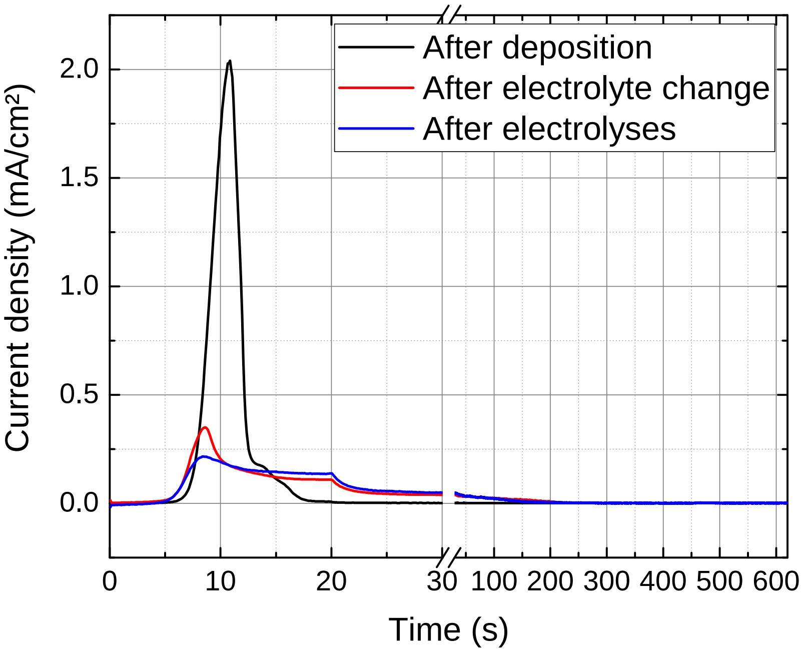

Figure 5.16: Current density transients of the stripping of Cu, which was potentiostatically deposited on n-Si with a continuous Au layer of 16 nm thickness. The stripping curves were recorded directly after deposition (black), after electrolyte change (red) and after an additional series of electrolyses (blue). In the first 20 s, the potential was scanned from -0.16 V to +0.84 V vs SHE with 50 mV/s, then it was kept constant at +0.84 V vs SHE for 600 s. Further parameters: Electrolytes: CO_2-saturated 50 µM $CuSO_4$ and 100 mM K_2SO_4 (Cu deposition and black curve) and 75 mM K_2CO_3 + 100 mM H_3PO_4 saturated with CO_2 (red and blue curve); Cu deposition: -0.16 V vs SHE for 1200 s; electrolyses: 10 min each at -1.4 V, -1.6 V and -1.8 V vs SHE [Mai17].

fields led to a deeper incorporation of Cu into the Au matrix.

5.6.2 Chemical deposition

Although the Cu layers, which were electrochemically deposited, could be well used for CO_2RR experiments, a high surface roughness of the resulting layers was expected due to the diffusion-limited deposition. In order to check for an influence of the surface morphology on the product spectrum and for possibly altered CO_2RR selectivities, it is useful to compare the product spectrum from an electrochemically Cu-plated sample to one of an electrode, which was plated by a chemical plating solution (for the resulting product distributions see section 5.6.3). The solution used here, Expt Seedplate from Atotech, was designed to yield very smooth layers, which is in contrast to the rougher surfaces from a diffusion limited electrochemical process, and to allow for very slow deposition rates so that very thin Cu layers can be produced. In order to evaluate the usability of the described method, it is important to check its selectivity, in particular towards Cu deposition on SiO_2 between the structures, its dependence on deposition parameters such as the temperature and the electrochemical performance of the resulting layers.

First, the selectivity of the process, i.e. how much larger the deposition rate on Au was compared to the one on Si, was tested using XPS. Therefore, a blank piece of Si and one with

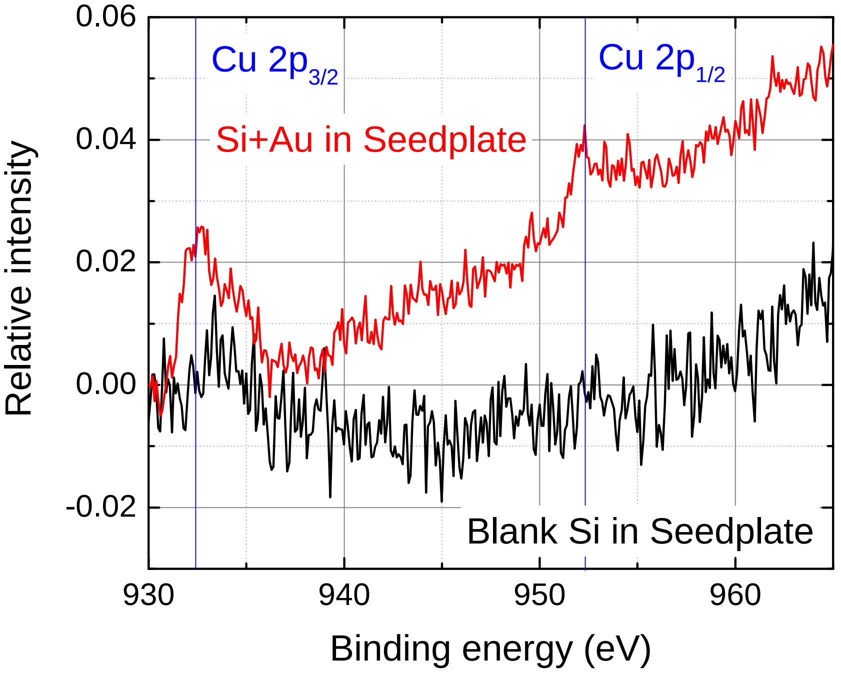

Figure 5.17: XP spectra of the Cu2p region of a blank and a Au-structured Si sample immersed in Seedplate solution before XPS. X-ray energy: 1486.6 eV. The spectra were normalized with respect to the Si2p peak and the background was subtracted.

10 µm Au structures were both immersed in Seedplate solution and rinsed (according to the protocol described in section 3.1.5) before mounting in the XPS chamber[6]. Normalized detail spectra of the Cu2p region of these two samples (figure 5.17) show that Cu is indeed deposited on the sample carrying Au structures. On the pure Si sample, also traces of the Cu2p$_{3/2}$ peak were found close to the detection limit, but only about 1/2 of the peak height compared to the other sample[7]. Considering that only about 20% of the area are covered by Au structures, this means that the deposition rate on Au is more than one order of magnitude higher than on Si, but that the process is not perfectly selective.

For an analysis of the influence of different parameters in the chemical deposition on their electrochemical properties, an electrochemical characterization method composed of several steps was used: After immersing a bulk Au sample into tempered Seedplate solution and rinsing it (cf. section 3.1.5 for the detailed protocol), the sample was mounted into the electrochemical cell. The cell was filled with buffered electrolyte (75 mM K_2CO_3 + 100 mM H_3PO_4) under potential control at -0.16 V vs SHE and then purged with CO_2 for about 30 min (an exemplary transient of current density and potential recorded using a sample with a deposition temperature of 29 °C is shown in figure 5.18). The cathodic current due to the reduction of dissolved O_2 reduced over this time period. After this preparation, the potential was cycled down to -0.66 V vs SHE to compare the HER/CO_2RR-related cathodic current density of the deposited layers at this potential. Then, Cu stripping was performed by first ramping up to +0.84 V vs SHE within 250 s and then holding this potential for 350 s. This long stripping time was introduced since it turned out that a single ramp was not sufficient to strip all Cu from the

---

[6] The one without Au was measured by Francesco Casablanca in the WSI custom built device. Although the machines are not identical, they have an equal ratio between signals and background.

[7] For a comparison of spectra from two different XPS devices, both spectra were normalized to a Si2p peak height of 1 and then the background in the Cu2p region was subtracted.

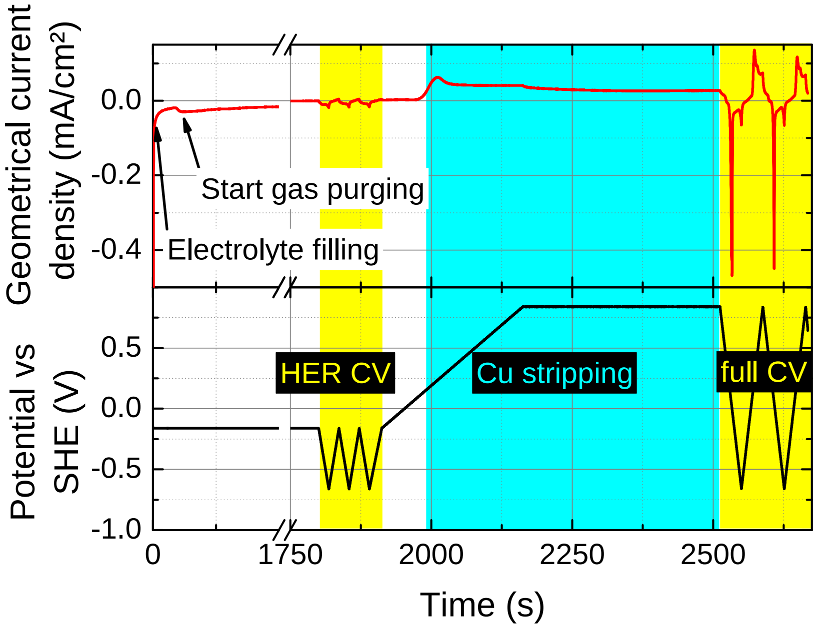

Figure 5.18: Potential (bottom) and current density (top) transient of the potentiostatic method used to evaluate the performance of chemically deposited Cu layers on Au, here of one deposited at a temperature of 29 °C. Directly after starting the potential control at -0.16 V vs SHE, electrolyte was filled in and CO_2 purging was started. After 1800 s, three CV scans into negative direction were performed before stripping off the Cu using a potential ramp with a subsequent potential hold at +0.84 V vs SHE of 600 s in total. Then, two more CV cycles over the complete potential range were added. Electrolyte: 75 mM K_2CO_3 + 100 mM H_3PO_4 saturated with CO_2.

surface, probably due to Cu atoms alloyed into the Au surface (cf. also section 5.6.1). Therefore, a total stripping time of 600 s was chosen as a standard for these measurements. Finally, two more CV cycles were performed after stripping. They showed prominent Cu deposition and stripping peaks in every cycle, which means that the stripped Cu is not effectively transported away. In addition, the reduction current density at -0.66 V vs SHE reached more negative values, which is consistent with literature data, where Au (and as a consequence also Au surfaces with lower Cu coverage) was reported to be more active towards HER and CO_2RR than Cu [Hor85].

It is also probable, that the diffusion-limited electrochemical redeposition of previously stripped Cu leads to rougher surfaces compared to the originial ones from the chemical Seedplate process, which is optimized towards smooth surfaces. This roughness could then cause an increased surface area and consequently an increased current. In this section, only the geometrical current density (which does not account for roughness) is evaluated; it consequently shows an increase, which would be less pronounced in the actual microscopic current density.

Since temperature is an important parameter for virtually all chemical processes, its influence on the resulting Cu layers and their performance was examined. According to the manufacturer, the deposition temperature should lie between 25 °C and 35 °C. Therefore, this range, or more accurately the range between 27 °C and 34 °C, was used for a series of platings and characterizations. Especially the charge of the first stripping peak and the HER current at

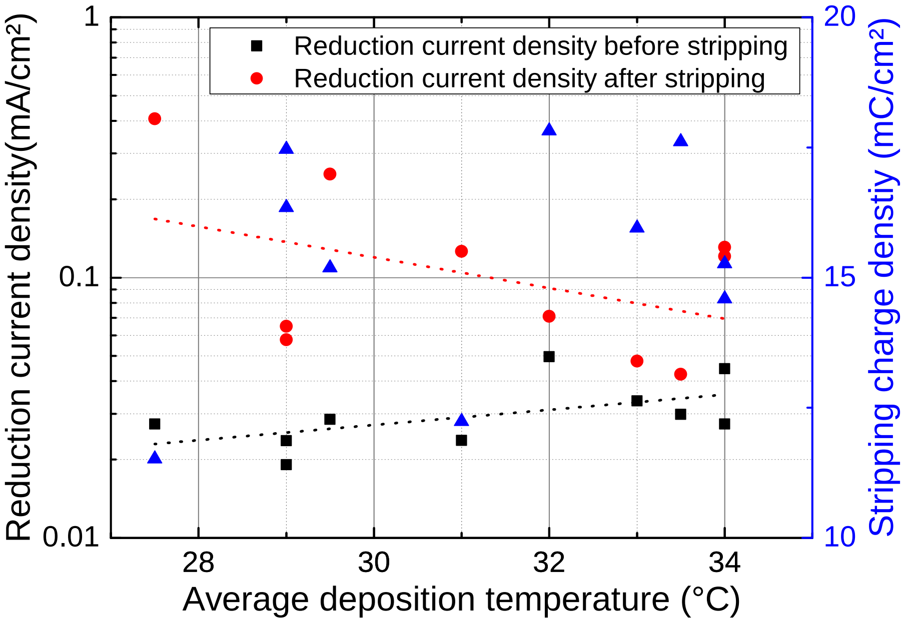

Figure 5.19: Reduction current density at -0.66 V vs SHE before (black) and after stripping/redeposition (red) of the Cu layer as well as the charge density of the first Cu stripping (blue) against the average deposition temperature. The dashed lines are exponential fits to the current density data. The data points were determined using the measurement protocol shown in figure 5.18. Electrolyte: 75 mM K_2CO_3 + 100 mM H_3PO_4 saturated with CO_2.

-0.66 V vs SHE before and after stripping/redeposition were evaluated for a series with different temperatures (cf. figure 5.19). The variance of the data was quite high, but still one can see that the influence of deposition temperature on the amount of stripped (and therefore also on deposited) Cu was very low. Concerning the reduction current density before stripping, an increase of 56 ±28 % upon temperature increase from 27 °C to 34 °C (determined by exponentially fitting the dataset) is found, while the current density after stripping decreases by 58± 41 %. Despite the large error of the data, the first observation could again be explained by an increasing roughness of the original Cu layer with higher deposition temperature. And although the uncertainty in reduction current density after stripping is quite high if plotted against temperature, there is a strong correlation between stripping charge and the activity after redeposition (cf. figure 5.20): the less Cu is detected, the higher is the activity, which would again be in line with an increased activity of Au surfaces with lower Cu coverage.

5.6.3 Influence of the Cu deposition method on the product distribution

In order to evaluate the impact of the deposition method used for the preparation of Cu surfaces on Au, the resulting product distributions on a pair of identical p-Si samples with 350 nm structure size and a comparable Cu coverage of about 40 MLeq were measured with GC analysis for 2 illumination intensities (18 mW/cm^2 and 21.7 mW/cm^2 at 444 nm corresponding to illumination normalized current densities of -4.1 mA/cm^2 and -5.3 mA/cm^2) in CO_2-saturated 75 mM K_2CO_3 + 100 mM H_3PO_4 solution. The weighted product gas concentrations (as defined in equation 3.1) resulting from both samples were very comparable, especially the ones for H_2 and CO (cf. figure 5.21). On the other hand, the CH_4 concentration of the sample plated with Seedplate solution is higher than the value of the electrochemically plated one, while the C_2H_4 concentration is lower. A different surface morphology could in-

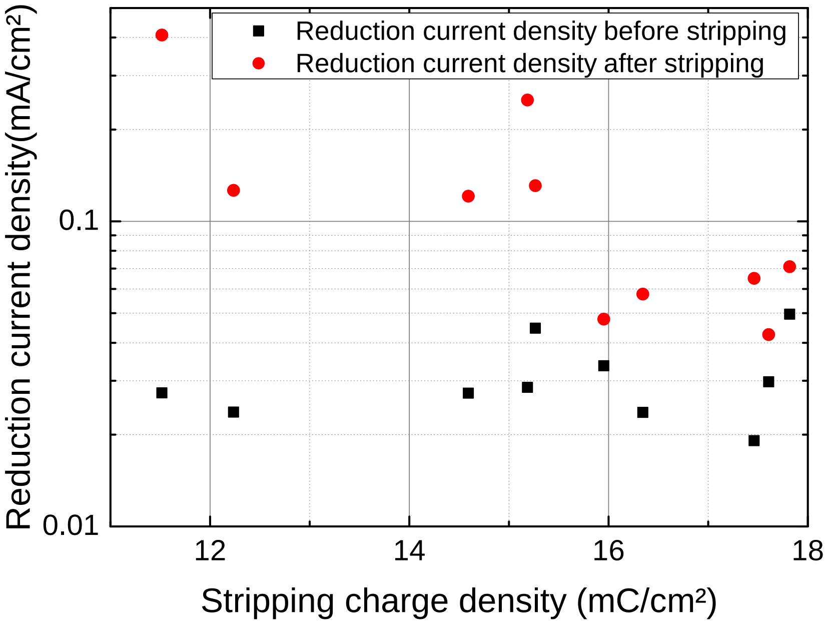

Figure 5.20: Reduction current density at -0.66 V vs SHE before (black) and after stripping/redeposition (red) of the Cu layer against the charge density of the first Cu stripping. The data points were determined using the measurement protocol shown in figure 5.18. Electrolyte: 75 mM K_2CO_3 + 100 mM H_3PO_4 saturated with CO_2.

deed explain this behavior since the product distribution does strongly depend on surface orientation and C_2H_4 is mainly produced on Cu(100) surfaces. E.g. it was shown by Hori et al. using single crystals that Cu(111) has a ratio of 5.7 between the Faraday efficiencies of CH_4 and C_2H_4, while it is 0.1 for Cu(711) [Hor02]. Still, it is remarkable that products distributions do not differ too much between the two samples, although the sample plated with Seedplate was exposed to air for several minutes between deposition and electrolyses. Possibly, the largest part of the resulting Cu oxide was reduced again under CO_2RR conditions.

Summarizing the comparison between the introduced Cu plating methods, one can conclude that both are usable for subsequent electrochemical CO_2RR and only slightly differ in the resulting product spectra. Due to the reduced reproducibility, the unavoidable oxidation after deposition and the unknown recipe of the commercial plating solution, the electrochemical method was chosen for all experiments in the following.

5.6.4 Stability of Cu layers

Despite their attractive product spectrum, Cu surfaces have a severe problem, which prevents the application of electrochemical CO_2RR, namely the deactivation of Cu layers during CO_2RR. It has been extensively discussed in the literature and this discussion shall be summarized in the following. There are at least two explanations, which are supported by various publications, and it is plausible that both of them - trace metal contaminations and the deposition of organic reduction byproducts - poison the Cu surfaces.

The metal contamination theory is substantiated by experiments of Hori et al [Hor05] who found that a pre-electrolysis of commercially available reactants can drastically extend the duration of hydrocarbon production and Wuttig et al. [Wut15], who found a similar effect when cleaning the electrolyte with a chelation agent (solid-supported iminodiacetate resin) before electrolysis. Despite painstaking efforts for cleanliness, the concentrations of metal

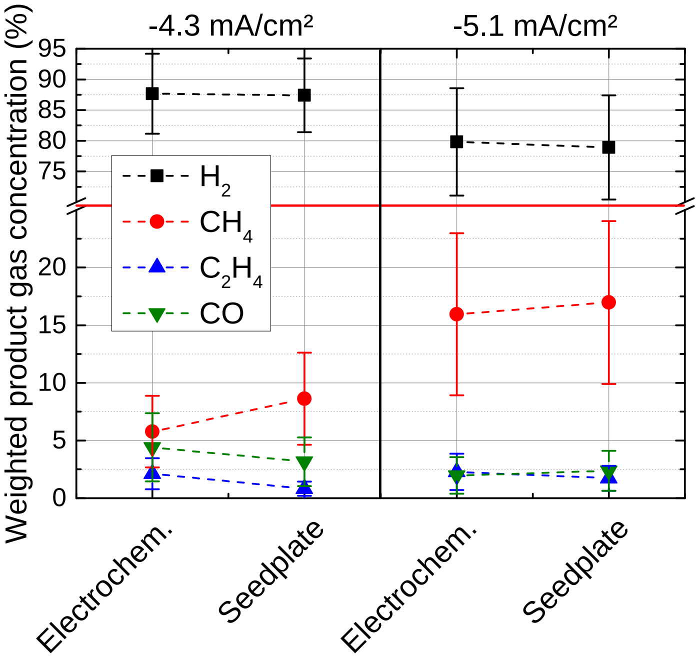

Figure 5.21: Weighted product gas concentrations of H_2, CO, CH_4 and C_2H_4 for two p-Si samples with 350 nm Au structures plated with 40 MLeq of Cu, once using electrochemical deposition, once using Seedplate solution. The electrolyses were performed under illumination limited conditions at current densities of -4.1 mA/cm^2 (left) and -5.3 mA/cm^2 (right). Further parameters: Electrolyte: 75 mM K_2CO_3 + 100 mM H_3PO_4 saturated with CO_2; Electrochemical Cu deposition: 20 min at -0.16 V vs SHE in 50 µM $CuSO_4$ + 100 mM K_2SO_4 saturated with CO_2. Electrolyses: 24.1 min at -1.76 V vs SHE under illumination at 444 nm wavelength and 18 mW/cm² (left); 20 min at -1.76 V vs SHE under illumination at 444 nm wavelength and 21.7 mW/cm² (right). Current densities are given with respect to the illuminated area. Reproduced from [Mai17].

ions in the electrolytes can never reach zero so that also the deposition of metal impurities cannot be completely excluded.

On the other hand, De Wulf et al. first proposed that a graphitic carbon species, which occurs as a side product of CO_2RR to CH_4, poisons the electrode surface [DeW89]. More recent works about highly C_2H_4-selective nanostructured Cu derivatives support the latter hypothesis because they show much less deactivation than catalysts with more CH_4 yield [Xie14, Che15a, Kas15].

Both hypotheses are equally supported by the possibility of re-activation of the catalytic properties by pulsed oxidation of the Cu surface [Shi93, Jer94].

A third possibility for a long-term change in catalytic behavior could be a loss of "subsurface" oxygen, which was reported to drastically increase the C_2H_4 selectivity of Cu [Cav17]. However, this hypothesis is undermined by experiments and simulations, which found a surprising stability of this subsurface oxygen [Liu17, Cav17].

For the following experiments, series of electrolyses on Cu-plated surfaces, we estimated the systematic deviation stemming from Cu deactivation by comparing the product spectrum of the first and last one of a series of eight electrolyses on Cu-plated Au nanostructures of 350 nm size on p-Si. An illumination of 18 mW/cm² at 444 nm wavelength resulted in an average current density of 4.1 mA/cm^2 (normalized to the illuminated area) at a potential of

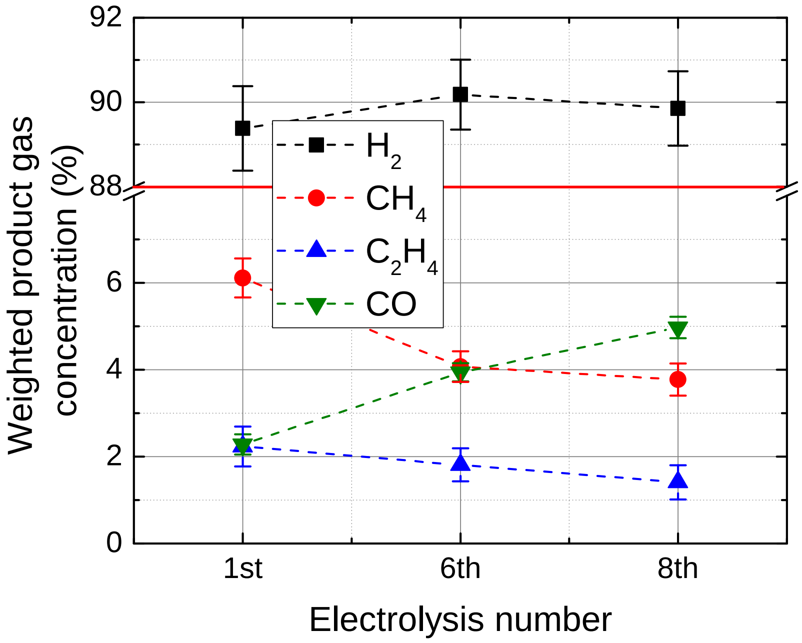

Figure 5.22: Weighted product gas concentrations for H_2, CO, CH_4 and C_2H_4 recorded on p-Si sample carrying 350 nm Au structures plated with Cu. The results of three measurements out of a series of 10 electrolyses at potentials between -0.99 V and -1.81 V vs SHE in 75 mM K_2CO_3 + 100 mM H_3PO_4 solution under illumination with 18 mW/cm^2 at a wavelength of 444 nm are shown [Mai17]. In this figure, only statistical errors are regarded.

-1.81 V vs SHE, but due to illumination limitation (cf. also section 5.3), still 4.0 mA/cm^2 could be measured at -1.61 V vs SHE. Therefore, the weighted product gas concentrations of the main gaseous products for the first electrolysis (-1.81 V vs SHE), the 6th electrolysis (-1.81 V vs SHE) and the 8th one (-1.61 V vs SHE)[8] are shown in figure 5.22. Although the H_2 concentration does not change much, one can observe that the CO yield increases, while the ones for CH_4 and C_2H_4 decrease. This observation is also quite typical for Cu deactivation reported in the literature [Hor05, Xie14, Che15a, Kas15, Wut15].

5.7 Influence of size of Cu/Au nanostructures on electrochemical activity

It is interesting to investigate if the electrochemical reactivity of Cu-plated Au structures also exhibits a structure-size dependence. Again, a series of such nanostructures with sizes between 1400 nm and 75 nm on p-Si is measured by cyclic voltammetry and electrolyses with product analysis. In contrast to the Au structures, which were examined in section 5.5.2, they were electroplated by Cu according to the procedure described in section 3.1.5 before the characterization. After 20 min deposition at a potential of -0.16 V vs SHE, Cu layers of thicknesses between 40 and 80 MLeq were determined by Cu stripping after the electrolyses. This shall be thick enough to assume that the underlying Au did not influence the electrochemical behavior any more.

In LSVs of Cu-plated Au structures (1400 nm structures with 70 MLeq Cu, 350 nm structures

---

[8] This number of experiments roughly corresponds to the number of electrolyses in e.g. figure 5.24.

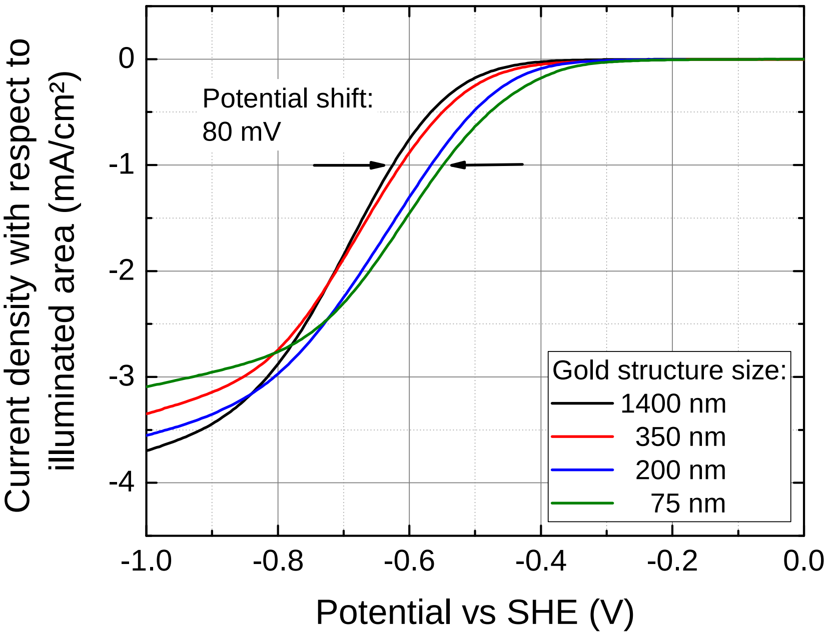

Figure 5.23: Linear sweep voltammograms of Cu-plated Au nanosquares on p-Si with thermal oxide and sizes of 1400 nm, 350 nm, 200 nm and 75 nm. The current densities are given with respect to the illuminated area. Further parameters: Cu layer thickness: 70 MLeq (1400 nm), 40 MLeq (350 nm), 60 MLeq (200 nm and 75 nm); illumination: 444 nm, 20 mW/cm^2; electrolyte: 75 mM K_2CO_3 + 100 mM H_3PO_4 saturated with CO_2; scan rate: 50 mV/s in negative direction.

with 40 MLeq Cu, as well as 200 nm and 75 nm structures with 60 MLeq Cu each) under illumination at a wavelength of 444 nm and an intensity of 20 mW/cm^2 in 75 mM K_2CO_3 + 100 mM H_3PO_4 saturated with CO_2, a similar trend with size as before was observed: The potential necessary for a current density of -1 mA/cm^2 (with respect to the illuminated area) was about 80 mV less negative for the 75 nm structures compared to the 1400 nm ones (cf. figure 5.23), which was less than the shift measured with unplated structures (cf. figure 5.11). While the difference between 200 nm and 75 nm structures makes up about 50 % of the total shift in the experiment without Cu plating, the corresponding curves do only slightly shift in the Cu-plated dataset. The most plausible explanation for this discrepancy lies in the variations in the saturation current density as well as the remaining slope in the LSVs for large negative bias. The reason for this behavior could be a strong variation between the MIS interfaces within this set of samples.

In order to elucidate the CO_2RR performance of such samples, product analyses after series of electrolysis measurements with varying current density (again adjusted by the illumination intensity in the illumination limited regime) were performed and the gaseous products from three Cu-plated samples with structure sizes between 1400 nm and 200 nm (Cu layer thickness: 60 MLeq (1400 nm), 40 MLeq (350 nm), 80 MLeq (200 nm)) on p-Si were measured from high to low current densities[9] using GC (cf. figure 5.24). The electrolysis time was increased indirectly proportionally to the illumination intensity starting from 20 min at 21.7 mW/cm^2 illumination intensity and 444 nm wavelength (corresponding to a current density of about

---

[9] This measurement order leads to a systematic error due to a degradation of the Cu layers over the course of the electrolysis, which can be estimated using the series of electrolyses under constant illumination in figure 5.22 in section 5.6.4.

5.1 mA/cm^2 with respect to the illuminated area) to 31 min at 14 mW/cm^2 (3.5 mA/cm^2). The latter electrolysis time was also used for the intensities of 12 mW/cm^2 (2.9 mA/cm^2) and 10 mW/cm^2 (2.5 mA/cm^2) to assure a constant time interval between two GC measurements. One can observe a clear dependence of the product distribution on the current density for all structure sizes: With decreasingly negative current density, the weighted product gas concentration of H_2 increases, while the ones of CH_4 and C_2H_4 decrease. The weighted product gas concentration of CO first rises before decreasing again. Although the rate determining step - at least for the route to CH_4 on Cu - is claimed to be already the first electron transfer [Kor15], it appears plausible that a higher overpotential reduces a larger share of the adsorbed CO to CH_4: Since there is a certain probability for the CO molecules to desorb before being reduced further and the reaction speed increases with more negative overpotential, this increasing overpotential assists the reduction of CO. For the formation of C_2H_4, the rate-determining step is the dimerization of two adsorbed CO molecules with electron transfer to $OCCO^-$ (cf. figure 2.5), so that it is even more straight-forward that increasing overpotential shifts the product distribution from CO to C_2H_4. These trends qualitatively match the results, which were reported by Hori et al. [Hor89].

At the same time, a decrease in the structure size from 1400 nm to 200 nm reduces the weighted product gas concentrations for CH_4, C_2H_4 and CO by a factor of 2-3, while the one of H_2 increases. This trend is even more pronounced than the one observed for electrolyses on unplated Au structures with variable size (cf. figure 5.13): Also there, the weighted product gas concentration for CO_2 reduction products decreases with decreasing structure size and increasing density of structure edges, while at the same time the H_2 concentration increases.

5.8 Discussion of size-dependent overpotential and product distribution

Summarizing the results of the size series with Au nanostructures (cf. figures 5.11 to 5.13), there is a significant enhancement of cathodic current with Au structure decreasing in size from 1400 nm to 75 nm. According to the product distribution, HER is more enhanced than CO_2RR. Three independent observations - the independence of the purely electrical ("dry") j-U curves from the structure size (cf. figure 5.2), the independence of the observed effect from the type and level of Si doping and the change in product distribution with decreasing structure size - strongly suggest that the observed size effect does not stem from electrical properties of the MIS interface. Additionally, more recent measurements by Johannes Wüllenweber ([Wü18]) showed that this influence of structure size on the electrochemical performance is strongly pH-dependent and also occurs without CO_2, which also points towards a purely electrochemical mechanism related to HER in alkaline environment.

One striking consequence of the size series is that the structures with different diameter strongly differ in the total length of their structure rims. If the LSVs of different Au structures on p-Si are normalized with respect to the total edge length (cf. figure 5.11(b)), the systematic potential shift with size almost disappears. We therefore conclude that the process, which is responsible for the enhancement, has to occur at the rims of the structures.

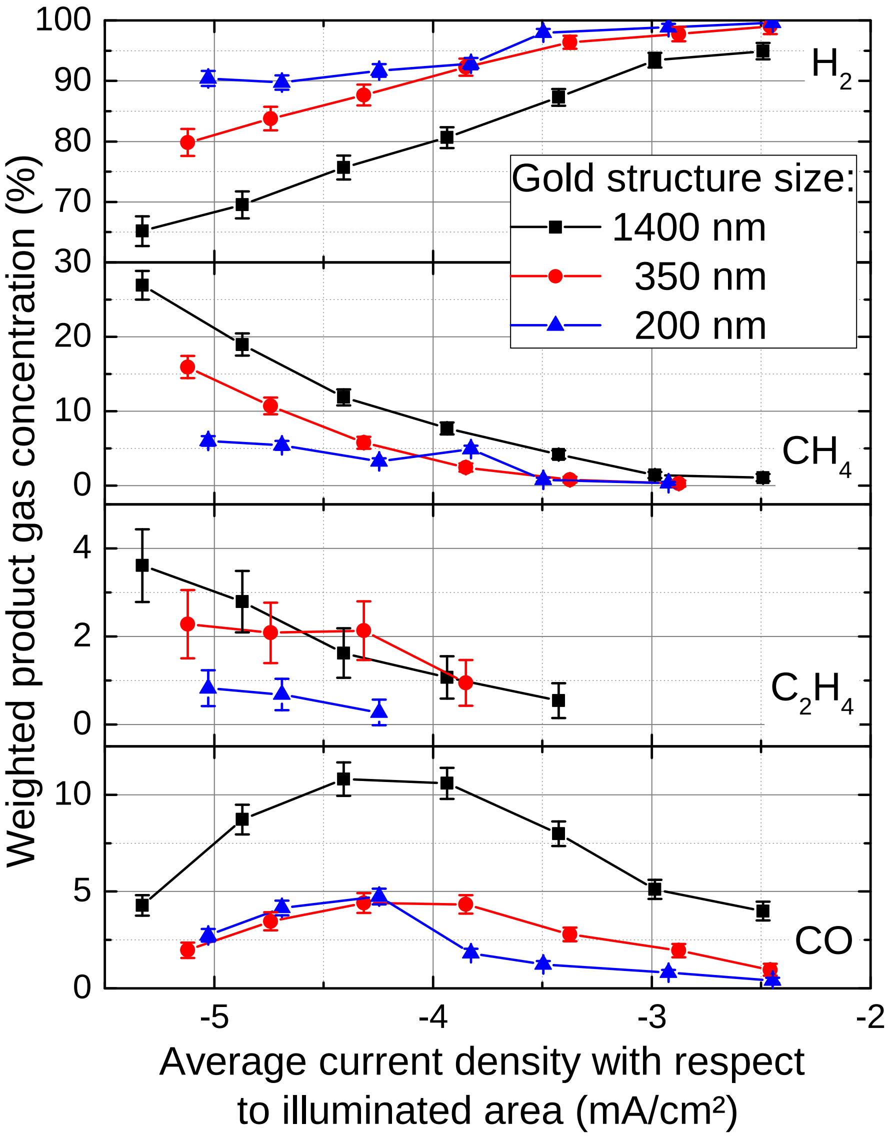

Figure 5.24: Weighted product gas concentrations from electrolysis measurements with Cu-plated Au nanosquares on p-Si with thermal oxide and structure sizes between 1400 nm and 200 nm measured by GC as a function of the current density in the illumination limited regime at -1.76 V vs SHE. Further parameters: Cu layer thickness: 60 MLeq (1400 nm), 40 MLeq (350 nm), 80 MLeq (200 nm); illumination: 444 nm, intensity between 10 mW/cm^2 (31 min electrolysis time) and 21.7 mW/cm^2 (20 min electrolysis time); Electrolyte: 75 mM K_2CO_3 + 100 mM H_3PO_4 saturated with CO_2. Reproduced from [Mai17].

Together with the pH dependence of the current enhancement for the HER observed by Wüllenweber ([Wü18]), a plausible explanation lies in a bifunctional mechanism similar to the one described by Subbaraman, Danilovic and coworkers [Sub11, Dan12]. They found that the HER in alkaline environment on certain metal catalysts is enhanced in the presence of $Ni(OH)_2$ clusters compared to metal surfaces without functionalization, although the activities do not reach the ones of the blank metal electrodes in acidic solution [Dan12]. In the case of an acidic pH, protons can be very easily transferred from H_3O^+ to the surface to form adsorbed H_{ads} (Volmer step, see equation 2.14 for the steps of HER), while the alkaline reaction pathway involves the dissociation of H_2O into H_{ads} and OH^- [Chi98][10]. While typical

---

[10] In both cases, an electron transfer is connected to the H^+ transfer.

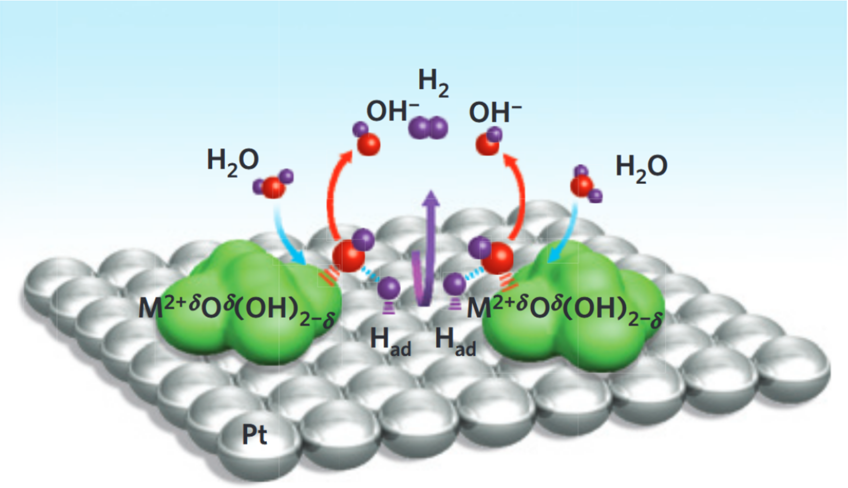

Figure 5.25: Schematic illustrating the mechanism of bifunctional HER in alkaline media on a Pt electrode (gray) functionalized by metal hydroxide clusters (green): H_2O adsorbs on the metal hydroxide particle where it decomposes into OH and H. OH^- is desorbed from there while the H atom moves to the Pt surface where it undergoes a Tafel step towards H_2. Image from [Sub12].

metallic HER catalysts, as e.g. platinum (Pt) have a low barrier for Heyrovsky and Tafel steps (both forming molecular H_2 from H_{ads}), their activation barrier for water dissociation in alkaline pH is larger so that the reaction becomes slower. As an example, the overpotential for a current density of 5 mA/cm^2 shifts from 0.03 V (pH=1) to 0.13 V (pH=13) on Pt surfaces, on Au it increases from 0.33 V to 0.63 V [Dan12]. In contrast, hydroxides are good H_2O dissociation catalysts with a low activity for H_2 formation. The explanation proposed in the mentioned articles was that the combination of both materials could lead to an increased overall performance: First, metal hydroxide clusters enhance the dissociation of H_2O at the boundary between metal and metal hydroxide in contact to the electrolyte. This results in H^* adsorbed to the metal and OH^* adsorbed to the hydroxide cluster. The latter adsorbent is reduced to a OH^- ion by an electron delivered from the metal via tunneling and desorbed, while the H^* atom is dimerized to H_2 (Heyrovsky or Tafel step) on the metal surface, which is highly active for this step (cf. figure 5.25). Since this process is different from H_2 evolution in acidic electrolyte, the explanation is in line with the above mentioned pH dependence.

Although the chemistry of $Ni(OH)_2$ and $Si(OH)_x$ differs significantly, it is possible that they lead to a similar bifunctional mechanism. Another hint for this explanation is that Au is one of the materials with the largest difference in overpotentials between HER in alkaline and acidic media. Such metals show the biggest effect of $Ni(OH)_2$ functionalization. Danilovic et al. found a difference in overpotential of about 300 mV at 5 mA/cm^2 between alkaline and acidic pH and an overpotential decrease of 250 mV at 5 mA/cm^2 due to $Ni(OH)_2$ functionalization of the Au surface [Dan12]. Under the assumption that SiO_2 or $Si(OH)_x$ is also active for water dissociation following a similar mechanism, this is in line with the arguments that the explanation could also be valid for our observations.

The existence of an enhancement of the HER by $Ni(OH)_2$ has been generally accepted, but there are different explanations for it, in particular from Ledezma-Yanez et al.: By comparing the activity of Pt(111) with respect to HER and H adsorption between pH values of 11 and 13, they found that both processes were further slowed down in more alkaline environment

[LY17]. This cannot be solely explained by the mechanism of Subbaraman et al. [Sub11], but rather by a pH-dependent potential of zero free charge (pzfc). At the pzfc, the energetic effort for the reorganization of interfacial water is minimal and therefore, a more alkaline pH, which would shift the pzfc further away from the HER region, could explain the decelerated H adsorption and HER. In contrast, in the presence of $Ni(OH)_2$, the pzfc on the Pt(111) surfaces is shifted closer to the HER equilibrium potential and the reaction speed is increased. Transferred to our system, the presence of SiO_2 would also shift the pzfc on the adjacent Au surfaces.

It is not possible to judge from our experiments, which explanation is the correct one since they both describe the same effect, namely an activity enhancement of the HER in alkaline environment by $Ni(OH)_2$. Therefore, both theories are regarded as possible explanations for the influence of the structure size on the kinetics of the HER/CO_2RR described here.

Besides the bifunctional mechanism and a shift of the pzfc, there exist also various other theories for size-dependent effects, which could influence the performance of photoelectrochemical processes. The following paragraphs compile these possible explanations together with an assessment of their plausibility.

The first one to be considered is the explanation by diffusion limitation. The corresponding theory is based on a depletion of reactants or a pH shift in the vicinity of a surface, on which an electrocatalytic reaction takes place, and the observation that transport of matter is connected to the geometry of the electrode. According to this idea, one would expect a size-dependent transition from three-dimensional diffusion to one-dimensional diffusion resulting in an increasing difference between the different structure sizes with increasingly negative current density. However, in the LSVs from our experiments there is already a potential shift with varying structure size at very small current densities and the curves are virtually parallel (cf. figure 5.11). In addition, there are calculations by Lee et al., which predict that diffusion to microelectrode arrays is mainly dependent on the ratio between structure size and pitch size[Lee01]. This ratio is nearly constant in our arrays (cf. table 3.2) and therefore we consider diffusion as unlikely to be the origin of our size effect.

One further example for an enhanced activity with decreasing structure size in a similar system was given by Esposito et al. [Esp13], who showed an effect analogue to one described above for Pt/SiO_2/Si photoelectrodes. Their system differed from ours in the catalyst, which was Pt instead of Au, in the structure size, which ranged up to 500 µm and in the surrounding oxide layer, which was only 2 nm thick. The explanation given consists of an inversion layer in the Si close to the Si/SiO_2/electrolyte interface combined with H spillover from Pt to the SiO_2 where the adsorbed H atoms undergo a Heyrovsky step towards H_2. The process based on the inversion layer is excluded as the explanation for the size effect in our system because it would be induced by the semiconductor and should already appear in "dry" j-U curves, but not on p^{++}-Si. Due to the much thicker oxide layer on our samples, current flow through the oxide cannot occur in our sample layout. The corresponding idea of reduction steps taking place on the oxide surface is therefore also made very unprobable, although they could happen close to the Au structures by tunneling of electrons. If the direction of H spillover would be inverted (which would be reasonable due to the weaker ability for HER of metals compared to hydroxides, cf. [Dan12]), one would end up with a process corresponding to the bifunctional catalysis described above.

A system even more similar to ours, namely coinage metal particles on p-Si, was examined by Hinogami et al. [Hin98]. They observed a significant enhancement of HER and CO_2RR for particulate compared to continuous metal layers. Due to the self-organized fabrication, the particle sizes varied between some ten and some hundred nm and they did not use Ti and SiO_2 between Si and the particles. Still, they observed a shift of up to 500 mV compared to bulk metal electrodes and continuous metal layers on Si. The explanation of the authors was that the contact area between particles and substrate was not continuous, but consisted of patches of about 5 nm diameter. According to a theoretical band alignment model (cf. [Nak92]), this would result in a change in band bending at the metal/semiconductor contact. Again, this explanation can be excluded for our system since it is dependent on the semiconductor side of the samples and since our structures have a reliably continuous contact area due to the evaporation process.

It was also found by various researchers that there is an interaction between nanoparticles and their substrates, in particular small Au nanoparticles (<10 nm) supported on TiO_2 [Har97, Cos01, Hay13]. The activity of such nanoparticles is strongly dependent on particle size and substrate material. Proposed explanations for this phenomenon are an influence of the substrate on the electronic structure of the particles and the emergence of reaction sites, which are activated by oxygen atoms in the vicinity of the material interface [Cos01, Hay13]. This explanation is not well suitable to our system since structure size and support material are very different, but it cannot be completely excluded.

Another theory for the size effect related to the increasing edge length could be based on a different electric field in the vicinity of the structures. The capacitances of double layers in front of Au and SiO_2 are very different so that the charge distribution and double layer structure at the interfaces between the two materials differ from the situation on a flat Au surface. There is a strong influence of the double layer on electrode kinetics so that this mechanism is another possible source of the observed effect. It is also not excluded that it very differently affects the HER in acidic and alkaline solutions.

Additionally, a common explanation for increasing activity of nanostructures with decreasing size is based on an increased number of active sites [Wie03, Wel06, Sha11, Bru11]. The particles used in the respective studies are commonly much smaller than our nanostructures, which are polycrystalline with a high grain and defect density for all structure sizes (cf. figure 3.4). On all surfaces, the apparent grain size lies at about 15-30 nm. However, it remains to be tested if extraordinarily active undercoordinated sites predominantly occur on the structure edges.

In principle, the complete discussion of different size-dependent effects on Au nanostructures can be equally applied to the Cu-plated case. Also here, there seems to be a mechanism related to the structure edges that accelerates the HER more than the CO_2RR. And again, the most plausible explanations are a bifunctional mechanism at the metal/SiOH interface or a shift in the pzfc. Also the finding that the potential shift with Cu-plated structures (80 mV, cf. figure 5.23) is reduced compared to the one of pristine Au structures (140 - 170 mV, cf. figures 5.11 and 5.12) would be in line with the observations of Subbaraman et al.[Sub12] that the effect of $Ni(OH)_2$ on the activity of Cu is significantly reduced compared to the one on Au.

In the case of Cu-plated structures, it would also be imaginable that there is an influence of structure size on the electrochemical Cu layer growth. However, this hypothesis is made less plausible by the results from section 5.6.3, where the product distribution of electrolyses using Au structures, which were either plated electrochemically or chemically, do not differ significantly (cf. figure 5.21): If there would be an influence of structure size on the Cu layer growth, e.g. by mass transport limitation of Cu^{2+} ions, there should be a much larger difference in the behavior of the differently plated Au structures. Although this does not exclude a size effect on the layer growth, it seems very unprobable, that a size-dependent change of Cu surface morphology is the main reason for the shift in product distribution in figure 5.24.

5.9 Summary and outlook

The main goal of this chapter was to examine the influence of mesoscopic structuring on the electrochemical activity of MIS electrodes, with a focus on the role of structure size. Previous studies, in particular an article by Hinogami et al. already described a strong activity enhancement for the electrochemical CO_2 reduction on coinage metal nanoparticles compared to continuous films [Hin98]. However, the given explanation based on an altered band-bending at nanoscaled contacts under irregular metal nanoparticles motivated the investigation of the characteristics and origin of this size-dependence using well-defined arrays of Au nanodisks and nanosquares on Si.

In contrast to this explanation, we found strong indications against the MIS interface being the main source for the observed impact of structure size: The first hint was that no significant size-induced enhancement was found in the "dry" j-U characteristics of MIS contacts. At the same time, Au structures were more active for the HER and CO_2RR than continuous Au films and their activity further increased with decreasing structure size: The overpotential necessary for a current density of 1 mA/cm² reduced by 140-170 mV for Au structures and by 80 mV for Cu/Au structures, when the structure size was decreased from 1400 nm to 75 nm. The interpretation of an electrochemical process was further supported by the observation that a similar shift was found using Au structures on normally doped and degenerately doped p-Si. Furthermore, we found a shift of the product distribution of CO_2RR to more H_2 and less carbon based products (CH_4, C_2H_4 and CO) both on pure and Cu-plated Au structures with decreasing diameter. This observation can only be explained electrochemically; probably the main part of the activity enhancement is caused by the HER. In addition, the proportionality between the current increase with decreasing structure sizes and the total edge length of the structures made it plausible that the relevant effect occurred at the three-phase boundary between SiO_2, Au or Cu and electrolyte.

These central experiments were supported by a characterization of the illumination limitation occurring for reduction reactions on illuminated p-Si, by an assessment of sample stability and by a comparison between the behavior of electrochemically and chemically deposited Cu layers on Au structures with respect to CO_2 reduction. The latter experiment showed that the Cu deposition method only has a minor impact on the CO_2RR product spectrum.

Concerning the explanation for the observed size effect, two proposed mechanisms for the enhancement of the HER on Pt in the presence of $Ni(OH)_2$ in alkaline environment [Sub11, LY17] could indeed be transferred in order to explain the behavior of our system:

The first one lies in a bifunctional mechanism, which consists of the dissociation of H_2O molecules at the three-phase boundary between electrolyte, Au or Cu and SiO_2 or $Si(OH)_x$, followed by H_2 formation from adsorbed H^* on the metal and reduction of OH^* towards OH^- on the $SiO_2/Si(OH)_x$ surface. The second explanation is made up by a shift of the potential of zero free charge on the metal surface by the adjacent SiO_2 surface. If it shifted the pzfc closer towards potentials, where the HER occurs, the energy for reorganizing the interfacial water network would be reduced, resulting in an increased reaction rate.

Other explanations based on an increased occurrence of active undercoordinated sites close to the edges, metal-substrate interactions or a change in the double layer potential distribution seem less convincing, but cannot be completely excluded.

Therefore, an important goal for a continuation of the project is to verify if the structure edges are indeed the active centers of the samples, e.g. by scanning electrochemical microscopy (SECM). In addition, one has to distinguish between a bifunctional and other mechanisms. The most promising approach for this task would be the deposition and structuring of SiO_2 on a continuous Au substrate. If the activity enhancement of the HER can still be observed there, this could rule out explanations based on undercoordinated sites. A simplified version of this experiment is a deposition of SiO_2 nanoparticles on a Au substrate.

As a next step, one could exchange the SiO_2 (either between Au nanodisks on Si or as SiO_2 structures on Au) by a different insulating material, e.g. Si_3N_4 or Al_2O_3, or probe size effects with other metals such as Pt, which can rather easily be integrated into the current sample fabrication process. In addition, it seems to be promising to exchange the electrolyte by unbuffered $KHCO_3$ solution, which is reported to yield a higher CO_2RR selectivity compared to the phosphate buffer solution used here since it leads to a stronger increase in surface pH [Hor89].

In order to achieve a more thorough understanding of the mechanism of the size effect, it can also be rewarding to characterize the reaction kinetics by a study based on rotating disk electrode measurements. A description of a size dependence of the exchange current density would permit further conclusions about the involved processes.

A more ambitious change in sample layout could involve special Cu nanoparticles, which are very selective towards C_2H_4 production and do much less suffer from poisoning of the catalyst surface (as described in [Xie14, Che15a, Kas15]).

Chapter 6

Plasmonic effects in electrochemistry

In recent years, there has been increasing interest in plasmon-ehanced photochemistry [Chr12, Mar13, Kal14a, Kal14b, Lin15, Zha17, Son18] and photoelectrochemistry [War12, Wan12, Zha13, Nal16, Wan17, Wu18]. Most of these studies reported effects based on plasmonic heating [Gov07, Che08, Adl09, Yen09, Wan13, Bor16] and plasmonic sensitization of high-bandgap semiconductors (SCs), where the excitation of localized surface plasmon resonances (LSPRs) with photon energies considerably lower than the energy of the bandgap of the SC enables charge transfer to the SC by hot carrier injection [Spi12, Wan12, Cla14]. Next to these publications, effects of a direct interaction between LSPRs and heterogeneous reactions were reported, more precisely an enhanced electron transfer into adsorbed species, which can stimulate chemical transformations [Chr11, Chr12]. In addition, plasmon-enhanced adsorption of reactants [Sun09] and desorption of products [Hoh88] was proposed.
So far, most publications deal with heterogeneous catalysis, and the influence of LSPRs on electrochemical reactions is much less investigated. All plasmonic effects reported in electrochemical environment either focus on bandgap sensitization [Liu11] or on enhanced electron transfer [Wan17]. Remarkably, the influence of plasmonic heating has only been studied for photochemical systems [Gov07, Che08, Adl09, Yen09, Wan13, Bor16] and not in an electrochemical context, so that already an investigation of plasmonic heating in an electrochemical environment would be interesting. Another conceivable interaction, which could also increase the reaction rate, namely a plasmonic excitation resonant with molecular vibrations of reactants, has not been reported for any system yet.
In this work, we investigated if the latter mechanism could be observed for the CO_2RR on Au structures with suitable plasmonic resonances. There are several reasons why this system is particularly appropriate for the described purpose: First, the CO_2 reduction reaction on Au has a significant activation barrier in the first step, the reduction of CO_2 to adsorbed CO_2^-, which involves a change of configuration of the CO_2 molecule from linear to bent [Kor15]. Thus, it appears likely that the activation barrier is significantly reduced for a molecule in an excited vibrational bending mode. Second, CO_2 shows two excitation modes between 2.7 µm and 2.8 µm, which are combinations of asymmetric stretching with symmetric stretching and bending quanta [Ger95]. Although the absorptivity of these modes is limited, they allow for the use of shorter wavelengths than the pure bending modes between 14 µm and 16 µm, making them more suitable for the coupling to LSPR modes. Both the strength of the plasmonic field enhancement and the number of edges with enhanced electric fields decreases with increasing structure size (by simply having less structures on the same surface area). Furthermore, when using a D_2O-based instead of a H_2O-based electrolyte, absorption in the wavelength range of the combination modes by the electrolyte - and therefore the influence of electrolyte heating - is considerably suppressed, although it prohibits the use of conven-

tional buffers with a high proton content. In addition, the LO-NIL fabrication of our structures allows the resulting LSP resonances to be tuned into the mid-IR, in contrast to using nanoparticles or substrates with lower refractive index, which are limited to much shorter wavelengths. Third, the electrochemical CO_2RR in aqueous electrolytes is always accompanied by the HER. On Au, CO and H_2 are the only products that occur in significant amounts. Hence, a first indication for a possible change in selectivity can be obtained without having to deal with the quantitative analysis of both liquid and gaseous CO_2 reduction products. In view of application, the selectivity issues of the electrochemical CO_2RR would make it rewarding if one particular reaction pathway could be selectively enhanced.

Before discussing possible interactions between LSPRs and electrochemical reactions, this chapter starts with simulations (cf. section 6.1) and the characterization of plasmonic resonances in Au nanostructures on Si (cf. section 6.2). Especially their resonance wavelength, but also their intensity depend very strongly on nanostructure geometry, the nature of the metal/insulator/semiconductor interface and the dielectric surrounding. The influence of these parameters is studied by numerical simulations and optical spectroscopy. In section 6.3, it is shown that these resonances can also be found via the wavelength-dependence of the current density in illumination-limited photoelectrochemical experiments. The most important part of this chapter is an examination of infrared LSPRs resonant with molecular vibrations of CO_2 with a particular focus on the impact of such vibrations on the electrochemical performance of the CO_2RR (cf. section 6.4). Since the excitation of LSPRs by illumination is connected to a temperature increase, this also requires to consider the role of temperature, in particular in the context of plasmonic heating. This is done by an extensive discussion of the time-dependent heat transport in the system, supported by analytical and numerical modeling (cf. section 6.5). A short conclusion (section 6.6) completes this chapter.

6.1 Simulations of the electric field

The most common approach towards the analysis of plasmonic resonances is a simulation and visualization of the electric field, which evolves around the oscillating electron ensemble within a metal nanostructure coupled to an electromagnetic field, making up a LSPR. In principle, LSPRs on metal nanostructures under illumination are described by simultaneously solving the Maxwell equations in all points in space and especially at the interfaces between a metal nanostructure and its dielectric surrounding. The most common implementation of this problem is realized by finite difference time-domain (FDTD) simulations on a 3D grid containing one nanostructure (see section 3.7 for details of the simulation model). These simulations were used to confirm that the experimentally measured plasmonic resonances of our structures are in line with theory, to predict suitable dimensions of structures tuned to certain resonances and to estimate the actual field enhancement close to the structures.

One example for the result of such a simulation, a horizontal 2D cut through a 3D simulation volume showing the absolute value of the relative field enhancement[1] around a 420 nm Au nanosquare on Ti/SiO_2/Si illuminated with light of 2.8 µm wavelength, is shown in figure 6.1.

---

[1] The field enhancement is the ratio between the actual electric field strength at the respective position and the one of the incoming plane wave. This plane wave models a constant illumination.

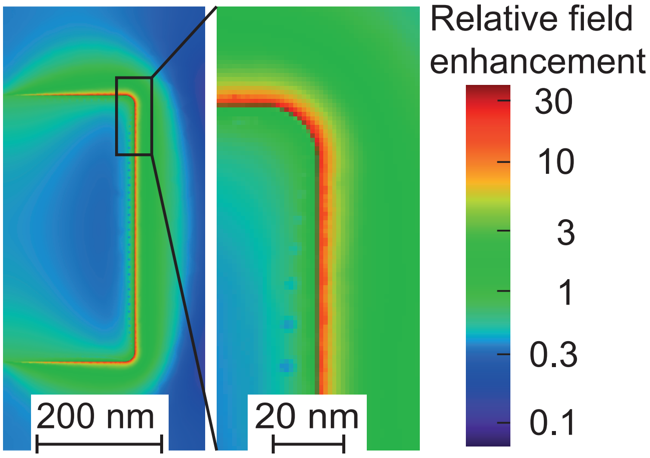

Figure 6.1: Absolute value of the relative field enhancement in and around a 420 nm large Au structure supported on Si under illumination with light of 2.8 µm wavelength. The cut is located within the Au structure, 0.2 nm above its lower boundary (simulation with COMSOL by Robin Nagel).

The position of this cut is within the Au, 0.2 nm above its lower boundary. Due to the symmetric geometry, only half of the simulated area is depicted. It is very typical that the maximal field enhancement is found around the edges of the structure where it reaches a value of 30, corresponding to an intensity enhancement factor of about 1000. Inside the Au, the field is actually reduced due to the electrical conductivity of the Au structure.
By evaluating the reflected, absorbed and transmitted intensity as a function of the illumination wavelength, one can obtain reflectivity, absorptivity and transmittivity spectra. In the following (section 6.2), such simulated reflection spectra are compared to the experimental data from various series of samples with varying diameters, thicknesses and interfaces.

6.2 Optical characterization

In order to study the interaction between LSPRs and molecular vibrations, it is necessary to tune the resonance wavelength of the LSPRs to be resonant with the molecular vibration mode. It is known that many geometrical and dielectric parameters of noble metal nanostructures influence their plasmonic behavior (cf. section 2.3.1). Since the LO-NIL process allows for an adjustment of thickness and diameter of the resulting Au structures, it can be used to tune the plasmonic resonance towards a wavelength, which is desirable in certain experiments, e.g. a resonance with molecular vibrations of CO_2. To verify this tunability, diameter and thickness of the nanostructures were varied in two series of measurements. All samples were produced by LO-NIL using Si with 1-2 nm plasma oxide. A Ti adhesion layer of 3 nm thickness was introduced beneath all Au structures. In order to cover the necessary spectral range using Si, which is not transparent in the visible range, their resonances were measured in the reflectivity mode of the UV-Vis-NIR spectrometer. The spectra were normalized relative to the reflectivity of Si without nanostructures and compared to FDTD simulations; for the simulations, literature values for the reflectivity from Chelikowsky et al. [Che74] were used. The simulations shown in this section were performed by Tianyue Zhang using the software Lumerical FDTD solutions (for details see section 3.7).

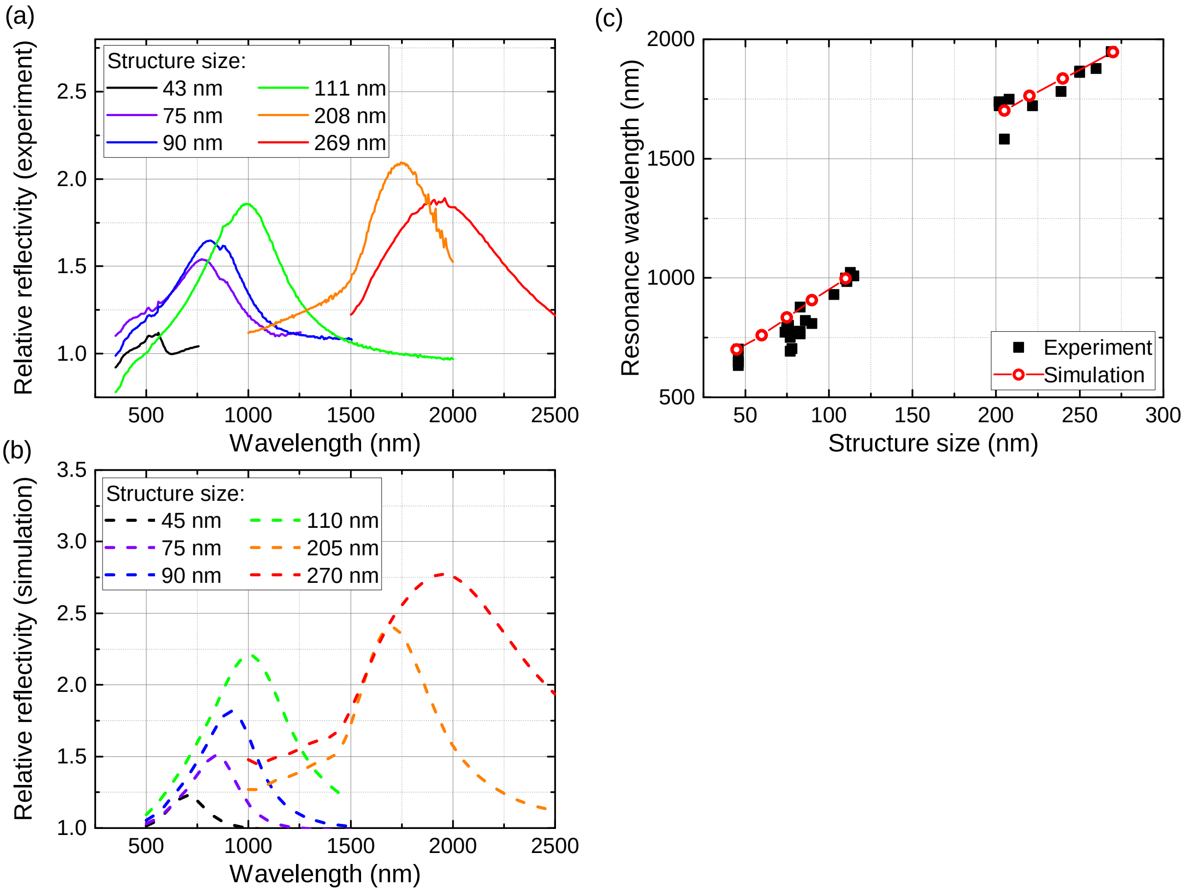

Figure 6.2: Reflectivity spectra of plasmonically active nanostructures with a thickness of 3 nm Ti + 18±2 nm Au on p-Si with 1-2 nm plasma oxide as a function of the feature size. (a) Experimental (samples fabricated by LO-NIL) and (b) simulated reflectivity spectra normalized with respect to a blank Si substrate. (c) Resonance wavelengths as obtained from fitting Lorentz functions to an extended set of experimental (filled squares) and simulated spectra (open circles) vs. structure size [Nag17].

Starting with the influence of the structure diameter, figure 6.2 shows plasmonic reflection spectra of a series of samples, in which the structure size was varied between 45 nm and 270 nm. Up to a size of 130 nm, the structures were nanodisks, while they were nanosquares with rounded edges for the larger sizes. Their periodicity was 90 nm for the 45 nm structures, 150 nm for the structures between 75 nm and 130 nm and 430 nm for the nanosquares with sizes between 200 nm and 270 nm. Most striking is the clear redshift with increasing structure diameter both in experiments and simulations (cf. figure 6.2). This is in line with previous works where both an increasing aspect ratio (here defined as diameter/thickness) [Lee06, Lan06, Zor11] and increasing total size [Moc02] led to a redshift. Still, there are two differences between simulations and experiments: The peak intensity in the experiments was significantly smaller than in the simulations, which can be explained by the influence of measurement geometry on direct reflection and scattering of the incoming light: In the simulations, light reflected under arbitrary angles was considered, while the UV-Vis-NIR spectrometer only measured direct reflection. In addition, there was a systematic blueshift of the experimental data points compared to the simulations. An explanation for this was given by Rodríguez-Cantó et al. who examined similar structures and observed a comparable blueshift

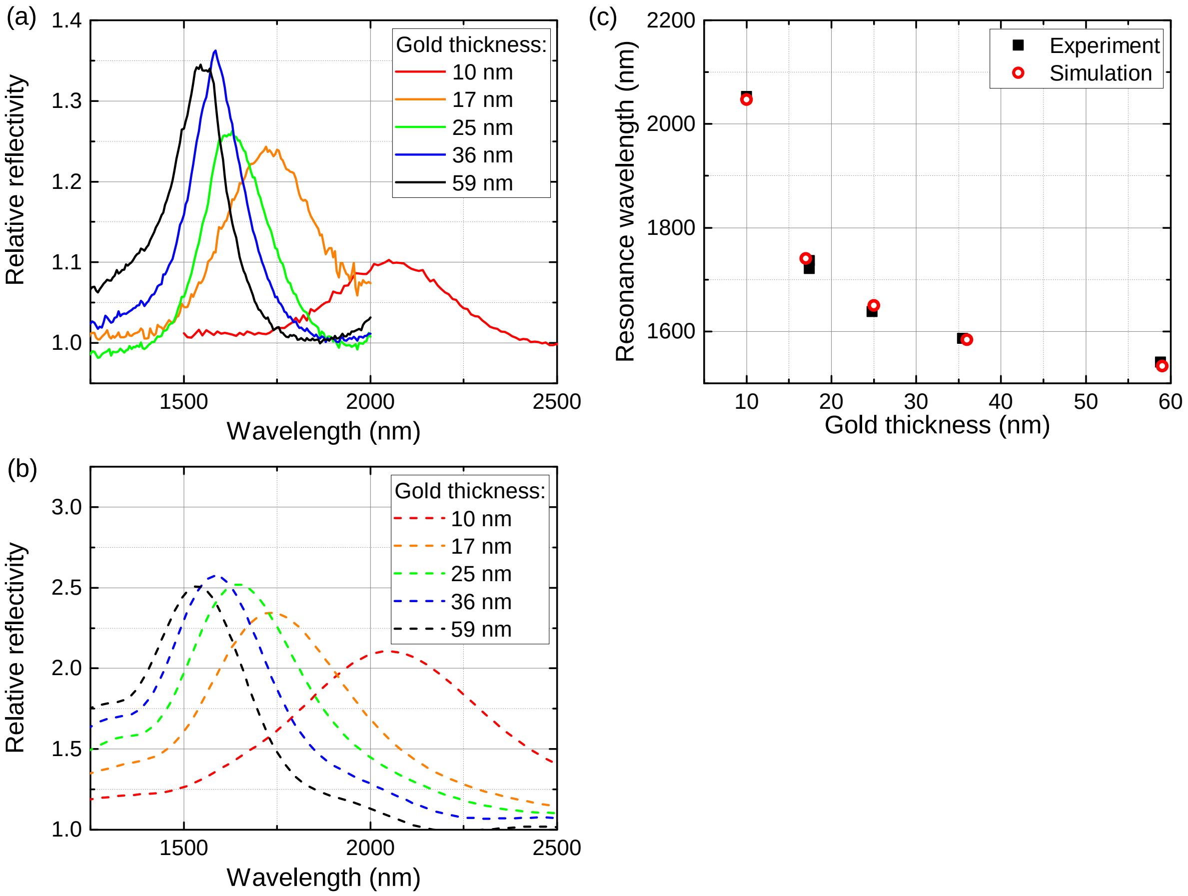

Figure 6.3: Reflectivity spectra of plasmonically active Au nanosquares with a feature size of 200± 4 nm and variable Au thickness on p-Si with 1-2 nm plasma oxide. (a) Experimental (samples fabricated by LO-NIL) and (b) simulated reflectivity spectra normalized with respect to a blank Si substrate for varying Au thickness. (c) Resonance wavelengths as obtained from fitting Lorentz functions to the experimental (filled squares) and simulated spectra (open circles) vs. size of the structures showing identical behavior. All samples contained a 3 nm Ti layer between Au and substrate [Nag17].

[RC11]. They claimed that this would come from an imperfect structure shape with rounded edges, which would also apply to our structures. Although the curvature of the nanosquare edges was already considered in the simulation geometry, the top edges of the structures were still rounded in the experiments and sharp in the simulations. This explanation would also elucidate why this difference increased with decreasing structure size. Other reasons could be a limited reproducibility in the fabrication process, which would be responsible for single values with a too low resonance wavelength, e.g. at 204 nm in figure 6.2(c), or that the SiO_2 layer is slightly underestimated by the value of 1 nm in the simulations.
Another possibility to change the aspect ratio is a variation of the Au layer thickness, which was done for a set of 200 nm nanosquares (cf. figure 6.3). Just as before, an increasing aspect ratio, here caused by a reduction of Au layer thickness, led to a redshift. In this series, the agreement between experiments and simulations was almost ideal.

Even more interesting is the impact of the metal/substrate interface on the optical properties. In the literature, the presence of a Ti adhesion layer is reported to cause so-called plasmon damping [Aou09, Hab12, Sie13], a reduction of the plasmonic resonance and scat-

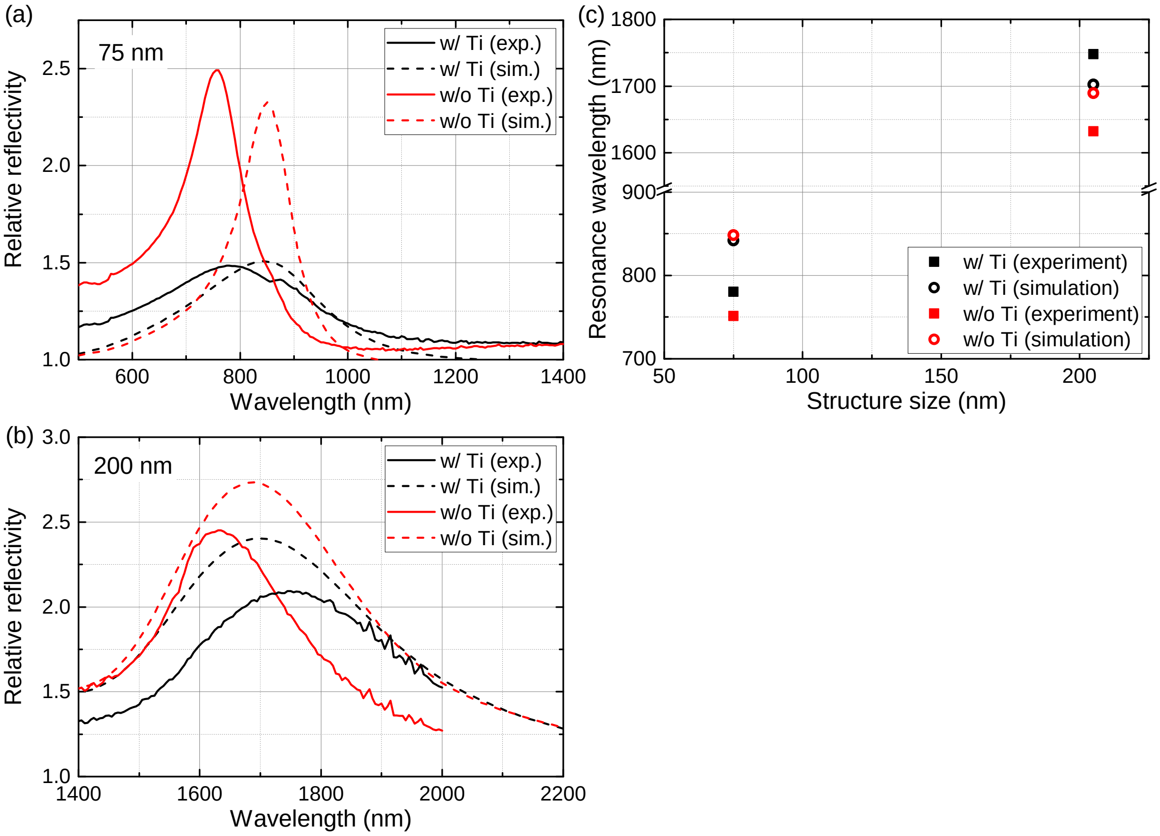

Figure 6.4: Reflectivity spectra of the plasmonic resonance peaks of nanostructures fabricated by LO-NIL on p-Si with 1-2 nm plasma oxide with feature sizes of (a) 75±3 nm and (b) 200±4 nm in comparison to simulated reflectivity spectra. The thickness of the metal structures with Ti adhesion layer is 3 nm Ti + 18±2 nm Au, for the structures without Ti it is 21±2 nm Au. For each structure size, experimental (line) and simulated (dashed) spectra for structures with and without Ti are presented. (c) Resonance wavelengths as obtained from fitting Lorentz functions to the experimental (filled squares) and simulated spectra (open circles) with and without Ti. While the resonance wavelength was only slightly shifted by the Ti layer, the intensity of the resonance was significantly reduced. The reflectivities were normalized relative to a blank Si substrate [Nag17].

tering. In our experiments and simulations, we compared 75 nm and 200 nm structures with either 3 nm Ti + 18±2 nm Au (black lines in figure 6.4) or 21±2 nm Au thickness (red lines in figure 6.4). For all datasets, we could observe plasmon damping in the presence of Ti, but we observed a blueshift of the resonance upon replacement of the Ti layer in the experiments, especially for the 200 nm samples. This was not reproduced in the simulations. However, it is possible, that the difference in resonance between the experimental spectra with 200 nm structure size was caused by the statistical variation between different 200 nm samples, as the observed shift has the same size as the variance of the 200 nm data points in figure 6.2. Here, it only gives the impression of a large systematic shift because it is shown in a more narrow spectral range. The lower effect of plasmon damping between the 200 nm curves is probably due to an overall high reflectivity, which approaches total reflection for the measurements without Ti and thus reduces the measurable difference.

The behavior of the metal/insulator/semiconductor interface is not only influenced by its material composition, but also by the fabrication method of the structures. Even for identi-

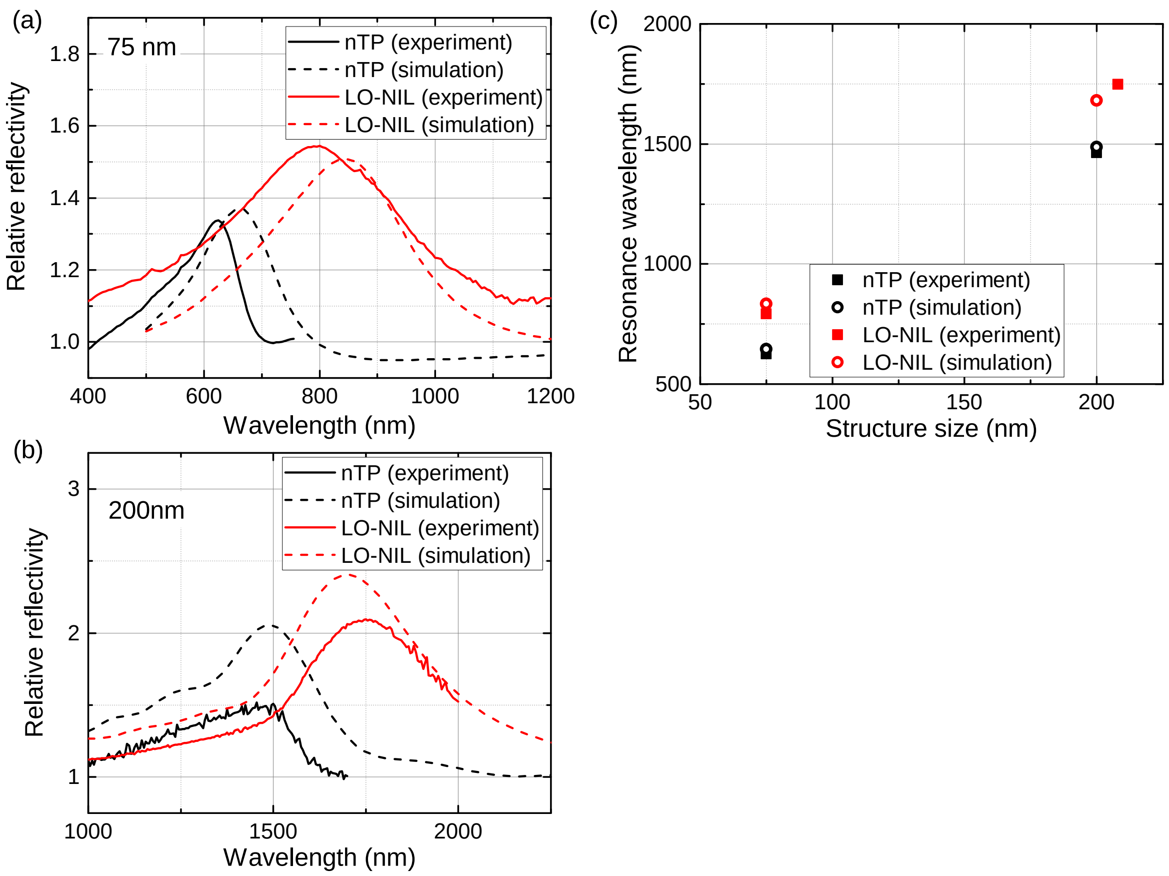

Figure 6.5: Reflectivity spectra of the plasmonic resonance peaks of Au nanostructures fabricated by nTP and LO-NIL with feature sizes of (a) 75±3 nm and (b) 200±4 nm and a thickness of 3 nm Ti + 18±2 nm Au on p-Si with 1-2 nm plasma oxide. The reflectivities were normalized relative to a blank Si substrate. For each structure size, experimental (straight line) and simulated spectra (dashed) for both fabrication methods are shown. While the simulations depicted as "LO-NIL" were calculated using ideal values, an air layer of 2 nm thickness between Ti and SiO_2 was introduced for the "nTP" simulations. (c) Resonance wavelengths as obtained from fitting Lorentz functions to the experimental (filled squares) and simulated spectra (open circles) of the nTP samples as well as for the LO-NIL samples [Nag17].

cal geometrical parameters, nTP structures are significantly blueshifted compared to LO-NIL samples (cf. figure 6.5). In order to test the hypothesis of voids (which was presented in section 5.1) with typical sizes of 2-5 nm^2 at the metal-semiconductor interface of the nTP structures, a flat air layer of 2 nm thickness was introduced between Ti and SiO_2 in the simulations for simplicity reasons. In figure 6.5, one can see that this simple modification already led to a reasonable prediction of the experimental results.

In order to distinguish between effects of roughness and Ti oxidation, samples made by both fabrication methods, each with and without Ti layer, were compared (cf. figure 6.6). Also without a Ti layer under the Au structures, and thus without the possibility that Ti oxidizes, a significant shift between LO-NIL and nTP samples was found.

The last important parameter studied was the influence of the dielectric environment. Here, we examined the consequence of a change of the substrate material to glass, which has a sig-

---

[2] estimated from the RMS value of the surface roughness on the front side of the structures

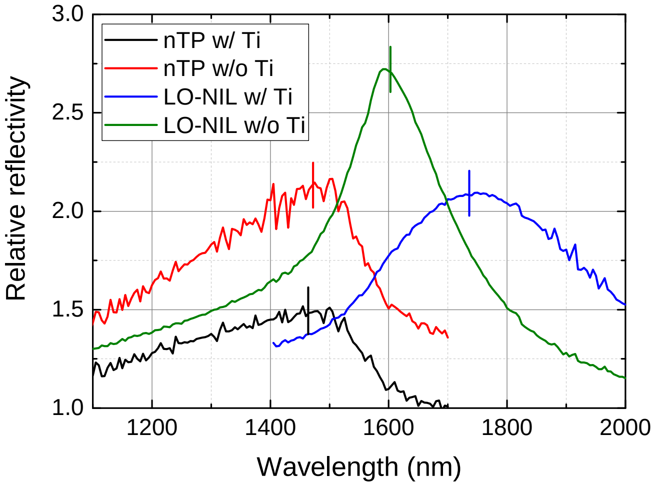

Figure 6.6: Experimental reflectivity spectra of the plasmonic resonance peaks of 200 nm nanostructures on p-Si with 1-2 nm plasma oxide fabricated by nTP or LO-NIL, respectively, with and without a Ti adhesion layer. In both cases the nTP resonance peak is blueshifted compared to the LO-NIL one [Nag17].

nificantly lower dielectric constant ($\epsilon \approx 2.25$) than Si ($\epsilon \approx 15.5$) (at an exemplary wavelength of 600 nm) [Gre08]. Little surprisingly, the resulting spectra were significantly blueshifted (cf. figure 6.7). Also the differences between nTP and LO-NIL samples reduce from 21% (75 nm structures) and 16% (200 nm structures) to 9% and 10%, respectively, by changing the substrate from Si to glass. This is consistent with the explanation based on air-filled voids between structures and substrates since the dielectric constant of air (ϵ=1) is much closer to the value of glass so that the impact of voids on glass is less pronounced than on Si.

For the Si-based samples carrying Au structures with near infrared (NIR) resonances, which are examined in section 6.4, it is possible to measure in transmission mode as Si is transparent around the resonances (cf. also section 2.1.1). In these spectra, plasmonic resonances can be identified as pronounced minima. For the measurement of the following spectra, the samples were wetted with the same D_2O-based electrolyte as in the electrochemical experiments below and then covered by a thin cover glass slide. Thus, the influence of the dielectric environment on the plasmonic resonances was considered and the resonance was supposed to be identical to the one in the electrochemical experiments. All of these spectra were normalized with respect to blank Si with electrolyte and glass cover slide and are shown in figure 6.8(a) for samples with nanosquares of 260 nm and 420 nm size. As explained in more detail in section 6.4, these samples sizes induced plasmonic resonances at 2.0 µm and 2.8 µm in aqueous electrolytes. The 420 nm sample with 2.8 µm resonance was chosen in order to probe interactions between LSPRs and two vibrational combination modes of CO_2 lying between 2.7 µm and 2.8 µm (yellow area in figure 6.8(a) [Ger95]), the 260 nm sample with 2.0 µm resonance was used to cross-check the influence of this vibrational mode. In the electrochemical experiments of section 6.4, these samples were illuminated by directing the light of a halogen lamp through bandpass filters with central wavelengths of 2.0 µm and 2.8 µm (for details of the optical setup see section 3.3.3), the transmission spectra of which are also shown in figure 6.8(a). The structures used were optimized to fit to the transmission maxima of these bandpass filters at 2.0 µm and 2.8 µm, but after a series of electrolysis measurements,

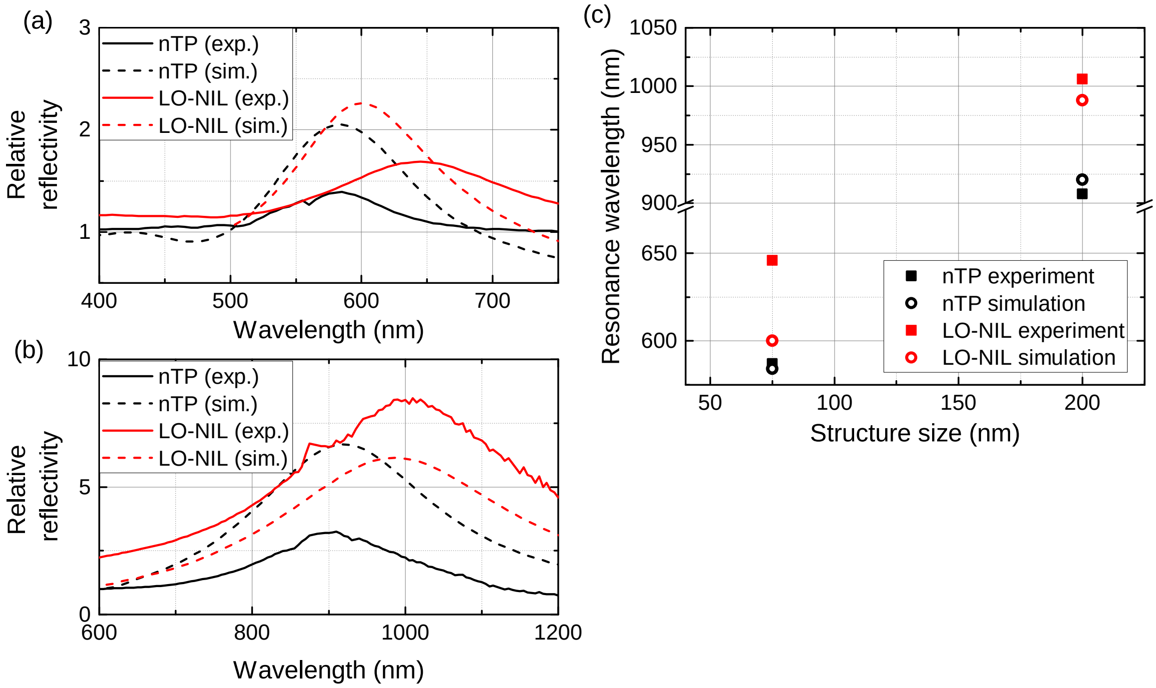

Figure 6.7: Experimental and simulated reflectivity spectra of the plasmonic resonance peaks of nanostructures with a thickness of 3 nm Ti + 18±2 nm Au and a feature sizes of (a) 75±3 nm and (b) 200 nm fabricated by nTP and LO-NIL on glass. While the simulations depicted as "LO-NIL" were calculated using ideal values, an air layer of 2 nm thickness between Ti and SiO_2 was introduced for the "nTP" simulations. (c) Resonance wavelengths as obtained from fitting Lorentz functions to the experimental (black filled squares) and simulated (black open circles) spectra of the nTP samples as well as to the experimental (red filled squares) and simulated spectra (red open circles) of the LO-NIL samples [Nag17].

the actual resonances were distinctly blueshifted to about 1.8 µm and 2.6 µm wavelength. To avoid contaminations of the samples inside the spectrometer, the "wetted" spectra in figure 6.8(a) were only recorded after the electrochemical measurements. However, a spot test with a 420 nm sample before and after electrolysis measurements (figure 6.8(b)) showed a significant blueshift from 2.78 µm to 2.69 µm (determined by the positions of Lorentz peak fits to these spectra). This was attributed to sample degradation at the structure edges under electrolysis conditions (cf. also the SEM image in figure 5.8).

6.2.1 Estimation of errors

For the UV-Vis-NIR spectra shown above the following deviations are estimated: The structure dimensions vary about 2 nm in thickness resulting in a relative shift of the resonance of about 2% for typical thickness values and about 5 nm in diameter leading to a relative shift in the resonance of 3% for the smallest and 1% for the largest structures. The main error in the reflectivity spectra is a deviation in the intensity of about 5% resulting from a sample tilt (and a variable intensity offset of up to 10% in figure 6.8) while the wavelength accuracy is estimated to be better than 1%.

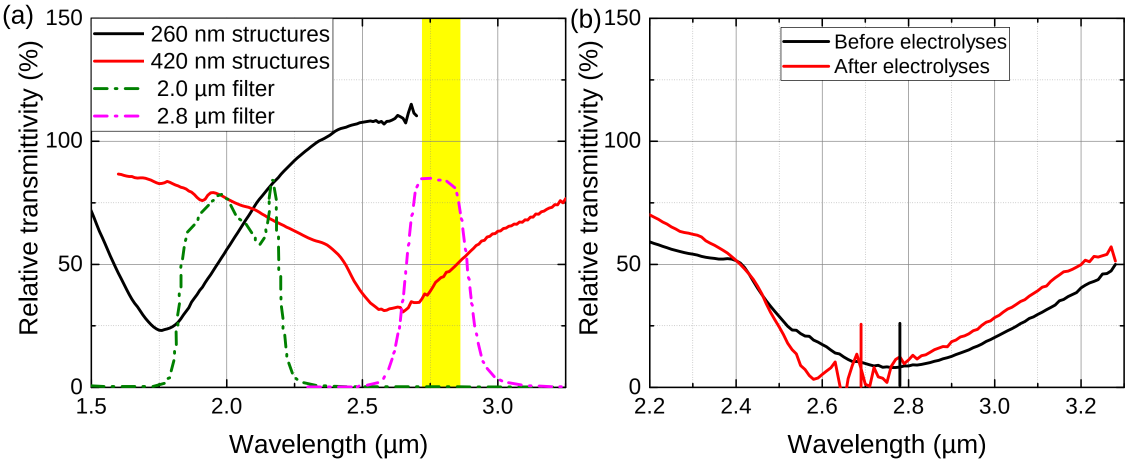

Figure 6.8: (a) NIR transmission spectra of Au structures with sizes of 260 nm and 420 nm on n-Si with 1-2 nm plasma oxide after electrolysis measurements wetted with 50 mM potassium carbonate (K_2CO_3) in D_2O normalized to a wetted Si sample without Au structures. The dashed curves show the transmission spectra of the bandpass filters used in the photoelectrochemical measurements (cf. section 6.3), the yellow marking shows the wavelength region of the vibrational combination modes of CO_2. (b) NIR transmission spectra of dry Au structures with 420 nm size on n-Si with 1-2 nm plasma oxide before (black) and after (red) electrolysis measurements. The vertical lines indicate the maxima of Lorentz peak fits and shifted from 2.78 µm to 2.69 µm.

6.3 Plasmonic resonances in electrochemical experiments

Plasmonic resonances can be observed not only in UV-Vis-NIR spectroscopy, they also occur in photoelectrochemical measurements. An easy and descriptive way to identify them is exploiting the illumination limitation explained in section 5.3. Therefore, one records cyclic voltammograms with illumination limitation just as in figure 5.4. The saturation current density in this limitation regime can be used to calculate the external quantum efficiency (EQE) for a known photon flux. By varying the wavelength while keeping the photon flux constant, one can measure EQE spectra under electrochemical conditions. If the Si substrate is illuminated through the nanostructures, the number of photons absorbed inside the Si absorber is reduced due to scattering by the LSPR and one obtains a minimum of the EQE around the LSPR wavelength. For the spectrum in figure 6.9, CVs of 77 nm structures on p-Si in 0.1 M $KHCO_3$ + 5 mM K_2HPO_4 + 50 mM KH_2PO_4 solution saturated with CO_2 between -1.86 V and -0.16 V vs SHE were recorded at a scan rate of 200 mV/s and under a photon flux of $1 \cdot 10^{-19} \frac{\mathrm{Photons}}{\mathrm{m^2 s}}$. The EQEs determined from the current density at -1.86 V vs SHE yield a spectrum with a minimum around 680 nm wavelength. Note that the minimum is less pronounced than the minima in figure 6.8 because photons, which are scattered by an angle between 0° and 90°, can still be absorbed in Si and therefore contribute to the measured current, while they are not recorded in the spectrometer detector. The minimum here is somewhat blueshifted compared to the data shown in figure 6.2, although immersion in electrolyte should lead to a redshift. It is possible that also here a degradation of the sample after several electrochemical measurements shifted the resonance.

This method also works for Cu-plated structures (plasmonic resonances of core-shell nanostructures are explained e.g. in [Tia07]), shown in figure 6.9 for the same 77 nm sample, which

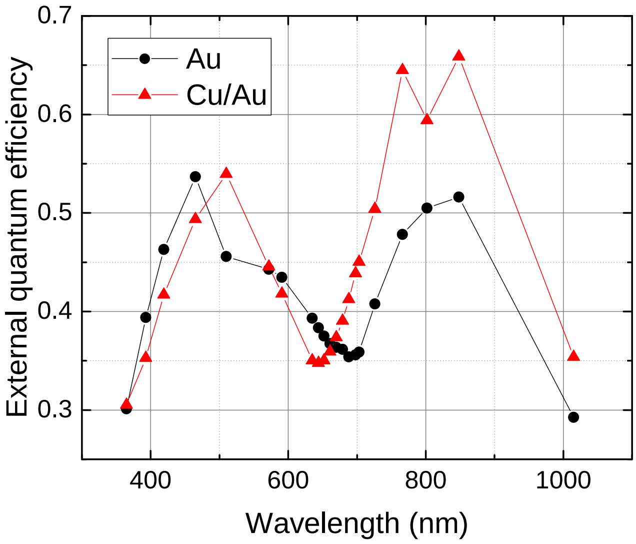

Figure 6.9: External quantum efficiencies determined from the saturation current density in the illumination limited regime using 77 nm Au nanodisks on p-Si with 1-2 nm plasma oxide (black) and the same sample plated with about 7 MLeq of Cu (red). Electrolyte: 0.1 M $KHCO_3$ + 5 mM K_2HPO_4 + 50 mM KH_2PO_4 saturated with CO_2, photon flux: $1 \cdot 10^{-19} \frac{\text{Photons}}{\text{m}^2\text{s}}$. These measurements were performed together with Josef Zimmermann.

was plated in 100 mM K_2SO_4 + 100 µM $CuSO_4$ solution at a potential of -0.01 V vs SHE for 120 s resulting in a coverage of about 7 MLeq. The resonance for this measurement series at about 640 nm was blueshifted compared to the one without Cu. Since the plasmonic resonance wavelengths resulting from Cu and Au particles do not differ too much (cf. [Zem87]), one can assume in first order that a Cu-plated structure would behave similar to a pure Au one with slightly larger dimensions. A slight blueshift could already be explained by a smaller aspect ratio due to the Cu plating. Still, it is possible, that also a continuing sample degradation was the reason for the obseverd shift. Looking at the two spectra in figure 6.9, it is also striking that the Cu-plated structures showed a higher EQE for wavelengths above 700 nm. This can only be partly explained by a tail of the plasmonic peak in the spectrum of the pure Au structures.

6.4 Plasmonic excitation of molecular vibrations and plasmonic heating

The question, if and how LSPRs can influence the performance of electrochemical reactions, is even more interesting than shifts in plasmonic resonance wavelengths. The following section, which deals with this topic, is therefore the heart of the chapter about plasmons. From a scientific point of view, the by far most interesting effect would lie in the resonant excitation of molecular vibrations through LSPRs, which has never been reported before. Since we found that the impact cannot be very large - if it is measurable at all - especially compared to the total reduction current under electrolysis conditions, the experiment was optimized towards a high sensitivity. A drastic improvement was achieved by chopping the light, which in our case comes from a halogen lamp passed through a bandpass filter (cf. section 3.3.3 for experimental details). The resulting current modulations can be measured much more accu-

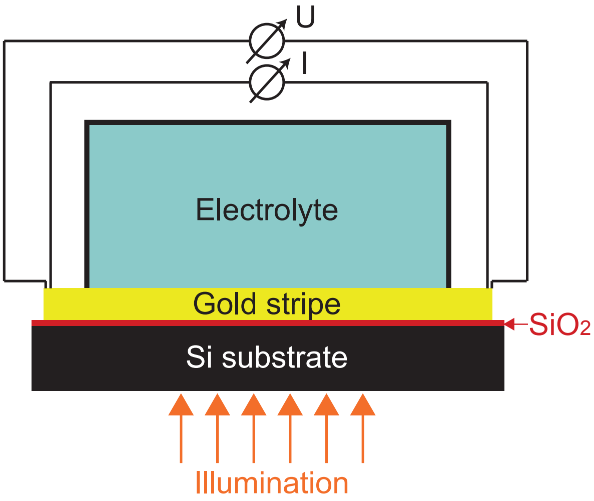

Figure 6.10: Sketch of the measurement geometry of the electrolyte heating measurements using a Au stripe in 4-point wiring configuration (not to scale).

rately than changes in current density or product distribution between two longer electrolysis measurements. In order to test the existence of such a small effect, one not only needs suitable samples and measurement instruments. It is also very important to consider and suppress other consequences of illumination such as the photoeffect or heating as much as possible. Most challenging is the differentiation between different plasmonic mechanisms, which occur under similar conditions, as e.g. plasmonic heating could be expected next to any other plasmonic effects in a system with LSPRs.

6.4.1 Influence of heating and temperature

Before discussing the actual electrochemical experiments in section 6.4.3, the role of heating, in particular of electrolyte heating under illumination, is evaluated in the following. The best way to do this is to build up a setup, which allows for the measurement of the surface temperature in a situation comparable to the later experiments, only without any LSPRs and faradaic reactions.

For a measurement of electrolyte and substrate heating, the temperature-dependent resistance of a Au stripe on Si with an isolating thermal SiO_2 layer between Au and Si is used for temperature measurements because it is well compatible with the sample fabrication process and allows for very sensitive temperature measurements in 4-point wiring configuration as shown in figure 6.10. The Au stripe has a width of 23 µm, a thickness of 100 nm and a length of 11 mm, about 9 mm of which are immersed in electrolyte, and 7 mm are illuminated from the back[3]. At each end of the stripe, quadratic patches of 1 mm^2 are attached and contacted using conductive epoxy and copper wires of 0.1 mm diameter.

Under illumination, the electrolyte in the vicinity of the stripe heats up and transfers heat into the Au stripe. The dependence of the temperature shift δT in the Au stripe can be derived from a change in current, δI, under constant applied potential. For small temperature

---

[3] The measurement method can only measure the resistance of the complete Au wire, of heated and unheated regions together. Therefore the initial temperature values are corrected by a factor of 1.57, which would correspond to an illumination of the complete wire.

variations, it can be linearized as

$$\delta T = \frac{1}{\alpha} \cdot \frac{\delta R}{R} \approx -\frac{1}{0.0034\mathrm{K}^{-1}} \cdot \frac{\delta I}{I} \tag{6.1}$$

with the temperature T, temperature coefficient of resistance α and resistance of the Au stripe R. For a better measurement accuracy, the current through the Au wire was measured with chopped illumination. The obtained data were then Fourier transformed using Welch's method (cf. section 3.8) and the resulting peak-to-peak amplitude was interpreted.

The situation for the Au stripe differs from the one of the nanostructure arrays. In particular, the light transmittivity differs between a 100 nm thick massive stripe and sub-wavelength nanostructures with a thickness below 20 nm. Also the geometry of heat transport, which is discussed in section 6.5.3, is different for these two geometries. Therefore, the resulting temperatures certainly deviate from the ones evolving on arrays of nanostructures, but the relative influence of various parameters can still be studied.

In order to find out, how heating and heat transport depend on electrolyte and illumination, the temperature amplitude under illumination chopped with 0.33 Hz was determined under various experimental conditions: Measurements in a dry cell were contrasted with such which were performed in a cell filled with D_2O- and H_2O-based electrolytes with CO_2 and Ar purging as well as D_2O and H_2O without salt (leading to 8 different combinations). For each electrolyte, illumination wavelengths of both 2.0 µm and 2.8 µm were used (at an equal intensity of 80 mW/cm²).

The first two points indicated as "dry" in figure 6.11 only showed a tiny amplitude and no significant wavelength dependence. When the cell was filled with electrolyte, the situation was different as the heating generally increased. In addition, it was possible to observe several trends: First, there was a strong dependence on the solvent of the electrolyte: H_2O led to more warming than D_2O for both wavelengths. Second, there was a general trend that the heating at 2.8 µm was stronger than at 2.0 µm. The third difference was found between the 2.8 µm values of as-bought D_2O and D_2O-based electrolyte; the introduction of $K_2CO_3 \cdot 1.5H_2O$ led to an increase in the temperature amplitude. Fourth, there seemed to be barely a difference if CO_2 was dissolved in the electrolyte.

At first sight, it is remarkable that the dry sample was heated much less compared to the case with electrolyte in front of the electrode, although the heat capacity of the dry system was drastically reduced. Consequently, this means that the impact of substrate heating by illumination was very small. This observation is even more striking since the temperature amplitude caused by substrate heating was not decreased due to shadowing by the wide Au stripe as it would be for electrolyte heating. Therefore it is assumed that substrate heating can be neglected for interpretation of the electrochemical measurements.

The trends in the heating of wetted samples permit several conclusions concerning electrolyte heating: From figure 6.12, which shows the wavelength-dependent penetration depths of H_2O and D_2O, one can see that H_2O absorbs much stronger than D_2O in the complete relevant range and that in H_2O there is a factor of 180 difference in absorption between 2.0 µm and 2.8 µm in contrast to D_2O where the penetration depth at 2.0 µm is hardly the double value as at 2.8 µm. Still, there is about 0.1% of H_2O left in the D_2O used and since its absorptivity at 2.8 µm is so dominating, a significant part of the difference in electrolyte

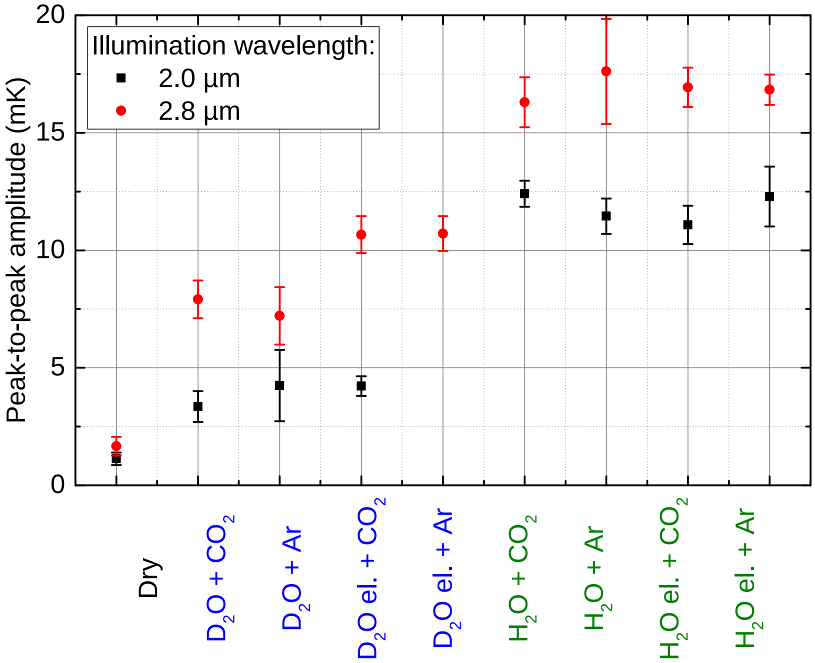

Figure 6.11: Temperature increase in a Au stripe on thermal $SiO_2/n\text{-}Si$ in air ("dry"), D_2O and H_2O, each in pure form and as electrolyte ("el.") with 50 mM K_2CO_3 purged with CO_2 and Ar illuminated with infrared light chopped at a frequency of 0.33 Hz. The black squares are recorded under illumination at 2.0 µm, the red circles at 2.8 µm wavelength. The error bars indicate the standard deviation derived from a set of 4 measurements. Further parameters: four times 4 min measurement time per point; voltage applied to the Au stripe: 650 mV.

heating between the two wavelengths is attributed to this “light water contamination”. From the absorptivity data in figure 6.12, one would expect that the heating of H_2O at 2.8 µm would be at least a factor of 180 higher than all other points, but in the experiment, it was less than a factor of 2. Apparently, the temperature amplitude grew much less than proportionally to the absorptivity. The reason for this dependence probably lay in the geometry of the heat transport, which is visualized below in figure 6.19 and discussed in section 6.5.3.

The difference between D_2O and D_2O-based electrolyte can be explained by the H_2O content of the $K_2CO_3 \cdot 1.5H_2O$ salt. It led to additional 0.15% of H_2O content, which could explain this change. At 2.0 µm, the difference in absorptivity between both solvents was much smaller so that tiny H_2O contents did not have such a large impact. However, it means that H_2O in the electrolyte significantly affected the absorptivity and hence the electrolyte heating.

The negligible influence of CO_2 may sound surprising, but since less than 1 out of 1000 molecules in the electrolyte was CO_2 (the mole fraction is $7.1 \cdot 10^{-4}$ at atmospheric pressure [Car91]) and the molar absorption coefficient of H_2O (30 $\frac{1}{\text{mol cm}}$ [Bay63]) is much larger than the one of CO_2 (1.3 $\frac{1}{\text{mol cm}}$ [Smi86]), it is clear that the impact of CO_2 on the total absorptivity was much smaller than the resolution of the experiment.

Although the measurement of plasmonic heating would be even more interesting than substrate and electrolyte heating, it was not possible to measure it reliably because the Au stripe method did not work properly on Au nanostructures used. Since the stripe was in intimate

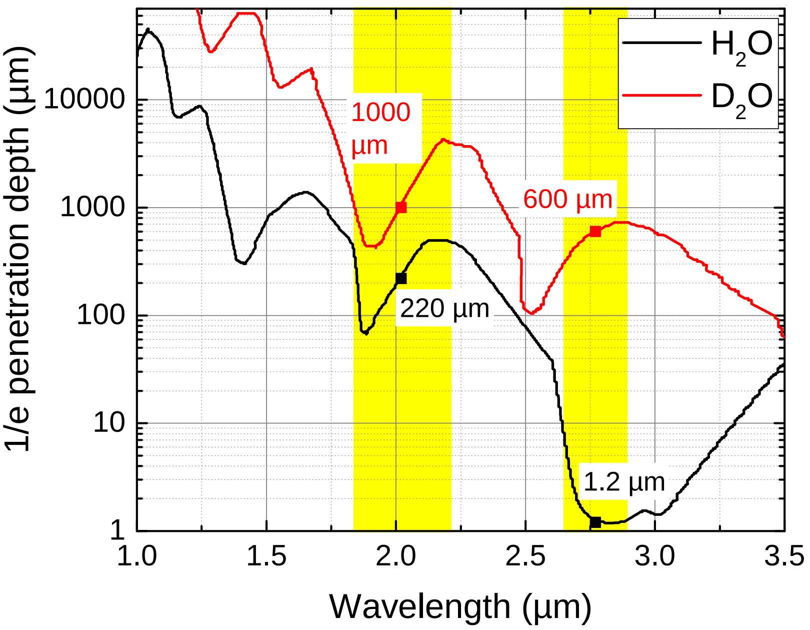

Figure 6.12: 1/e-penetration depth of infrared radiation in H_2O (black) and D_2O (red). The yellow areas indicate the transmission regions of the 2.0 µm and 2.8 µm bandpass filters and the points indicate the penetration depths at the central wavelengths of the bandpass filters, which are described in section 3.3.3. Reproduced from [Bay63].

contact to the nanostructures, which had an ohmic contact to the underlying n-Si[4], it could not be avoided that current flows through the substrate underneath the structures. Since the conductivity of Si increases with temperature, while the one of Au decreases, no quantification of temperature is possible and the plasmonic heating could not be directly measured.

6.4.2 Influence of heat transport on involved timescales

Not only the dependence of surface heating on different electrolyte compositions and illumination wavelengths is important, also the frequency dependence of a modulated heating via illumination can give valuable hints about the typical time constants involved. In the discussion below (cf. section 6.5.3), it is explained that the time constants of electrolyte heating and plasmonic effects differ and that the dependence of the resulting current modulation on the chopping frequency can give valuable information. In order to measure the frequency dependence of electrolyte heating, two frequency series of the temperature amplitude in a Au stripe in H_2O illuminated at 2.0 µm and 2.8 µm were performed. Again, a constant voltage was applied between the ends of the Au stripe and the illumination-induced current modulations were used to calculate the temperature amplitude according to equation 6.1. The corresponding measurements presented in figure 6.13 show that there was a slightly higher amplitude at 2.8 µm, where the absorption coefficient is much higher than at 2.0 µm, over the whole frequency range of the experiment.

The frequency-dependent curves can be quite well fitted with a $C \cdot f^n$ function[5]. This results

---

[4] The use of p-Si, which creates a Schottky contact, was avoided because it shows a pronounced photoeffect in the semiconductor. Modulated reflections of surrounding light by the chopper at the same frequency as the heating modulation could introduce a large error.

[5] Resulting in linear curves on a double-logarithmic scale

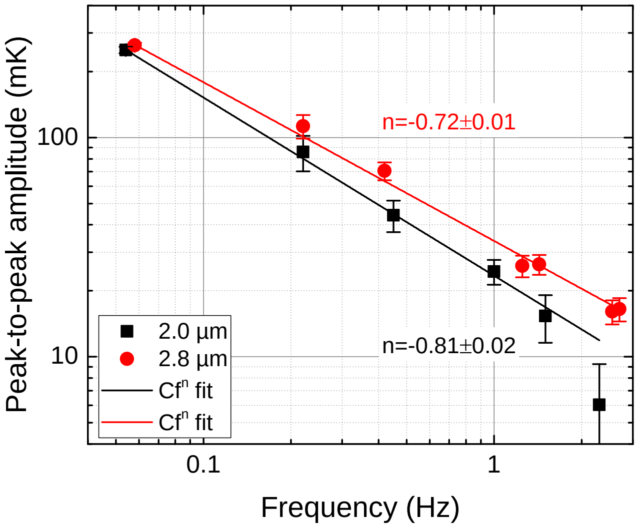

Figure 6.13: Frequency dependence of the electrolyte heating of a Au stripe in H_2O under illumination at 2.0 µm (black) and 2.8 µm (red) illumination with equal intensity. The error bars indicate the error stemming from the finite background level in the Fourier spectra. The higher absolute amplitude compared to figure 6.11 stems from a change in the optical setup between both series. Further parameters: 4 min measurement time per point; voltage applied to the Au stripe: 700 mV (2.0 µm); 675 mV (2.8 µm).

in exponents of $n_{2.0\ \mu m}$ =-0.81±0.02 and $n_{2.8\ \mu m}$ =-0.72±0.01. The different slopes are in line with the different absorptivity at the two illumination wavelengths (cf. also the discussion in section 6.5.3).

6.4.3 Plasmonic effects on the electrochemical performance

In order to probe the existence of an interaction between LSPRs and molecular vibrations, various electrolysis measurements with modulated illumination were performed. This required a method for the distinction between electrolyte heating, plasmonic heating and the plasmonic molecular vibration effect. The first approach for distinguishing these contributions was to perform potentiostatic electrolyses under chopped illumination and then measure the amplitude of the resulting current modulation. Since this experiment was performed in various configurations - in and out of plasmonic resonance, in and out of the resonance with molecular vibrations of CO_2 and with CO_2 and Ar purging - it was possible to draw conclusions about the involved mechanisms.

Such measurements were performed in the course of this work using 260 nm (resonance at 2.0 µm) and 420 nm Au structures (resonance at 2.8 µm) on n-Si with a structured back contact. Current densities of 5.3 to 6.3 mA/cm^2 were obtained in CO_2-saturated 50 mM K_2CO_3 in D_2O under a potential of -1.36 V (420 nm structures, 2.8 µm resonance) respectively -1.56 V (260 nm structures, 2.0 µm resonance) vs SHE for both samples[6]. The samples were each illuminated with chopped light at wavelengths of 2.0 µm and 2.8 µm at a chopping frequency of 3.6 Hz, and each electrolysis of 4 min length was split into 40 s segments, which were Fourier transformed according to Welch's method (cf. section 3.8). Figure 6.14 exemplarily shows the

---

[6] The potential for each sample was chosen such that background current density around 6 mA/cm^2 was achieved and then kept constant over this series. Unfortunately, the samples suffered from degradation under electrolysis conditions so that the current density decreased over a series of measurements. Therefore, the maximum and minimum current density are given for each measurement series.

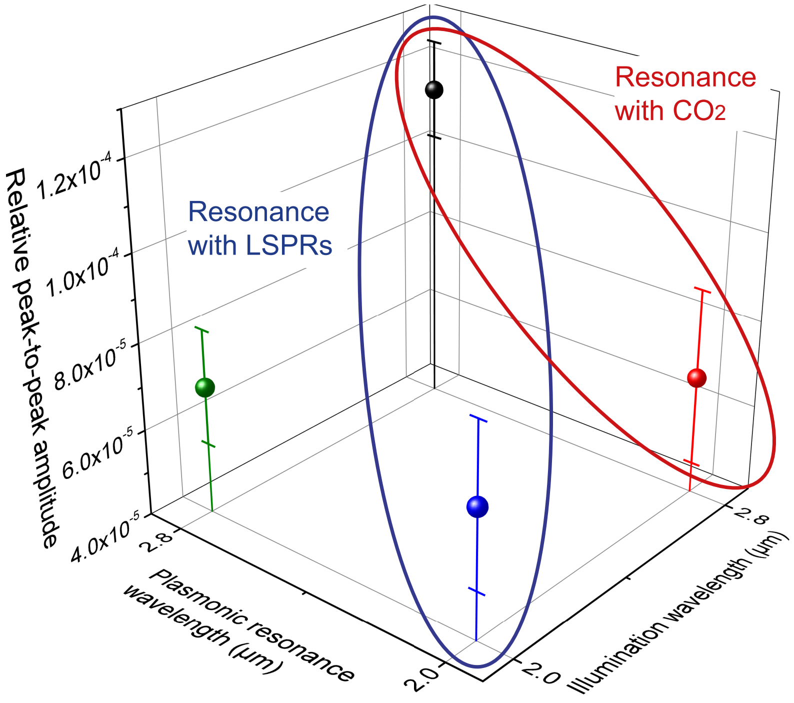

Figure 6.14: Relative peak-to-peak amplitude of the current density variation under illumination with IR radiation of 2.0 µm and 2.8 µm and two Au nanosquare sizes with plasmonic resonances at 2.0 µm (260 nm nanosquares on n-Si with 1-2 nm plasma oxide) and 2.8 µm (420 nm nanosquares on n-Si with 1-2 nm plasma oxide), respectively. The blue ellipse indicates where the wavelengths of illumination and LSPRs are in resonance, the red ellipse shows the resonance between illumination and CO_2. The error bars depict the standard deviation of a set of 8 measurements. Further parameters: chopping frequency: 3.6 Hz; electrolyte: CO_2-saturated 50 mM K_2CO_3 in D_2O; applied voltage: -1.36 V (420 nm structure) resp. -1.56 V (260 nm structure) vs SHE; total current density: between -5.3 and -6.3 mA/cm^2.

relative peak-to-peak amplitudes of the current density variations for a set of four measurements where both illumination and plasmonic resonance wavelengths took values of 2.0 µm and 2.8 µm each. We found similar amplitudes for both excitation wavelengths for the 2.0 µm sample, while the 2.8 µm sample resonantly illuminated at 2.8 µm showed significantly more amplitude than at 2.0 µm illumination as well as both points recorded with the 2.0 µm sample. This wavelength also corresponded to the resonance of a combined molecular vibration mode in CO_2. If only electrolyte heating was present, there should not be a difference in the behavior of the two samples and it seems to be likely that the differences can be attributed to LSPRs.

Still, the data do not yet definitely prove that CO_2 vibrational modes were involved. A careful interpretation needs to consider further aspects, in particular that the electrolyte heating is much stronger at 2.8 µm than at 2.0 µm as shown in figure 6.11. In addition, electrolyte heating was not only influenced by the wavelength-dependent absorptivity of the electrolyte, but it was also reduced by the scattering of light at plasmonic resonances. This means that for identical illumination intensity, the power actually available for electrolyte heating was even reduced under plasmonically resonant illumination. For the 2.0 µm sample, the amplitude of the off-resonance experiment (at 2.8 µm illumination) should consequently be even more increased compared to the amplitude at the resonance at 2.0 µm than without LSPRs present.

Therefore, it would be wrong to exclude plasmonic heating from the apparently equal amplitudes of the two illumination wavelengths on the 2.0 µm sample. Without any plasmonic effect under illumination with 2.0 µm wavelength, one would not expect this equality at identical illumination intensity. This is already a hint that a plasmonic effect occurred for both samples, when they were resonantly illuminated.

A simple correction of the intensity reduction by plasmonic scattering would require to determine the absolute value of light transmission through the Au structures from other measurements, e.g. UV-Vis-NIR spectra (cf. figure 6.8). However, this is not possible since also photons scattered by angles below 90° contribute to electrolyte heating, while they are not considered in UV-Vis-NIR spectroscopy, which only measures direct transmission. All in all, this means that a mere comparison of amplitudes under various illumination and electrolyte conditions was not sufficient to determine the origin of the increased modulation amplitude of the 2.8 µm sample under resonant illumination with 2.8 µm wavelength.

A much more reliable method was to consider the frequency dependence of the amplitudes under different illumination wavelengths. A promising approach was to perform a complete matrix of 12 measurement series based on 3 different samples (1400 nm nanosquares with plasmonic resonance far in the mid-IR[7], 420 nm nanosquares with plasmonic resonance at 2.8 µm resulting in a double resonance including molecular vibrations of CO_2 and 260 nm nanosquares with plasmonic resonance at 2.0 µm), 2 different electrolytes (50 mM K_2CO_3 solution saturated with CO_2 and 50 mM H_2SO_4 solution saturated with Ar, both based on D_2O) and 2 different excitation wavelengths (2.0 µm and 2.8 µm). Just as above, potentiostatic electrolyses of 4 min length under chopped IR illumination were performed and the resulting current transients were Fourier transformed using Welch's method. One can see distinctive differences in the frequency dependence of measurement series under different conditions. In the following, the exponent n of a simple $C \cdot f^n$ fit was used as a measure for the influence of plasmonic and electrolyte heating.

The first set of measurement series to be discussed is the one obtained with the 1400 nm structures. As explained above, their plasmonic resonance was far away from the illumination wavelengths employed. Without scattering of light by LSPRs, we further assumed that there were only quantitative differences between the light absorption at 2.0 µm and 2.8 µm wavelength and that it would be possible to compensate the different electrolyte heating by increasing the illumination intensity at 2.0 µm accordingly. In a measurement with equal intensity (not shown), the current modulation at 2.0 µm wavelength was decreased by a factor of 2.3 compared to 2.8 µm illumination. Therefore, the intensity for the 2.0 µm measurement was increased to 180 mW/cm^2, while it was kept at 80 mW/cm^2 for the 2.8 µm measurement. As shown in figure 6.15, the resulting frequency series both in H_2SO_4 (figure 6.15(a)) and K_2CO_3 (figure 6.15(b)) showed exponents between n=-0.77 and n=-0.98. It would be reasonable that the curves with 2.0 µm illumination are slightly steeper because of the lower absorptivity of the electrolyte (cf. also section 6.5.3). However, this trend was only visible for the measurements in K_2CO_3, while the H_2SO_4 curves showed a flatter slope. A possible

---

[7] The exact value of this resonance was not be determined, as it lies far outside the spectral range of the spectrometer used ending at 3.3 µm. A simple extrapolation of the values from figure 6.2 would lead to a resonance at about 7-9 µm. It is therefore assumed, that no LSPRs were excited on this sample.

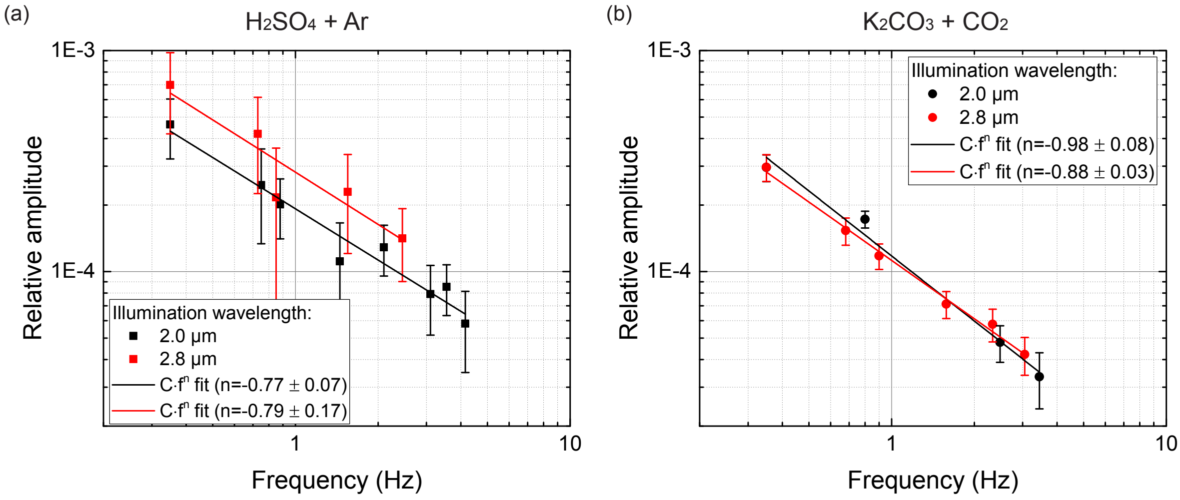

Figure 6.15: Relative peak-to-peak amplitudes of the current density variation of 1400 nm nanosquares on n-Si with 1-2 nm plasma oxide (plasmonic resonance out of range) under illumination with IR radiation of 2.0 µm at an intensity of 180 mW/cm^2 and 2.8 µm wavelength at an intensity of 80 mW/cm^2 as a function of the chopping frequency in (a) Ar-saturated 50 mM H_2SO_4 in D_2O and (b) CO_2-saturated 50 mM K_2CO_3 in D_2O. The error bars were calculated from the background in the Fourier spectra. Further experimental conditions: applied voltage: -0.635 V (H_2SO_4) resp. -1.46 V (K_2CO_3) vs SHE; total current density: -3.0 to -7.2 mA/cm^2 (H_2SO_4) resp. -9.3 to -12.0 mA/cm^2 (K_2CO_3). The intensity at 2.0 µm was increased by a factor of 2.3 compared to the one at 2.8 µm.

explanation for at least a part of this difference could lie in the larger error[8] of the H_2SO_4 dataset in figure 6.15(a), which could also influence the fitted slope. In addition, there was a strong decrease in sample activity in all H_2SO_4 datasets - possibly due to contaminations (cf. discussion of errors in section 6.2.1). This activity decrease could indeed affect the fitted exponents, although its influence was mitigated by the non-monotonic ordering of the chopping frequencies employed[9]. Still, on the one hand, the resulting decreasing current density led to an unfavorable signal-to-noise ratio, on the other hand, the 2.8 µm data set in H_2SO_4 was recorded under very low current densities and therefore its relative amplitudes were increased (cf. also section 6.4.4). In comparison, the K_2CO_3 measurements were quite stable and here the curves lay well upon each other as one would expect it if the electrolyte absorptivity was compensated by the illumination intensity.

This situation changed when plasmonically active samples were measured. At a resonance wavelength of 2.8 µm (420 nm nanosquares), one could expect plasmonic heating and the resonant excitation of molecular vibrations to occur. The slopes for the series at 2.0 µm wavelength both in H_2SO_4 (figure 6.16(a)) and K_2CO_3 (figure 6.16(b)) were n=-0.92 and n=-1.01, which was interpreted as electrolyte heating. More importantly, the slopes were indeed significantly reduced for the resonant curves (2.8 µm illumination): In H_2SO_4, it was n=-0.6 and

---

[8] Due to the uncorrelated phases of the complex values of signal and Fourier background (as illustrated in figure 3.9), the background induced a statistical error, which determined the error bar. Here, the background level differed significantly between both measurement series.

[9] In order to decrease the influence of transient effects, a set of chopping frequencies was chosen before each measurement. Starting at the lowest frequency of about 0.3 Hz, every second value was skipped, while the frequency was increased until the highest value was reached. Then, these skipped values were measured in decreasing order.

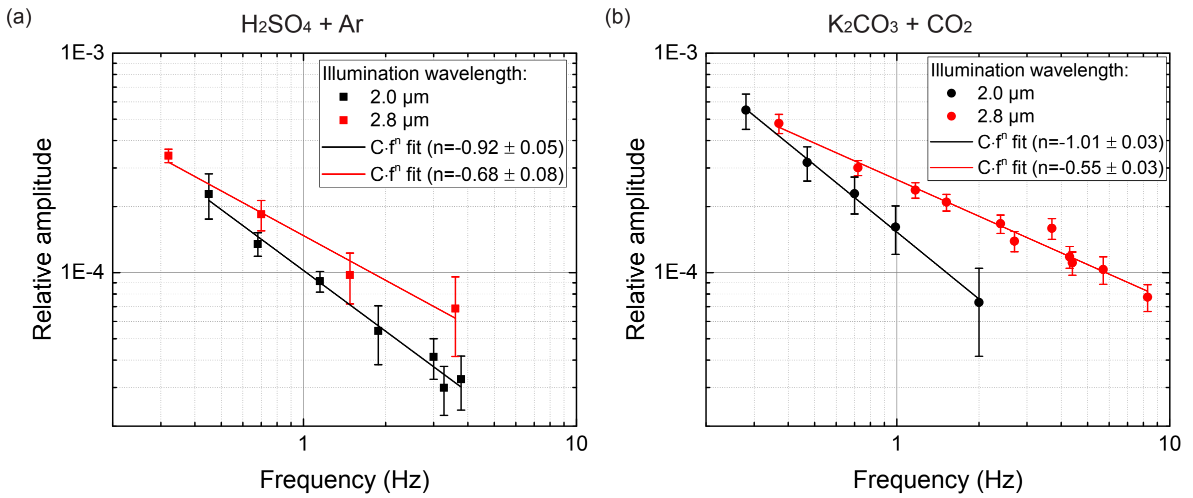

Figure 6.16: Relative peak-to-peak amplitudes of the current density variation of 420 nm nanosquares on n-Si with 1-2 nm plasma oxide (plasmonic resonance at 2.8 µm) under illumination with IR radiation of 2.0 µm and 2.8 µm wavelength at an intensity of 80 mW/cm^2 as a function of the chopping frequency in (a) Ar-saturated 50 mM H_2SO_4 in D_2O and (b) CO_2-saturated 50 mM K_2CO_3 in D_2O. The error bars were calculated from the background in the Fourier spectra, except the points at 3.3-3.6 Hz in part (a) where they show the standard deviation between 8 measurements. The measurements of part (b) were recorded using another, identical sample under increased total illumination intensity. Further experimental conditions: applied voltage: -0.66 V (H_2SO_4) resp. -1.36 V (K_2CO_3) vs SHE; total current density: -2.2 to -8.5 mA/cm^2 (H_2SO_4) resp.-5.5 to -7.6 mA/cm^2 (K_2CO_3).

in K_2CO_3, it was even n=-0.55. Note that a different sample was used for each electrolyte due to sample degradation connected to a blueshift of the resonance over time.

Another important experiment for the interpretation of the plasmonic behavior is a set of frequency series with 260 nm structures, which were resonant at 2.0 µm wavelength (cf. figure 6.17). The two series here were recorded using one sample, which also showed a blueshift in the plasmonic resonance from 2.0 µm to 1.8 µm over the course of the measurements. So, one can assume that the resonance was more reliably met in the H_2SO_4 measurements (figure 6.17)(a)) than in the ones in K_2CO_3 (figure 6.17)(b)). Although the resulting resonant curves (at 2.0 µm) in both electrolytes showed a less steep slope, the exponents varied between n=-0.70 in H_2SO_4 and n=-0.51 in K_2CO_3. Remarkably, the exponents of the non-resonant conditions showed a similar trend and decreased from n=-0.98 to n=-0.80. This trend was opposite to the one observed with the 1400 nm structures (where the K_2CO_3 curves were steeper). It requires further experiments to state if this trend is real and how it can be interpreted.

6.4.4 Influence of applied potential

Next to the frequency, it is also interesting, how the applied potential influences the amplitude of the current modulations. A series of electrolyses with 8 min duration at potentials between -1.49 V and -1.22 V vs SHE (IR-drop corrected) on samples with the same structure sizes as above was performed. The relative current modulations at a chopping frequency of 3.6±0.3 Hz and an illumination intensity of 80 mW/cm^2 determined by Fourier transformation using Welch's method are shown in figure 6.18. The general trend of all series was that the relative current modulation decreased with increasingly negative overpotential.

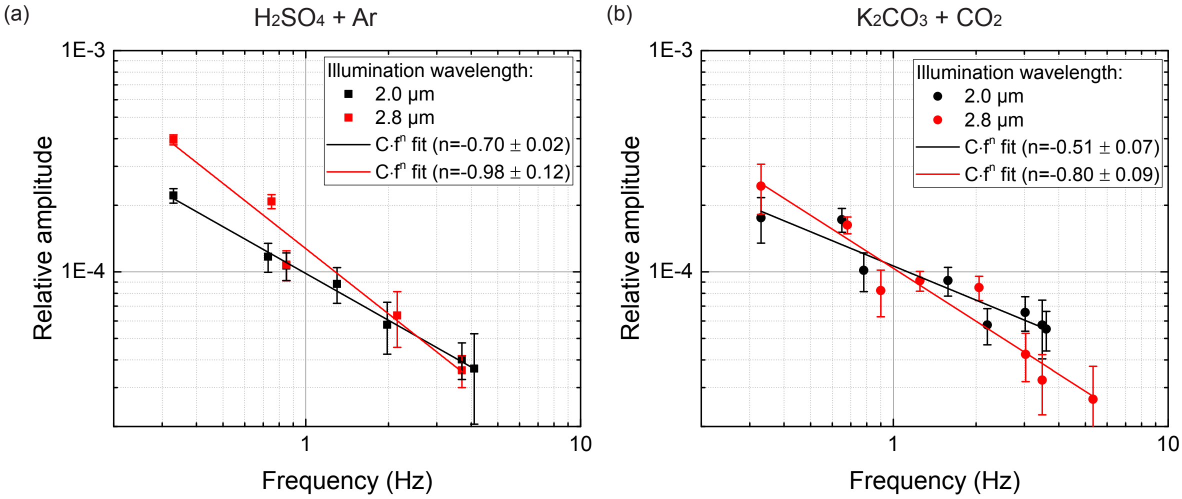

Figure 6.17: Relative peak-to-peak amplitudes of the current density variation of 260 nm nanosquares on n-Si with 1-2 nm plasma oxide (plasmonic resonance at 2.0 µm) under illumination with IR radiation of 2.0 µm and 2.8 µm wavelength at an intensity of 80 mW/cm^2 as a function of the chopping frequency in (a) Ar-saturated 50 mM H_2SO_4 in D_2O and (b) CO_2-saturated 50 mM K_2CO_3 in D_2O. The error bars were calculated from the background in the Fourier spectra, except the points at 3.5-3.7 Hz where they show the standard deviation between 6 resp. 7 measurements. Further experimental conditions: applied voltage: -0.635 V (H_2SO_4) resp. -1.46 V (K_2CO_3) vs SHE; total current density: -2.8 to -6.9 mA/cm^2 (H_2SO_4) resp. -3.6 to -4.7 mA/cm^2 (K_2CO_3).

On the other hand, the absolute current density increased with increasingly negative overpotential so that the relative error decreased at the same time. Similar to the data in the previous sections, one can see that the amplitudes of the 260 nm sample do not differ much between the two wavelengths, while the amplitude at 2.8 µm was much higher than at 2.0 µm for the other two sizes, which substantiates the explanation of a plasmonic effect.

6.4.5 Discussion of errors

The large error bars and variations between individual electrochemical measurements discussed above already give a hint towards large errors in the measurements, which are discussed in more detail in the following. One severe systematic source of errors lies in the experimental conditions, which were not very stable. As shown in (figure 6.8(b)), the plasmonic resonances can drift during series of electrolyses. Since the resonances were excited at fixed wavelengths, this can lead to a reduction of the plasmonic resonances over time.

A second source of errors was the use of D_2O-based electrolytes, which typically contained more contaminations (including metals) than H_2O-based ones. One reason was the lower purity of D_2O bought in bottles compared to freshly produced ultrapure water. The second reason lay in the necessity to dry all cell parts before filling with electrolyte. Contaminations resulting from this could accumulate on the sample surface and gradually change its electrochemical behavior. This could either occur as a drift within one measurement or as a long-term drift in the measurement series. In both cases, it was useful to strip off these contaminants at higher potentials between the individual electrolyses, but an accumulation could never be completely avoided.

In order to maximize the exposed surface area with high field enhancement, which was

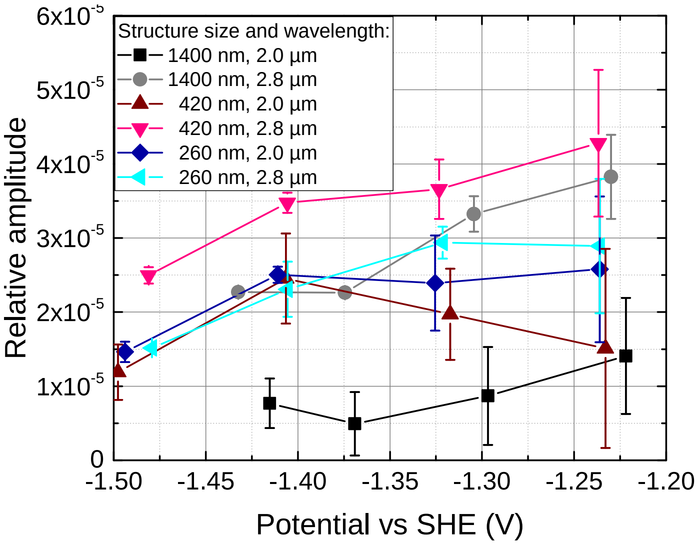

Figure 6.18: Relative peak-to-peak amplitudes of the current density variation of nanosquares with 1400 nm, 420 nm and 260 nm size under illumination with IR radiation of 2.0 µm and 2.8 µm wavelength at an intensity of 80 mW/cm^2 as a function of the applied potential in CO_2-saturated 50 mM K_2CO_3 in D_2O and a chopping frequency of 3.6±0.3 Hz. The error bars show the standard deviation between 2 (-1.48 V vs SHE) to 6 (-1.23 V vs SHE) measurements. The horizontal shift between the measurement series was caused by the IR drop correction with different current densities. Average current densities: -4.6±0.4 mA/cm^2 @ -1.23 V vs SHE to -18.1±0.6 mA/cm^2 @ -1.42 V vs SHE (1400 nm sample), -1.7±0.2 mA/cm^2 @ -1.24 V vs SHE to -5.4±0.5 mA/cm^2 @ -1.48 V vs SHE (420 nm and 260 nm samples).

mainly located at the sidewalls of the structures, no thermal oxide layer was used for these experiments. As a consequence, a certain current contribution could flow over the unstructured SiO_2 surface between the structures.

Most of the measurements shown above were recorded close to the detection limit of the setup, so that they reacted sensitively on spurious signals. Therefore, an important statistical error was caused by the background of the periodograms, which was generated by noise, by current jumps due to bubble movement and by current drifts. As explained in section 3.8, the quadratic subtraction of the background should already have compensated the constant component of the background noise, but a contribution from noise remained. For all data points based on only one measurement, the background level in the Fourier spectra divided by the square root of the number of time intervals used for averaging was an upper limit, for the points consisting of more measurements, the standard deviation between the measurements of this set was taken.

In addition to this background, electromagnetic noise from other devices in the surrounding of the experiment could cause spurious signal, which typically appeared as distinct peaks, e.g. at 50 Hz, as frequency bands and as an additional background. These disturbances showed a temporally very irregular behavior and can barely be predicted and influenced. Some of the missing points in the frequency series above and some extraordinarily large error bars were caused by such disturbances. The noise contribution of the disturbances was also treated by the background correction explained above.

Especially for higher chopping frequencies, it was important to have a chopping device with a good frequency stability. For the first measurements (figures 6.13 and 6.16(b)), a servo motor from a rotating disk electrode with a large chopping wheel was used. It showed frequency fluctuations of about 0.3% within one measurement, which could reduce the signal for higher frequencies. To avoid this, the servo motor was replaced by a stepper motor attached to a vertically rotating slotted cylinder resulting in a frequency stability of 0.03%. Unfortunately, this needed a change in the optical setup, which reduced the illumination intensity so that all measurements except the two indicated above were made with this reduced intensity.

6.5 Discussion

6.5.1 Optical characterization

The optical measurements and simulations of section 6.2 showed different resonance wavelengths between geometrically equal structures fabricated by different methods, namely a blueshift of nTP samples compared to those made by LO-NIL: Although the surface of nTP structures was rougher and richer in defects than the one of LO-NIL structures, this is probably not the correct explanation for this large blueshift. On the contrary, a moderate roughness was reported to cause a slight redshift [Tru11, RF09]. Also the influence of so-called ear defects - edge grains on the nanostructures - was studied by Trügler et al. who again only found a tiny redshift [Tru14]. However, there could be a relationship between the resonance shift and the roughness of the Au layer of the nTP samples: In the nTP process, the evaporated Au surface with a finite roughness was brought into contact with the rigid substrate itself. This probably led to the occurrence of surface defects and voids between Ti and SiO_2. In contrast, the LO-NIL samples, which were evaporated under high vacuum conditions, were expected to have void-free interfaces between all layers so that they well corresponded to the situation in the simulations. The voids inside the nTP interface can only be filled with vacuum or air, both of which have a lower refractive index than SiO_2 and Si. As the simulations in figure 6.5 show, even a simplified geometry with a flat air layer of 2 nm thickness could fairly well reproduce the experimental data. This difference in interface quality is also in line with electrochemical data from figure 5.1, where the necessary overpotential applied on nTP structures was much higher than on corresponding ones made by LO-NIL.

Another explanation could be that the transfer-printing process itself led to an exposure of the Ti layer to air and that the O_2 plasma pretreatment, which was carried out on the Ti surface, could also lead to a change in material properties, in particular a (partly) oxidation of the Ti layer. For the LO-NIL process, Au was evaporated onto the Ti layer within a vacuum chamber so that Ti oxidation should be drastically reduced. As figure 6.6 shows, there was also a significant shift between two samples made by nTP and LO-NIL without Ti adhesion layer. We can therefore conclude that the interface voids significantly contributed to the resonance shift. However, the shift between nTP and LO-NIL sample was larger in the presence of a Ti layer. This difference could be a hint that Ti oxidation or an increased roughness due to the Ti layer could also play a role. However, one can observe that the LO-NIL structures differed in their resonance wavelength while the nTP ones did not. If Ti oxidation caused the observed shift, one would expect that the shift occurred between the nTP samples and that the LO-NIL samples had a more constant resonance wavelength. Therefore, it is more probable, that the shift between the two LO-NIL samples was rather caused by fabrication imperfections leading to deviations in the resonance wavelength (cf. also the variation at 200 nm in figure 6.2(c)).

6.5.2 Influence of the photoelectric effect

Before discussing the plasmonic effects on the electrochemical experiments from section 6.4.3, some other illumination-induced effects are considered. The most obvious contribution of illumination to an increasing current is the photoelectric effect inside the Si substrate, which can easily dominate the observed behavior. In our experiments, it was therefore suppressed by two measures: First, the experiments were performed using n-Si, which did not show a significant photovoltage (in contrast to p-Si samples with Au/Ti contacts; cf. also section 2.1.1). Second, the remaining photoelectric effect in n-Si, which was mainly attributed to a change in conductivity, was strongly dependent on the illumination wavelength. For wavelengths below 1.1 µm (corresponding to the bandgap energy of 1.1 eV), the absorptivity was high indicating a strong photoelectric effect. Therefore it was necessary to prevent photons in this range from reaching the sample, which was done by a suitable wavelength filter (cf. experimental setup in section 3.3.3).

6.5.3 Influence of heat transfer and temperature

The second consequence of illumination, which was even more important for the presented experiment, lies in warming of the sample and its surrounding. Before evaluating the mechanisms and time evolution of heating and heat transport, the influence of temperature on electrochemical reactions is discussed. As the heat transport connected to electrolyte and plasmonic heating shows a non-trivial spatial and temporal behavior, a detailed discussion including the difference between heat transport in different directions as well as models for temperature transients under periodic excitations are necessary. Therefore, an analytical model with alternating excitation and disexcitation phases with constant rates is developed below, followed by time-dependent simulations of heat transfer within the electrolyte.

Temperature dependence of electrochemical reactions

In electrochemical experiments, the reactivity is measured in the form of a current. For the investigation of the influence of heating, it is therefore important to evaluate the temperature dependence of the individual processes determining the current.

The first equation to be discussed is the Butler-Volmer equation, which deals with reaction kinetics. Its simplified form for reduction reactions in sufficient distance to equilibrium reads:

$$j = -j_0(T)\mathrm{exp}\left(-\frac{(1-\alpha)F\eta}{RT}\right) \tag{6.2}$$

It contains two explicitly temperature-dependent terms (neglecting the temperature dependence of η): one is the exponential term $\mathrm{exp}\left(\frac{-(1-\alpha)F\eta}{RT}\right)$ with the charge transfer coefficient α, the Faraday constant F, the overpotential η, the gas constant R and the temperature T, one is the exchange current density $j_0(T)$, which follows the Arrhenius relation:

$$j_0(T) = Fa_{\mathrm{ox}}c_0k_0'\mathrm{exp}\left(-\frac{e_{\mathrm{b,red}}}{RT}\right) \tag{6.3}$$

with the activity a_{ox} of the oxidized species, the unit concentration $c_0 = 1$ mol/l, a temperature-independent coefficient k_0' and the barrier height $e_{\mathrm{b,red}}$ (also called activation energy) [Kri15]. This leads to the following temperature dependence:

$$\begin{aligned} j &= -Fa_{\mathrm{ox}}c_0k_0'\mathrm{exp}\left(-\frac{e_{\mathrm{b,red}}+(1-\alpha)F\eta}{RT}\right) \\ \frac{\partial j/\partial T}{j} &= \frac{e_{\mathrm{b,red}}+(1-\alpha)F\eta}{RT^2} \end{aligned} \tag{6.4}$$

Since the barrier heights for the HER and the CO_2RR on Au are not known, the problem cannot be exactly solved. There is indeed experimental data for the barrier height of the oxygen reduction reaction (ORR). For the ORR on Pt, values between 17 kJ/mol [Ena89] and 80 kJ/mol [O'G82, Par92] can be found; for Pd, an activation energy of 39 kJ/mol was reported [SP07]. Furthermore, the HER on Pt in alkaline environment was found to have an activation energy of 29 kJ/mol [She10]. Therefore the result of the following estimation, in which the above mentioned values are used, only serves as a qualitative guideline. Remarkably, the sign of the temperature dependence according to equation 6.4 can be negative or positive; it becomes zero, if the overpotential (multiplied by 1 - α and the Faraday constant F) is equal to the activation barrier. For realistic conditions with moderate overpotentials, the absolute value of j typically increases with increasing temperature. For a charge transfer coefficient of $\alpha = 0.5$, an overpotential of $\eta =$ -1 V (typical value for our electrolysis conditions) and an activation barrier of $e_{\mathrm{b,red}}$ = 80 kJ/mol, this yields an increase of the current density of 4 %/K[10]. For an overpotential of -1.6 V, the temperature dependence would disappear. This shows that the reaction kinetics strongly depend on temperature, that they contribute much to the overall temperature dependence of electrochemical reaction rates (probably they are the dominant factor) and that this effect very sensitively depends on the involved activation energies and the overpotential.

Besides the kinetics, there is a significant influence of temperature on the equilibrium values of redox reactions as predicted by the Nernst equation, which describes the dependence of the equilibrium electrode potential E_{el} on the concentrations of the involved species [Kri15]. For the HER in alkaline media with estimated activities of $a_{\mathrm{H_2O}} = 1$, $a_{\mathrm{H_2}} = 10^{-3}$ and $a_{\mathrm{OH^-}} = 10^{-3}$, $n = 2$ transferred electrons and a temperature dependence of the standard electrode potential $\frac{\partial E^0_{\mathrm{el}}}{\partial T}$=-0.84 mV/K (this value already covers entropic contributions influencing the difference in free enthalpy upon temperature change [Bra89]), one obtains

$$\begin{aligned} E_{\mathrm{el}} &= E^0_{\mathrm{el}} + \frac{RT}{nF}\mathrm{ln}\left(\frac{\prod_{\mathrm{ox}} a_i^{|\nu_i|}}{\prod_{\mathrm{red}} a_j^{|\nu_j|}}\right) \\ \frac{\partial E_{\mathrm{el}}}{\partial T} &= \frac{\partial E^0_{\mathrm{el}}}{\partial T} + \frac{R}{nF}\mathrm{ln}\left(\frac{\prod_{\mathrm{ox}} a_i^{|\nu_i|}}{\prod_{\mathrm{red}} a_j^{|\nu_j|}}\right) = \\ &= -0.84\mathrm{mV/K} + 0.9\mathrm{mV/K} = 0.06\mathrm{mV/K} \end{aligned} \tag{6.5}$$

---

[10] For all equations in this section, an environment temperature of 298 K is assumed. Due to several simplifications and assumptions, in particular missing literature values for important parameters of our system, all numerical results are only used for estimations of the order of magnitude of the involved processes.

Since the activities of the involved species change upon reaction and the literature value $\frac{\partial E^0_{\mathrm{el}}}{\partial T}$ depends on many external parameters[11], the resulting potential shift is connected to a large error. For the values used here, a shift by 1 K would only lead to a change in current density of 0.2%/K in current density, but for other reactions or activites, values in the % range can evolve so that an impact of temperature on the equilibrium potential can get comparable to the other effects discussed in this section.

Another temperature-dependent factor in electrocatalysis is mass transport limitation. It should generally be avoided, when kinetic effects shall be examined, but at the current densities observed within this thesis - typically leading to a mixed reaction and mass transfer control - mass transport by diffusion and migration has to be considered. Independent from the absolute value of the diffusion coefficients of individual species, the impact of temperature on the diffusion coefficient D_{T1} and on the electrolytic conductivity can be predicted according to the Stokes-Einstein relation:

$$\begin{aligned}\frac{D_{T2}}{D_{T1}} &= \frac{T_2 \mu_{T1}}{T_1 \mu_{T2}} = \frac{299\,\mathrm{K}\cdot 0.90\mathrm{mPa/s}}{298\,\mathrm{K}\cdot 0.88\mathrm{mPa/s}} = 1.026\\ \frac{\partial D_{\mathrm{el}}/\partial T}{D} &= 2.6\%/\mathrm{K} \end{aligned} \tag{6.6}$$

with the charge carrier mobility μ_T at a temperature T.

The last effect discussed here, the one of temperature on ion migration in the electrolyte can be estimated by its impact on ionic conductivity, which can only be described phenomenologically. According to Kuyucak and Chung, it increases by about 2%/K [Kuy94].

Heating mechanisms

When our electrochemical cell was illuminated, there were different locations, where light was absorbed, resulting in corresponding heating mechanisms, which are distinguished and discussed in the following.

For our doping density of less than $5 \cdot 10^{15}$ cm^{-3}, the remaining absorptivity should lie below 0.07 cm^{-1} above 2 µm wavelength [Spi57], which corresponds to an absorption of less than 0.3% of the incoming radiation within the 400 µm thick sample (this can explain why only a very small contribution of substrate heating was found in the experiments in section 6.4.1).

Consequently, the major part of the radiation, which is not reflected or scattered by LSPRs, reaches the electrolyte, where it is absorbed resulting in electrolyte heating. When we look closer, this heating consists of two processes: The radiation first excites molecular vibrations of molecules in the electrolyte, mainly H_2O. Then, these excitations dissipate their energy on a ps to ns timescale leading to unordered excitations, which are equivalent to an ordinary temperature increase of the electrolyte.

A third important heating contribution lies in plasmonic heating, which acts very locally at the Au surface [Gov07, Che08, Adl09, Yen09, Wan13, Bor16]. Since the latter mechanism already is a very important plasmonic effect, while the ones mentioned first are rather unwanted, it is important to distinguish between electrolyte and plasmonic heating.

At this point, it shall be noted, that there has been virtually no investigation of the impact of

---

[11] For example, the temperature dependence of the standard electrode potential can take values of $\frac{\partial E^0_{\mathrm{el}}}{\partial T} = 0$ mV/K for the HER from protons or a value of $\frac{\partial E^0_{\mathrm{el}}}{\partial T} = +0.51$ mV/K for the redox pair $H^+/H(g)$ [Bra89].

plasmonic heating on electrochemistry in the literature. Probably, other researchers have not spent too much effort on it, as it has been estimated that at a typical solar irradiation intensity of 100 mW/cm², only a transient temperature increase between 0.4 mK (single Au nanoparticle with 100 nm diameter in water [Gov07]) and 1-10 mK (Ag nanocubes [Chr11, Kal14a][12]) would be expected.

The fourth heating effect, which lies in a slow temperature increase of the complete setup during operation, is not considered since it is independent from the chopping frequency. Therefore it does not give significant contributions to the modulated signal and it is neglected in the discussion.

Time evolution of different heating mechanisms

Besides plasmonic heating, it is expected that absorption of light within the electrolyte significantly contributes to a warming of the surrounding and the surface of the sample. As shown in the experiments using a Au stripe (cf. section 6.4.1), it actually makes up the major contribution in situations without plasmonic resonances.

A comprehensive treatment of the time evolution of temperatures around the electrode surface is indeed complex. In general, there can always be a superposition of effects with different time constants, which complicate the interpretation. Even electrolyte heating alone could have separate timescales for thermal transport in different directions, e.g. away from the interface (z direction) and lateral transport (x and y direction) from the illuminated spot to the areas around it. Also a laterally inhomogeneous electrolyte heating due to light scattering and reflection at the Au structures leads to a spatial temperature variation. The actual time scales, on which heat transfer occurs in the experiments, are strongly dependent on the values of light penetration depth, Au structure size and the typical dimension of the respective heating mechanism. Figure 6.19 qualitatively shows how heating with different structure dimensions can take place and in the following, it shall be estimated, how the geometry of the sample influences the heat transport, in particular the response to different chopping frequencies.

Starting with the case of structures, which are equally large or larger than the penetration depth of light (figure 6.19(a, d)), the light absorption and consequently the heating is vertically and horizontally inhomogeneous. In the case of the 23 µm wide Au stripe in H_2O-based electrolyte illuminated at 2.8 µm wavelength, where the heat is deposited close to the solid-liquid interface and where much heat can directly flow into the substrate before warming the Au test stripe, the influence of lateral heat transport is important and the temperature amplitude is significantly reduced compared to a situation with a laterally more uniform heating. This could explain the only slight difference in the temperature amplitude between 2.0 µm and 2.8 µm in H_2O, where the absorptivity differs by two orders of magnitude, in figure 6.11. Probably, due to the geometry of the Au stripe, which is virtually intransparent for IR radiation, one could expect that it heats more uniformly for lower electrolyte absorptivities, i.e. a deeper penetration of the radiation into the electrolyte. For high absorptivities, there is significantly stronger heating at the edges of the stripe compared to the center. Although the high thermal conductivity of Au prevents larger temperature gradients inside it, temper-

---

[12] Kale et al. write that 10 K temperature increase would correspond to 10^6 mW/cm², which is not consistent to the value of 10 mK at 100 mW/cm² they give in the same paragraph [Kal14a].

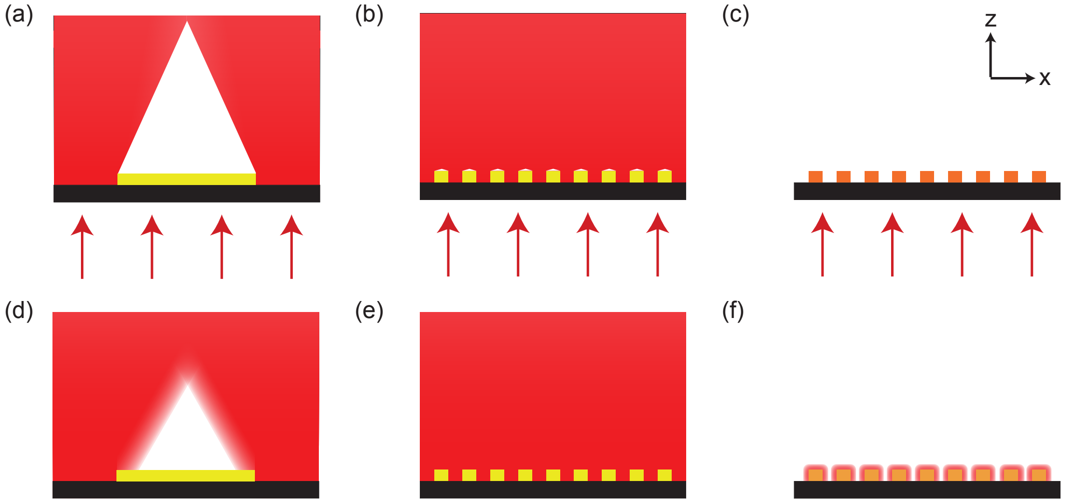

Figure 6.19: Schematic representation of (a-c) heating power density and (d-f) heat transport in differently structured systems represented by the temperature distribution after switching off illumination: For a structure, which is equally large or larger than the penetration depth ((a) and (d)), the heating is vertically and horizontally inhomogeneous and diffraction at the edges and lateral heat transport plays a significant role. In a system with structures, which are smaller than the penetration depth ((b) and (e)), diffraction and sub-wavelength effects lead to a laterally quite homogeneous electrolyte heating and a negligible role of lateral heat transport. Plasmonic heating ((c) and (f)) takes place within the Au structures and leads to heat transport in all directions. Red arrows depict illumination, red areas either heating power density or temperature increase, respectively. All dimensions are not to scale and warming of the Si substrate is not shown due to its small magnitude.

ature gradients inside the electrolyte remain and cause an inhomogeneous heat influx. The consequence of this is that the measured temperature is effectively reduced compared to the electrolyte temperature at the edge of the Au stripe.

Going on to the limiting case of structures much smaller than the wavelength, there is a strong influence of diffraction up to so-called extraordinary optical transmission[13] combined with a long penetration depth of the incoming light. In this case, the heating is laterally quite homogenenous and consequently, lateral heat transport can be completely neglected (figure 6.19(b, e)).

Since we look for signs of plasmonic heating, it is also important to describe its temporal behavior. According to the explanation in section 2.3.2, plasmonic heating directly heats the Au nanostructures via electron-electron, electron-phonon and phonon-phonon relaxations. These processes are much faster than the subsequent heat transport into and through the surrounding medium (as shown in figure 6.19(c, f)), so they are regarded as an instantaneous heating of the Au nanosquare volume. In the following, it is estimated, on which timescales the heat dissipated in the Au structures distributes in our geometry, both in lateral and verti-

---

[13] This describes a strong increase in transmission through arrays of sub-wavelength structures [Ebb98].

cal direction[14].

First, it is important to evaluate the geometry of the developing temperature profile and the temporal behavior of heat transport in lateral and vertical direction. For electrolyte heating, one only has minor temperature modulations in lateral direction (cf. figure 6.19(b, e)). In contrast, the contribution of plasmon heating, where heat is only dissipated in the Au structures, results in a strong lateral modulation of heating power and temperature (cf. figure 6.19(c, f)). The spatio-temporal behavior of this system is not trivial, but it can be tackled by a diffusion model, which was originally developed to describe the mass transport towards quadratic arrays of circular microelectrodes [Sch88]: For short timescales, a hemispherical diffusion profile evolves around each microelectrode. Then, the diffusion zones of neighboring microelectrodes start overlapping and finally converge to linear diffusion. This model can be easily adapted to the situation of thermal transport here, since the mathematical descriptions of heat transport and mass transport are equivalent; only the diffusion constant D for chemical species in the electrolyte has to be replaced by the term $\frac{\kappa}{c_\mathrm{p}\rho}$ with the thermal conductivity κ, the isobaric heat capacity c_p and the mass density ρ. The most important information from this model is, on which timescale the hemispherical (diffusion respectively temperature) profile transforms into a linear profile. Adapting the model of Scharifker [Sch88] to our situation, this transition occurs around a transition time t_trans:

$$t_\mathrm{trans} = \frac{c_\mathrm{p}\rho}{\pi\kappa}\left(\frac{l^2 - d^2/2}{d}\right)^2 \tag{6.7}$$

for structures with a diameter d and a pitch l. In water ($\frac{\kappa}{c_\mathrm{p}\rho} = 1.4\cdot 10^{-7}\,\frac{\mathrm{m}^2}{\mathrm{s}}$), one gets transition times of 2.1 µs for a heating modulated with a period length of l = 700 nm (for d = 420 nm structures) and 0.8 µs for l = 430 nm and d = 260 nm. At the time t_trans, one has a thickness of the linear temperature diffusion layer in the range of l.

Therefore, the temporal behavior on timescales, which are available to our experimental methods[15], is dominated by vertical heat transport, although the lateral heat transport does certainly influence the absolute values of the temperature amplitudes.

Frequency dependence of periodic illumination - analytical

According to this argumentation, we use one-dimensional modeling for the treatment of the temporal behavior of the heat transport in our system. The first model discussed here investigates the situation of alternating heating and cooling phases induced by chopped illumination under the assumption of heat transport into a heat sink, which is proportional to the temperature difference between the region of interest and the environment. The model can be analytically solved and it is just as well appropriate for any situation with alternating phases of constant excitation and exponential relaxation, e.g. the light-induced excitation of electronic or vibrational states in molecules by chopped illumination. In particular, this

---

[14] In addition to the direct heating of the metal, there is a contribution of plasmonic heating over photon absorption in the electrolyte in the hot spots close to the Au structure edges since the absorption of heat at a certain point in space is proportional to the light intensity and an intensity enhancement of up to 10^3 is predicted in the hot spots. These modulations are not treated separately, as they are even finer structured than the plasmonic heating of the metal structures and the temperature gradients induced by them influence the system behavior on an even shorter timescale.

[15] Due to the low amplitude of modulations faster than several Hz and the mechanical chopping, only timescales in the range between 0.1 s and a few seconds are accessible.

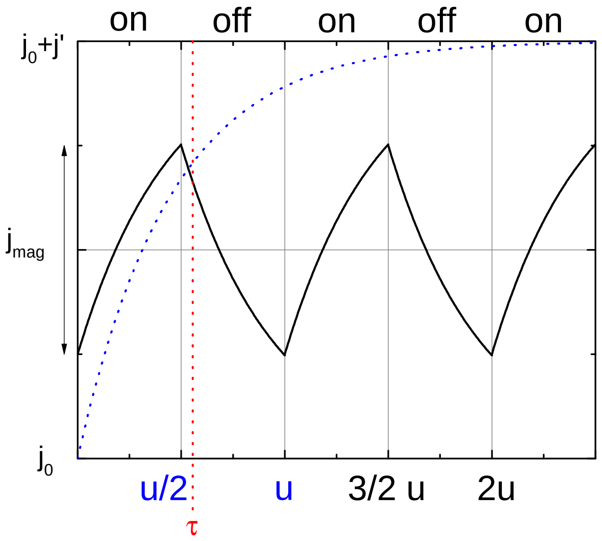

Figure 6.20: Temporal behavior of an arbitrary photoexcited effect with a typical time constant τ. The blue dotted curve shows the transient of j after switching on illumination without modulation. The black curve shows the behavior of j upon chopping with a frequency $f = \frac{1}{u}$.

model treats the dependence of such excitations on the chopping frequency.

For this model we assume that illumination can increase an initial current density j_0 to a new equilibrium value of $j_0 + j'$ (limiting value for infinite illumination time)[16]. The current increase is triggered by switching on the illumination at $t = 0$. Then, the current density transient is described by a simple exponential equation depending on the typical timescale τ, in which the difference to the illuminated equilibrium $j_0 + j'$ decreases by a factor of $\frac{1}{e}$:

$$j = j_0 + j' \cdot \left(1 - \exp\left(-\frac{t}{\tau}\right)\right) \tag{6.8}$$

If the current density j relaxes back to j_0 with the same time constant after turning off the illumination and if the light is modulated with a square-wave function with equally long on and off periods, the time transient gets centered around a mean value of $j_0 + 0.5j'$ for times much longer than τ (cf. figure 6.20). j_{mag} is the difference between maximum and minimum of this periodic curve. For a minimum value of j at $t = 0$[17], the transient starts at $j_0 + 0.5j' - 0.5j_{\mathrm{mag}}$, but approaches $j_0 + j'$ during the excitation period according to:

$$j = j_0 + 0.5(j' - j_{\mathrm{mag}}) + 0.5(j' + j_{\mathrm{mag}}) \cdot \left(1 - \exp\left(-\frac{t}{\tau}\right)\right) = j_0 + j' - (0.5j' + 0.5j_{\mathrm{mag}}) \cdot \exp\left(-\frac{t}{\tau}\right) \tag{6.9}$$

---

[16] For the derivation of the model it is not important, if the current increase is caused by temperature increase, molecular or electronic excitations, although the involved timescales are very different.

[17] Considering the case that the periodic excitation already started long enough before $t = 0$.

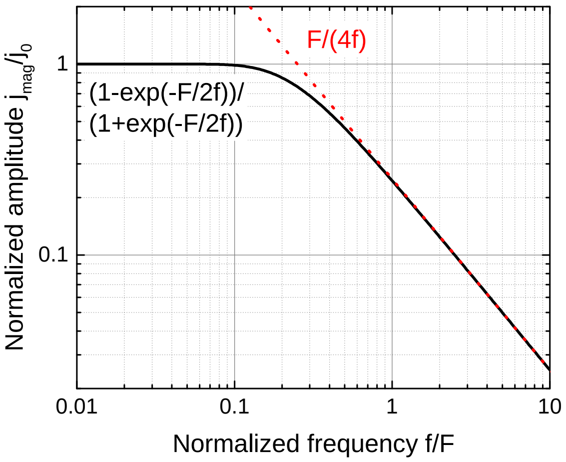

Figure 6.21: Visualization of the frequency dependence of the analytical model according to equation 6.10 (black) together with its high-frequency behavior according to $\frac{j_{\text{mag}}}{j'} = \frac{F}{4f}$ (red).

If the period length is u, a maximum of $j_0 + 0.5j' + 0.5j_{\text{mag}}$ is reached at $t = 0.5u$, leading to

$$\begin{aligned} j(0.5u) = j_0 + j' - (0.5j' + 0.5j_{\text{mag}}) \cdot \exp\left(-\frac{u}{2\tau}\right) &= j_0 + 0.5j' + 0.5j_{\text{mag}} \\ j' - (j' + j_{\text{mag}}) \cdot \exp\left(-\frac{u}{2\tau}\right) &= j_{\text{mag}} \\ j_{\text{mag}} &= j' \cdot \frac{(1 - \exp(-\frac{u}{2\tau}))}{(1 + \exp(-\frac{u}{2\tau}))} \\ j_{\text{mag}} &= j' \cdot \frac{\left(1 - \exp\left(-\frac{F}{2f}\right)\right)}{\left(1 + \exp\left(-\frac{F}{2f}\right)\right)} \end{aligned} \tag{6.10}$$

with the chopping frequency $f = \frac{1}{u}$ and the characteristic frequency of the system $F = \frac{1}{\tau}$. If the typical frequency F of the transient is much slower than the chopping frequency f, equation 6.10 converges to $j_{\text{mag}} = j' \cdot \frac{F}{4f}$, if it is much faster, a constant value of $j_{\text{mag}} = j'$ is approached (cf. figure 6.21).

This model based on exponential decay is true for systems like excitations in molecules, electronic states or similar mechanisms, which follow exponential transients. Their decay is only depending on the number of excited molecules, not on the number of molecules in the ground state. For heat transport in realistic geometries, the whole situation gets more complex: A simple exponential decay would require a heat sink, which remains at a constant temperature. The exact curve shape of a realistic transient with a heat sink, which can warm up, therefore deviates from the described exponential behavior, but shows a similar qualitative behavior. A comparison of the analytical model to 1D simulations is given in the following section.

Frequency dependence of periodic illumination - simulations

In order to explore, how well this analytical model can describe the actual situation, a simple time-dependent finite-differences simulation of the one-dimensional heat equation is performed. The important difference to the previous model is that the simulation can now deal with asymmetries induced by the heat transport over a discrete interface (representing

the substrate) and into a bulk volume (representing the electrolyte). In addition, the heating by illumination can be described by an exponentially decreasing heating power inside the electrolyte or by a discrete heating at the surface such as, e.g., plasmonic heating.
The simulation is based on the 1D heat equation with heat source $\dot{q}_\mathrm{V}(z)$ (which has the dimension of a volumetric power density):

$$\frac{\partial T}{\partial t} = \frac{\kappa}{c_\mathrm{p}\rho}\frac{\partial^2 T}{\partial z^2} + \frac{1}{c_\mathrm{p}\rho}\dot{q}_\mathrm{V}(z) \tag{6.11}$$

The boundary conditions of the simulation are made up by two heat sinks at environment temperature T_0, which are differently connected to the calculated electrolyte volume. The electrolyte at the end of the mass transfer boundary layer in a distance of L=500 µm from the electrode surface[18] is simply modeled by

$$T\Big|_{z=L} = T_0 \tag{6.12}$$

The situation at the electrode interface is more complex and the Si substrate with air behind is modeled by an infinite heat sink coupled to the simulation volume via an interfacial thermal conductance G. The combination of the discrete interfacial thermal conductance and the continuous heat flow in the volume adjacent to the interface induces a discontinuity into the temperature profile and therefore, it has to be treated carefully. It can be described by a flow diagram, which includes the heat flow over the interface $\dot{Q}_\text{interface} = G\Delta T\Big|_\text{interface}$ (including the temperature difference over the interface $\Delta T\Big|_\text{interface}$), the heat flow into the electrolyte $\dot{Q}_\text{electr} = \kappa\frac{\partial T}{\partial z}\Big|_{z=^+0}$ [19] and the heat influx at the first point of the calculation area $\dot{Q}_\text{interface} = \dot{q}_\mathrm{V}(0)dz$ with the grid element size dz[20]:

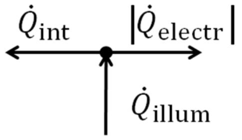

The directions of the arrows in the flow diagram consider the case of $\frac{\partial T}{\partial z}\Big|_{z=^+0} < 0$ and one has to include that the net sum of these flow contributions leads to a change in interface temperature of $c_\mathrm{p}\rho dz\frac{\partial T}{\partial t}\Big|_{z=0}$. This results in the boundary condition

$$\begin{aligned} c_\mathrm{p}\rho dz\frac{\partial T}{\partial t}\Big|_{z=0} &= \kappa\frac{\partial T}{\partial z}\Big|_{z=^+0} - G\Delta T\Big|_\text{interface} + \dot{q}_\mathrm{V}(0)dz \\ \frac{\partial T}{\partial t}\Big|_{z=0} &= \frac{\kappa}{c_\mathrm{p}\rho dz}\frac{\partial T}{\partial z}\Big|_{z=^+0} - \frac{G\Delta T\Big|_\text{interface}}{c_\mathrm{p}\rho dz} + \frac{\dot{q}_\mathrm{V}(0)}{c_\mathrm{p}\rho} \end{aligned} \tag{6.13}$$

---

[18] Under diffusion-controlled conditions, convection of the electrolyte is induced. A typical value for the thickness of the resulting mass transfer boundary layer is 500 µm [Pin86], therefore it is assumed that the environment temperature is present at this distance.

[19] Note that this contribution can be positive and negative, depending on the type of heating.

[20] The use of dz permits to both consider plasmonic/surface heating and electrolyte heating. This contribution is in particular important for the case of plasmonic/surface heating, where it is $\dot{Q}_\text{interface} = I_\text{ill}$. For electrolyte heating, in vanishes in the limit of $dz \to 0$

Using this representation, a descriptive picture is that the ratio between the heat flows $\dot{Q}_{\mathrm{interface}}$ and $\dot{Q}_{\mathrm{electr}}$ is not constant in time, but varies with a change of the electrolyte temperature in front of the interface. This can be considered as the source of different temporal behavior and frequency dependence.

For all points except the first one at the interface, equation 6.11 is discretized on a 1D grid with 100 discrete steps of dz = 5 µm each and a time resolution of dt = 100 µs by a simple forward Euler algorithm:

$$T_i(t_{j+1}) = T_i(t_j) + \frac{\kappa dt}{c_{\mathrm{p}}\rho dz^2}(T_{i+1}(t_j) + T_{i-1}(t_j) - 2T_i(t_j)) + \frac{dt}{c_{\mathrm{p}}\rho}\dot{q}_{\mathrm{V}}(z) \qquad (6.14)$$

with temperature values $T_i(t_j)$ at position i and timestep number j[21]. Heating is only applied for the first half-period of the modulation, in the second half-period without illumination, $\dot{q}_{\mathrm{V}}(z)$ is set to 0.

The calculation of the interface temperature $T_1(t_j)$ is somehow more complicated since it needs to consider the boundary condition from equation 6.13. The term $\frac{\kappa}{c_{\mathrm{p}}\rho}\frac{\partial^2 T}{\partial z^2}$ from equation 6.11, which represents the continuous heat flow to both sides is therefore replaced by one term, which represents the heat transport into the calculation area $\frac{\kappa}{c_{\mathrm{p}}\rho dz}\frac{\partial T}{\partial z}\Big|_{z=+0}$ and one term representing the heat transport over the boundary $\frac{G}{c_{\mathrm{p}}\rho dz}\Delta T\Big|_{\mathrm{interface}}$. In order to make the algorithm stable for large values of G, or rather for conditions of $\frac{Gdt}{c_{\mathrm{p}}\rho dz} > 1$, the equation for the first point is discretized using a backward Euler algorithm[22]:

$$\begin{aligned}\delta T_1(t_{j+1}) &= \delta T_1(t_j) + \frac{\kappa dt}{c_{\mathrm{p}}\rho dz^2}(\delta T_2(t_{j+1}) - \delta T_1(t_{j+1})) - \frac{Gdt}{c_{\mathrm{p}}\rho dz}\delta T_1(t_{j+1}) + \frac{dt}{c_{\mathrm{p}}\rho}\dot{q}_{\mathrm{V}}(0)\\ \delta T_1(t_{j+1}) &= \left(\delta T_1(t_j) + \frac{\kappa dt}{c_{\mathrm{p}}\rho dz^2}\delta T_2(t_{j+1}) + \frac{dt}{c_{\mathrm{p}}\rho}\dot{q}_{\mathrm{V}}(0)\right) / \left(1 + \frac{\kappa dt}{c_{\mathrm{p}}\rho dz^2} + \frac{Gdt}{c_{\mathrm{p}}\rho dz}\right) \qquad (6.15)\end{aligned}$$

With temperature increases of $\delta T_i(t_j) = T_i(t_j) - T_{\mathrm{environment}}$. Another condition for the stability of the Euler algorithm is that a reduction of the grid element size by a factor of m requires a reduction of the time interval by m^2. Therefore the minimum grid element size dz is a limiting factor for the accuracy of the calculation.

In order to compare electrolyte heating, plasmonic heating and combinations of these two mechanisms, we used four different heating vectors $\dot{q}_{\mathrm{V}}(z)$, which have the dimension of a volumetric power density and represent the source term of the heat equation:

- Electrolyte heating with a light penetration depth of $d_{\mathrm{ill}} = 100$ µm (representing D_2O with 0.1% H_2O content at 2.8 µm) and an illumination intensity of I_{ill} = 40 mW/cm²[23] is modeled by a Lambert-Beer type heating power density:

$$\dot{q}_{\mathrm{V}}(z) = \frac{I_{\mathrm{ill}}}{d_{\mathrm{ill}}}\exp\left(-\frac{z}{d_{\mathrm{ill}}}\right) = 4000\,\mathrm{mW/cm^3}\cdot\exp\left(-\frac{z}{0.1\,\mathrm{mm}}\right)$$

---

[21] This equation takes the same form for calculations of the absolute temperature T and the temperature difference to the environment δT.

[22] A complete implementation of the backward algorithm would however drastically complicate the calculation without being necessary. Therefore, the forward algorithm is kept for the other points as it drastically simplifies the calculation. Since $T_2(t_{j+1})$ is calculated before $T_1(t_{j+1})$ the calculation can still be implemented relatively simply.

[23] The transmission of the Si substrates is about 50%, so the incoming intensity of I_{ill}=80 mW/cm² is reduced by this factor.

- Electrolyte heating with a light penetration depth of $d_{\text{ill}} = 1000$ µm (representing D_2O at 2.0 µm) and an illumination intensity of I_{ill} = 40 mW/cm² gives[24]:

$$\dot{q}_{\text{V}}(z) = 400\ \text{mW/cm}^3 \cdot \exp\left(-\frac{z}{1\ \text{mm}}\right)$$

- Plasmonic heating and electrolyte heating with a penetration depth of 1.2 µm as it occurs in H_2O at 2.8 µm are both modeled by a heating vector, which has a single non-zero entry at its first position (referred to as "surface heating" in the following):

$$\dot{q}_{\text{V}}(0) = \frac{I_{\text{ill}}}{dz} = 80000\ \text{mW/cm}^3$$
$$\dot{q}_{\text{V}}(z \neq 0) = 0$$

This representation is also justified for the 1.2 µm light penetration depth, as it cannot be resolved by a simulation with dz=5 µm.

Furthermore, a case named "combined heating" is analyzed. It is the linear combination of an electrolyte heating vector with d_{ill} =1000 µm and a surface heating vector, which is scaled with a factor ν in order to achieve similar impact of both mechanisms:

$$\dot{q}_{\text{V}}(0) = \nu \cdot 80000\ \text{mW/cm}^3 + 400\ \text{mW/cm}^3 \cdot \exp\left(-\frac{z}{1\text{mm}}\right)$$
$$\dot{q}_{\text{V}}(z \neq 0) = 400\ \text{mW/cm}^3 \cdot \exp\left(-\frac{z}{1\text{mm}}\right)$$

An exemplary heating power profile with $d_{\text{ill}} = 100$ µm as well as the boundary conditions are shown in figure 6.22(a).

The actual simulations start with the situation of δT = 0 in all points. Then, the described system of equations (6.14 and 6.15) including the respective heating vector is solved for $\frac{1}{2Fdt}$ timesteps (with F being the chopping frequency). After this half-period with heating, the illumination is switched off, which is represented by an additional number of $\frac{1}{2Fdt}$ timesteps with $\dot{q}_{\text{V}}(z)$ = 0. Since the temperature increases after such a period are not 0 again, one encounters a long-term behavior, which is typically approached within a few periods. In order to be sure to evaluate the behavior in the quasi-equilibrium state, 20 periods were calculated for each parameter set and the peak-to-peak amplitudes of the interface temperature in the 20th period were analyzed. Figure 6.22(b) shows such temperature distributions at the end of the 20th heating period, respectively of the 20th cooling period for illumination with a penetration depth of 100 µm, an interfacial thermal conductance of G = 4 kW/m^{2}K and a chopping frequency of 3.33 Hz. Although the heating power density is maximal at z = 0, the cooling power of the boundary condition leads to the observation that the temperature maximum is shifted to z = 80 µm.

A very important parameter is the interfacial thermal conductance G and there is no obvious choice for it. If one models a finite connection to an infinite heat sink over a water/metal/semiconductor interface with G = 20 MW/m^{2}K as a typical value for metal-semiconductor interfaces estimated according to [Lye06] and of G = 100 MW/m^{2}K for a hy-

---

[24] Note that not the complete incoming power is absorbed in a volume with 500 µm thickness, a part is transmitted and the total heat influx into the calculation area is lower than for the other situations.

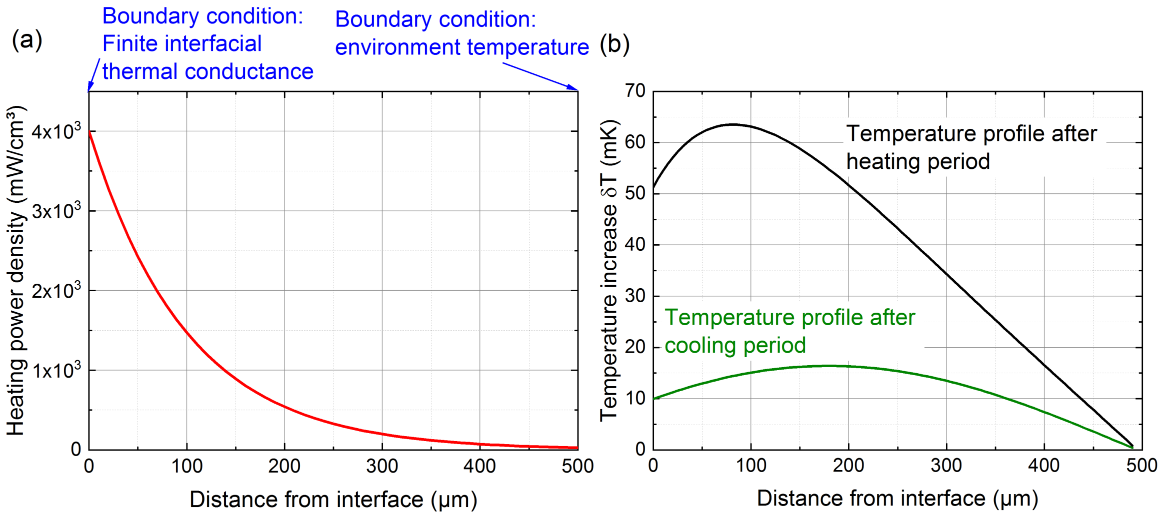

Figure 6.22: (a) Spatial distribution of the exponentially decaying heating power density with d_{ill} =100 µm (red) and boundary conditions (blue). (b) Temperature profile after the 20th heating period (black) and after the subsequent cooling period (green) using a frequency of 3.33 Hz and an interfacial thermal conductance of 4 kW/m^{2}K. Note, that δT represents the temperature increase with respect to the environment here.

drophilic metal-water interface [Ge06] (combining both values in a series connection), one would only get a maximum interface temperature increase of

$$\Delta T\Big|_{\mathrm{interface}} = \frac{\dot{Q}_{\mathrm{int}}}{G} = 24\,\mu K \qquad (6.16)$$

for an effective heating intensity of 40 mW/cm². Even when considering the thermal resistance of a 400 µm thick Si substrate with $G = 400$ kW/m^{2}K in addition to the electrolyte/Au/Ti/SiO$_2$/Si interface, one would end up with a temperature variation of 1 mK.

If the typical relative modulations of the current density up to the 10^{-3} range (as a low chopping frequency limit according to, e.g., figure 6.15) with an estimated temperature effect in the range of 1%/K (cf. section 6.5.3) should be modeled, one would rather need temperature variations in the 100 mK range. This could mean, that simply assuming the Si substrate as a heat sink is not sufficient as probably the heat transport from the substrate into the surrounding may be more decisive. In order to achieve a temperature rise of 100 mK under continuous illumination, one could treat the complete surrounding at the interface side, in particular the heat transport away from the Si/air interface, as an effective interfacial conductance of G = 4 kW/m^{2}K. The numerical values stemming from such a simulation have to be treated with care, but an exact 3D modeling of the complete setup and its surrounding exceeds the scope of this discussion. Still, it is possible to draw qualitative conclusions about consequences of changes in the absorption behavior by exponentially decaying heating power density (representing electrolyte heating) or surface heating (as a model for plasmonic heating).

Figure 6.23(a) shows time transients of the interface temperature increase δT for a chopping frequency of 0.33 Hz and an interfacial thermal conductance of G = 400 kW/m^{2}K derived from the simulations with light absorption in the electrolyte (100 µm and 1 mm penetration depth, intensity 40 mW/cm²), surface heating (intensity: 40mW/cm²) and combined heating (electrolyte heating with 1 mm penetration depth and 40 mW/cm² added to surface heating

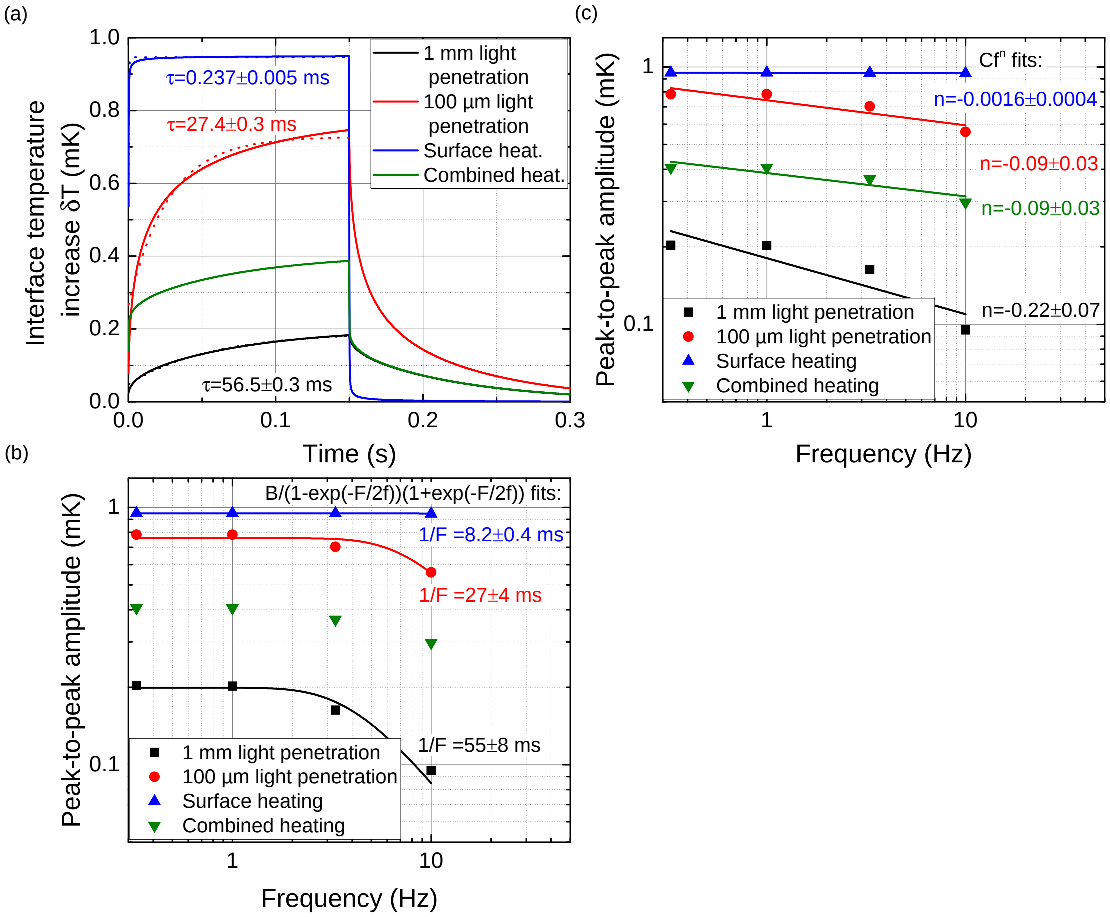

Figure 6.23: (a) Simulated time transients of the interface temperature increase for the 20th heating and cooling period at the Si/H_2O interface heated with an exponentially decaying heating power, penetration depths 100 µm and 1 mm (intensity 40 mW/cm²) as well as surface heating (intensity 40 mW/cm²) and combined heating (electrolyte heating with 40 mW/cm² and surface heating with 8.6 mW/cm²) at a chopping frequency of 3.33 Hz. For the first three curves, the dashed lines represent exponential fits of the heating period, they are shown together with the resulting fitted time constant. The peak-to-peak temperature amplitudes derived from these simulations as a function of the frequency are shown with (b) $B\frac{1-\exp(-F/2f)}{1+\exp(-F/2f)}$ fits (only for the curves with one single heating mechanism) and (c) $C \cdot f^n$ fits. The interfacial thermal conductance was $G = 400\,\mathrm{kW/m^2K}$.

with 8.6 mW/cm² were chosen since they contribute equally to the temperature amplitude at 0.33 Hz). One can see that the interface temperature increased during the first half-period with illumination (0 - 0.15 s)[25] and asymptotically approached a certain equilibrium level. During the second half-period (0.15 - 0.3 s), it relaxed to the initial value again. A more localized heat deposition indeed increased the temperature amplitude (although much less than proportional) and led to a shorter effective timescale. Analogously to the analytical model from above (cf. figure 6.20), one would assume an exponential behavior in time for conditions with a cooling power proportional to the temperature increase. Especially for the curve with 1 mm light penetration, this condition was well fulfilled; for the ones with 100 µm light penetration and surface heating, there were deviations from the exponential behavior. The

---

[25] The point $t = 0$ was set to the beginning of the 20th period, the first 19 periods with a total duration of 5.7 s are not shown.

simulated curve shape did not saturate in the same way as a real exponential function, but on a much longer timescale, because the regions of the calculation area further away from the interface warmed up more slowly. Nevertheless, the resulting exponential fits to the first half-period of the time transients yielded 1/e-timescales of 56.5 ms (d_{ill} = 1 mm), 27.4 ms (d_{ill} = 100 µm) and 0.237 ms (surface heating). This fit was not done for the case of combined heating, which consisted of two heating mechanisms with different spatial and temporal characteristic; it was therefore not reasonable to fit the corresponding curve with one timescale. Remarkably, one can well see in the curve of combined heating, how the very fast impact of the surface heating led to jumps after switching the illumination on (0 s) and off (0.15 s), while the rest of the transient was parallel to the curve with 1 mm light penetration.

In order to shed light on the frequency behavior of the different heating mechanisms, the length of the illumination period or the chopping frequency, respectively, was varied and the minimum and maximum values of the 20th cycle were then used to extract the peak-to-peak amplitude of the temperature. Corresponding to the analytical model from equation 6.10, a $B\frac{1-\exp(-F/2f)}{1+\exp(-F/2f)}$ fit to the resulting frequency series (figure 6.23(b)) was performed. While the $1/F$ timescales for d_{ill} = 1 mm and d_{ill} = 100 µm (55 ms and 27 ms) quite well corresponded to the values from the exponential fits, the timescale of 8.2 ms for surface heating did not fit to the value from above. Using the mentioned parameters, the analytical model was therefore only suitable to describe electrolyte heating, but not surface heating. The most striking deviation between the simulated curves and the analytical model lay in a quick approach of a $1/F$-dependence of the peak-to-peak amplitude for higher frequencies f (a shift from a constant to the $1/F$-dependence within a factor of 10 in the chopping frequency, cf. also figure 6.21) by the $B\frac{1-\exp(-F/2f)}{1+\exp(-F/2f)}$ curve in contrast to a flatter behavior of the simulated data points. The simple $C\cdot f^n$ function, which was used to fit the same dataset in figure 6.23(c), also showed a distinct variation in the exponent n depending on the heating mechanism. While it was -0.22 for d_{ill} = 1 mm, it became -0.09 for d_{ill} = 100 µm and -0.0016 for surface heating. The combined heating, which consisted of contributions with d_{ill} = 1 mm and surface heating, led to a value of -0.09, which lay between the values of the involved heating mechanisms. Compared to the analytical model, the $C\cdot f^n$ fit did not reproduce the saturation of the simulated curves for low frequencies, but it could appropriately model the behavior for higher frequencies.

At this point, it should be noted that this saturation for low frequencies was only observed due to the boundary conditions of the simulations, which assumed a constant temperature outside the boundaries. In the experiment, the environment also slightly heated up, so that it took much longer to achieve a stable temperature and to reach a saturation for low chopping frequencies. This argument was supported by additional simulations (not shown here), in which a prolongation of the simulation grid led to a more $C\cdot f^n$-like behavior of the frequency series. Therefore, due to the assumption that surface and electrolyte heating simultaneously occurred in the experiments, and since a more simple fitting function is generally preferable, the experiments in section 6.4.3 were also fitted by a $C\cdot f^n$ function. Although the n values from the simulations had lower absolute values than the experimental ones - probably due to an oversimplification of the situation in the simulations (especially the approximation of the electrolyte/Au/Ti/SiO_2/Si/air "interface" by an effective interfacial thermal conductance at G) - they showed that heating closer to the surface indeed led to a less negative value of n.

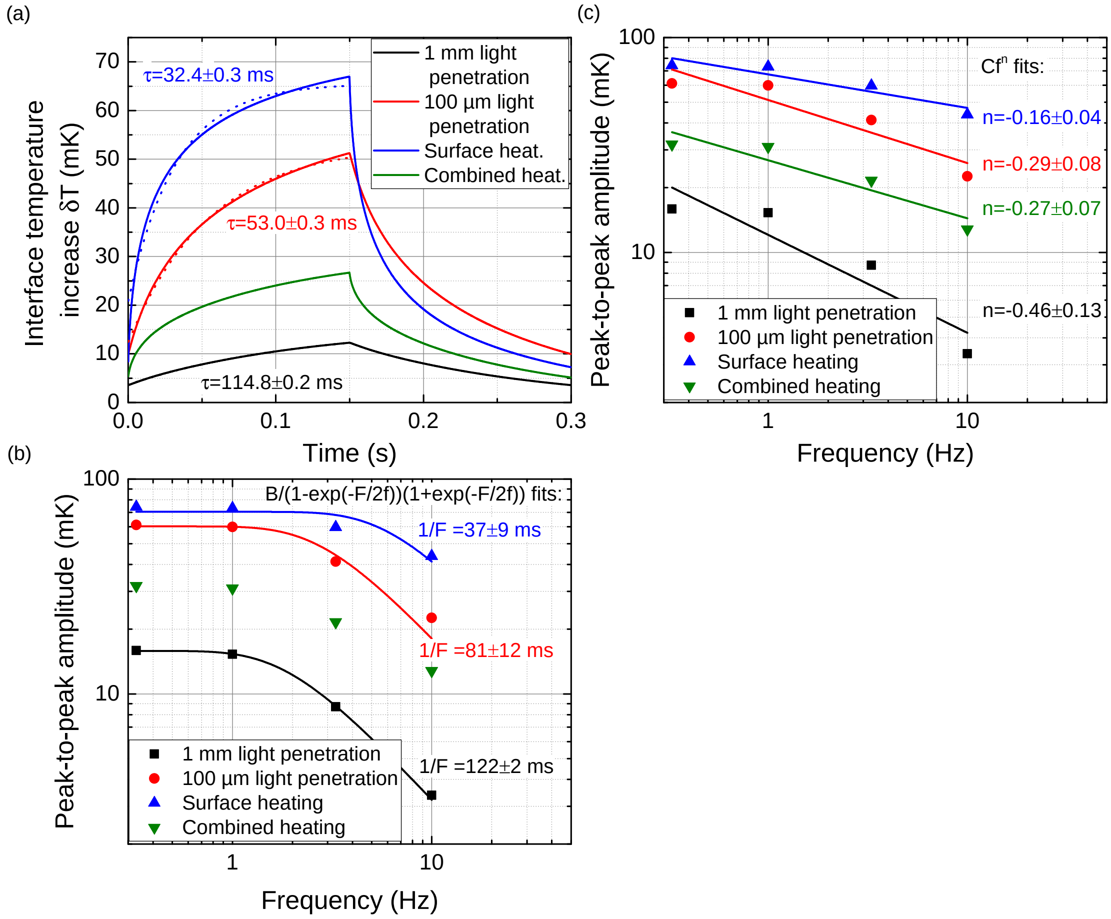

Figure 6.24: (a) Simulated time transients of the interface temperature increase for the 20th heating and cooling period at the Si/H_2O interface heated with an exponentially decaying heating power, penetration depths 100 µm and 1 mm (intensity 40 mW/cm²) as well as surface heating (intensity 40 mW/cm²) and combined heating (electrolyte heating with 40 mW/cm² and surface heating with 8.6 mW/cm²) at a chopping frequency of 3.33 Hz. For the first three curves, the dashed lines represent exponential fits of the heating period, they are shown together with the resulting fitted time constant. The peak-to-peak temperature amplitudes derived from these simulations as a function of the frequency are shown with (b) $B\frac{1-\exp(-F/2f)}{1+\exp(-F/2f)}$ fits (only for the curves with one single heating mechanism) and (c) $C \cdot f^n$ fits. The interfacial thermal conductance was $G = 4$ kW/m^{2}K.

According to the argumentation that the experiments suggested a temperature increase close to 100 mK, the simulations were repeated with an interfacial thermal conductance of $G = 4$ kW/m^{2}K. Under this condition, the time transients of the temperature in figure 6.24(a) were even better approximated by exponential fitting curves, which led to increased time constants of 114.8 ms ($d_{\text{ill}} = 1$ mm), 53.0 ms ($d_{\text{ill}} = 100$ µm) and 32.4 ms (surface heating). This can be rationalized by the reduced heat transport over the interface at $z = 0$, which caused a higher share of the heat energy to flow through the electrolyte taking more time. Also the $B\frac{1-\exp(-F/2f)}{1+\exp(-F/2f)}$ fits to the resulting frequency series in figure 6.24(b) confirmed this trend: They yield $1/F$ time constants of 122 ms ($d_{\text{ill}} = 1$ mm), 81 ms ($d_{\text{ill}} = 100$ µm) and 37 ms (surface heating). Here, the discrepancy between the time constant values of the surface heating was much smaller than in the case of $G = 400$ kW/m^{2}K. This was reasonable since a significant share of heat has to flow through the electrolyte now, leading to a more comparable time transient.

The $C \cdot f^n$ fits in figure 6.24(c) yielded values of n = -0.46 for d_{ill} = 1 mm, n = -0.29 for d_{ill} = 100 µm, n = -0.16 for surface heating and n = -0.27 for combined heating. This reproduced the trend that n became more negative for heating closer to the interface, but the n values were generally much more negative than in figure 6.23(c) and were therefore more similar to the ones in the experiments. Together with the observation that the absolute temperature amplitudes were closer to the ones of the experiment (which were estimated from the Au stripe measurements in figure 6.13 and from relative current variations in the 10^{-3} range corresponding to temperature amplitudes around 100 mK), it seems that the second dataset better reproduced the complex boundaries of the real experiment.

6.5.4 Origin of plasmonic effects

This theoretical foundation shall now be used to interpret the experiments with respect to the origin of the observed plasmonic effect. As the fitted exponent n of the frequency series seems to give valuable information about the involved timescales, it is the major parameter for the following interpretation.

Using the non-resonant samples with 1400 nm structure size, the values of n varied between -0.77 and -0.98 (cf. figure 6.15). Looking at figure 6.16 obtained with the 420 nm structures, which were plasmonically resonant to molecular CO_2 vibrations at 2.8 µm, one can see that there is a reduction of n from values between -0.92 and -1.01 at 2.0 µm illumination wavelength to values between -0.68 and -0.55 at 2.8 µm. This can be observed in Ar-saturated 50 mM H_2SO_4 in D_2O as well as in CO_2-saturated 50 mM K_2CO_3 in D_2O. This indicates that there is a plasmonic effect on the electrochemical reactions and that it is also there without CO_2 present. The even lower absolute value of the exponent of n=-0.55 in K_2CO_3 with CO_2 could be a hint that there is indeed a contribution of a resonant excitation of molecular vibrations in CO_2-saturated K_2CO_3. Nevertheless, in the measurements at hand, the difference is within the error tolerance. Hence, the observation should be verified with optimized experiments using a stronger light source. Again, it has to be noted that all samples showed severe degradation resulting in a shift of the plasmonic resonance from 2.8 µm to 2.6 µm (cf. also figure 6.8), which also contributes to the variations between the measurements.

The hypothesis that plasmonic heating causes a major contribution to the current enhancement under illumination is also substantiated by the series with the 260 nm sample (figure 6.17): In both electrolytes, the absolute value of the slope is significantly reduced when the illumination wavelength is changed from 2.8 µm to 2.0 µm, where it excites the plasmonic resonance. This is in line with the simulations of plasmonic heating. Since 2.0 µm is not the wavelength of the above mentioned CO_2 vibration modes, it is another hint that an enhanced CO_2RR rate by excitation of these modes is not the dominating effect in our experiments. However, we cannot exclude from our data that molecular vibrations of H_2O molecules, which are excited by the enhanced field in the vicinity of the LSPRs, contribute to a current increase by a reduced energy barrier for H_2O dissociation in an analogous process as one explained above for vibrational modes of CO_2.

In comparison to these measurements, the frequency curves derived from the simulations are generally less steep (cf. section 6.5.3) and the absolute values of the temperature increase from the simulations have to be treated with care, but they clearly show that a heat dissipa-

tion closer to the electrolyte/electrode interface leads to a strong reduction of this slope in the frequency dependence. The simulations could also show that the n value resulting from a "combined heating" vector, consisting of a summation of pure electrolyte heating and pure surface heating, lies between the values for the individual heating mechanisms.
Summarizing the above results, one can observe distinct intervals of the parameter n for experiments with plasmonic resonances ($-0.70 \leq n \leq -0.51$) and non-resonant measurements ($-1.01 \leq n \leq -0.77$), although there is a strong variation between the individual measurements. This is not in line with the postulated effect of a resonant excitation of molecular vibrations. Such an excitation is predicted to follow an exponential temporal behavior, leading to a frequency dependence of the amplitude of the form $B\frac{1-\exp(-F/2f)}{1+\exp(-F/2f)}$ as predicted in section 6.5.3. In addition, the effect would feature typical timescales of fs to ns, so that it would appear as an instantaneous excitation without frequency dependence on a Hz scale. Since our measurements do not saturate on a frequency-independent plateau and do not systematically depend on the presence of CO_2, they suggest plasmonic heating as the dominant plasmonic mechanism. Nevertheless, it cannot be excluded that other plasmonic effects, in particular the transfer of hot electrons from the metal structures into the adjacent molecules, are present, but they would also be predicted to appear frequency-independent for the chopping frequencies used here. Following the same argumentation as for the molecular vibrations, these processes do not significantly contribute to the observed current increase. The latter two effects could also be reduced significantly by the incoherent illumination used, which induces much less field enhancement than a coherent light source.
When the absolute values of the current modulations are compared to those, which were estimated using the temperatures values from the resistive measurements in figure 6.11, one can find that both lie in the 10^{-4} range (assuming an influence of temperature on the current density in the %/K range as derived in section 6.5.3, in particular by equation 6.4). Although the geometries of both experiments and the corresponding geometry of heat transport differ significantly, this observation supports the plausibility of the explanation of the described behavior via temperature modulations.

6.6 Summary and outlook

This chapter dealt with the question, if and how LSPRs can influence electrochemical reactions, in particular by resonantly exciting molecular vibrations in CO_2, which could reduce the energy barrier for the dissociation of these molecules. In addition, plasmonic heating can also lead to an increased reaction rate by accelerated kinetics.
In order to resonantly excite molecular vibration modes by LSPRs, it is necessary to tune the plasmonic resonance wavelength to the one of the chosen molecular vibration. Therefore, it was shown that it is possible to tune the plasmonic resonances of Au nanostructures from the visible range into the near-infrared by changing their size using the method of Lift-Off Nanoimprint Lithography. Various parameters, in particular structure diameter, aspect ratio (diameter/thickness), interface quality as well as the dielectric environment were observed to influence the resonance wavelengths of the structures. The dependence of the LSPRs on these properties was characterized by reflectivity measurements, which were very well confirmed by FDTD simulations.

Fabricating structures with a resonance in the short wavelength infrared range allowed us to test the postulated enhancement of the reaction rate of the CO_2RR by resonant excitation of bending vibrations using potentiostatic electrolysis experiments with chopped illumination. It could indeed be shown that plasmonic resonances can measurably influence electrochemical reactions, which is a worthwhile proof of principle. The frequency dependence of the measured current modulations differed between illumination wavelength in and out of the plasmonic resonance. However, the modulation amplitude did not saturate for high frequencies and a change in the chopping frequency dependence in the presence of LSPRs appeared for plasmonic resonances both in resonance with the molecular vibrations and outside. Therefore, we concluded that plasmonic heating is the main source of the observed current modulation. This interpretation was further supported by analytical and numerical modeling of the involved heat transport, which also resulted in a change of the frequency dependence between situations with and without plasmonic heating.

The main problem connected to the experiments shown was an unfavorable relation between modulation amplitude and the size of errors in the experiment. However, many improvements of the setup would be possible. So far, the experiments were only conducted using a spectrally filtered halogen lamp, which is orders of magnitudes less intensive than modern laser sources. Therefore, a repetition of the experiments with a more sophisticated setup would promise much more detailed insights. The use of a laser source with a continuous wave power of 1 W would not only increase all signals by a factor of 30, it would also be more monochromatic (this means that a larger share of the photons goes into the respective resonances) and coherent, which should be beneficial for an actual field enhancement. For the evaluation of a possible excitation of molecular vibrations, it would be even more valuable to use a laser, which is tunable over a range of 100-200 nm, e.g. by using optical parametrical amplification (OPA). This could then be used to spectrally tune the laser over the molecular resonance and check for a resulting wavelength-dependence of the current modulation.

On the other hand, if the focus should be shifted to a more thorough investigation of plasmonic heating, it would be possible to optimize the setup towards an application in the NIR, more precisely the region between 1200 nm and 1500 nm. In this region, cheap and powerful fiber lasers at wavelengths around 1500 nm [Min90, Spi04] and in the range of 1300 nm to 1400 nm are available. Even the spectral power of the current halogen lamp would be significantly higher in this spectral region. The strong reduction of absorption of infrared radiation in H_2O below 1500 nm wavelength (more than 1 mm penetration depth according to figure 6.12) is very beneficial as it reduces direct electrolyte heating. This would in turn allow for the avoidance of D_2O, which would drastically simplify the experiment and improve the cleanliness. Furthermore, a LSPR in this wavelength region corresponding to a structure size around 180 nm should be more intensive than for longer wavelengths. In order to quantify the influence of plasmonic heating on the reaction kinetics, it would also be necessary to calibrate the temperature dependence of the examined reaction current using a precise thermostat.

Another interesting experiment would be the use of a pulsed laser with very high pulse intensities, which would permit to reach surface temperatures 10 or 20 K above the environment temperature for very short times. Thus, one could reach a non-linear region of the current response to the temperature according to equation 6.4. The resulting intensity dependence would then allow one to draw valuable conclusions about the involved plasmonic effects, in particular plasmonic heating.

It is also known that the field enhancement in plasmonic hot spots is drastically increased for smaller inter-particle distances and at sharp edges [Li15]. Therefore, it would be promising to optimize the nanostructures accordingly by systematic simulations, a new NIL stamp designed this way and an improvement of the LO-NIL process towards sharper edges and shorter inter-particle distances. Even if the structure edges can only be slightly sharpened, a closer arrangement of the nanostructures will at the same time increase plasmonic effects, and decrease the transmission of light, which would reduce the infrared radiation intensity and consequently the direct electrolyte heating outside the plasmonic hot spots.

Chapter 7

Conclusion

This thesis deals with the reactivity of mesoscopic Au and Cu/Au structures on Si substrates. In particular it examines the impact of electrode structuring with variable feature size on the photoelectrochemical CO_2 reduction activity. The central questions connected to the structure size are twofold: First, it was investigated whether a reduction of feature dimensions leads to an increased cathodic current density and a change in product distribution of electrochemical CO_2RR and HER. Second, the impact of localized surface plasmons, which were tuned to be resonant with molecular vibrations of CO_2, on the CO_2RR was studied. In this context, the hypothesis of accelerated CO_2 dissociation by resonant excitation of molecular vibrations and a resulting enhancement of the electrochemical performance was tested. Since a sensitive product analysis is essential for the investigation of the CO_2RR, a third topic, namely the development, realization and characterization of a cold trap system for DEMS, was presented.

The motivation for this cold trap is that the major gaseous products from the CO_2RR , namely H_2, CH_4, C_2H_4 and CO, are diluted in CO_2 and H_2O for typical product gas mixtures. Since the latter two species lead to a spurious background in the signals from DEMS measurements, a selective freeze-out of them can drastically increase the sensitivity of the method. For this purpose, a novel cold trap, which allows for the detection of H_2, CH_4, C_2H_4 and CO in 1 ml gas samples with detection limits between 0.1 ppm (H_2) and 10 ppm (CO), was developed, built and calibrated during this work. This is a factor of 20-10000 more sensitive than the GC system used so far. In addition, the minimum interval between two electrolyses is reduced from 35 minutes (for GC analysis) to 10 minutes; the remaining time is mainly determined by the electrolyte purging between the electrolyses.

For a quantitative analysis of the results from such measurements, it is necessary to disentangle the signals of the product compounds from six mass channels so that the initial composition of a product gas before injection can be determined. Therefore, sophisticated correction methods were developed for the separation of the individual contributions of each species and also for the consideration of the freeze-out of C_2H_4 in the presence of solid CO_2. Together with a good vacuum system, a stable temperature control and a precise calibration, this allowed us to perform sensitive measurements.

The starting point for the next topic was if the rate of electrochemical reduction reactions on MIS electrodes is influenced by structuring and feature size of the surfaces. In the literature, a significantly enhanced performance of structured MIS electrodes compared to continuous ones had been reported and assigned to an influence of the metal-semiconductor interface [Hin98, Esp13].

In our electrochemical experiments we also found a much higher activity of structured electrodes and a strong size dependence: The overpotential necessary for a certain current density reduced by 140-170 mV for Au structures and 80 mV for Cu/Au structures upon structure size reduction from 1400 nm to 75 nm, while no significant size-induced change of the j-U characteristics was found in "dry" measurements of MIS contacts. Together with the observation that a similar shift was found using Au structures on normally doped and degenerately doped p-Si, we concluded that the MIS interface did not significantly contribute to the measured size dependence. Remarkably, the measured current was almost proportional to the total edge length of the structures. Consequently, the experiments suggest that an electrochemical process occurring at the three-phase boundary between SiO_2, Au or Cu and electrolyte was responsible for the enhanced activity of the electrodes with decreasing metal structure sizes. This explanation including an electrochemical origin of the overpotential reduction with decreasing feature size was further supported by a shift of the product distribution of CO_2RR to more H_2 and less carbon based products (CH_4, C_2H_4 and CO) both on pure and Cu-plated Au structures with decreasing diameter.

One convincing explanation for this behavior is a bifunctional mechanism, which occurs for HER in alkaline environment. It involves the dissociation of H_2O molecules at the three-phase boundary between electrolyte, Au or Cu and SiO_2 or $Si(OH)_x$ with subsequent H_2 formation from adsorbed H^* on the metal and reduction of OH to OH^- on the $SiO_2/Si(OH)_x$ surface (cf. also [Sub11]). Alternatively, the effect can be explained by a shift of the potential of zero free charge (pzfc) on the metal surface by the adjacent SiO_2 surface. Such a shift of the pzfc closer towards potentials, where the HER occurs, could reduce the reorganization energy for the interfacial water network and consequently accelerate the electrochemical reactions [LY17].

The subject of the last chapter of this thesis was the question if and how LSPRs influence electrochemical reaction rates. Also these resonances occur on Au nanostructures and depend on the structure size. By varying the geometrical properties of Au nanodisks and nanosquares supported on Si, it is possible to tune the LSPRs from the visible into the short-wavelength infrared range. Using the sample fabrication method of Lift-Off Nanoimprint Lithography, we could modify various parameters, in particular structure diameter, aspect ratio (diameter/thickness), interface quality as well as the dielectric environment. It was found in reflectivity measurements that all these properties influence the LSPRs. The experimental results were very well confirmed by FDTD simulations.

In particular, the control of the sample fabrication parameters allowed the LSPRs to be adjusted to a molecular vibration mode of CO_2 at 2.8 µm wavelength. The hypothesis of an enhanced CO_2 dissociation by resonant excitation of bending vibrations was tested using potentiostatic electrolysis experiments with chopped illumination. A small plasmonic activity enhancement was indeed measured. However, a modified frequency dependence, which is consistent to plasmonic heating, is observed in a wide parameter range - with and without CO_2 and for structures with different resonance wavelengths. This suggests that plasmonic heating rather than the target excitation of a particular molecular vibration of CO_2 is the major source for the increased activity of the samples under resonant illumination. It could however still be possible to prove a contribution of directly excited CO_2 vibrations to the observed current increase if a further optimization of the experimental conditions can increase the signal-to-noise ratio and make the measurements more reproducible.

Finally, one can conclude, that each of the three topics of this work can give a small contribution to the scientific field of artificial photosynthesis: First, the development of a cold trap attached to a DEMS system allows for very sensitive and fast measurements of typical product gases from the CO_2RR. Second, an improved understanding of the overpotential reduction observed for the HER on Au and Cu/Au nanostructures with decreasing size in slightly alkaline environment can be useful for the development of efficient HER catalysts in alkaline media. Third, the studies about the impact of plasmonic heating on electrochemical reactions may not lead to an application, but make up a valuable puzzle piece for the fundamental understanding of plasmonic processes in electrochemical environment.

List of publications

[1] B. Stoib, S. Filser, N. Petermann, H. Wiggers, M. Stutzmann, and M. S. Brandt: *Thermal conductivity of mesoporous films measured by Raman spectroscopy*, Applied Physics Letters **104**, 161907 (2014).

[2] B. Stoib, S. Filser, J. Stötzel, A. Greppmair, N. Petermann, H. Wiggers, G. Schierning, M. Stutzmann, and M. S. Brandt: *Spatially resolved determination of thermal conductivity by Raman spectroscopy*, Semiconductor Science and Technology **29**, 124005 (2014).

[3] R. D. Nagel, S. Filser, T. Zhang, A. Manzi, K. Schönleber, J. Lindsly, J. Zimmermann, T. L. Maier, G. Scarpa, K. Krischer, and P. Lugli: *Nanoimprint methods for the fabrication of macroscopic plasmonically active metal nanostructures*, Journal of Applied Physics **121**, 084305 (2017).

[4] S. P. Schwaminger, R. Surya, S. Filser, A. Wimmer, F. Weigl, P. Fraga-García, and S. Berensmeier: *Formation of iron oxide nanoparticles for the photooxidation of water: Alteration of finite size effects from ferrihydrite to hematite*, Scientific Reports **7** (2017).

[5] S. Filser, T. L. Maier, R. D. Nagel, W. Schindler, P. Lugli, M. Becherer, and K. Krischer: *Photoelectrochemical reactivity of well-defined mesoscale gold arrays on* SiO_2 */Si substrates in* CO_2*-saturated aqueous electrolyte*, Electrochimica Acta **268**, 546 (2018).

Bibliography

[Adl09] J. R. Adleman, D. A. Boyd, D. G. Goodwin, and D. Psaltis: *Heterogenous Catalysis Mediated by Plasmon Heating*, Nano Letters **9**, 4417 (2009).

[Age15] J. W. Ager, M. R. Shaner, K. A. Walczak, I. D. Sharp, and S. Ardo: *Experimental demonstrations of spontaneous, solar-driven photoelectrochemical water splitting*, Energy Environ. Sci. **8**, 2811 (2015).

[ALSA17] Air-Liquide-S.-A.: *Gas Encyclopedia Air Liquide*, https://encyclopedia.airliquide.com/ (2017).

[Ani74] S. Anisimov, B. Kapeliovich, and T. Perel'man: *Electron emission from metal surfaces exposed to ultrashort laser pulses*, Soviet Phys. JETP **39**, 375 (1974).

[Aou09] H. Aouani, J. Wenger, D. Gérard, H. Rigneault, E. Devaux, T. W. Ebbesen, F. Mahdavi, T. Xu, and S. Blair: *Crucial Role of the Adhesion Layer on the Plasmonic Fluorescence Enhancement*, ACS Nano **3**, 2043 (2009).

[Ava14] T. Avanesian and P. Christopher: *Adsorbate Specificity in Hot Electron Driven Photochemistry on Catalytic Metal Surfaces*, The Journal of Physical Chemistry C **118**, 28017 (2014).

[Bat92] N. Batina, T. Will, and D. M. Kolb: *Study of the initial stages of copper deposition by in situ scanning tunnelling microscopy*, Faraday Discussions **94**, 93 (1992).

[Bay63] J. Bayly, V. Kartha, and W. Stevens: *The absorption spectra of liquid phase H_2O, HDO and D_2O from 0.7 µm to 10 µm*, Infrared Physics **3**, 211 (1963).

[BH14] M. E. Boot-Handford, J. C. Abanades, E. J. Anthony, M. J. Blunt, S. Brandani, N. Mac Dowell, J. R. Fernández, M.-C. Ferrari, R. Gross, J. P. Hallett, R. S. Haszeldine, P. Heptonstall, A. Lyngfelt, Z. Makuch, E. Mangano, R. T. J. Porter, M. Pourkashanian, G. T. Rochelle, N. Shah, J. G. Yao, and P. S. Fennell: *Carbon capture and storage update*, Energy Environ. Sci. **7**, 130 (2014).

[Boh04] C. F. Bohren and D. R. Huffman: *Absorption and scattering of light by small particles*, Wiley-VCH, Weinheim (2004).

[Bor16] T. Bora, D. Zoepfl, and J. Dutta: *Importance of Plasmonic Heating on Visible Light Driven Photocatalysis of Gold Nanoparticle Decorated Zinc Oxide Nanorods*, Scientific Reports **6**, 26913 (2016).

[Bra89] S. G. Bratsch: *Standard Electrode Potentials and Temperature Coefficients in Water at 298.15 K*, Journal of Physical and Chemical Reference Data **18**, 1 (1989).

[Bru71] S. Bruckenstein and R. R. Gadde: *Use of a porous electrode for in situ mass spectrometric determination of volatile electrode reaction products*, Journal of the American Chemical Society **93**, 793 (1971).

[Bru11] T. Bruelle, W. Ju, P. Niedermayr, A. Denisenko, O. Paschos, O. Schneider, and U. Stimming: *Size-Dependent Electrocatalytic Activity of Gold Nanoparticles on HOPG and Highly Boron-Doped Diamond Surfaces*, Molecules **16**, 10059 (2011).

[Car91] J. J. Carroll, J. D. Slupsky, and A. E. Mather: *The Solubility of Carbon Dioxide in Water at Low Pressure*, Journal of Physical and Chemical Reference Data **20**, 1201 (1991).

[Cav17] F. Cavalca, R. Ferragut, S. Aghion, A. Eilert, O. Diaz-Morales, C. Liu, A. L. Koh, T. W. Hansen, L. G. M. Pettersson, and A. Nilsson: *Nature and Distribution of Stable Subsurface Oxygen in Copper Electrodes During Electrochemical CO_2 Reduction*, The Journal of Physical Chemistry C **121**, 25003 (2017).

[Cha01] W.-J. Chang, M.-P. Houng, and Y.-H. Wang: *Electrical properties and modeling of ultrathin impurity-doped silicon dioxides*, Journal of Applied Physics **90**, 5171 (2001).

[Che74] J. R. Chelikowsky and M. L. Cohen: *Electronic structure of silicon*, Physical Review B **10**, 5095 (1974).

[Che08] X. Chen, H. Zhu, J. Zhao, Z. Zheng, and X. Gao: *Visible Light Driven Oxidation of Organic Contaminants in Air with Gold Nanoparticle Catalysts on Oxide Supports*, Angewandte Chemie **120**, 5433 (2008).

[Che15a] C. S. Chen, A. D. Handoko, J. H. Wan, L. Ma, D. Ren, and B. S. Yeo: *Stable and selective electrochemical reduction of carbon dioxide to ethylene on copper mesocrystals*, Catalysis Science & Technology **5**, 161 (2015).

[Che15b] Y. Chen, K. Sun, H. Audesirk, C. Xiang, and N. S. Lewis: *A quantitative analysis of the efficiency of solar-driven water-splitting device designs based on tandem photoabsorbers patterned with islands of metallic electrocatalysts*, Energy & Environmental Science **8**, 1736 (2015).

[Chi98] M. Gennero de Chialvo and A. Chialvo: *Kinetics of hydrogen evolution reaction with Frumkin adsorption: re-examination of the Volmer–Heyrovsky and Volmer–Tafel routes*, Electrochimica Acta **44**, 841 (1998).

[Cho97] A. I. Chou, K. Lai, K. Kumar, P. Chowdhury, and J. C. Lee: *Modeling of stress-induced leakage current in ultrathin oxides with the trap-assisted tunneling mechanism*, Applied Physics Letters **70**, 3407 (1997).

[Chr11] P. Christopher, H. Xin, and S. Linic: *Visible-light-enhanced catalytic oxidation reactions on plasmonic silver nanostructures*, Nature Chemistry (2011).

[Chr12] P. Christopher, H. Xin, A. Marimuthu, and S. Linic: *Singular characteristics and unique chemical bond activation mechanisms of photocatalytic reactions on plasmonic nanostructures*, Nature Materials **11**, 1044 (2012).

[Cla14] C. Clavero: *Plasmon-induced hot-electron generation at nanoparticle/metal-oxide interfaces for photovoltaic and photocatalytic devices*, Nature Photonics **8**, 95 (2014).

[Cos01] F. Cosandey and T. E. Madey: *GROWTH, MORPHOLOGY, INTERFACIAL EFFECTS AND CATALYTIC PROPERTIES OF Au ON* TiO_2, Surface Review and Letters **08**, 73 (2001).

[Dan12] N. Danilovic, R. Subbaraman, D. Strmcnik, K.-C. Chang, A. P. Paulikas, V. R. Stamenkovic, and N. M. Markovic: *Enhancing the Alkaline Hydrogen Evolution Reaction Activity through the Bifunctionality of* $Ni(OH)_2$ */Metal Catalysts*, Angewandte Chemie **124**, 12663 (2012).

[Daw76] P. H. Dawson (ed.): *Quadrupole mass spectrometry and its applications*, North-Holland Publ. Co, Amsterdam (1976), oCLC: 2332072.

[DDBSSTG17] Dortmund-Data-Bank-Software-&-Separation-Technology-GmbH: *Dortmund Data Bank*, www.ddbst.com/en/EED/PCP/VAP C1050.php (2017).

[DeW89] D. W. DeWulf: *Electrochemical and Surface Studies of Carbon Dioxide Reduction to Methane and Ethylene at Copper Electrodes in Aqueous Solutions*, Journal of The Electrochemical Society **136**, 1686 (1989).

[Dun17] M. Dunwell, Q. Lu, J. M. Heyes, J. Rosen, J. G. Chen, Y. Yan, F. Jiao, and B. Xu: *The Central Role of Bicarbonate in the Electrochemical Reduction of Carbon Dioxide on Gold*, Journal of the American Chemical Society **139**, 3774 (2017).

[Dut18] A. Dutta, C. E. Morstein, M. Rahaman, A. Cedeño López, and P. Broekmann: *Beyond Copper in* CO_2 *Electrolysis: Effective Hydrocarbon Production on Silver-Nanofoam Catalysts*, ACS Catalysis **8**, 8357 (2018).

[Ebb98] T. W. Ebbesen, H. J. Lezec, H. F. Ghaemi, T. Thio, and P. A. Wolff: *Extraordinary optical transmission through sub-wavelength hole arrays*, Nature **391**, 667 (1998).

[Eil16] A. Eilert, F. S. Roberts, D. Friebel, and A. Nilsson: *Formation of Copper Catalysts for* CO_2 *Reduction with High Ethylene/Methane Product Ratio Investigated with In Situ X-ray Absorption Spectroscopy*, The Journal of Physical Chemistry Letters **7**, 1466 (2016).

[Ena89] M. A. Enayetullah: *Activation Parameters for Oxygen Reduction Kinetics in Trifluoromethane Sulfonic Acid Systems*, Journal of The Electrochemical Society **136**, 3369 (1989).

[Esp13] D. V. Esposito, I. Levin, T. P. Moffat, and A. A. Talin: *H_2 evolution at Si-based metal–insulator–semiconductor photoelectrodes enhanced by inversion channel charge collection and H spillover*, Nature Materials **12**, 562 (2013).

[ET19] Engineering-Toolbox: *Engineering ToolBox*, https://www.engineeringtoolbox.com/ (2019).

[Fil18] S. Filser, T. L. Maier, R. D. Nagel, W. Schindler, P. Lugli, M. Becherer, and K. Krischer: *Photoelectrochemical reactivity of well-defined mesoscale gold arrays on SiO_2/Si substrates in CO_2-saturated aqueous electrolyte*, Electrochimica Acta **268**, 546 (2018).

[FNR17] Fachagentur-Nachwachsende-Rohstoffe: *http://biogas.fnr.de/daten-und-fakten/faustzahlen/*, http://biogas.fnr.de/daten-und-fakten/faustzahlen/ (2017).

[Ge06] Z. Ge, D. G. Cahill, and P. V. Braun: *Thermal Conductance of Hydrophilic and Hydrophobic Interfaces*, Physical Review Letters **96** (2006).

[Ger61] H. Gerischer: *Über den Ablauf von Redoxreaktionen an Metallen und an Halbleitern*, Zeitschrift für Physikalische Chemie **27**, 48 (1961).

[Ger95] P. Gerakines, W. Schutte, J. Greenberg, and E. F. van Dishoeck: *The Infrared Band Strengths of H_2O, CO and CO_2 in Laboratory Simulations of Astrophysical Ice Mixtures*, Astronomy and Astrophysics **296**, 810 (1995).

[Gov07] A. O. Govorov and H. H. Richardson: *Generating heat with metal nanoparticles*, Nano Today **2**, 30 (2007).

[Gre08] M. A. Green: *Self-consistent optical parameters of intrinsic silicon at 300 K including temperature coefficients*, Solar Energy Materials and Solar Cells **92**, 1305 (2008).

[Gro18] R. Gross, A. Marx, D. Einzel, and S. Geprägs: *Festkörperphysik - Aufgaben und Lösungen*, De Gruyter Studium, de Gruyter, Berlin Boston (2018), second edn., oCLC: 1013472916.

[Gup06] N. Gupta, M. Gattrell, and B. MacDougall: *Calculation for the cathode surface concentrations in the electrochemical reduction of CO_2 in $KHCO_3$ solutions*, Journal of Applied Electrochemistry **36**, 161 (2006).

[Hö79] J. Hölzl and F. K. Schulte: *Work function of metals*, in J. Hölzl, F. K. Schulte, and H. Wagner (eds.), *Solid Surface Physics*, vol. 85, Springer Berlin Heidelberg, Berlin, Heidelberg (1979), 1–150.

[Hab12] T. G. Habteyes, S. Dhuey, E. Wood, D. Gargas, S. Cabrini, P. J. Schuck, A. P. Alivisatos, and S. R. Leone: *Metallic Adhesion Layer Induced Plasmon Damping and Molecular Linker as a Nondamping Alternative*, ACS Nano **6**, 5702 (2012).

[Hab13] S. N. Habisreutinger, L. Schmidt-Mende, and J. K. Stolarczyk: *Photocatalytic Reduction of CO_2 on TiO_2 and Other Semiconductors*, Angewandte Chemie International Edition **52**, 7372 (2013).

[Hac91] T. Hachiya, H. Honbo, and K. Itaya: *Detailed underpotential deposition of copper on gold(III) in aqueous solutions*, Journal of Electroanalytical Chemistry and Interfacial Electrochemistry **315**, 275 (1991).

[Har90] T. Hartung and H. Baltruschat: *Differential electrochemical mass spectrometry using smooth electrodes: adsorption and hydrogen/deuterium exchange reactions of benzene on platinum*, Langmuir **6**, 953 (1990).

[Har97] M. Haruta: *Size- and support-dependency in the catalysis of gold*, Catalysis Today **36**, 153 (1997).

[Has09] R. S. Haszeldine: *Carbon Capture and Storage: How Green Can Black Be?*, Science **325**, 1647 (2009).

[Hay10] W. M. Haynes, D. R. Lide, and C. Press (eds.): *CRC handbook of chemistry and physics: a ready-reference book of chemical and physical data*, CRC Press, Boca Raton, Fla. (2010), 91st edn., oCLC: 778185226.

[Hay13] B. E. Hayden: *Particle Size and Support Effects in Electrocatalysis*, Accounts of Chemical Research **46**, 1858 (2013).

[Her01] E. Herrero, L. J. Buller, and H. D. Abruña: *Underpotential Deposition at Single Crystal Surfaces of Au, Pt, Ag and Other Materials*, Chemical Reviews **101**, 1897 (2001).

[Hin98] R. Hinogami, Y. Nakamura, S. Yae, and Y. Nakato: *An Approach to Ideal Semiconductor Electrodes for Efficient Photoelectrochemical Reduction of Carbon Dioxide by Modification with Small Metal Particles*, The Journal of Physical Chemistry B **102**, 974 (1998).

[Hoh88] W. Hoheisel, K. Jungmann, M. Vollmer, R. Weidenauer, and F. Träger: *Desorption stimulated by laser-induced surface-plasmon excitation*, Physical Review Letters **60**, 1649 (1988).

[Hor85] Y. Hori, K. Kikuchi, and S. Suzuki: *Production of CO and CH_4 in electrochemical reduction of CO_2 at metal electrodes in aqueous hydrogencarbonate solution.*, Chemistry Letters **14**, 1695 (1985).

[Hor89] Y. Hori, A. Murata, and R. Takahashi: *Formation of hydrocarbons in the electrochemical reduction of carbon dioxide at a copper electrode in aqueous solution*, Journal of the Chemical Society, Faraday Transactions 1: Physical Chemistry in Condensed Phases **85**, 2309 (1989).

[Hor94] Y. Hori, H. Wakebe, T. Tsukamoto, and O. Koga: *Electrocatalytic process of CO selectivity in electrochemical reduction of CO_2 at metal electrodes in aqueous media*, Electrochimica Acta **39**, 1833 (1994).

[Hor02] Y. Hori, I. Takahashi, O. Koga, and N. Hoshi: *Selective Formation of C2 Compounds from Electrochemical Reduction of CO_2 at a Series of Copper Single Crystal Electrodes*, The Journal of Physical Chemistry B **106**, 15 (2002).

[Hor05] Y. Hori, H. Konishi, T. Futamura, A. Murata, O. Koga, H. Sakurai, and K. Oguma: *"Deactivation of copper electrode" in electrochemical reduction of CO2*, Electrochimica Acta **50**, 5354 (2005).

[Jer94] B. Jermann and J. Augustynski: *Long-term activation of the copper cathode in the course of CO_2 reduction*, Electrochimica Acta **39**, 1891 (1994).

[Ji14] L. Ji, M. D. McDaniel, S. Wang, A. B. Posadas, X. Li, H. Huang, J. C. Lee, A. A. Demkov, A. J. Bard, J. G. Ekerdt, and E. T. Yu: *A silicon-based photocathode for water reduction with an epitaxial $SrTiO_3$ protection layer and a nanostructured catalyst*, Nature Nanotechnology **10**, 84 (2014).

[Joh72] P. B. Johnson and R. W. Christy: *Optical Constants of the Noble Metals*, Physical Review B **6**, 4370 (1972).

[Kai77] J. Kaiser and R. Hamming: *Sharpening the response of a symmetric nonrecursive filter by multiple use of the same filter*, IEEE Transactions on Acoustics, Speech, and Signal Processing **25**, 415 (1977).

[Kal14a] M. J. Kale, T. Avanesian, and P. Christopher: *Direct Photocatalysis by Plasmonic Nanostructures*, ACS Catalysis **4**, 116 (2014).

[Kal14b] M. J. Kale, T. Avanesian, H. Xin, J. Yan, and P. Christopher: *Controlling Catalytic Selectivity on Metal Nanoparticles by Direct Photoexcitation of Adsorbate–Metal Bonds*, Nano Letters **14**, 5405 (2014).

[Kan06] S. Kaneco, H. Katsumata, T. Suzuki, and K. Ohta: *Electrochemical Reduction of CO_2 to Methane at the Cu Electrode in Methanol with Sodium Supporting Salts and Its Comparison with Other Alkaline Salts*, Energy & Fuels **20**, 409 (2006).

[Kas15] R. Kas, R. Kortlever, H. Yılmaz, M. T. M. Koper, and G. Mul: *Manipulating the Hydrocarbon Selectivity of Copper Nanoparticles in CO_2 Electroreduction by Process Conditions*, ChemElectroChem **2**, 354 (2015).

[Kem15] E. Kemppainen, A. Bodin, B. Sebok, T. Pedersen, B. Seger, B. Mei, D. Bae, P. C. K. Vesborg, J. Halme, O. Hansen, P. D. Lund, and I. Chorkendorff: *Scalability and feasibility of photoelectrochemical H_2 evolution: the ultimate limit of Pt nanoparticle as an HER catalyst*, Energy & Environmental Science **8**, 2991 (2015).

[Kir16] S. Kirner, P. Bogdanoff, B. Stannowski, R. van de Krol, B. Rech, and R. Schlatmann: *Architectures for scalable integrated photo driven catalytic devices-A concept study*, International Journal of Hydrogen Energy **41**, 20823 (2016).

[Kor15] R. Kortlever, J. Shen, K. J. P. Schouten, F. Calle-Vallejo, and M. T. M. Koper: *Catalysts and Reaction Pathways for the Electrochemical Reduction of Carbon Dioxide*, The Journal of Physical Chemistry Letters **6**, 4073 (2015).

[Kri15] K. Krischer and K. Schönleber: *Physics of energy conversion*, De Gruyter textbook, Walter de Gruyter GmbH & Co. KG, Berlin; Boston (2015).

[Kuh12] K. P. Kuhl, E. R. Cave, D. N. Abram, and T. F. Jaramillo: *New insights into the electrochemical reduction of carbon dioxide on metallic copper surfaces*, Energy & Environmental Science **5**, 7050 (2012).

[Kuh14] K. P. Kuhl, T. Hatsukade, E. R. Cave, D. N. Abram, J. Kibsgaard, and T. F. Jaramillo: *Electrocatalytic Conversion of Carbon Dioxide to Methane and Methanol on Transition Metal Surfaces*, Journal of the American Chemical Society **136**, 14107 (2014).

[Kum12] B. Kumar, M. Llorente, J. Froehlich, T. Dang, A. Sathrum, and C. P. Kubiak: *Photochemical and Photoelectrochemical Reduction of* CO_2, Annual Review of Physical Chemistry **63**, 541 (2012).

[Kuw03] H. Kuwata, H. Tamaru, K. Esumi, and K. Miyano: *Resonant light scattering from metal nanoparticles: Practical analysis beyond Rayleigh approximation*, Applied Physics Letters **83**, 4625 (2003).

[Kuy94] S. Kuyucak and S.-H. Chung: *Temperature dependence of conductivity in electrolyte solutions and ionic channels of biological membranes*, Biophysical Chemistry **52**, 15 (1994).

[Lan06] C. Langhammer, Z. Yuan, I. Zorić, and B. Kasemo: *Plasmonic Properties of Supported Pt and Pd Nanostructures*, Nano Letters **6**, 833 (2006).

[Lee01] H. J. Lee, C. Beriet, R. Ferrigno, and H. H. Girault: *Cyclic voltammetry at a regular microdisc electrode array*, Journal of Electroanalytical Chemistry **502**, 138 (2001).

[Lee06] K.-S. Lee and M. A. El-Sayed: *Gold and Silver Nanoparticles in Sensing and Imaging: Sensitivity of Plasmon Response to Size, Shape, and Metal Composition*, The Journal of Physical Chemistry B **110**, 19220 (2006).

[Li12] Q. Li: *Design and construction of a differential electrochemical mass spectrometry (DEMS) setup for investigating the photoelectrochemical reduction of* CO_2, Diploma Thesis, Technical University of Munich, München (2012).

[Li15] W. Q. Li, G. Wang, X. N. Zhang, H. P. Geng, J. L. Shen, L. S. Wang, J. Zhao, L. F. Xu, L. J. Zhang, Y. Q. Wu, R. Z. Tai, and G. Chen: *Geometrical and morphological optimizations of plasmonic nanoarrays for high-performance SERS detection*, Nanoscale **7**, 15487 (2015).

[Lin99] S. Link and M. A. El-Sayed: *Spectral Properties and Relaxation Dynamics of Surface Plasmon Electronic Oscillations in Gold and Silver Nanodots and Nanorods*, The Journal of Physical Chemistry B **103**, 8410 (1999).

[Lin15] S. Linic, U. Aslam, C. Boerigter, and M. Morabito: *Photochemical transformations on plasmonic metal nanoparticles*, Nature Materials **14**, 567 (2015).

[Liu11] Z. Liu, W. Hou, P. Pavaskar, M. Aykol, and S. B. Cronin: *Plasmon Resonant Enhancement of Photocatalytic Water Splitting Under Visible Illumination*, Nano Letters **11**, 1111 (2011).

[Liu17] C. Liu, M. P. Lourenço, S. Hedström, F. Cavalca, O. Diaz-Morales, H. A. Duarte, A. Nilsson, and L. G. M. Pettersson: *Stability and Effects of Subsurface Oxygen in Oxide-Derived Cu Catalyst for* CO_2 *Reduction*, The Journal of Physical Chemistry C **121**, 25010 (2017).

[LY17] I. Ledezma-Yanez, W. D. Z. Wallace, P. Sebastián-Pascual, V. Climent, J. M. Feliu, and M. T. M. Koper: *Interfacial water reorganization as a pH-dependent descriptor of the hydrogen evolution rate on platinum electrodes*, Nature Energy **2** (2017).

[Lye06] H.-K. Lyeo and D. G. Cahill: *Thermal conductance of interfaces between highly dissimilar materials*, Physical Review B **73** (2006).

[Mag90] O. M. Magnussen, J. Hotlos, R. J. Nichols, D. M. Kolb, and R. J. Behm: *Atomic structure of Cu adlayers on Au(100) and Au(111) electrodes observed by in situ scanning tunneling microscopy*, Physical Review Letters **64**, 2929 (1990).

[Mah18] N. Mahmood, Y. Yao, J.-W. Zhang, L. Pan, X. Zhang, and J.-J. Zou: *Electrocatalysts for Hydrogen Evolution in Alkaline Electrolytes: Mechanisms, Challenges, and Prospective Solutions*, Advanced Science **5**, 1700464 (2018).

[Mai07] S. A. Maier: *Plasmonics: fundamentals and applications*, Springer, New York (2007).

[Mai17] T. L. Maier: *Characterization of gold/copper nanostructures on silicon electrodes for applications in photoelectrochemical CO_2 conversion*, Master's Thesis, Technical University of Munich, München (2017).

[Mar13] A. Marimuthu, J. Zhang, and S. Linic: *Tuning Selectivity in Propylene Epoxidation by Plasmon Mediated Photo-Switching of Cu Oxidation State*, Science **339**, 1590 (2013).

[May19] M. M. May and K. Rehfeld: *ESD Ideas: Photoelectrochemical carbon removal as negative emission technology*, Earth System Dynamics **10**, 1 (2019).

[Mea64] C. A. Mead and W. G. Spitzer: *Fermi Level Position at Metal-Semiconductor Interfaces*, Physical Review **134**, A713 (1964).

[Mei83] M. Meier and A. Wokaun: *Enhanced fields on large metal particles: dynamic depolarization*, Optics Letters **8**, 581 (1983).

[Min90] J. Minelly and M. Suyama: *Wavelength combining fused-taper couplers with low sensitivity to polarisation for use with 1480 nm-pumped erbium-doped fibre amplifiers*, Electronics Letters **26**, 523 (1990).

[Moc02] J. J. Mock, M. Barbic, D. R. Smith, D. A. Schultz, and S. Schultz: *Shape effects in plasmon resonance of individual colloidal silver nanoparticles*, The Journal of Chemical Physics **116**, 6755 (2002).

[Nag16] R. D. Nagel, T. Haeberle, M. Schmidt, P. Lugli, and G. Scarpa: *Large Area Nano-transfer Printing of Sub-50-nm Metal Nanostructures Using Low-cost Semi-flexible Hybrid Templates*, Nanoscale Research Letters **11** (2016).

[Nag17] R. D. Nagel, S. Filser, T. Zhang, A. Manzi, K. Schönleber, J. Lindsly, J. Zimmermann, T. L. Maier, G. Scarpa, K. Krischer, and P. Lugli: *Nanoimprint methods for the fabrication of macroscopic plasmonically active metal nanostructures*, Journal of Applied Physics **121**, 084305 (2017).

[Nag19] R. D. Nagel: *PhD thesis (in preparation)*, PhD Thesis, Technical University of Munich, München (2019).

[Nah17] S. Nahar, M. Zain, A. Kadhum, H. Hasan, and M. Hasan: *Advances in Photocatalytic CO_2 Reduction with Water: A Review*, Materials **10**, 629 (2017).

[Nak92] Y. Nakato and H. Tsubomura: *Silicon photoelectrodes modified with ultrafine metal islands*, Electrochimica Acta **37**, 897 (1992).

[Nak15] A. Nakamura, Y. Ota, K. Koike, Y. Hidaka, K. Nishioka, M. Sugiyama, and K. Fujii: *A 24.4% solar to hydrogen energy conversion efficiency by combining concentrator photovoltaic modules and electrochemical cells*, Applied Physics Express **8**, 107101 (2015).

[Nal16] A. Naldoni, F. Riboni, U. Guler, A. Boltasseva, V. M. Shalaev, and A. V. Kildishev: *Solar-Powered Plasmon-Enhanced Heterogeneous Catalysis*, Nanophotonics **5** (2016).

[NIS18] NIST: *NIST Chemistry WebBook*, NIST Chemistry WebBook (2018).

[O'G82] W. O'Grady and J. Zagal: *Mechanism of O_2 reduction in super acids*, The Electrochemical Society Extended Abstracts **82-2**, 486 (1982).

[O'N51] M. J. O'Neal and T. P. Wier: *Mass Spectrometry of Heavy Hydrocarbons*, Analytical Chemistry **23**, 830 (1951).

[Pal03] E. D. Palik (ed.): *Handbook of optical constants of solids. 3: [...]*, Acad. Press, San Diego, Calif. (2003).

[Par92] A. Parthasarathy: *Temperature Dependence of the Electrode Kinetics of Oxygen Reduction at the Platinum/Nafion® Interface—A Microelectrode Investigation*, Journal of The Electrochemical Society **139**, 2530 (1992).

[Phi62] J. C. Phillips: *Band Structure of Silicon, Germanium, and Related Semiconductors*, Physical Review **125**, 1931 (1962).

[Pin86] P. N. Pintauro: *An electrochemical method for determining natural convection mass transfer boundary-layer thicknesses*, International Journal of Heat and Mass Transfer **29**, 741 (1986).

[Qia14] J. Qiao, Y. Liu, F. Hong, and J. Zhang: *A review of catalysts for the electroreduction of carbon dioxide to produce low-carbon fuels*, Chem. Soc. Rev. **43**, 631 (2014).

[RC11] P. Rodríguez-Cantó, M. Martínez-Marco, F. J. Rodríguez-Fortuño, B. Tomás-Navarro, R. Ortuño, S. Peransí-Llopis, and A. Martínez: *Demonstration of near infrared gas sensing using gold nanodisks on functionalized silicon*, Optics Express **19**, 7664 (2011).

[RF09] J. Rodríguez-Fernández, A. M. Funston, J. Pérez-Juste, R. A. Álvarez Puebla, L. M. Liz-Marzán, and P. Mulvaney: *The effect of surface roughness on the plasmonic response of individual sub-micron gold spheres*, Physical Chemistry Chemical Physics **11**, 5909 (2009).

[Sch88] B. R. Scharifker: *Diffusion to ensembles of microelectrodes*, Journal of Electroanalytical Chemistry and Interfacial Electrochemistry **240**, 61 (1988).

[Sch10] W. Schmickler and E. Santos: *Interfacial electrochemistry*, Springer, Berlin (2010), second edn., oCLC: 845617119.

[Sch13] K. J. P. Schouten, E. Pérez Gallent, and M. T. M. Koper: *Structure Sensitivity of the Electrochemical Reduction of Carbon Monoxide on Copper Single Crystals*, ACS Catalysis **3**, 1292 (2013).

[Sch14] K. J. P. Schouten, E. Pérez Gallent, and M. T. Koper: *The influence of pH on the reduction of CO and CO2 to hydrocarbons on copper electrodes*, Journal of Electroanalytical Chemistry **716**, 53 (2014).

[Sch15a] M. Schalenbach, T. Hoefner, P. Paciok, M. Carmo, W. Lueke, and D. Stolten: *Gas Permeation through Nafion. Part 1: Measurements*, The Journal of Physical Chemistry C **119**, 25145 (2015).

[Sch15b] K. Schönleber: *Self-organization phenomena during the electrodissolution of silicon*, PhD Thesis, Technical University of Munich, München (2015).

[Sch15c] M. Schreier, L. Curvat, F. Giordano, L. Steier, A. Abate, S. M. Zakeeruddin, J. Luo, M. T. Mayer, and M. Grätzel: *Efficient photosynthesis of carbon monoxide from* CO_2 *using perovskite photovoltaics*, Nature Communications **6** (2015).

[Sha11] M. Shao, A. Peles, and K. Shoemaker: *Electrocatalysis on Platinum Nanoparticles: Particle Size Effect on Oxygen Reduction Reaction Activity*, Nano Letters **11**, 3714 (2011).

[She10] W. Sheng, H. A. Gasteiger, and Y. Shao-Horn: *Hydrogen Oxidation and Evolution Reaction Kinetics on Platinum: Acid vs Alkaline Electrolytes*, Journal of The Electrochemical Society **157**, B1529 (2010).

[Shi93] R. Shiratsuchi: *Pulsed Electroreduction of* CO_2*] on Copper Electrodes*, Journal of The Electrochemical Society **140**, 3479 (1993).

[Sie13] T. Siegfried, Y. Ekinci, O. J. Martin, and H. Sigg: *Engineering Metal Adhesion Layers That Do Not Deteriorate Plasmon Resonances*, ACS Nano **7**, 2751 (2013).

[Sin15] M. R. Singh, E. L. Clark, and A. T. Bell: *Thermodynamic and achievable efficiencies for solar-driven electrochemical reduction of carbon dioxide to transportation fuels*, Proceedings of the National Academy of Sciences **112**, E6111 (2015).

[Smi86] A. Smith: *The Coblentz Society Desk Book of Infrared Spectra*, Coblentz Society, Incorporated (1986).

[Smi16] W. A. Smith: *Photoelectrochemical Cell Design, Efficiency, Definitions, Standards, and Protocols*, in S. Giménez and J. Bisquert (eds.), *Photoelectrochemical Solar Fuel Production*, Springer International Publishing, Cham (2016), 163–197.

[Son18] H. Song, X. Meng, T. D. Dao, W. Zhou, H. Liu, L. Shi, H. Zhang, T. Nagao, T. Kako, and J. Ye: *Light-Enhanced Carbon Dioxide Activation and Conversion by Effective Plasmonic Coupling Effect of Pt and Au Nanoparticles*, ACS Applied Materials & Interfaces **10**, 408 (2018).

[SP07] J. Salvador-Pascual, S. Citalán-Cigarroa, and O. Solorza-Feria: *Kinetics of oxygen reduction reaction on nanosized Pd electrocatalyst in acid media*, Journal of Power Sources **172**, 229 (2007).

[Spi57] W. Spitzer and H. Y. Fan: *Infrared Absorption in n-Type Silicon*, Physical Review **108**, 268 (1957).

[Spi04] C. Spiegelberg, J. Geng, Y. Hu, Y. Kaneda, S. Jiang, and N. Peyghambarian: *Low-Noise Narrow-Linewidth Fiber Laser at 1550 nm (June 2003)*, Journal of Lightwave Technology **22**, 57 (2004).

[Spi12] P. Spinelli, V. E. Ferry, J. van de Groep, M. van Lare, M. A. Verschuuren, R. E. I. Schropp, H. A. Atwater, and A. Polman: *Plasmonic light trapping in thin-film Si solar cells*, Journal of Optics **14**, 024002 (2012).

[Ste11] M. Sterner, M. Jentsch, and U. Holzhammer: *Energiewirtschaftliche und ökologische Bewertung eines Windgas-Angebotes*, Fraunhofer Institut für Windenergie und Energiesystemtechnik (IWES) Kassel (2011).

[Ste18] W. Steffen, J. Rockström, K. Richardson, T. M. Lenton, C. Folke, D. Liverman, C. P. Summerhayes, A. D. Barnosky, S. E. Cornell, M. Crucifix, J. F. Donges, I. Fetzer, S. J. Lade, M. Scheffer, R. Winkelmann, and H. J. Schellnhuber: *Trajectories of the Earth System in the Anthropocene*, Proceedings of the National Academy of Sciences **115**, 8252 (2018).

[Sub11] R. Subbaraman, D. Tripkovic, D. Strmcnik, K.-C. Chang, M. Uchimura, A. P. Paulikas, V. Stamenkovic, and N. M. Markovic: *Enhancing Hydrogen Evolution Activity in Water Splitting by Tailoring Li+-Ni(OH)$_2$-Pt Interfaces*, Science **334**, 1256 (2011).

[Sub12] R. Subbaraman, D. Tripkovic, K.-C. Chang, D. Strmcnik, A. P. Paulikas, P. Hirunsit, M. Chan, J. Greeley, V. Stamenkovic, and N. M. Markovic: *Trends in activity for the water electrolyser reactions on 3d M(Ni,Co,Fe,Mn) hydr(oxy)oxide catalysts*, Nature Materials **11**, 550 (2012).

[Sun09] S. Sun, W. Wang, L. Zhang, M. Shang, and L. Wang: *Ag@C core/shell nanocomposite as a highly efficient plasmonic photocatalyst*, Catalysis Communications **11**, 290 (2009).

[Sze07] S. M. Sze and K. K. Ng: *Physics of semiconductor devices*, Wiley-Interscience, Hoboken, N.J. (2007).

[Tan12] W. Tang, A. A. Peterson, A. S. Varela, Z. P. Jovanov, L. Bech, W. J. Durand, S. Dahl, J. K. Nørskov, and I. Chorkendorff: *The importance of surface morphology in controlling the selectivity of polycrystalline copper for CO$_2$ electroreduction*, Phys. Chem. Chem. Phys. **14**, 76 (2012).

[Tia07] Z.-Q. Tian, B. Ren, J.-F. Li, and Z.-L. Yang: *Expanding generality of surface-enhanced Raman spectroscopy with borrowing SERS activity strategy*, Chemical Communications , 3514 (2007).

[Tro18] C. Trompoukis, A. Abass, J.-W. Schüttauf, T. Bosserez, J. Rongé, J. Lauwaert, J. A. Martens, and R. Baets: *Porous multi-junction thin-film silicon solar cells for scalable solar water splitting*, Solar Energy Materials and Solar Cells **182**, 196 (2018).

[Tru11] A. Truegler, J.-C. Tinguely, J. R. Krenn, A. Hohenau, and U. Hohenester: *Influence of surface roughness on the optical properties of plasmonic nanoparticles*, Physical Review B **83** (2011).

[Tru14] A. Truegler, J.-C. Tinguely, G. Jakopic, U. Hohenester, J. R. Krenn, and A. Hohenau: *Near-field and SERS enhancement from rough plasmonic nanoparticles*, Physical Review B **89** (2014).

[Urb14] F. Urbain, K. Wilken, V. Smirnov, O. Astakhov, A. Lambertz, J.-P. Becker, U. Rau, J. Ziegler, B. Kaiser, W. Jaegermann, and F. Finger: *Development of Thin Film Amorphous Silicon Tandem Junction Based Photocathodes Providing High Open-Circuit Voltages for Hydrogen Production*, International Journal of Photoenergy **2014**, 1 (2014).

[Urb15] F. Urbain, V. Smirnov, J.-P. Becker, U. Rau, J. Ziegler, B. Kaiser, W. Jaegermann, and F. Finger: *Application and modeling of an integrated amorphous silicon tandem based device for solar water splitting*, Solar Energy Materials and Solar Cells **140**, 275 (2015).

[Urb16] F. Urbain, J.-P. Becker, V. Smirnov, J. Ziegler, F. Yang, B. Kaiser, W. Jaegermann, S. Hoch, A. Maljusch, U. Rau, and F. Finger: *Influence of the operating temperature on the performance of silicon based photoelectrochemical devices for water splitting*, Materials Science in Semiconductor Processing **42**, 142 (2016).

[Urb17] F. Urbain, P. Tang, N. M. Carretero, T. Andreu, L. G. Gerling, C. Voz, J. Arbiol, and J. R. Morante: *A prototype reactor for highly selective solar-driven CO_2 reduction to synthesis gas using nanosized earth-abundant catalysts and silicon photovoltaics*, Energy & Environmental Science **10**, 2256 (2017).

[Var16a] A. S. Varela, W. Ju, T. Reier, and P. Strasser: *Tuning the Catalytic Activity and Selectivity of Cu for CO_2 Electroreduction in the Presence of Halides*, ACS Catalysis **6**, 2136 (2016).

[Var16b] A. S. Varela, M. Kroschel, T. Reier, and P. Strasser: *Controlling the selectivity of CO_2 electroreduction on copper: The effect of the electrolyte concentration and the importance of the local pH*, Catalysis Today **260**, 8 (2016).

[Wü05] P. Würfel: *Physics of solar cells: from principles to new concepts*, Wiley-VCH, Weinheim (2005).

[Wü18] J. Wüllenweber: *Bifunctional Mechanism of Hydrogen Evolution on n-Type Silicon Electrodes Decorated with Mesoscopic Gold Structures*, Bachelor's Thesis, Technical University of Munich, München (2018).

[Wal10] M. G. Walter, E. L. Warren, J. R. McKone, S. W. Boettcher, Q. Mi, E. A. Santori, and N. S. Lewis: *Solar Water Splitting Cells*, Chemical Reviews **110**, 6446 (2010).

[Wan12] P. Wang, B. Huang, Y. Dai, and M.-H. Whangbo: *Plasmonic photocatalysts: harvesting visible light with noble metal nanoparticles*, Physical Chemistry Chemical Physics **14**, 9813 (2012).

[Wan13] C. Wang, O. Ranasingha, S. Natesakhawat, P. R. Ohodnicki, M. Andio, J. P. Lewis, and C. Matranga: *Visible light plasmonic heating of Au–ZnO for the catalytic reduction of CO_2*, Nanoscale **5**, 6968 (2013).

[Wan17] C. Wang, X.-G. Nie, Y. Shi, Y. Zhou, J.-J. Xu, X.-H. Xia, and H.-Y. Chen: *Direct Plasmon-Accelerated Electrochemical Reaction on Gold Nanoparticles*, ACS Nano **11**, 5897 (2017).

[War12] S. C. Warren and E. Thimsen: *Plasmonic solar water splitting*, Energy Environ. Sci. **5**, 5133 (2012).

[Was45] H. Washburn, H. Wiley, S. Rock, and C. Berry: *Mass Spectrometry*, Industrial & Engineering Chemistry Analytical Edition **17**, 74 (1945).

[Wel67] P. Welch: *The use of fast Fourier transform for the estimation of power spectra: A method based on time averaging over short, modified periodograms*, IEEE Transactions on Audio and Electroacoustics **15**, 70 (1967).

[Wel06] C. M. Welch and R. G. Compton: *The use of nanoparticles in electroanalysis: a review*, Analytical and Bioanalytical Chemistry **384**, 601 (2006).

[Wie03] A. Wieckowski, E. R. Savinova, and C. G. Vayenas (eds.): *Catalysis and electrocatalysis at nanoparticle surfaces*, Marcel Dekker, New York (2003).

[Wol84] O. Wolter and J. Heitbaum: *Differential Electrochemical Mass Spectroscopy (DEMS) - a New Method for the Study of Electrode Processes*, Berichte der Bunsengesellschaft für physikalische Chemie **88**, 2 (1984).

[Won06] A. Wonders, T. Housmans, V. Rosca, and M. Koper: *On-line mass spectrometry system for measurements at single-crystal electrodes in hanging meniscus configuration*, Journal of Applied Electrochemistry **36**, 1215 (2006).

[Wu18] N. Wu: *Plasmonic metal–semiconductor photocatalysts and photoelectrochemical cells: a review*, Nanoscale **10**, 2679 (2018).

[Wut15] A. Wuttig and Y. Surendranath: *Impurity Ion Complexation Enhances Carbon Dioxide Reduction Catalysis*, ACS Catalysis **5**, 4479 (2015).

[Xie14] J.-F. Xie, Y.-X. Huang, W.-W. Li, X.-N. Song, L. Xiong, and H.-Q. Yu: *Efficient electrochemical CO_2 reduction on a unique chrysanthemum-like Cu nanoflower electrode and direct observation of carbon deposite*, Electrochimica Acta **139**, 137 (2014).

[Yen09] C.-W. Yen and M. A. El-Sayed: *Plasmonic Field Effect on the Hexacyanoferrate (III)-Thiosulfate Electron Transfer Catalytic Reaction on Gold Nanoparticles: Electromagnetic or Thermal?*, The Journal of Physical Chemistry C **113**, 19585 (2009).

[You17] J. L. Young, M. A. Steiner, H. Döscher, R. M. France, J. A. Turner, and T. G. Deutsch: *Direct solar-to-hydrogen conversion via inverted metamorphic multi-junction semiconductor architectures*, Nature Energy **2**, 17028 (2017).

[Yu70] A. Yu: *Electron tunneling and contact resistance of metal-silicon contact barriers*, Solid-State Electronics **13**, 239 (1970).

[Zem87] E. J. Zeman and G. C. Schatz: *An accurate electromagnetic theory study of surface enhancement factors for silver, gold, copper, lithium, sodium, aluminum, gallium, indium, zinc, and cadmium*, The Journal of Physical Chemistry **91**, 634 (1987).

[Zha13] X. Zhang, Y. L. Chen, R.-S. Liu, and D. P. Tsai: *Plasmonic photocatalysis*, Reports on Progress in Physics **76**, 046401 (2013).

[Zha17] X. Zhang, X. Li, D. Zhang, N. Q. Su, W. Yang, H. O. Everitt, and J. Liu: *Product selectivity in plasmonic photocatalysis for carbon dioxide hydrogenation*, Nature Communications **8**, 14542 (2017).

[Zie14] J. Ziegler, B. Kaiser, W. Jaegermann, F. Urbain, J.-P. Becker, V. Smirnov, and F. Finger: *Photoelectrochemical and Photovoltaic Characteristics of Amorphous-Silicon-Based Tandem Cells as Photocathodes for Water Splitting*, ChemPhysChem **15**, 4026 (2014).

[Zim17] J. Zimmermann: *Plasmonic Catalysis of the Electrochemical Reduction of Carbon Dioxide on Gold Nanostructures through the Excitation of Molecular Vibration Modes*, Master's Thesis, Technical University of Munich, München (2017).

[Zor11] I. Zorić, M. Zäch, B. Kasemo, and C. Langhammer: *Gold, Platinum, and Aluminum Nanodisk Plasmons: Material Independence, Subradiance, and Damping Mechanisms*, ACS Nano **5**, 2535 (2011).